

ABSTRACT

KALANYAN, BERC. Atomic Layer Deposition and Nucleation of Metals and Metal Oxides: Selective Area Reactions and Conformal 3D Processing. (Under the direction of Gregory N. Parsons).

Modern electronic devices require nanoscale integration of conductive materials. Atomic layer deposition (ALD) is a vacuum-based technique that is used to produce conformal thin films over complex substrate geometries with Angstrom-level thickness control. As electronic device geometries become more spatially complex, an in depth understanding of ALD surface chemistry is increasingly important, particularly during the initial stages of thin film nucleation. This work focuses closely on applications for which ALD is critically needed in order to deposit conductive films in a surface selective fashion or into high surface area substrates.

Atomic layer deposition has been an important part of integrated circuit manufacturing for more than a decade. Metal interconnect fabrication for integrated circuits typically requires a sequence of lithography, deposition, planarization, and etch steps. Each process step needs to be spatially aligned with the previous step with nm accuracy. Pattern alignment errors are compounded by the number of steps needed to produce the desired features, especially as fabrication moves to the 10 nm node and beyond. Area selective metal ALD is an emerging technology that may enable self-aligned patterns without the use of blocking layers. If metal deposition can be confined to areas where it is needed, perfect pattern alignment can be realized and lithography steps may be eliminated. By choosing inherently selective ALD chemistries (e.g. SiH_4/WF_6) and appropriate process conditions, one can favor surface selective deposition. One aspect of this thesis focuses on nucleation and

growth characteristics of W ALD on Si:H and SiO₂ surfaces with various surface treatments and modified gas pulsing schemes.

A second area of inquiry concerns the integration of tungsten coatings onto textiles for electrically conductive textiles. For this work, a tungsten ALD process is developed using a dilute silane (SiH₄) precursor. Film thickness, mass gain, and conductivity saturation are demonstrated for the process and applied to high surface area microstructured nylon-6 nonwoven mats. Low temperature ALD using WF₆ and 2% SiH₄ can yield highly conductive coatings on nylon-6 microfiber mats. Coated mats are flexible and supple with effective conductivities of ~1,000 S/cm. We explore the effects of alumina nucleation layers, the magnitude of reactant exposure, and deposition temperature on coatings properties. Conformally coated nylon mats maintain their conductivity after being flexed and this metal ALD process demonstrates solvent-free functionalization of textiles for electronic applications.

Conductive thin film coatings are also an important component in solar energy conversion devices. Thin TiO₂ films are routinely deposited into mesoporous oxide scaffolds for photoelectrochemical and dye-sensitized solar cell applications. The high surface area and mesoporosity of the scaffolds present challenges for ALD processes, specifically as process chemistry and conditions relate to coating uniformity. We investigate ALD deposition into porous structures in real time with the quartz crystal microbalance technique. We use conventional and hold-step precursor exposures to understand the effect of reactant diffusion and byproduct purging during ALD. Mesoporous films (10-20 nm particles) cast up to 15 μm thick are used for ALD TiO₂ infiltration and uniformity studies. To highlight the importance of reaction chemistry, we choose two dissimilar titanium sources: titanium tetrachloride

(TiCl₄) and titanium tetraisopropoxide (TTIP). We compare film uniformities with secondary ion mass spectrometry depth profiling and discuss processing conditions needed to produce conformal coatings. We find that ALD processes with TTIP produce significantly more uniform films as compared with the TiCl₄ precursor.

© Copyright 2014 Berc Kalanyan

All Rights Reserved

Atomic Layer Deposition and Nucleation of Metals and Metal Oxides:
Selective Area Reactions and Conformal 3D Processing

by
Berc Kalanyan

A dissertation submitted to the Graduate Faculty of
North Carolina State University
in partial fulfillment of the
requirements for the degree of
Doctor of Philosophy

Chemical Engineering

Raleigh, North Carolina

2015

APPROVED BY:

Dr. Gregory N. Parsons
Committee Chair

Dr. Michael D. Dickey

Dr. Peter S. Fedkiw

Dr. Walter W. Weare

DEDICATION

To my family, friends, and fiance for their support and understanding during my long journey toward this document.

BIOGRAPHY

Berc Kalanyan grew up in Istanbul, Turkey until he immigrated to the United States in 2000. After attending high school near Philadelphia, he earned his bachelors degrees in chemical engineering and English literature from Lehigh University in 2009. During his undergraduate education, he completed two summer research programs at public universities, one of which was with Professor Gregory Parsons at NC State University. He subsequently pursued a Ph.D. in chemical engineering under the guidance of Prof. Parsons. His research centered around the development of conductive atomic layer deposition (ALD) processes, with specific applications in selective area deposition, conductive textiles, and electrochemical energy devices. Research interests with respect to ALD include early nucleation, surface chemistry, *in situ* diagnostics, and new processing schemes. Berc also has experience with photoelectrochemistry, electrodeposition, and electrochemical energy devices. Berc was awarded a National Research Council fellowship to study ALD process diagnostics at the National Institute of Standards and Technology (NIST) in Gaithersburg, MD. He will begin his appointment in early 2015.

ACKNOWLEDGMENTS

I would like to thank Chemical and Biomolecular Engineering departmental staff, faculty, and my coworkers for all their help and support. I am grateful to Dr. Parsons for his mentorship and attentiveness to his students. Additionally, I am grateful for equipment and measurement support I received from staff at the Analytical Instrumentation Facility.

TABLE OF CONTENTS

LIST OF TABLES.....	x
LIST OF FIGURES.....	xi
CHAPTER 1. Introduction and Background.....	1
1.1 Introduction to Atomic Layer Deposition.....	1
1.2 Materials Grown by ALD.....	3
1.2.1 Metals deposition from metal halide sources.....	3
1.2.2 Conductive metal oxides.....	6
1.3 Substrates for ALD processing.....	8
1.3.1 Silicon and silica.....	9
1.3.2 Polyamides.....	10
1.4 References.....	18
CHAPTER 2. Low Temperature Atomic Layer Deposition of Tungsten using Tungsten Hexafluoride and Highly-diluted Silane in Argon.....	26
2.1 Abstract.....	26
2.2 Introduction.....	27
2.3 Results and Discussion.....	29
2.3.1 Growth Rate versus Temperature and SiH ₄ Exposure.....	29
2.3.2 Film Structure and Composition.....	32
2.4 Experimental.....	35
2.5 Acknowledgments.....	39
2.6 References.....	48

CHAPTER 3. Highly Conductive and Flexible Nylon-6 Nonwoven Fiber Mats Formed using Tungsten Atomic Layer Deposition.....	50
3.1 Abstract.....	50
3.2 Introduction.....	51
3.3 Experimental.....	52
3.4 Results and Discussion.....	57
3.4.1 W ALD Growth Rate Calibration on Anodic Aluminum Oxide.....	57
3.4.2 W ALD Nucleation and Conformality on Nylon-6 Nonwovens.....	58
3.4.3 Effect of WF ₆ and SiH ₄ Exposure on W ALD on Nylon Fibers.....	60
3.4.4 Reactant Species Transport through the 3D Fiber Network.....	61
3.4.5 Mechanical Response of W-Coated Nylon-6 Nonwovens.....	63
3.5 Summary and Conclusions.....	64
3.6 Acknowledgments.....	64
3.7 References.....	75
CHAPTER 4. Selective Nucleation of Tungsten ALD on Silicon and Silicon Oxide.....	77
4.1 Abstract.....	77
4.2 Introduction.....	78
4.3 Background.....	79
4.4 Experimental.....	82
4.4.1 Substrate surface preparation.....	82
4.4.2 Reactor configuration.....	82
4.4.3 Gas pulsing sequences for tungsten growth.....	83

4.4.4 Characterization methods.....	84
4.5 Results and Discussion.....	85
4.5.1 Substrate dependent nucleation of W on Si and SiO ₂	85
4.5.2 Nucleation control by a modified ALD scheme.....	88
4.5.3 Influence of reactor walls and wafer loading effects on deposition.....	92
4.6 Summary and Conclusions.....	94
4.7 Acknowledgments.....	95
4.8 References.....	109
CHAPTER 5. Effect of Precursor Chemistry and Delivery Conditions on Coating Uniformity In Mesoporous Metal Oxide Scaffolds During ALD Processes.....	113
5.1 Abstract.....	113
5.2 Introduction.....	114
5.3 Experimental.....	117
5.4 Results and Discussion.....	120
5.4.1 Mass uptake on planar TiO ₂	122
5.4.2 Mass uptake on mesoporous TiO ₂	124
5.4.3 Pore filling of mesoporous TiO ₂ and ITO scaffolds.....	129
5.5 Summary and Conclusions.....	130
5.6 Acknowledgements.....	132
5.7 References.....	142
CHAPTER 6. Tungsten atomic layer deposition using WF ₆ and a silyl pyrazine reducing agent.....	144

6.1 Abstract.....	144
6.2 Introduction.....	144
6.3 Experimental.....	146
6.4 Results and Discussion.....	148
6.5 Summary and Conclusions.....	155
6.6 Acknowledgments.....	155
6.7 References.....	162
APPENDICES.....	164
APPENDIX A1. Reproducible Fabrication of High-Performance Silicon Photocathodes for Water Splitting.....	165
A1.1 Abstract.....	165
A1.2 Introduction.....	165
A1.3 Experimental.....	168
A1.4 Results and Discussion.....	171
A1.5 Summary and Conclusions.....	174
A1.6 References.....	185
APPENDIX A2. Atomic Layer Deposited Oxides for Passivation of Silicon Photoanodes for Solar Photoelectrochemical Cells.....	187
A2.1 Abstract.....	187
A2.2 Introduction.....	187
A2.3 Materials and Methods.....	189
A2.3.1 Atomic Layer Deposition.....	189

A2.3.2 Electrode Preparation and Testing.....	189
A2.4 Results and Discussion.....	191
A2.4.1 Electrodes on FTO Glass.....	191
A2.4.2 Electrodes on Ag-coated Glass.....	193
A2.4.3 Tandem PV-PEC Electrodes.....	194
A2.5 Conclusions.....	194
A2.6 Acknowledgments.....	194
A2.7 REFERENCES.....	201
APPENDIX B1. Stable anatase TiO ₂ coating on quartz fibers by atomic layer deposition for photoactive light-scattering in dye-sensitized solar cells*.....	202
APPENDIX B2. Stabilization of [Ru(bpy) ₂ (4,4'-(PO ₃ H ₂)bpy)] ²⁺ on Mesoporous TiO ₂ with Atomic Layer Deposition of Al ₂ O ₃ *.....	203
APPENDIX B3. Solution-Processed, Antimony-Doped Tin Oxide Colloid Films Enable High-Performance TiO ₂ Photoanodes for Water Splitting*.....	204
APPENDIX B4. Stabilizing Small Molecules on Metal Oxide Surfaces Using Atomic Layer Deposition*.....	206
APPENDIX B5. Three-dimensional self-assembled photonic crystals with high temperature stability for thermal emission modification*.....	208
APPENDIX B6. Solar water splitting in a molecular photoelectrochemical cell*.....	209
APPENDIX B7. Crossing the divide between homogeneous and heterogeneous catalysis in water oxidation*.....	210
APPENDIX B8. Atomic Layer Deposition of TiO ₂ on Mesoporous nanoITO: Conductive Core–Shell Photoanodes for Dye-Sensitized Solar Cells*.....	211

LIST OF TABLES

Table A1.S1. Experimental conditions reported for voltammograms from p-Si photocathodes plotted in the main text (Figure 1). Cells marked with a diamond (♦) indicate that the data were not reported in the referenced article.....179

Table A2.1. Ellipsometry results from bare and passivated n-Si photoanodes constructed on Ag-coated glass back contacts. Oxide growth was measured as the difference between native SiO₂ thickness before and after each electrochemical measurement. Dark and light measurements each consisted of 5 sweeps from -0.5 to 4 V and back to -0.5 V vs Ag/AgCl. The scan rate was 20 mV/s. A control electrode was also tested under the same conditions but not connected to the potentiostat. The control sample did not show any oxide growth.....200

LIST OF FIGURES

Figure 1.1. A typical A/B type ALD cycle with TMA and H ₂ O as reactant and co-reactant. Graphic courtesy of Gregory Parsons.....	12
Figure 1.2. ALD window sketch illustrating the possible shapes the growth per cycle curve can take as a function of temperature. Possible contributors to low or high growth rates include incomplete surface reaction, desorption of surface sites, precursor condensation, or precursor decomposition. Figure reproduced from 92.....	13
Figure 1.3. Sketch demonstrating various thin film growth modes observed during ALD. Vertical axis n denotes increasing number of reaction cycles. The growth modes shown are: (a) Frank-van der Merwe, (b) Volmer-Weber, (c) Stranski-Krastanov. Figure reproduced from 31.....	14
Figure 1.4. Growth rate as a function of deposition cycles for (a) substrate independent growth, (b) substrate-enhanced growth, (c) substrate-inhibited growth of type 1, and (d) substrate-inhibited growth of type 2. Figure reproduced from 31.....	15
Figure 1.5. Growth of native SiO _x as a function of time under laboratory room conditions. The surface is a small piece of piranha cleaned Si(100) wafer treated with a 30 second NH ₄ F-buffered aqueous HF solution dip, followed by a 30 second deionized H ₂ O rinse. Native oxide thickness was measured using a spectroscopic ellipsometer (J.A. Woollam Company, alpha-SE).....	16
Figure 1.6. Chemical representation of polyamide-6. One repeat unit is shown.....	17
Figure 2.1. Schematic view of the hot-wall tube flow ALD reactor used for these studies. The reactor has three precursor/reactant feed lines and two independent heating zones. Needle valves control silane and tungsten hexafluoride flow.....	40
Figure 2.2. Tungsten film thickness versus number of ALD cycles as measured by X-ray reflectivity. Deposition proceeded at 225°C using WF ₆ /N ₂ /2%SiH ₄ /N ₂ = 1/30/60/30 seconds, respectively. The pressure change during the silane exposure was 0.5 Torr corresponding to (0.02×0.5)Torr × 60 sec = 6·10 ⁵ L. The thickness for the film with 150 cycles was obtained by profilometry, demonstrating consistent thickness values from reflectivity and profilometry.....	41
Figure 2.3. Omega-2Theta scans from tungsten deposited at 225°C using a silane exposure of ~6×10 ⁵ L. In (a) the critical angle is shown for a typical ALD tungsten thin film. Reflections from 50 and 100 cycles of tungsten are shown in (b).....	42

Figure 2.4. ALD temperature window for the WF6/2% SiH4 process using SiH4 exposure of $\sim 6 \times 10^5$ L. An approximately flat temperature window appears between 200 and 300 °C. Some runs (\blacktriangle) showed very low growth rates, as discussed in the text.....43

Figure 2.5. Tungsten thickness per cycle after 100 ALD cycles at 150 °C plotted versus SiH4 exposure using a fixed WF6 exposure. Silane exposure was adjusted by changing the exposure time at fixed partial pressure, and by changing the partial pressure with fixed exposure time. The symbols correspond to the total pressure change during the dilute silane exposure. All the data sets fall on a single trend line indicating the silicon reaction rate scaling is no dependent on silane dilution. Growth shows gradual saturation with increasing silane exposure.....44

Figure 2.6. X-ray diffraction results from W samples deposited at three different temperatures using a silane exposure of 1.2×10^6 L. The data shows increasing crystallinity at higher deposition temperature.....45

Figure 2.7. SIMS depth profile showing W and Si signals collected from W samples deposited using 100 cycles at 150, 250, and 350°C. The silane \square P and exposure time are 0.5 Torr and 30 seconds, respectively, corresponding to 1.2×10^6 L.....46

Figure 2.8. SIMS depth profile of W films formed using 100 ALD cycles using different SiH4 exposure at 150°C. Data shows a small increase in silicon content with increasing silane exposure.....47

Figure 3.1. Top-down SEM micrographs of anodic aluminum oxide samples treated with different thicknesses of ALD tungsten at 250,000X magnification (scale bars are 200 nm). The imaged AAO substrates have approximately 250 nm diameter pores. Image (a) is an uncoated substrate. Image (b), (c), and (d) were collected after 25 cycles of Al2O3 and 25, 45, and 100 cycles of W respectively at 200°C. These images show pore shrinkage due to increasing ALD coating thicknesses. Samples coated with higher cycle numbers show increasingly rounded edges and softer features in the nanometer scale due to the conformality of the coatings.....66

Figure 3.2. Tungsten film thickness versus ALD cycle number on AAO and silicon substrates. Samples are pre-treated with 25 cycles of Al2O3 and processed at 200°C. Film thickness on the AAO were extracted from top-down SEM images of AAO pores shown in Figure 1.....67

Figure 3.3. A cross-sectional view of AAO pores with: (a) 45 cycles; and (b) 100 cycles of W ALD after breaking the coated AAO. The AAO templates are pre-treated with 25 cycles of Al2O3 and processed at 200°C. In each image, an inner tube of tungsten is surrounded by an outer AAO substrate shell, and the W thickness increases with ALD cycle number. The arrow in image (a) points to the outer side-wall of a W tube where the AAO shell was removed....68

Figure 3.4. Photograph showing nonwoven nylon-6 fiber mats after coating with 100 cycles of W ALD at 140°C. The sample on the left is not treated with Al₂O₃, resulting in poor tungsten nucleation on the fibers, whereas the sample on the right shows proper W nucleation as a result of pre-treatment with 25 cycles of Al₂O₃ at 140°C.....69

Figure 3.5. Micrographs of nylon-6 fibers (Allasso, Winged Fibers™) coated with 25 cycles of Al₂O₃ followed by 100 cycles of W at 160°C. The dark contrast is from the tungsten coating, which grows conformally around the fiber wings. The Al₂O₃ deposition is not visible at these magnifications. A cross-sectional SEM image of a PA-6 fibril is shown in (d), reproduced with permission from Allasso Industries Inc.....70

Figure 3.6. The effect of SiH₄ and WF₆ exposure on substrate mass gain after 25 Al₂O₃ cycles and 100 W ALD cycles at 145°C. The data points show mass uptake on the nylon fiber mat for: (open triangles) increasing silane exposure with fixed WF₆ exposure (= ~2×10⁵ L); and (closed squares) increasing WF₆ with fixed silane exposure (= ~4.5×10⁵ L). The pressure change during silane and WF₆ doses was 0.5 and 0.2 Torr, respectively. For films with 20% or more mass loading, the maximum error of the mean for fractional mass increase was ±5%, as shown by the error bars. The lines are a guide for the eye.....71

Figure 3.7. Fiber mat effective conductivity as a function of SiH₄ and WF₆ exposure for 25 cycles of Al₂O₃ and 100 cycles of W deposition at 145°C. The data symbols correspond to the samples shown in Figure 6. The conductivity is approximately 1000 S/cm, independent of exposure conditions when sufficient coating thickness is present. The data points show effective conductivity on the nylon fiber mat for: (open triangles) increasing silane exposure with fixed WF₆ exposure (= ~2×10⁵ L); and (closed squares) increasing WF₆ with fixed silane exposure (= ~4.5×10⁵ L). The lines are a guide for the eye. Each data point represents an average of 7 measurements for each sample. The standard error of the mean is smaller than the size of the data points.....72

Figure 3.8. The effect of varying silane dose times and short silane doses combined with varying hold times on W mass uptake on nylon-6 fiber mats. All samples were coated with 25 Al₂O₃ and 100 W cycles at 145°C. For the “hold” sequence, the silane dose time is set at 10 seconds after which the reactor is closed for a set hold time between 20 and 120 seconds. The remainder of the ALD cycle proceeded unchanged. We also compare runs done with different silane dose times without the hold step (triangle symbols, data from Figure 6). With the 10 second silane exposure, the hold step does not enhance W mass uptake on the fiber mat substrates. The error bars represent an uncertainty of ±5% in the mass loading analysis.....73

Figure 3.9. Change in conductivity for conducting layers deposited on fiber substrates when the fiber mats are bent around increasingly smaller cylinders. The conductivity of ZnO on polypropylene fibers is approximately 20 S/cm as prepared, but it decreases substantially upon bending. Similar experiments for the W-coated nylon studied here shows ~90% conductivity retention upon bending. Data from ZnO coated polypropylene is from reference

20. Tungsten-coated samples were prepared with 25 Al ₂ O ₃ and 100 W cycles at 145°C. Each data point represents the mean of two conductivity values collected from each sample, and the error bars show typical variation.....	74
Figure 4.1. Micrographs of W nucleation on Si:H and SiO ₂ substrates. ALD cycle numbers are indicated on each frame. Scale bars correspond to 200 nm.....	96
Figure 4.2. SE parameter delta (Δ) is plotted as indicators of W nucleation on Si:H and SiO ₂ surfaces. Diamond (\blacklozenge) symbols indicate Si:H, circles (\bullet) indicate SiO ₂ (C), and triangles (\blacktriangle) indicate SiO ₂	97
Figure 4.3. SE parameter delta is indicators of W nucleation on different surfaces prepared with different gas pulsing sequences. Diamonds (\blacklozenge) denote Si:H, circles (\bullet) indicate SiO ₂ (C), and triangles (\blacktriangle) correspond to SiO ₂ surfaces. Filled symbols represent A/B and hollow symbols represent A/H/B ALD cycles.....	98
Figure 4.4. Micrographs of W nucleation on Si:H, SiO ₂ (C), and SiO ₂ with A/B (top rows) and A/H/B processes (bottom rows). ALD cycle numbers are indicated on each frame. Scale bars correspond to 200 nm.....	99
Figure 4.5. Film thickness measured by XRR for (\blacklozenge) Si:H and (\bullet) SiO ₂ (C) surfaces. Data reported include the thickness of the silicide interface. Filled symbols represent A/B and hollow symbols represent A/H/B ALD pulsing sequences.....	100
Figure 4.6. XPS spectra for the W 4f region on SiO ₂ substrates, after 30 cycles of: a) A/B; b) A+H/B; c) A/B+H; and d) A+H/B+H.....	101
Figure 4.7. SE parameter delta (Δ) is plotted for Si:H and SiO ₂ surfaces. Diamond (\blacklozenge) symbols indicate Si:H and triangles (\blacktriangle) indicate SiO ₂ . The black symbols are from the conventional A/B process, while the gray symbols indicate the modified A/B+H process...102	102
Figure 4.8. Film thickness on Si:H substrates measured by XRR for (\blacklozenge) A/B, (\blacklozenge) A/H/B, and (\blacklozenge) A/B+H gas pulsing sequences (gray diamonds). Thickness points in the plot include the thickness of the silicide interface.....	103
Figure 4.9. Photographs of one Si:H and SiO ₂ surfaces that were loaded simultaneously into the ALD reactor. On the left, one Si:H surface is upstream from two SiO ₂ chips. On the right, Si:H is downstream from the SiO ₂ surfaces. The large black arrow indicates gas flow direction and small white arrows point to spurious W deposition due to loading effects. Wafer pieces are ~ 15x15 mm.....	104

Figure 4.10. Photographs of Au-patterned SiO₂ surfaces that were processed coated with: (a) 0 cycles; (b) 30 A/B cycles; (c) 30 A/B+H cycles at 220°C. The distance between the Au strips is ~5 mm.....105

Figure 4.S1. Time traces for m/z 30, 2, 279, 86, and 20 are shown for the SiH₄/WF₆ ALD process. The data are representative for steady-state deposition in an empty reactor at 220°C. Gas phase products are from gas-solid reactions on reactor walls and substrate holder.....106

Figure 4.S2. Photographs of W nucleation on Si:H and SiO₂(C) substrates. ALD cycle numbers are indicated on each frame. Surfaces shown are 5 x 5 mm in size.....107

Figure 4.S3. XPS spectra from the C 1s region for SiO₂(C) and SiO₂ substrates. Carbon content is significantly higher on the SiO₂(C) surface.....108

Figure 5.1. SIMS depth profile from a 5 μm thick nanoITO scaffold coated with 60 cycles of TiCl₄/H₂O at 150°C. The location of the ITO/FTO and FTO/glass interfaces are deduced from changes in the SnO⁻ and Si⁻ secondary ion counts.....133

Figure 5.2. SIMS depth profile showing TiO⁻/SnO⁻ secondary ion ratio as an indicator of coating uniformity. Two scaffold depths are shown: (a) 5 μm and (b) 15 μm of nanoITO. Both scaffolds have 60 cycles of TiCl₄/H₂O applied at 150°C, with 1s exposures and 60s purges. Sputter time has been normalized to nominal nanoITO film thickness.....134

Figure 5.3. Mass uptake measurements from a planar QCM crystal. Panel (a) shows linear mass increase during 200 cycles of deposition on the crystal. The blue curve denotes the TiCl₄/H₂O process and the red curve denotes the TTIP/H₂O process. A magnified section of panel (a) is shown in panel (b). Individual mass gain and loss values from TiCl₄, TTIP, and H₂O exposures are given as mass gain:loss ratios. Arrows indicate the beginning of exposure and purge steps.....135

Figure 5.4. Mass uptake measurements from a high surface area QCM crystal (nanoTiO₂). Panel (a) shows mass uptake during 5 cycles of the TiCl₄/H₂O ALD process. Panel (b) shows the same measurement for the TTIP/H₂O chemistry. For both chemistries, exposure and purge times are 1s and 60s, respectively. Above each main panel are the mass gain trends for the entire process (60 ALD cycles). Individual mass gain and loss values from TiCl₄, TTIP, and H₂O exposures are given as a gain/loss ratio. Below each panel are the corresponding pressure pulses recorded during each measurement.....136

Figure 5.5. Mass uptake measurements showing the effect of 60 s gas hold steps inserted into the ALD sequence. Exposure and purge times are the same as in Figure 4.....137

Figure 5.6. Plan-view SEM images of nanoTiO₂ scaffolds with: (a) no coating; (b) TiCl₄/H₂O 1 s exposures; (c) TiCl₄/H₂O, 60 s exposures; (d) TTIP/H₂O 1 s exposures; and

(e) TTIP/H ₂ O 60 s exposures. All coatings were applied at 150°C. Scale bars are 300 nm and the images were collected under the same conditions without sputtering of conductive films.	138
Figure 5.7. Mass uptake measurements on nanoTiO ₂ showing the effect of extended hold and purge steps. Exposure, hold, and purge times are 1 s, 60 min, and 60 min. Only 5 cycles were recorded. The process conditions are the same as in Figure 4.....	139
Figure 5.8. SIMS depth profiles from a 5 μm thick nanoITO scaffold coated with (a) 60 cycles of TiCl ₄ /H ₂ O, (b) 200 cycles of TiCl ₄ /H ₂ O, and (c) 350 cycles of TTIP/H ₂ O at 150°C.....	140
Figure 5.9. Microbalance data from nanoTiO ₂ coated crystals showing changes in mass uptake per cycle after a large number of ALD cycles. Panel (a) shows 200 cycles of TiCl ₄ /H ₂ O and panel (b) shows data recorded during 350 cycles of TTIP/H ₂ O. The gray curve in (a) has been magnified by 5x for clarity.....	141
Figure 6.1. Analog scan recorded in a clean, Al ₂ O ₃ -coated, deposition chamber while DHP was introduced into the chamber in short (0.1 s) pulses. Background signal from the reactor chamber was subtracted out in order to show peaks associated with DHP.....	156
Figure 6.2. Analog scan recorded in sequence during DHP (top row) and WF ₆ (middle and bottom rows) exposures. A second WF ₆ exposure is shown to illustrate surface saturation. Some species of interest are labeled with their corresponding m/z value. Dashed (gray) lines have been magnified by a factor of 10 for clarity.....	157
Figure 6.3. Selected reactant and product species tracked during 50 cycles of DHP/WF ₆ at 120°C (bottom row) and 220°C (top row). Traces for m/z = 146, 279, 73, 77, and 20 are shown. The reactor chamber was empty during the measurements.....	158
Figure 6.4. SEM images from depositions carried out at 220°C: (a) 50 cycles DHP/WF ₆ on Si; (b) 50 cycles DHP/WF ₆ on SiO ₂ ; (c) 10 cycles SiH ₄ /WF ₆ on Si; and (d) 50 cycles SiH ₄ /WF ₆ on SiO ₂ . All scale bars represent 300 nm.....	159
Figure 6.5. Photoelectron spectra from Si and SiO ₂ surfaces processed with 50 cycles of DHP/WF ₆ at 120°C (bottom row) and 220°C (top row). F 1s, N 1s, and C 1s regions are shown with some of the peaks identified with labels.....	160
Figure 6.6. Photoelectron spectra from Si and SiO ₂ surfaces processed with 50 cycles of DHP/WF ₆ at 120°C (left panel) and 220°C (right panel). For each surface, the W 4f region is shown with peak identifications.....	161

Figure A1.1. Representative polarization curves for p-Si photocathodes from the literature. From right to left, the curves were replotted from (a) *J. Electroanal. Chem.* 228 1987, (b) *Electrochem. Commun.* 12 2010, (c) *Energy Environ. Sci.* 4 2011, (d) *Appl. Phys. Lett.* 42 1983, (e) *Appl. Surf. Sci.* 75 1994, and (*) this article. Specific experimental conditions for the data are tabulated in the supplemental information. Inset: Current matching in tandem PEC systems is shown as two intersecting IV curves. The blue curves (solid and dashed) represent the cathode with two different series resistance values and the orange curve corresponds to the anode. The green rectangle represents the maximum power at which one of the devices can operate. Dashed horizontal lines I1 and I2 correspond to the maximum current at which the tandem cell can operate with series resistance R1 and R2 respectively.

.....175

Figure A1.2. Electrical resistance in diamond scratched back contacts is physically modeled using resistors wired in series with the working electrode. Higher resistor values impede photocurrent rise, analogous to our observations with electrodes that have poor back contacts. Inset shows the reciprocal slopes of IV curves plotted against resistor value.....176

Figure A1.3. Comparison of electrodes constructed using different native oxide removal methods: No treatment (native oxide is present as a control), mechanically abraded using tungsten carbide pen, mechanically abraded using diamond pen, chemically etched using 10 M HF, and a combination of diamond abrasion and HF etching applied in sequence. The inset shows evaporated Au and Al back contacts compared to a diamond abraded back contact. The series of steps used to construct a diamond abraded back contact are enumerated on the right.

.....177

Figure A1.4. The influence of back contact geometric area on the performance of silicon photocathodes. Polarization curves are shown for electrodes with small, medium, and large InGa back contacts. Geometric areas for the metal contacts are 0.16, 0.24, and 0.90 cm² respectively (photographed in inset).....178

Figure A1.S1. The position of the HER is shown for two Pt mesh electrodes (~5 cm² surface area each) stored in concentrated H₂SO₄. Scans are recorded in 0.5M H₂SO₄ (pH = 0) electrolyte at 20 mV/s. For comparison, a p-Si(111) electrode is also shown measured under 1 sun illumination, immediately after dipping in NH₄F and rinsing under DI water.....181

Figure A1.S2. Electron micrographs of Si back contacts with (a) no contact preparation, (b) tungsten carbide scratching, and (c) diamond scribing. Scale bars represent 240 μm. Horizontal, vertical, and diagonal trenches are evident in (b) and (c).....182

Figure A1.S3. Reproducibility characteristics from three silicon cathodes with back contacts prepared by mechanical scratching using a diamond pen. Saturation occurs at approximately -0.2 V vs NHE, but noise from bubble release makes this interpretation difficult. We attribute variations in saturation current density to several source of error, including vertical sample

positioning as well as sample rotation with respect to the incident beam (off-normal rotation). Small variations in electron rotation can result in current density differences up to $\pm 10\%$ (shown in Figure S4).....183

Figure A1.S4. Current density dependence on illumination angle of incidence is shown for a cathode prepared by diamond abrading the back surface. The same electrodes is measured repeatedly at different angles of incidence. The successive increase in series resistance is due to surface oxide formation when illumination is blocked as electrode rotation is adjusted. Compared to current densities at normal incidence, rotated electrodes show a roughly cosine dependence on the angle of illumination. The vertical position of the electrode is controlled reproducibly with an o-ring, and is therefore not a significant source of error in measurements. Noise is due to steady-state gas evolution on the electrode surface.....184

Figure A2.1.1. Current and potential plots from bare n-Si photoanodes showing dark and photocurrent decay with each voltammetric sweep. Current in dark (dashed line) is shown for only the first 5 cycles while current under illumination (solid line) is repeated for 20 linear sweeps at a scan rate of 20 mV/s in 0.5M H₂SO₄. Inset is a photograph of an electrode showing the exposed Si face surrounded by gray epoxy; a silver wire contact housed in a glass tube is visible on the left.....195

Figure A2.1.2. Voltammogram taken from bare (dashed line) and 3.3 nm ALD TiO₂ coated (solid line) n-Si electrodes on FTO substrates. Both traces show photoelectrochemical oxidation of water under solar illumination at a scan rate of 20 mV/s in 0.5M H₂SO₄. A single sweep is shown.....196

Figure A2.1.3. A typical voltammogram from a ZnO coated n-Si photoanode taken at 20 mV/s in 0.5M H₂SO₄. Here the coating thickness is 0.8 nm. Inset shows current-potential characteristics in dark. Five sweeps are shown for each plot.....197

Figure A2.1.4. Voltammogram from a TiO₂ coated n-Si photoanode taken at 100 mV/s in 0.5M H₂SO₄. The ALD TiO₂ coating is 1.9 nm thick with a 1.4 nm catalytic Co metal layer on top. Prior to catalyst deposition, the metal oxide film was annealed at 450°C for 30 minutes. Inset shows dark current-potential characteristics with a different current scale. Five sweeps are shown for each plot.....198

Figure A2.1.4. Two-electrode voltammogram from a photovoltaic-photoelectrochemical tandem device with light chopping every 3 seconds. Here a small (~1 cm²) p-Si electrode is connected in series with an a-Si off-the-shelf solar cell. The solar cell supplies about 2.4 V of potential to the electrode driving proton reduction in an acidic environment (0.5M H₂SO₄). The staircase pattern shows the effect of light chopping.....199

CHAPTER 1. Introduction and Background

1.1 Introduction to Atomic Layer Deposition

Atomic layer deposition (ALD) is a cyclic vacuum deposition process based on self-limiting gas-solid reactions. In a typical process, two vapor-phase reactants are pulsed into a heated vacuum chamber in alternating fashion, with an inert gas purge following each reactant pulse. Upon exposure to the first reactant, surfaces with the appropriate functionality become saturated with chemisorbed species. Surface reactions proceed to completion and terminate the surface with ligands that are reactive only with the second reactant (i.e. co-reactant), but not with the first. Byproducts and excess reactant are removed from the reactor with an inert gas purge, completing the first half-cycle. Exposure to the second reactant and a second purge step complete one full cycle. Due to the self-limiting nature of the surface reactions, excess reactant exposure does not produce excess deposition on a solid surface, and a known thickness of material is deposited during each ALD cycle. Consequently, ALD processes produce extremely conformal films over high aspect ratio structures with discrete control over film thickness.

A typical A/B type ALD cycle is shown in Figure 1.1 where the four gas pulsing steps are shown: Precursor A dose; precursor A purge; precursor B dose; and precursor B purge. In this example, precursor A is trimethyl aluminum (TMA) and precursor B is water (H₂O). Using this scheme a wide variety of materials can be deposited at precise thicknesses down to several Angstroms. Some examples of material classes include metals^{1,2}, organic-inorganic hybrids³, conductive oxides^{4,5}, high-κ dielectric oxides^{6,7}, oxide semiconductors^{8,9}, superconductors^{10,11}, hard coatings (nitrides^{12,13}, carbides^{10,14}), porous frameworks¹⁵, ternary¹⁶

and quaternary¹⁷ compounds, 2-dimensional materials^{18,19}, and polypeptides²⁰. Processing temperatures range from room temperature when using plasma enhanced ALD²¹ to high temperatures for noble metal ALD²². Typical ALD processes operate at low²³ or high vacuum²⁴, depending on purity requirements, but recent developments present the viability of atmospheric pressure²⁵ and spatial^{26,27} ALD growth at low temperatures and sometimes using atmospheric plasma sources²⁸. Depending on precursor size²⁹ and reactive surface site density³⁰, ALD chemistries produce deposition rates that vary from $<0.5 \text{ \AA/cycle}$ for many metal oxides up to 6 \AA/cycle for large metals such as W. Deposition rates are strongly influenced by the amount of energy (thermal or plasma) supplied to the substrate surface. A common concept in ALD growth is the so-called “ALD window”, which defines a range of temperatures where steady-state deposition rate is constant (\AA/cycle), or temperature insensitive. Figure 1.2 illustrates a thermal ALD window (flat region) with various factors that explain low or high growth rates at the extreme ends of the window.

In an ideal ALD process each precursor dose would result in the deposition of exactly $\frac{1}{2}$ monolayer of material. Perfect $\frac{1}{2}$ monolayers do not form in real processes due to steric effects, namely the large size of the chemisorbed ligands on the surface³¹. The growth rate of films (\AA/cycle) also exhibit substrate-specific variations due to nucleation processes that take place during the initial stages of growth (in some cases more than 100 cycles). There are three types of growth modes that can occur in an ALD process: Two dimensional layer-by-layer growth (Frank-van der Merwe type), three-dimensional island growth (Volmer-Weber type), or layer-plus-island growth (Stranski-Krastanov type), also known as random growth. In Figure 1.3 a sketch illustrates the three growth regimes as a function of the number of

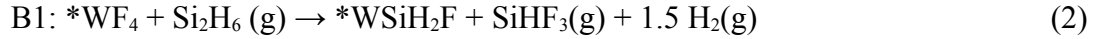
deposition cycles n . Intricacies of substrate-influenced initial growth can be observed by plotting growth rate against cycle number. Plots for various nucleation regimes are given in Figure 1.4. Instantaneous nucleation (a) would be achieved if the initial growth rate on the substrate surface is equal to the steady-state growth rate observed on the deposited material. Substrate-enhanced growth (b) can occur in the presence of a nucleation layer that has a higher number of reactive sites than the ALD half-layers themselves. Substrate-inhibited growth (c and d) can occur if there is a lower number of reactive sites on the substrate surface than on the ALD half-layers. Type 2 substrate-inhibited growth is an example of island growth, where the growth rate goes through a maximum before reaching a steady-state value, which is indicative of full substrate coverage and a return to two-dimensional growth.

1.2 Materials Grown by ALD

In this work, two classes of ALD synthesized materials will be discussed: Metals from metal halide sources and conductive metal oxides from halide and organometallic sources. Due to differences in deposition chemistries, these materials will be introduced separately.

1.2.1 Metals deposition from metal halide sources

Since the conception of self-limiting cyclical reaction chemistries, metals have been difficult to synthesize in a layer-by-layer fashion. Currently, a limited number of materials are accessible to ALD growth techniques. Many metal chemistries have been adapted from chemical vapor deposition (CVD), which is a more established technology compared to ALD. One of the earliest metal ALD processes was used to synthesize tungsten by the reduction of tungsten hexafluoride (WF_6) with silane (SiH_4)^{32,33}. The state of the art³⁴ understanding of the tungsten ALD chemistry can be written as two surface reactions:



The reactions above show stoichiometries for the $\text{Si}_2\text{H}_6/\text{WF}_6$ system, but the chemistry for the SiH_4/WF_6 system is similar. Compounds prefixed with an asterisk (*) denote adsorbed (surface) species. In a CVD process, the tungsten fluoride can also be reduced by H_2 , which proceeds by a combination of Rideal-Eley and Langmuir-Hinshelwood mechanisms³⁵. In the case of Si reduction of WF_6 on the surface (A1), a similar mechanism is likely to occur. Regarding reaction products, the above equations are written on empirical evidence that the primary byproduct of the WF_6 reduction are SiF_4 , HF, and H_2 . The Si_2H_6 reaction is known to be non-self-limiting. For instance, extended exposures to disilane result in silylene insertion into surface Si-H bonds^{36,37}. It is not known whether monosilane reactions on fluorinated tungsten surfaces are self-limiting. For either type of silane, vapor-phase products liberated during reaction are fluorosilanes and H_2 .

Another group 6 metal, molybdenum, has been shown to deposit in a self-limiting fashion with MoF_6 and a disilane reducing agent³⁸. Despite the similarities in precursor structure, Mo ALD films show higher Si content than W ALD films. Furthermore, *in situ* microbalance analyses have shown that the reaction mechanism for Mo deposition differs from W deposition, particularly during the silane exposure step. As with tungsten, each reaction cycle deposits more than a monolayer of material, which is evident in the high growth rates observed (6-7 Å/cycle). Furthermore, the $\text{MoF}_6/\text{Si}_2\text{H}_6$ process is highly temperature sensitive, with approximately constant deposition rates achieved only between

90 and 150°C. It should be noted that an earlier report has demonstrated Mo growth from MoCl₅ and Zn vapor³⁹. While this approach is viable, the high deposition conditions required for film growth (400-500°C) and Zn evaporation (390°C) make this process undesirable due to its high thermal requirements.

Another unusual metal deposited from a metal halide source is antimony. The precursors used were SbCl₃ and (Et₃Si)₃Sb at low temperatures (>95°C) for elemental Sb deposition⁴⁰. In addition to elemental Sb, mixed Sb compounds were also demonstrated using GeCl₂, GaCl₃, and AlCl₃ sources. Metal telluride and selenide compounds have also been prepared using similar methods⁴¹. The exact surface chemistry of tris(triethylsilyl)antimony is not well understood. However, the reaction mechanism is suspected to involve dehalosilylation and comproportionation.

Growth of other group 6 metals by ALD are notably absent due to the lack of volatile group 6 halides. The only other metal deposited by ALD from a halide source is iridium. Prepared from IrF₆ and H₂, thin Ir films have been demonstrated at elevated temperatures (350°C and above)⁴². Besides noble metals, early transition metal films are of particular interest to semiconductor device manufacturing. Industrially relevant transition metals have large and negative standard reduction potentials ($M^{X+} + Xe^- \rightarrow M^0$, for instance), which necessitate powerful reducing agents to deposit metallic films^{43,44}. One notable exception is Cu, which has a positive reduction potential. Recent developments in reducing agents hold promise for the deposition of Ti, Zn, Fe, Mn, Cr, Co, and Ni by ALD^{45,46}. For example, 1,4-bis(trimethylsilyl)-pyrazine based reducing agents can be tuned by preparing derivatives with different ligands on the 2,5 and 3,6 positions on the pyrazine ring. These types of reducing

agents are expected to be powerful enough to enable metal deposition by thermal ALD from volatile metal halide compounds. Deposition mechanisms, self-limiting behavior, film purity, and deposition rates for these types of reduction reactions are currently unknown.

A further topic of interest for metal deposition is plasma enhanced atomic layer deposition (PEALD). There have been a few studies on the hydrogen plasma (H*) reduction of metal halide precursor for the deposition of Ti and Ta^{47,48}. While common molecular co-reactants are not sufficiently reducing to strip halogen atoms from common metal halides, metallic films may be produced using atomic sources, as produced by plasmas. However, plasma processes add complexity to ALD, including mass transport limitations and damage to fragile substrates.

1.2.2 Conductive metal oxides

Metal oxides have been studied extensively from the early days of ALD. Many of the metal oxide forming reactions undergo the following two reaction steps:



Reactions A and B above represent the prototypical cyclical process for deposition of aluminum oxide (Al₂O₃), or alumina. To initiate the first step (A), the starting surface typically contains functional groups (such as hydroxyls) that permit reaction with the metal-containing precursor, in this case, trimethyl aluminum or TMA. The ligands produced on the surface then react with a co-reactant to form a film monolayer while also producing more reactive functional groups on the surface. During steady-state deposition (Al₂O₃ deposition on existing Al₂O₃ surfaces), the Al atom in TMA is in a +3 oxidation state, and when it reacts

with –OH sites, it exchanges ligands, but the formal metal oxidation state is not changed. This is also true when H₂O reacts with Al(CH₃) sites. Therefore, the reaction between H₂O and TMA during ALD is an example of an acid/base reaction where the ligands are exchanged without change in formal oxidation state of either species. Using the Brønsted–Lowry acid/base terminology for the TMA/water reaction above, the acid OH donates a proton to the base CH₃ ligand, so the O⁻ becomes the conjugate base and CH₄ is the conjugate acid. Again, the formal oxidation state of the metal is not changed.

This type of acid/base chemistry has been used to construct a library of self-terminating cyclic reactions that produce metal oxide thin films. While the focus of this section is on conductive metal oxides, some examples of metal oxides deposited by ALD, including dielectrics, are: Al₂O₃^{24,49}, Al-doped ZnO⁴, Bi₂O₃⁵⁰, Fe₂O₃⁸, Ga₂O₃⁵¹, HfO₂⁵², MoO₃⁵³, NiO⁵⁴, SiO₂^{6,24,55,56}, SnO₂^{57,58}, SrO⁵⁹, SrTiO₃⁶⁰, TiO₂^{9,61}, V₂O₃⁶², VO₂⁶³, ZnO⁶⁴, and ZrO₂⁶⁵. Many other oxides, doped materials, and mixed oxides are possible by ALD. Typical metal sources include metal halides and organometallic compounds, where organic ligands may be alkyls, cyclopentadienyls, alkoxides, *β*-diketonates, alkylamides, amidinates, and less frequently, acetates and carbonates. Some unusual precursor compounds include silylamides⁶⁶ and alkylsilyls⁴¹.

Most of the metal oxide compounds listed above are visible light transparent and have sufficient conductivity for various electronic applications. For instance, Al-doped ZnO (AZO) films are used as transparent conductive oxide (TCO) materials for electronic display applications. ALD AZO films are typically made using delta doping, namely by interleaving dopant cycles (using TMA, or other metal dopant sources) during an A/B type ALD

sequence⁶⁷. Similar TCO films, including P-doped⁶⁸ and Si-doped ZnO⁶⁹, and Sn-doped In₂O₃⁷⁰ are some example doped materials prepared by ALD.

Titanium dioxide (titania) films have been used extensively for their electronic properties. Ultrathin TiO₂ films have been recently used in electrochemical energy devices as passivation layers or blocking layers against back electron transfer. Titania is a hole conductor due to defect states. TiO₂ films can be prepared by ALD using a variety of Ti sources, including titanium tetrachlorid (TiCl₄)⁷¹, tetraiodide⁷², tetraisopropoxide (TTIP)⁷³, tetramethoxide⁹, and tetrakisdimethyl-amido (TDMAT)⁷³. Oxygen sources for the process include H₂O, O₂⁷⁴, O₃⁷⁵, and various metal alkoxides⁷⁶. The most common processes for TiO₂ deposition are TiCl₄/H₂O, TTIP/H₂O, and TDMAT/H₂O. The TiCl₄ source is problematic for certain applications due to the production of acidic byproducts (hydrochloric acid)^{77,78}. The organometallic Ti sources TTIP and TDMAT are generally preferred over the halides, with TDMAT producing films with remarkably low carbon content⁷⁹. The metal halide process has a very large process window, with highly temperature sensitive deposition rates. Meanwhile, the organometallic Ti sources decompose at high temperatures, and are generally usable under 300°C. ALD TiO₂ processes result in deposition rates from 0.3 to 1.0 Å/cy and generally produce amorphous films at temperatures <300°C.

1.3 Substrates for ALD processing

Substrates of interest in this document include silicon and polyamides. A brief description of the chemistry and surface preparation for these materials will be provided here.

1.3.1 Silicon and silica

Perhaps the most common substrate coated with ALD thin films is silicon. Crystalline Si has a diamond structure, with each Si atom bonded to its four nearest neighbors. Deposition phenomena (physisorption, chemisorption, reaction) occur on the exposed surfaces of silicon, which are defined by how the crystal is cleaved. Depending on the surface type, a number of oriented dangling bonds will be present on the surface⁸⁰. There are two common crystal planes of silicon that are used for surface studies: {100} and {111}. The Si(100) surface is one on which industrial semiconductor devices are built. The Si(111) surface, on the other hand, is important for surface science studies and is chemically passivated (hydrogenated) upon etching with hydrogen fluoride (HF) solutions⁸¹. Depending on the surface treatments applied (wet etch, plasma etch, vacuum anneal) a variety of surfaces are possible, including those with different dangling bond densities, step structures, surface reconstructions, and hydride and hydroxide terminations. For most purposes, including deposition studies and device fabrication, aqueous HF etching followed by deionized H₂O rinsing produces high-quality and predictable surfaces⁸². After hydrogen termination, the Si surface can rapidly grow a native oxide under ambient atmospheric conditions. Figure 1.5 shows ellipsometry data collected over the course of 4.5 hours that shows the rate of native oxide formation on a buffered HF etched Si wafer. The initial several Å of oxide form instantaneously. However, in the absence of *in vacuo* surface cleaning or termination, it is imperative that cleaned or hydrogenated wafers are loaded into a vacuum chamber within minutes of wet treatment for deposition studies.

Cleaved silicon surfaces are easily oxidized, even under ultra-high vacuum (UHV) conditions. Si wafers used for laboratory experiments typically arrive from the manufacturer with a layer of native oxide (SiO_x). This oxide can be produced upon exposure to air of an etched surface or can be prepared by oxidation in a standard cleaning solution, such as SC-1 followed by SC-2⁸³. The latter approach produces a surface oxide layer called a chemical oxide. These types of oxidation processes are self-limiting and produce oxide thicknesses less than 20 Å. Thicker oxide layers are produced by thermally oxidizing the surface in a diffusion furnace with a reactive atmosphere. Thermal oxide (SiO_2) is typically formed by heating wafers to above 700°C and exposing the surface to O_2 ^{84,85} (dry thermal oxide) or steam^{86,87}. Rapid thermal oxidation (with a flash lamp) is another method for producing thermal SiO_2 ^{88,89}. The thickness of thermal SiO_2 films are controlled by varying the oxidation time and can be made greater than 25 μm.

1.3.2 Polyamides

Among the oldest synthetic plastics used in consumer goods is nylon. Commonly used in textiles, nylon is a polyamide and comes in two common configurations: Nylon-6 (PA6) and nylon-6,6. Figure 1.6 shows the chemical structure for one repeat unit of PA6. Polymer substrates are a good choice for deposition studies because they can be readily functionalized with thin film coatings for electronic applications such as smart textiles and gas sensing. Textile applications, in particular, stand to benefit from vapor phase deposition techniques, such as ALD, in order to produce uniform and conformal coatings over complex fiber geometries. Nylon-6 substrates are commercially available as woven or nonwoven mats (textiles) with reasonably high surface areas and can have microscopically complex fiber

cross sections. These materials can generally be processed at elevated temperatures owing to the high melting point of 215°C of PA6⁹⁰. Furthermore, previous studies have shown that some of the reactive precursors used in ALD processes (such as TMA) can diffuse into fiber forming polymers, such as PA6, and result in the bulk modification of the polymer⁹¹. An example fiber substrate, used in this work, is a hydroentangled nonwoven mat produced by Allasso Industries, Morrisville NC. The mats consist of nylon-6 fibrils with multi-lobal cross sections, with diameters in the 1-10 μm range.

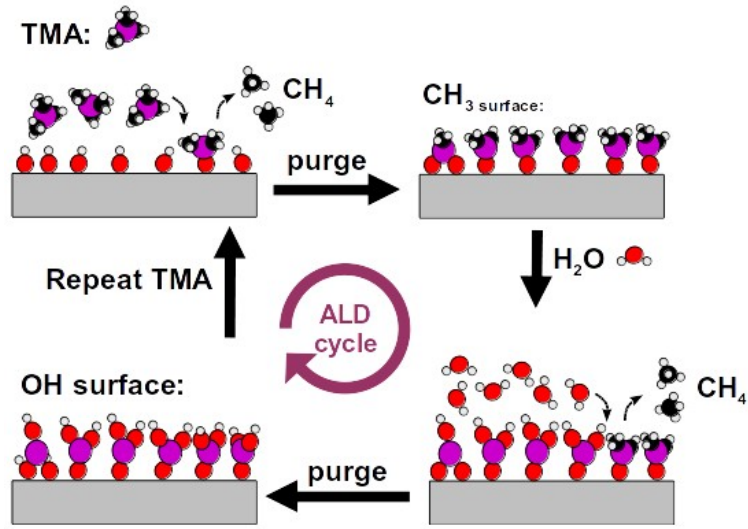


Figure 1.1. A typical A/B type ALD cycle with TMA and H₂O as reactant and co-reactant.

Graphic courtesy of Gregory Parsons.

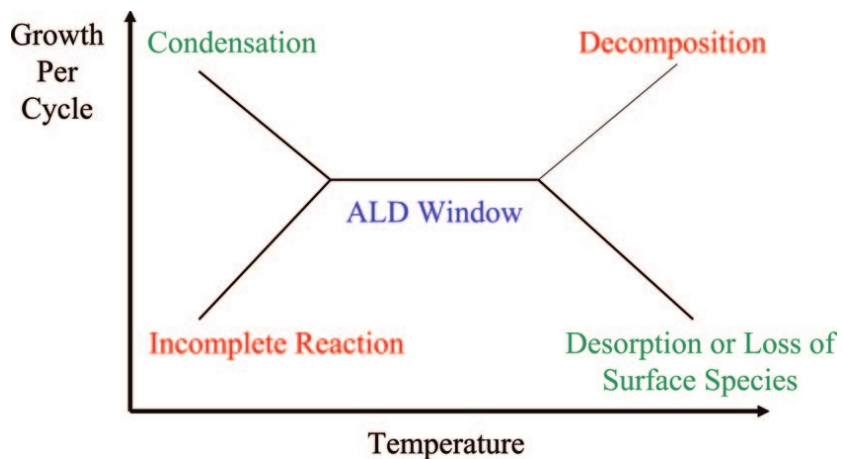


Figure 1.2. ALD window sketch illustrating the possible shapes the growth per cycle curve can take as a function of temperature. Possible contributors to low or high growth rates include incomplete surface reaction, desorption of surface sites, precursor condensation, or precursor decomposition. Figure reproduced from ⁹².

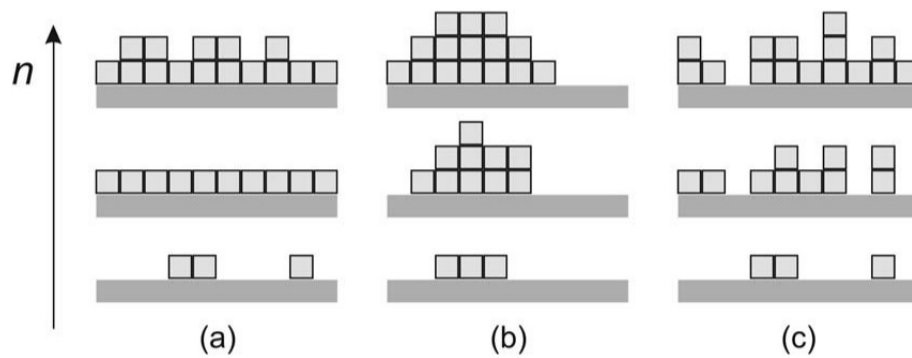


Figure 1.3. Sketch demonstrating various thin film growth modes observed during ALD. Vertical axis n denotes increasing number of reaction cycles. The growth modes shown are: (a) Frank-van der Merwe, (b) Volmer-Weber, (c) Stranski-Krastanov. Figure reproduced from ³¹.

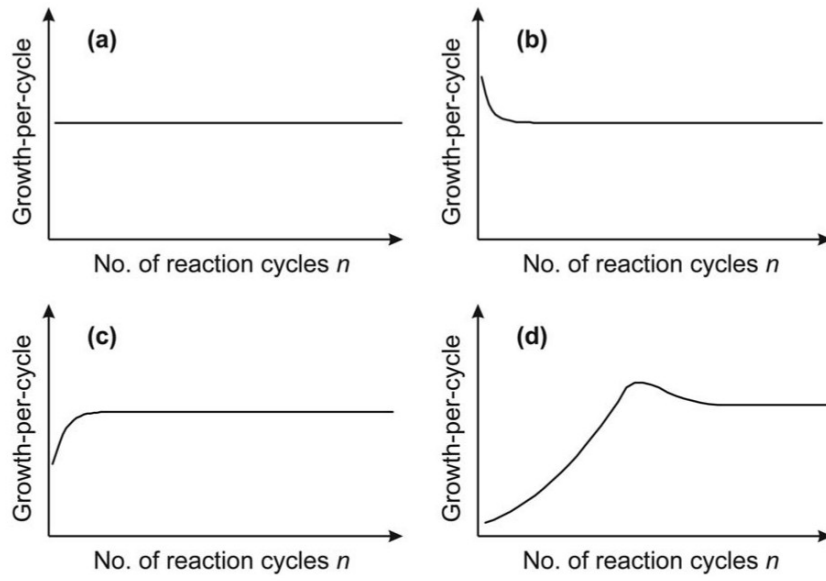


Figure 1.4. Growth rate as a function of deposition cycles for (a) substrate independent growth, (b) substrate-enhanced growth, (c) substrate-inhibited growth of type 1, and (d) substrate-inhibited growth of type 2. Figure reproduced from ³¹.

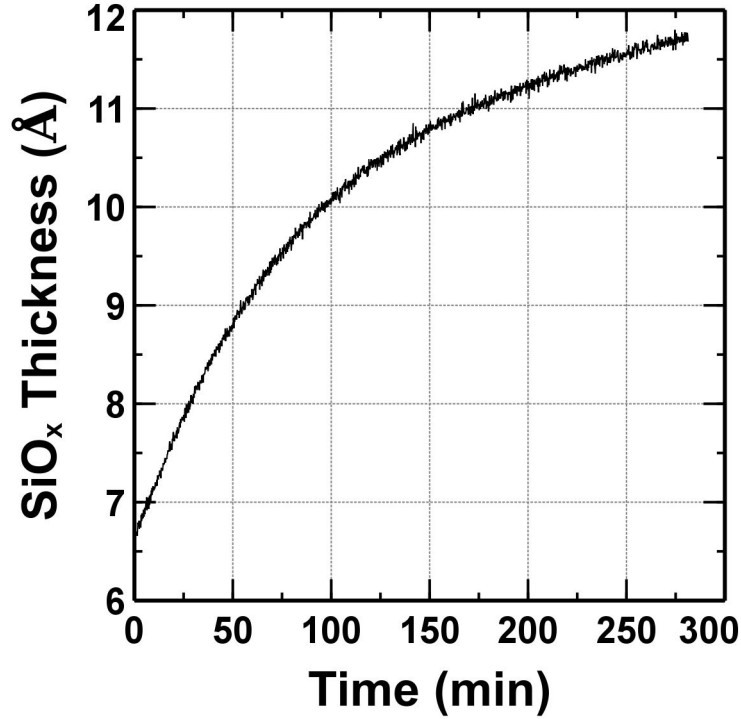


Figure 1.5. Growth of native SiO_x as a function of time under laboratory room conditions. The surface is a small piece of piranha cleaned Si(100) wafer treated with a 30 second NH₄F-buffered aqueous HF solution dip, followed by a 30 second deionized H₂O rinse. Native oxide thickness was measured using a spectroscopic ellipsometer (J.A. Woollam Company, alpha-SE).

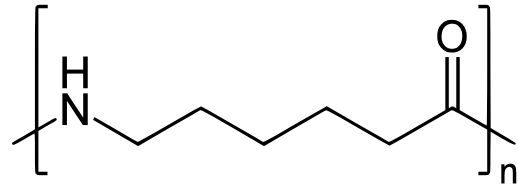


Figure 1.6. Chemical representation of polyamide-6. One repeat unit is shown.

1.4 References

- (1) Lim, B. S.; Rahtu, A.; Gordon, R. G. Atomic Layer Deposition of Transition Metals. *Nat Mater* **2003**, *2*, 749–754.
- (2) Kalutarage, L. C.; Martin, P. D.; Heeg, M. J.; Winter, C. H. Volatile and Thermally Stable Mid to Late Transition Metal Complexes Containing A-Imino Alkoxide Ligands, a New Strongly Reducing Coreagent, and Thermal Atomic Layer Deposition of Ni, Co, Fe, and Cr Metal Films. *J. Am. Chem. Soc.* **2013**, *135*, 12588–12591.
- (3) George, S. M.; Yoon, B.; Dameron, A. A. Surface Chemistry for Molecular Layer Deposition of Organic and Hybrid Organic-Inorganic Polymers. *Acc Chem Res* **2009**, *42*, 498–508.
- (4) Jiang, X.; Wong, F. L.; Fung, M. K.; Lee, S. T. Aluminum-Doped Zinc Oxide Films as Transparent Conductive Electrode for Organic Light-Emitting Devices. *Appl. Phys. Lett.* **2003**, *83*, 1875.
- (5) Kong, B. H.; Choi, M. K.; Cho, H. K.; Kim, J. H.; Baek, S.; Lee, J.-H. Conformal Coating of Conductive ZnO:Al Films as Transparent Electrodes on High Aspect Ratio Si Microrods. *Electrochem. Solid-State Lett.* **2010**, *13*, K12.
- (6) Du, Y.; Du, X.; George, S. M. SiO₂ Film Growth at Low Temperatures by Catalyzed Atomic Layer Deposition in a Viscous Flow Reactor. *Thin Solid Films* **2005**, *491*, 43–53.
- (7) Gusev, E. P.; Cabral, C.; Copel, M.; D'Emic, C.; Gribelyuk, M. Ultrathin HfO₂ Films Grown on Silicon by Atomic Layer Deposition for Advanced Gate Dielectrics Applications. *Microelectron. Eng.* **2003**, *69*, 145–151.
- (8) Lie, M.; Fjellvag, H.; Kjekshus, A. Growth of Fe₂O₃ Thin Films by Atomic Layer Deposition. *Thin Solid Films* **2005**, *488*, 74.
- (9) Pore, V.; Rahtu, A.; Leskelä, M.; Ritala, M.; Sajavaara, T.; Keinonen, J. Atomic Layer Deposition of Photocatalytic TiO₂ Thin Films from Titanium Tetramethoxide and Water. *Chem. Vap. Depos.* **2004**, *10*, 143.
- (10) Klug, J. A.; Proslie, T.; Elam, J. W.; Cook, R. E.; Hiller, J. M.; Claus, H.; Becker, N. G.; Pellin, M. J. Atomic Layer Deposition of Amorphous Niobium Carbide-Based Thin Film Superconductors. *J. Phys. Chem. C* **2011**, *115*, 25063–25071.

- (11) Ziegler, M.; Fritzsche, L.; Day, J.; Linzen, S.; Anders, S.; Toussaint, J.; Meyer, H.-G. Superconducting Niobium Nitride Thin Films Deposited by Metal Organic Plasma-Enhanced Atomic Layer Deposition. *Supercond. Sci. Technol.* **2013**, *26*, 025008.
- (12) Samal, N.; Du, H.; Luberoff, R.; Chetry, K.; Bubber, R.; Hayes, A.; Devasahayam, A. Low-Temperature (≤ 200 Degrees C) Plasma Enhanced Atomic Layer Deposition of Dense Titanium Nitride Thin Films. *J. Vac. Sci. Technol. A* **2013**, *31*, 01A137.
- (13) Kim, S.-H.; Kim, J.-K.; Lee, J. H.; Kwak, N.; Kim, J.; Jung, S.-H.; Hong, M.-R.; Lee, S. H.; Collins, J.; Sohn, H. Characteristics of ALD Tungsten Nitride Using B₂H₆, WF₆, and NH₃ and Application to Contact Barrier Layer for DRAM. *J. Electrochem. Soc.* **2007**, *154*, D435.
- (14) Hsu, I. J.; Kimmel, Y. C.; Jiang, X.; Willis, B. G.; Chen, J. G. Atomic Layer Deposition Synthesis of Platinum–tungsten Carbide Core–shell Catalysts for the Hydrogen Evolution Reaction. *Chem. Commun.* **2012**, *48*, 1063–1065.
- (15) Salmi, L. D.; Heikkilä, M. J.; Puukilainen, E.; Sajavaara, T.; Grosso, D.; Ritala, M. Studies on Atomic Layer Deposition of MOF-5 Thin Films. *Microporous Mesoporous Mater.* **2013**, *182*, 147–154.
- (16) Miikkulainen, V.; Leskelä, M.; Ritala, M.; Puurunen, R. L. Crystallinity of Inorganic Films Grown by Atomic Layer Deposition: Overview and General Trends. *J. Appl. Phys.* **2013**, *113*, 021301.
- (17) Thimsen, E.; Riha, S. C.; Baryshev, S. V.; Martinson, A. B. F.; Elam, J. W.; Pellin, M. J. Atomic Layer Deposition of the Quaternary Chalcogenide Cu₂ZnSnS₄. *Chem. Mater.* **2012**, *24*, 3188–3196.
- (18) Song, J.-G.; Park, J.; Lee, W.; Choi, T.; Jung, H.; Lee, C. W.; Hwang, S.-H.; Myoung, J. M.; Jung, J.-H.; Kim, S.-H.; *et al.* Layer-Controlled, Wafer-Scale, and Conformal Synthesis of Tungsten Disulfide Nanosheets Using Atomic Layer Deposition. *ACS Nano* **2013**, *7*, 11333–11340.
- (19) Tan, L. K.; Liu, B.; Teng, J. H.; Guo, S.; Low, H. Y.; Loh, K. P. Atomic Layer Deposition of a MoS₂ Film. *Nanoscale* **2014**, *6*, 10584–10588.
- (20) Fu, Y.; Li, B.; Jiang, Y.-B.; Dunphy, D. R.; Tsai, A.; Tam, S.-Y.; Fan, H.; Zhang, H.; Rogers, D.; Rempe, S.; *et al.* Atomic Layer Deposition of L-Alanine Polypeptide. *J. Am. Chem. Soc.* **2014**, *136*, 15821–15824.

- (21) Potts, S. E.; Keuning, W.; Langereis, E.; Dingemans, G.; van de Sanden, M. C. M.; Kessels, W. M. M. Low Temperature Plasma-Enhanced Atomic Layer Deposition of Metal Oxide Thin Films. *J. Electrochem. Soc.* **2010**, *157*, P66.
- (22) Park, K. J.; Doub, J. M.; Gougousi, T.; Parsons, G. N. Microcontact Patterning of Ruthenium Gate Electrodes by Selective Area Atomic Layer Deposition. *Appl. Phys. Lett.* **2005**, *86*, 051903.
- (23) Elam, J. W.; Groner, M. D.; George, S. M. Viscous Flow Reactor with Quartz Crystal Microbalance for Thin Film Growth by Atomic Layer Deposition. *Rev. Sci. Instrum.* **2002**, *73*, 2981–2987.
- (24) George, S. M.; Sneh, O.; Dillon, A. C.; Wise, M. L.; Ott, A. W.; Okada, L. A.; Way, J. D. Atomic Layer Controlled Deposition of SiO₂ and Al₂O₃ Using ABAB... Binary Reaction Sequence Chemistry. *Appl. Surf. Sci.* **1994**, *82–83*, 460–467.
- (25) Jur, J. S.; Parsons, G. N. Atomic Layer Deposition of Al₂O₃ and ZnO at Atmospheric Pressure in a Flow Tube Reactor. *ACS Appl Mater Interfaces* **2011**, *3*, 299–308.
- (26) Ellinger, C. R.; Nelson, S. F. Selective Area Spatial Atomic Layer Deposition of ZnO, Al₂O₃, and Aluminum-Doped ZnO Using Poly(vinyl Pyrrolidone). *Chem. Mater.* **2014**, *26*, 1514–1522.
- (27) Maydannik, P. S.; Kääriäinen, T. O.; Lahtinen, K.; Cameron, D. C.; Söderlund, M.; Soininen, P.; Johansson, P.; Kuusipalo, J.; Moro, L.; Zeng, X. Roll-to-Roll Atomic Layer Deposition Process for Flexible Electronics Encapsulation Applications. *J. Vac. Sci. Technol. A* **2014**, *32*, 051603.
- (28) Poodt, P.; Knaapen, R.; Illiberi, A.; Roozeboom, F.; Asten, A. van. Low Temperature and Roll-to-Roll Spatial Atomic Layer Deposition for Flexible Electronics. *J. Vac. Sci. Technol. A* **2012**, *30*, 01A142.
- (29) Ylilammi, M. Monolayer Thickness in Atomic Layer Deposition. *Thin Solid Films* **1996**, *279*, 124–130.
- (30) Puurunen, R. L. Correlation between the Growth-per-Cycle and the Surface Hydroxyl Group Concentration in the Atomic Layer Deposition of Aluminum Oxide from Trimethylaluminum and Water. *Appl. Surf. Sci.* **2005**, *245*, 6–10.
- (31) Puurunen, R. L. Surface Chemistry of Atomic Layer Deposition: A Case Study for the Trimethylaluminum/water Process. *J. Appl. Phys.* **2005**, *97*, 121301.

- (32) Klaus, J. ; Ferro, S. ; George, S. . Atomic Layer Deposition of Tungsten Using Sequential Surface Chemistry with a Sacrificial Stripping Reaction. *Thin Solid Films* **2000**, *360*, 145–153.
- (33) Yamamoto, Y.; Matsuura, T.; Murota, J. Surface Reaction of Alternately Supplied WF₆ and SiH₄ Gases. *Surf. Sci.* **1998**, *408*, 190–194.
- (34) Zaera, F. The Surface Chemistry of Atomic Layer Depositions of Solid Thin Films. *J. Phys. Chem. Lett.* **2012**, *3*, 1301–1309.
- (35) Hitchman, M. L.; Jobson, A. D.; Kwakman, L. F. T. Some Considerations of the Thermodynamics and Kinetics of the Chemical Vapour Deposition of Tungsten. *Appl. Surf. Sci.* **1989**, *38*, 312–337.
- (36) Grubbs, R. K.; Steinmetz, N. J.; George, S. M. Gas Phase Reaction Products during Tungsten Atomic Layer Deposition Using WF₆ and Si₂H₆. *J. Vac. Sci. Technol. B Microelectron. Nanometer Struct.* **2004**, *22*, 1811.
- (37) Grubbs, R. K.; Nelson, C. E.; Steinmetz, N. J.; George, S. M. Nucleation and Growth during the Atomic Layer Deposition of W on Al₂O₃ and Al₂O₃ on W. *Thin Solid Films* **2004**, *467*, 16–27.
- (38) Seghete, D.; Rayner, G. B.; Cavanagh, A. S.; Anderson, V. R.; George, S. M. Molybdenum Atomic Layer Deposition Using MoF₆ and Si₂H₆ as the Reactants. *Chem. Mater.* **2011**, *23*, 1668–1678.
- (39) Juppo, M.; Vehkamäki, M.; Ritala, M.; Leskelä, M. Deposition of Molybdenum Thin Films by an Alternate Supply of MoCl₅ and Zn. *J. Vac. Sci. Technol. A* **1998**, *16*, 2845–2850.
- (40) Pore, V.; Knapas, K.; Hatanpää, T.; Sarnet, T.; Kemell, M.; Ritala, M.; Leskelä, M.; Mizohata, K. Atomic Layer Deposition of Antimony and Its Compounds Using Dechlorosilylation Reactions of Tris(triethylsilyl)antimony. *Chem. Mater.* **2011**, *23*, 247–254.
- (41) Pore, V.; Hatanpää, T.; Ritala, M.; Leskelä, M. Atomic Layer Deposition of Metal Tellurides and Selenides Using Alkylsilyl Compounds of Tellurium and Selenium. *J. Am. Chem. Soc.* **2009**, *131*, 3478–3480.
- (42) Dussarra, C.; Gatineau, J. High Purity Iridium Thin Films Depositions Using the Inorganic IrF₆. In *Proceedings - Electrochemical Society*; Electrochemical Society, 2005; pp. 354–359.

- (43) Knisley, T. J.; Kalutarage, L. C.; Winter, C. H. Precursors and Chemistry for the Atomic Layer Deposition of Metallic First Row Transition Metal Films. *Coord. Chem. Rev.* **2013**, *257*, 3222–3231.
- (44) Ramos, K. B.; Saly, M. J.; Chabal, Y. J. Precursor Design and Reaction Mechanisms for the Atomic Layer Deposition of Metal Films. *Coord. Chem. Rev.* **2013**, *257*, 3271–3281.
- (45) Charles H. Winter; Joseph P. Klesko; Chatu T. Sirimanne. Silyl Elimination Reactions in the Atomic Layer Deposition of Titanium, Zinc, and Other Element Films, 2014.
- (46) Charles H. Winter; Joseph P. Klesko. High Purity Metallic Co and Ni Thin Films Using 1,4-Di-Tert-Butyl-1,3-Diazadienyl Precursors, 2014.
- (47) Rossnagel, S. M.; Sherman, A.; Turner, F. Plasma-Enhanced Atomic Layer Deposition of Ta and Ti for Interconnect Diffusion Barriers. *J. Vac. Sci. Technol. B Microelectron. Nanometer Struct.* **2000**, *18*, 2016–2020.
- (48) Kim, H.; Rossnagel, S. M. Growth Kinetics and Initial Stage Growth during Plasma-Enhanced Ti Atomic Layer Deposition. *J. Vac. Sci. Technol. -Vac. Surf. Films* **2002**, *20*, 802–808.
- (49) Lakomaa, E.-L.; Root, A.; Suntola, T. Surface Reactions in Al₂O₃ Growth from Trimethylaluminium and Water by Atomic Layer Epitaxy. *Appl. Surf. Sci.* **1996**, *107*, 107–115.
- (50) Hatanpää, T.; Vehkamäki, M.; Ritala, M.; Leskelä, M. Study of Bismuth Alkoxides as Possible Precursors for ALD. *Dalton Trans.* **2010**, *39*, 3219.
- (51) Choi, D.; Chung, K.-B.; Park, J.-S. Low Temperature Ga₂O₃ Atomic Layer Deposition Using Gallium Tri-Isopropoxide and Water. *Thin Solid Films* **2013**, *546*, 31–34.
- (52) Ritala, M.; Leskelä, M.; Niinistö, L.; Prohaska, T.; Friedbacher, G.; Grasserbauer, M. Development of Crystallinity and Morphology in Hafnium Dioxide Thin Films Grown by Atomic Layer Epitaxy. *Thin Solid Films* **1994**, *250*, 72–80.
- (53) Tseng, Y.-C.; Mane, A. U.; Elam, J. W.; Darling, S. B. Ultrathin Molybdenum Oxide Anode Buffer Layer for Organic Photovoltaic Cells Formed Using Atomic Layer Deposition. *Sol. Energy Mater. Sol. Cells* **2012**, *99*, 235–239.
- (54) Lindahl, E.; Ottosson, M.; Carlsson, J.-O. Atomic Layer Deposition of NiO by the Ni(thd)₂/H₂O Precursor Combination. *Chem. Vap. Depos.* **2009**, *15*, 186–191.

- (55) Sneh, O.; Wise, M.; Ott, A.; Okada, L.; George, S. Atomic Layer Growth of SiO₂ on Si(100) Using SiCl₄ and H₂O in a Binary Reaction Sequence. *Surf. Sci.* **1995**, *334*, 135–152.
- (56) Burton, B. B.; Kang, S. W.; Rhee, S. W.; George, S. M. SiO₂ Atomic Layer Deposition Using Tris(dimethylamino)silane and Hydrogen Peroxide Studied by in Situ Transmission FTIR Spectroscopy. *J. Phys. Chem. C* **2009**, *113*, 8249–8257.
- (57) Utriainen, M. Controlled Electrical Conductivity in SnO₂ Thin Films by Oxygen or Hydrocarbon Assisted Atomic Layer Epitaxy. *J. Electrochem. Soc.* **1999**, *146*, 189.
- (58) Mullings, M. N.; Hägglund, C.; Bent, S. F. Tin Oxide Atomic Layer Deposition from Tetrakis(dimethylamino)tin and Water. *J. Vac. Sci. Technol. A* **2013**, *31*, 061503.
- (59) Zhang, C. B.; Wielunski, L.; Willis, B. G. Formation of Strontium Template on Si(100) by Atomic Layer Deposition. *Appl. Surf. Sci.* **2011**, *257*, 4826–4830.
- (60) Lee, S. W.; Han, J. H.; Han, S.; Lee, W.; Jang, J. H.; Seo, M.; Kim, S. K.; Dussarrat, C.; Gatineau, J.; Min, Y.-S.; *et al.* Atomic Layer Deposition of SrTiO₃ Thin Films with Highly Enhanced Growth Rate for Ultrahigh Density Capacitors. *Chem. Mater.* **2011**, *23*, 2227–2236.
- (61) Aarik, J. Atomic-Layer Growth of TiO₂-II Thin Films. *Philos. Mag. Lett.* **1996**, *73*, 115–119.
- (62) Chen, X.; Pomerantseva, E.; Banerjee, P.; Gregorczyk, K.; Ghodssi, R.; Rubloff, G. Ozone-Based Atomic Layer Deposition of Crystalline V₂O₅ Films for High Performance Electrochemical Energy Storage. *Chem. Mater.* **2012**, *24*, 1255–1261.
- (63) Virginia Wheeler. Atomic Layer Deposition of Thin, Amorphous VO₂ Films for Passive Thermal Management, 2014.
- (64) Skarp, J. I.; Soininen, P. J.; Soininen, P. T. ALE-Reactor for Large Area Depositions. *Appl. Surf. Sci.* **1997**, *112*, 251–254.
- (65) Rahtu, A.; Ritala, M. Reaction Mechanism Studies on the Zirconium Chloride-Water Atomic Layer Deposition Process. *J. Mater. Chem.* **2002**, *12*, 1484–1489.
- (66) Kukli, K.; Ritala, M.; Pilvi, T.; Sajavaara, T.; Leskelä, M.; Jones, A. C.; Aspinall, H. C.; Gilmer, D. C.; Tobin, P. J. Evaluation of a Praseodymium Precursor for Atomic Layer Deposition of Oxide Dielectric Films. *Chem. Mater.* **2004**, *16*, 5162–5168.

- (67) Na, J.-S.; Peng, Q.; Scarel, G.; Parsons, G. N. Role of Gas Doping Sequence in Surface Reactions and Dopant Incorporation during Atomic Layer Deposition of Al-Doped ZnO. *Chem. Mater.* **2009**, *21*, 5585–5593.
- (68) Yuan, H.; Luo, B.; Campbell, S. A.; Gladfelter, W. L. Atomic Layer Deposition of P-Type Phosphorus-Doped Zinc Oxide Films Using Diethylzinc, Ozone and Trimethylphosphite. *Electrochem. Solid-State Lett.* **2011**, *14*, H181.
- (69) Yuan, H. Structural, Electrical and Optical Properties of Si Doped ZnO Films Grown by Atomic Layer Deposition. *J. Mater. Sci. Mater. Electron.* **2012**, *23*, 2075–2081.
- (70) Elam, J. W.; Baker, D. A.; Martinson, A. B. F.; Pellin, M. J.; Hupp, J. T. Atomic Layer Deposition of Indium Tin Oxide Thin Films Using Nonhalogenated Precursors. *J. Phys. Chem. C* **2008**, *112*, 1938–1945.
- (71) Aarik, J.; Aidla, A.; Uustare, T.; Sammelselg, V. Morphology and Structure of TiO₂ Thin Films Grown by Atomic Layer Deposition. *J. Cryst. Growth* **1995**, *148*, 268–275.
- (72) Aarik, J.; Aidla, A.; Uustare, T.; Kukli, K.; Sammelselg, V.; Ritala, M.; Leskelä, M. Atomic Layer Deposition of TiO₂ Thin Films from TiI₄ and H₂O. *Appl. Surf. Sci.* **2002**, *193*, 277–286.
- (73) Xie, Q.; Jiang, Y.-L.; Detavernier, C.; Deduytsche, D.; Van, M., Roland L.; Ru, G.-P.; Li, B.-Z.; Qu, X.-P. Atomic Layer Deposition of TiO₂ from Tetrakis-Dimethyl-Amido Titanium or Ti Isopropoxide Precursors and H₂O. *J. Appl. Phys.* **2007**, *102*, 083521/1–083521/6.
- (74) Schuisky, M.; Aarik, J.; Kukli, K.; Aidla, A.; Hårsta, A. Atomic Layer Deposition of Thin Films Using O₂ as Oxygen Source. *Langmuir* **2001**, *17*, 5508–5512.
- (75) Aarik, L.; Arroval, T.; Rammula, R.; Mändar, H.; Sammelselg, V.; Aarik, J. Atomic Layer Deposition of TiO₂ from TiCl₄ and O₃. *Thin Solid Films* **2013**, *542*, 100–107.
- (76) Ritala, M. Atomic Layer Deposition of Oxide Thin Films with Metal Alkoxides as Oxygen Sources. *Science* **2000**, *288*, 319–321.
- (77) Puurunen, R. L. Formation of Metal Oxide Particles in Atomic Layer Deposition During the Chemisorption of Metal Chlorides: A Review. *Chem. Vap. Depos.* **2005**, *11*, 79–90.
- (78) Leem, J.; Park, I.; Li, Y.; Zhou, W.; Jin, Z.; Shin, S.; Min, Y.-S. Role of HCl in Atomic Layer Deposition of TiO₂ Thin Films from Titanium Tetrachloride and Water. *Bull. Korean Chem. Soc.* **2014**, *35*, 1195–1201.

- (79) Yun, J.-Y.; Park, M.-Y.; Rhee, S.-W. Comparison of Tetrakis(dimethylamido)titanium and Tetrakis(diethylamido)titanium as Precursors for Metallorganic Chemical Vapor Deposition of Titanium Nitride. *J. Electrochem. Soc.* **1999**, *146*, 1804–1808.
- (80) Neergaard Waltenburg, H.; Yates, J. T. Surface Chemistry of Silicon. *Chem. Rev.* **1995**, *95*, 1589–1673.
- (81) Higashi, G. S.; Chabal, Y. J.; Trucks, G. W.; Raghavachari, K. Ideal Hydrogen Termination of the Si(111) Surface. *Appl. Phys. Lett.* **1990**, *56*, 656–658.
- (82) Cerofolini, G. F.; Meda, L. Chemistry at Silicon Crystalline Surfaces. *Appl. Surf. Sci.* **1995**, *89*, 351–360.
- (83) Kern, W. The Evolution of Silicon Wafer Cleaning Technology. *J. Electrochem. Soc.* **1990**, *137*, 1887–1892.
- (84) Taft, E. A. Thin Thermal Oxide on Silicon. *J. Electrochem. Soc.* **1984**, *131*, 2460–2461.
- (85) Yeh, T. H. Thermal Oxidation of Silicon. *J. Appl. Phys.* **1962**, *33*, 2849–2850.
- (86) Taft, E. A. Steam Oxidation of Silicon. *J. Electrochem. Soc.* **1989**, *136*, 3476–3478.
- (87) Harari, E. Dielectric Breakdown in Electrically Stressed Thin Films of Thermal SiO₂. *J. Appl. Phys.* **1978**, *49*, 2478–2489.
- (88) Ang, S. T.; Wortman, J. J. Rapid Thermal Oxidation of Silicon. *J. Electrochem. Soc.* **1986**, *133*, 2361–2362.
- (89) Fogarassy, E.; Slaoui, A.; Fuchs, C.; Regolini, J. L. Rapid Thermal Oxidation of Silicon Monoxide. *Appl. Phys. Lett.* **1987**, *51*, 337–339.
- (90) Palmer, R. J. Polyamides, Plastics. In *Encyclopedia of Polymer Science and Technology*; John Wiley & Sons, Inc., 2002.
- (91) Spagnola, J. C.; Gong, B.; Arvidson, S. A.; Jur, J. S.; Khan, S. A.; Parsons, G. N. Surface and Sub-Surface Reactions during Low Temperature Aluminium Oxide Atomic Layer Deposition on Fiber-Forming Polymers. *J. Mater. Chem.* **2010**, *20*, 4213.
- (92) George, S. M. Atomic Layer Deposition: An Overview. *Chem Rev* **2009**, *110*, 111–131.

CHAPTER 2. Low Temperature Atomic Layer Deposition of Tungsten using Tungsten Hexafluoride and Highly-diluted Silane in Argon

Berc Kalanyan¹, Mark D. Losego¹, Christopher J. Oldham¹, and Gregory N. Parsons¹

¹*North Carolina State University, Department of Chemical and Biomolecular Engineering, North Carolina 27695*

This chapter is a reprint of an article published in *Chemical Vapor Deposition* **2013**, *19*, 161–166.

2.1 Abstract

Inherent chemical hazards in atomic layer deposition (ALD) processes can be mitigated significantly by careful selection of precursor materials. This work describes the effect of silane exposure on W ALD growth when the silane is heavily diluted (2 at.%) in argon. A wide ALD temperature window from 200 to ~300°C is identified exhibiting a growth rate of between 5 and 6 Å per ALD cycle using SiH₄ and WF₆ exposures of ~6×10⁵ and ~5×10⁵ Langmuirs, respectively. For deposition at lower temperature (150°C), growth rates of ~4.5 Å/cycle are obtained using silane exposure of 30 seconds per cycle, where the inlet silane partial pressure is controlled at 40 mTorr (corresponding to 1.2×10⁶ L of silane). Compositional analysis by secondary ion mass spectroscopy and Auger electron spectroscopy show less than ~5 at.% Si in the W films, with the smallest Si content in films deposited at 300 °C. We also describe effects of hot-wall reactor preconditioning on film growth. We conclude that the dilute silane co-reactant offers an alternative to the common disilane, borosilane, or undiluted silane precursors, allowing well controlled W deposition at 150°C.

2.2 Introduction

Many atomic layer deposition (ALD) precursors are pyrophoric, flammable, and/or explosive. While passive safety features and process control measures are often in place to mitigate the inherent hazards of ALD precursors, hazard reduction by purposeful selection of precursors remains the most effective option for improving the safety of the chemical process. The Occupational Safety and Health Administration (OSHA) in the United States sets workplace standards for chemical hazards, allowable exposure limits, and hazard classification. In laboratory settings, such as in university research buildings, OSHA and local safety regulations dictate the allowable concentration limits for hazardous compounds. OSHA 1910.1200 App B.12 lists silane as a flammable gas above its pyrophoric limit when exposed to atmospheric water.^[1] However, at concentration of 2% in inert gas, silane (SiH_4) and disilane (Si_2H_6) are considered to be less dangerous for laboratory use. Here we use 2% (w/w) SiH_4 in Ar as a co-reactant and silicon source in the tungsten ALD process.

To develop a viable and robust ALD process, it is important that the selected precursors produce energetically favorable and kinetically fast half-reactions at the deposition temperature used. Many metal oxides can be produced by ALD, for example, using a reactive organometallic or metal halide in combination with an oxygen source (water, oxygen, ozone, or others) in an acid/base reaction sequence. Some of these precursors are sufficiently reactive that they are also pyrophoric and react spontaneously with ambient air. Metals are often formed through reductive schemes using metal β -diketonates, halides, acetylacetonates and other metal-ligand systems in combination with a reducing agent. Tungsten ALD proceeds using fluorosilane elimination chemistry, where WF_6 reacts with

surface W-Si-H_x groups to yield surface W-F_x and volatile SiH_xF_y.^[2,3] The exothermic conversion of SiH₄ (or often Si₂H₆) reactant to SiH_xF_y vapor therefore contributes to the favorable energetics of the overall growth reaction. A key problem with silane is that it is pyrophoric in air, but the ignition behavior is unpredictable and it does not always ignite in air immediately.^[1] Because silane is heavier than air, it can accumulate in gas cabinets or on floors and detonate when disturbed. Tungsten deposition is important for integrated circuit fabrication,^[3] and the uniformity and high conformality obtained by ALD makes it suitable for ultra-high aspect ratio structures in electronics^[4] and other applications^[5-7]. Other ALD processes also use silane or disilane as sacrificial reagents, including processes for molybdenum,^[8] W-C-N alloys,^[9] and others.

Most processes described to date utilize pure (undiluted) silane or disilane.^[2,10-12] Dilute silane has been used previously^[13], but effect of dilution or temperature on the required ALD exposures was not presented. In this work we explore how film growth and overall process requirements are affected by silane exposure using 2% SiH₄ in argon, and present parameters required to achieve good quality W ALD. We find that growth rate saturation scales with silane partial pressure and exposure time, indicating that the gas dilution does not negatively influence the rates of surface reactions that occur during the silane exposure step. Total processing time for 100 cycles of W was 3.5 hours. This was approximately 40 minutes longer than it would have taken to deposit the same number of cycles with pure (50x greater concentration) silane precursor.

2.3 Results and Discussion

2.3.1 Growth Rate versus Temperature and SiH_4 Exposure

Figure 2 shows the W film thickness (determined from X-ray reflectivity) plotted versus number of ALD cycles for deposition at 225°C on alumina-coated silicon. The silane exposure time was 60 seconds per cycle, and $\Delta P = 0.5$ Torr, corresponding to a fixed silane exposure of (0.02×0.5) Torr \times 60 sec = 6×10^5 L. The WF_6 exposure is fixed at $\sim 5 \times 10^5$ L which is sufficient for growth saturation, as described in the Experimental section below. Error bars representing standard error are included for each point but for some values the error bar is smaller than the data symbol. The data fit a linear trend with a slope of 6.1 Å/cycle. This is within the range of previously reported growth rates for W ALD.^[2,10–12] However, the growth per cycle for W ALD is known to depend on the extent of WF_6 and silane (or disilane) exposure. Furthermore, according to AES measurements, the extent of silicon growth during the silane exposure was shown to depend logarithmically on surface temperature, especially using high Si_2H_6 exposures (3×10^2 to 1×10^5 L).^[15] Smaller disilane exposures lead to less silicon uptake and therefore less W deposition during the WF_6 exposure. For example, smaller exposures of 2700 and 750 L for disilane and WF_6 respectively,^[2] led to a W growth rate of ~ 2.5 Å/cycle between 150 and 325 °C. For our experiments with larger silane exposures we used X-ray reflectivity to determine film thickness as shown in Figure 3, where the reflections become more frequent with increasing film thickness. The critical angle scan in panel (a) is used along with reflections in panel (b) to obtain film thicknesses of 27.5 and 57.6 nm for 50 and 100 cycles of W (225°C and

$\sim 6 \times 10^5$ L), respectively.. The following sections make use of thickness data obtained in this manner.

The effect of deposition temperature on the growth per cycle is shown in Figure 4. The SiH_4 and WF_6 exposures for these runs were fixed at $\sim 6 \times 10^5$ L and $\sim 5 \times 10^5$ L, respectively. The data show a broad ALD window with a growth rate of $\sim 6.0 \pm 0.5$ Å/cycle between 200 and 300°C, with a larger growth rate at 350°C. Previous reports show constant growth rates between ~ 150 and 325°C, consistent with our results.^[2]

Figure 4 also shows two data points (triangles) with very low growth rate at 250 and 275°C. These points reflect the importance of reactor preconditioning on W growth rate for low silane doses. When studying growth rate at low silane dosing using a series of depositions that systematically increased growth temperatures, we found growth rates that were abnormally lower than prior results using identical conditions. We traced this back to differences in the history of the chamber. However, this “chamber history” could not be restored with a simple pre-coat of 25 cycles of TMA/water. Instead, we found it necessary to use a pretreatment of 10^6 L or greater of silane exposure prior to low-dose conditions to achieve repeatable results. We ascribe this to a chamber wall conditioning effect. When we step-wise increase the deposition temperature in a series of ALD runs, the W-coated reactor wall (which is isothermal with the deposition surface) becomes more reactive with silane.^[15] This increased reactivity with the walls will deplete silane as the gas flows downstream, leaving less silane to react at the substrate surface, thereby limiting deposition during the WF_6 exposure. The two points with near zero growth rate in Figure 4 were collected after five consecutive runs using a relatively low silane exposure of $\sim 6 \times 10^5$ L. When we

preconditioned the chamber by doing a run using a larger ($\sim 10^6$ L) silane exposure, the growth rate with the $\sim 6 \times 10^5$ L silane dosing returned to following the trend shown in Figure 4. Since this effect occurs even with the alumina pretreatment, it suggests that the Al_2O_3 layer does not completely cover the W on the walls, or the alumina layer permits silicon or fluorine transport during the WF_6 reduction step. Accordingly, in order to report reproducible growth rate data we preceded each low silane exposure deposition with a conditioning run consisting of high silane exposures.

Figure 5 shows the effect of silane exposure on film growth rate using three different values of ΔP with various exposure times at 150°C . Growth rate data were collected using SiH_4/Ar ΔP of 0.5, 1 and 2 Torr (with a fixed N_2 partial pressure of 2 Torr) with gas pulse times of 10 to 60 seconds per cycle. This produces different silane exposures ($L = 0.02 \times \Delta P \times \text{time}$) Since the N_2 partial pressure is fixed, increasing the SiH_4/Ar ΔP changes the silane dilution fraction in the reactor chamber. By plotting the growth rate versus exposure, we can determine if the silane dilution in the range studied has any effect on the extent of the silane surface reaction. The growth rate versus exposure plotted in Figure 5 follows a single trend line, indicating the growth is not strongly affected by the dilution fraction. Growth reaches $\sim 4.9 \pm 0.2$ Å/cycle for silane exposure near 5×10^6 L at 150°C . Moreover, as exposure increases, the data trend shows ‘slow’ or ‘gradual’ saturation, (i.e. some continued silicon uptake on the growth surface during the silane dose step) consistent with previous W ALD studies using high silane exposures.^[15] Greater than one monolayer/cycle deposition rates are likely a result of extra Si deposition during the SiH_4 exposure. This phenomenon has been described previously for Si_2H_6 reactions with SiH_xF_y^* surface species where SiH_2 is inserted

into Si-H bonds.^[12, 16] We expect a similar mechanism for SiH₄ to be responsible for the higher than expected growth rates we observe.

With density and atomic weight $\rho = 19.25 \text{ g/cm}^3$ and $MW = 183.8 \text{ g/mol}$ respectively, the thickness of one W monolayer is expected to be $t_m = [(MW \times N_A)/\rho]^{1/3} = \sim 2.5 \text{ \AA}$, where N_A is the Avogadro constant. Therefore, the observed growth rate near 5 \AA/cycle corresponds to ~ 2 monolayers per cycle. The growth exceeds one monolayer because the silane reaction with the fluorinated tungsten surface produces more than one monolayer of tungsten silicide, which in turn allows more than one W layer to form during the subsequent WF₆ exposure step.^[16] The extent of silicide formation will depend on temperature and exposure, and the extent of silicon removal from the film will depend on the WF₆ exposure and reaction kinetics. Therefore, it is important to analyze the amount of silicon in the W film to fully characterize the W ALD reaction.

2.3.2 Film Structure and Composition

Figure 6 shows X-ray diffraction data from W ALD films on silicon substrates deposited at 150, 250, and 350°C. The films were 100 cycles of W deposited with 120 seconds silane pulse time per cycle at $\Delta P = 0.5 \text{ Torr}$, corresponding to $1.2 \times 10^6 \text{ L}$ of silane exposure. The two principal reflections centered near $2\theta = 40$ and 70° in the diffraction pattern match those for β -W (reference pattern 03-065-6453). Furthermore, crystallinity of the films increased with deposition temperature, as evidenced by increasing sharpness of the reflections in Figure 6. AFM analysis of the W films showed RMS roughness of 0.57 and 1.05 nm after 100 and 200 cycles, respectively, compared to less than 0.5 nm roughness on

the uncoated alumina/silicon substrate. Films deposited with cycle numbers greater than 200 lead to visible flaking of tungsten, consistent with uncompensated film stress.

We used dynamic SIMS to determine how composition changes with silane exposure. [12,17] Figure 7 shows the SIMS signals for Si^- and W^- ions collected from tungsten samples deposited at 150, 250, and 350°C. The films were 100 cycles of W deposited with 120 seconds silane pulse time per cycle at $\Delta P = 0.5$ Torr, corresponding to 1.2×10^6 L of silane exposure. At each sputter depth we detected fewer than 10 total counts of O^- , AlO^- , SiO_2^- , and WO_3^- up to the $\text{Al}_2\text{O}_3/\text{SiO}_2$ interface, indicating oxygen was below the SIMS detection limit in the film bulk. SIMS analysis on three different spots on each sample give very similar concentration profiles. Signals from Si^- and Si_2^- signals were detected in each film studied. Because ionization yields are not well known, the elemental concentrations cannot be directly quantified by SIMS. For example, the ionization yield of isolated silicon atoms in the W matrix is likely different from that of clustered silicon in W or silicon atoms in the crystalline substrate. The large sputter yield for Si relative to that for W leads to a Si:W signal ratio that is much larger than the atomic ratio in the sample. For some samples, we used Auger electron sputter depth profiling to characterize silicon content, and found that a W film deposited at 150°C using 3.0×10^6 L of silane yielded ~ 5 atomic % silicon in the film. SIMS analysis of a sample formed under the same conditions shows a Si:W signal ratio of 4.35. For the data in Figure 7, the Si:W signal ratio is 4.68, 2.86, and 2.01 for films deposited at 150, 250, and 350°C respectively using 1.2×10^6 L of silane, indicating more silicon in films deposited at lower temperatures. Figure 8 shows SIMS data from samples produced at 150°C with different values of silane exposure between 3×10^5 and 4.8×10^6 L.

The averaged Si:W signal ratio for these films is 4.35, 4.68, and 5.00 for silane exposure of 3.0×10^5 , 3.0×10^6 L and 4.8×10^6 L, respectively. Larger silane exposures with fixed WF_6 exposure tends to increase the amount of silicon left in the growing film.

During SIMS analysis, the sputter time needed to reach the W/ Al_2O_3 interface is approximately related to film thickness. The relationship is not precise because of species-dependent etch rates. The data in Figure 7 shows longer sputter times are needed to reach the interface, i.e. thicker films, for films deposited at higher temperatures, consistent with data in Figure 4. Step profilometry after sputtering gives crater depths of ~ 30 , 64, and 107 nm for the samples shown. Similarly, the results in Figure 8 show suggest a slight increase in growth rate with increasing silane dose, consistent with data in Figure 5.

Summary and Conclusions

We find that using heavily diluted SiH_4 in the SiH_4/WF_6 tungsten ALD process yields good quality W films with less than ~ 5 at.% silicon. Using silane exposure of 6×10^5 with large WF_6 exposure (5×10^5 L), the growth rate is 6.0 ± 0.5 Å/cycle within a temperature window between 200 and 300 °C. Using a dilute SiH_4 partial pressure of 2 Torr (corresponding to 0.04 Torr of SiH_4) relatively long dose times of ~ 30 seconds per cycle (corresponding to 1.2×10^6 L) were needed to approach growth saturation. The growth saturation scales consistently with changes in both silane exposure time and partial pressure, indicating that gas dilution does not impede the rates of surface reactions during the silane exposure step. Increasing silane exposure with a fixed WF_6 exposure, we see a ‘slow’ saturation in growth rate, indicating some continued but relatively slow silane consumption on the growth surface. The growth rate of 5-6 Å/cycle corresponds to ~ 2 W monolayers per

cycle. The growth rate and saturation results are consistent with growth mechanisms described for similar reactant exposures using higher silane or disilane partial pressure (i.e. using pure disilane reactant). The relative concentration of silicon remaining in the W film is affected by silane exposure and deposition temperature, but the silicon content can be minimized by choice of deposition temperature. Under some growth conditions, the growth rate in a hot-wall reactor configuration can be affected by reactor preparation. Specifically, growth rate results suggest that increasing the temperature from run-to-run will increase the rate of silane consumption on the W-coated reactor walls, leading to silane depletion and reduced film growth downstream in the target growth zone.

2.4 Experimental

We deposited tungsten in a custom built hot-walled ALD reactor constructed within a 2.4 m wide fume hood. The reactor is shown schematically in Figure 1. The reactor chamber is a 61 cm long stainless-steel tube (~4 cm inside diameter). The tube is heated using resistive heaters controlled by two proportional–integral–derivative (PID) controllers, and temperature is measured at three points along the tube using thermocouples mounted on the outer walls of the reactor tube. Calibration measurements show excellent agreement ($< 5^{\circ}\text{C}$) between the outer wall and deposition zone temperature. Precursors are delivered into the reaction zone through 0.635 cm diameter stainless steel tubes, heated to 70°C , and pressure is monitored using a convection enhanced Pirani gauge installed downstream from the reaction zone. Flow rate for each gas is metered using a needle valve. The gas switching is controlled pneumatically using actuated diaphragm valves controlled by custom LabVIEW software.

Before W ALD, we typically coated each substrate with ALD Al_2O_3 in the same reactor, at the same temperature as the W ALD. For Al_2O_3 we used 98% trimethyl aluminum (TMA) (Strem Chemicals) and reagent grade water (Ricca Chemicals) as precursors. The tungsten source was 99.9% tungsten hexafluoride (WF_6) from Sigma-Aldrich, and the silane was a dilute mixture (2% by weight) in 99.999% Ar (Custom Gas Solutions, Durham NC). The carrier and purge gas was 99.999% pure N_2 , and it passed through an Entegris GateKeeper inert gas purifier to remove any residual water before entering the reactor. Excess precursor and product gases are pumped out of the reactor using an Alcatel Pascal 2010SD rotary vane pump (9.7 L/min) filled with fluorocarbon oil (Fomblin 25/6 grade). Before reaching the pump, gases are scrubbed using an activated charcoal filter filters (Visi-Trap by Mass-Vac Inc.), to remove organic product vapors (e.g. from the TMA/ H_2O reaction), followed by a Sodasorb® filter to remove acid vapors. To maintain the reactor, we visually check the pump oil for residue, and we replaced both filters every six months. We find that the pump oil is visually clear for at least 6,000 tungsten cycles, which is approximately equivalent to consumption of a 225 g bottle of WF_6 at 1 second dose per cycle (i.e. after about sixty deposition runs).

Before each tungsten deposition, the carrier gas pressure was adjusted to the operating pressure of 2.0 Torr. A pressure of 2.0 Torr corresponds to a gas flow rate of approximately 20 standard cubic centimeters per minute (sccm) with a butterfly valve present before the pump. The gas flow rate was estimated by the measured pressure change versus time for flow of N_2 into the sealed reactor. Silicon wafers (p-type, (100) orientation) were purchased from WRS Materials (wafers manufactured by MEMC) and were used as received. Silicon was

cleaved into 1 x 1 cm pieces and loaded into the chamber using a flat sample boat, positioned at the midpoint of the reaction zone (30 cm downstream from gas inlet). ALD films were deposited directly on the native silicon oxide layer or on surfaces pretreated with ALD Al₂O₃.

After loading the samples, the reactor was pumped down to 80 mTorr followed by dry nitrogen flow for 30 minutes at the operating pressure to let the sample reach the growth temperature. Most samples were coated with 25 cycles of Al₂O₃ to promote W nucleation and adhesion. One Al₂O₃ ALD cycle followed the sequence TMA/N₂/H₂O/N₂ = 0.05/30/0.05/30 seconds respectively, producing 1.1-1.2 Å/cycle as determined by spectroscopic ellipsometry (J.A. Woollam Co. alpha-SE, using the CompleteEASE data analysis software package). Optical constants for Al₂O₃ were determined by fitting SE data from 1,000 cycles of ALD to a Cauchy model. A native SiO₂ layer of 1.7 nm, as measured for each wafer, was also included in our optical model.

The tungsten ALD sequence was typically WF₆/N₂/2%SiH₄/N₂ = 1/30/60/30 seconds, although saturated growth could also be achieved using shorter SiH₄ exposure times. The amount of SiH₄ delivered to the chamber was metered using a needle valve, so the silane exposure could be adjusted by either changing the silane dose time or by adjusting the associated needle valve to achieve the desired silane pressure. For instance, under N₂ flow and P = 0.5 Torr, a dose of 2% silane in Ar could increase the total reactor pressure to 1.5 Torr. The ΔP=1.0 Torr corresponds to an inlet silane partial pressure of 0.02 × 1.0 = 20 mTorr. A 60 second dose time corresponds to an overall exposure of 20 mTorr × 60 sec = 1.2×10⁶ Langmuirs, L (1 L = 10⁻⁶ Torr·s). The WF₆ cycle typically produces ΔP=1.0 Torr. However, using the Shomate equation to estimate the WF₆ gas phase heat capacity,^[14] the

thermal conductivity of WF_6 is $\sim 2\times$ larger than for N_2 . Therefore, the Pirani gauge will measure a pressure change that is $\sim 2\times$ larger than the true pressure change. The estimated WF_6 exposure is $1.0 \text{ Torr} \times 0.5 \times 1 \text{ sec} = 5 \times 10^5 \text{ L}$, and is fixed for all studies here. Also, the gas pumping speed may depend on the gas composition, which will also affect the values obtained. Therefore the calculated exposures are used as relative values to compare different process conditions.

The WF_6 exposure used is large enough to saturate the W ALD growth for the range of silane exposures used.^[15] A simple calculation for gas flow rate through the metering valve (Swagelok S-series) at the WF_6 tank outlet reveals that a 1 second pulse delivers 14.5 mmol or $\sim 9 \times 10^{21}$ molecules of WF_6 into the reactor. For a combined reactor and substrate surface area of $\sim 1500 \text{ cm}^2$, precursor consumption per cycle is $\sim 2 \times 10^{18}$ molecules. This is much smaller than the number of molecules delivered, demonstrating that the WF_6 dose is sufficient for saturated exposure. Furthermore, we found that runs performed with WF_6 0.5 s dose time yielded the same growth rates, also consistent with fully saturated growth for 1 s WF_6 exposure.

We used a PANalytical Empyrian X-ray diffraction system configured for reflectivity to measure W film thickness. The X-ray tube was run at 40 kV with a 20 mA emission current. Two divergence slits and a beam parallelizer were used to shape the beam. On the detector side, a parallel plate collimator and Cu slits were placed before the Xe gas tube. For each sample, critical incidence angle and several external reflections past the critical angle were recorded for thickness analysis. Film thickness was calculated from the critical angle

and the distance (in degrees) between adjacent reflections by a simple analysis using the Fresnel equations.

We characterized the W film composition using a time of flight secondary ion mass spectrometer (ToF-SIMS) instrument (TOF.SIMS5, ION TOF, Inc. Chestnut Ridge, NY) equipped with a Bi_n^{m+} ($n = 1 - 5$, $m = 1, 2$) liquid metal ion gun in dynamic SIMS mode. For the depth profiles, 1 keV low energy Cs^+ with 10 nA beam current was used to create a $200 \times 200 \mu\text{m}^2$ area, and the middle $50 \times 50 \mu\text{m}^2$ area was analyzed using 0.2 pA Bi_3^+ primary ion beam. Mass spectra contained peaks corresponding to: F^- , H^- , O^- , Si^- , Si_2^- , SiF_5^- , SiO_2^- , $^{182}\text{W}^-$, and $^{182}\text{WO}_3^-$. We sputtered down to the $\text{Al}_2\text{O}_3/\text{SiO}_2$ interface and tracked Si and W content of the thin films as a function of profiling depth. The position of the $\text{Al}_2\text{O}_3/\text{SiO}_2$ and SiO_2/Si interfaces corresponded to changes in O^- , AlO^- , and SiO_2^- signals. The negative secondary ion mass spectra obtained were calibrated using C^- , O^- , F^- , and WO_3^- .

2.5 Acknowledgments

We thank C. Zhou and F. Stevie at the Analytical Instrumentation Facility at NC State for their help with SIMS depth profiling experiments, and K. Arpin, A. Cloud, R. Haasch at the Frederick Seitz Material Research Laboratory at the University of Illinois for AES measurements. We also acknowledge partial support for B. K. through NSF project #1034374 in the Process and Reaction Engineering program.

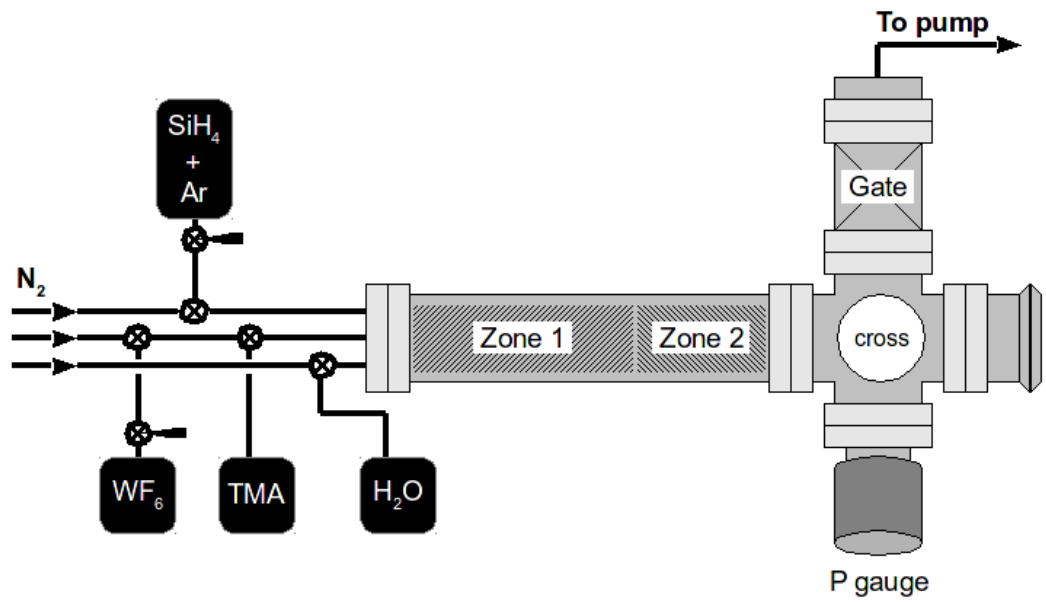


Figure 2.1. Schematic view of the hot-wall tube flow ALD reactor used for these studies. The reactor has three precursor/reactant feed lines and two independent heating zones. Needle valves control silane and tungsten hexafluoride flow.

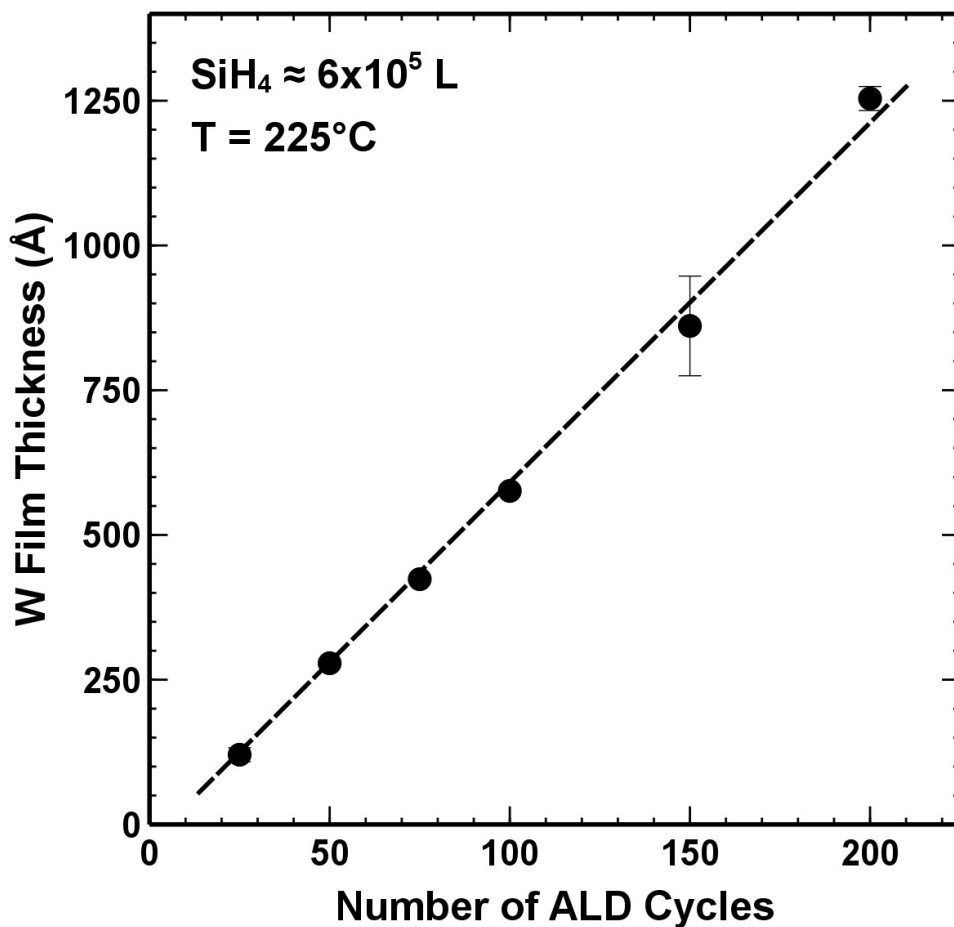


Figure 2.2. Tungsten film thickness versus number of ALD cycles as measured by X-ray reflectivity. Deposition proceeded at 225°C using WF₆/N₂/2%SiH₄/N₂ = 1/30/60/30 seconds, respectively. The pressure change during the silane exposure was 0.5 Torr corresponding to (0.02×0.5)Torr × 60 sec = 6·10⁵ L. The thickness for the film with 150 cycles was obtained by profilometry, demonstrating consistent thickness values from reflectivity and profilometry.

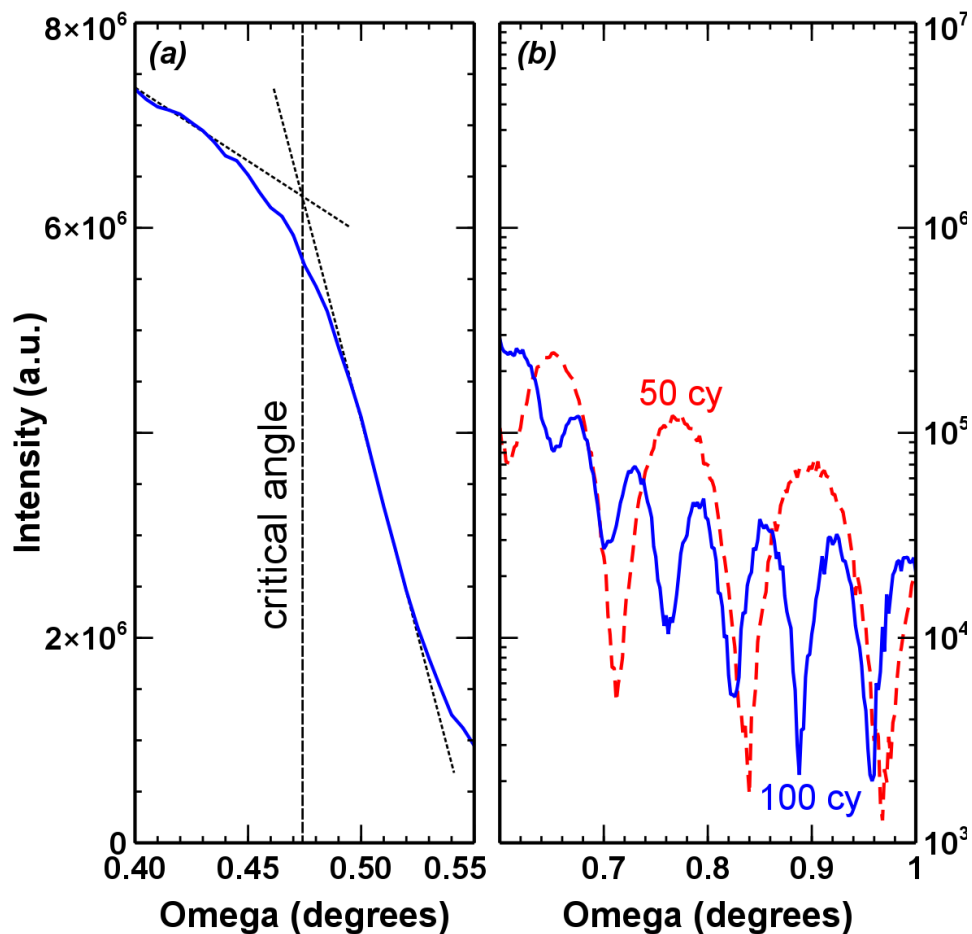


Figure 2.3. Omega-2Theta scans from tungsten deposited at 225°C using a silane exposure of $\sim 6 \times 10^5$ L. In (a) the critical angle is shown for a typical ALD tungsten thin film. Reflections from 50 and 100 cycles of tungsten are shown in (b).

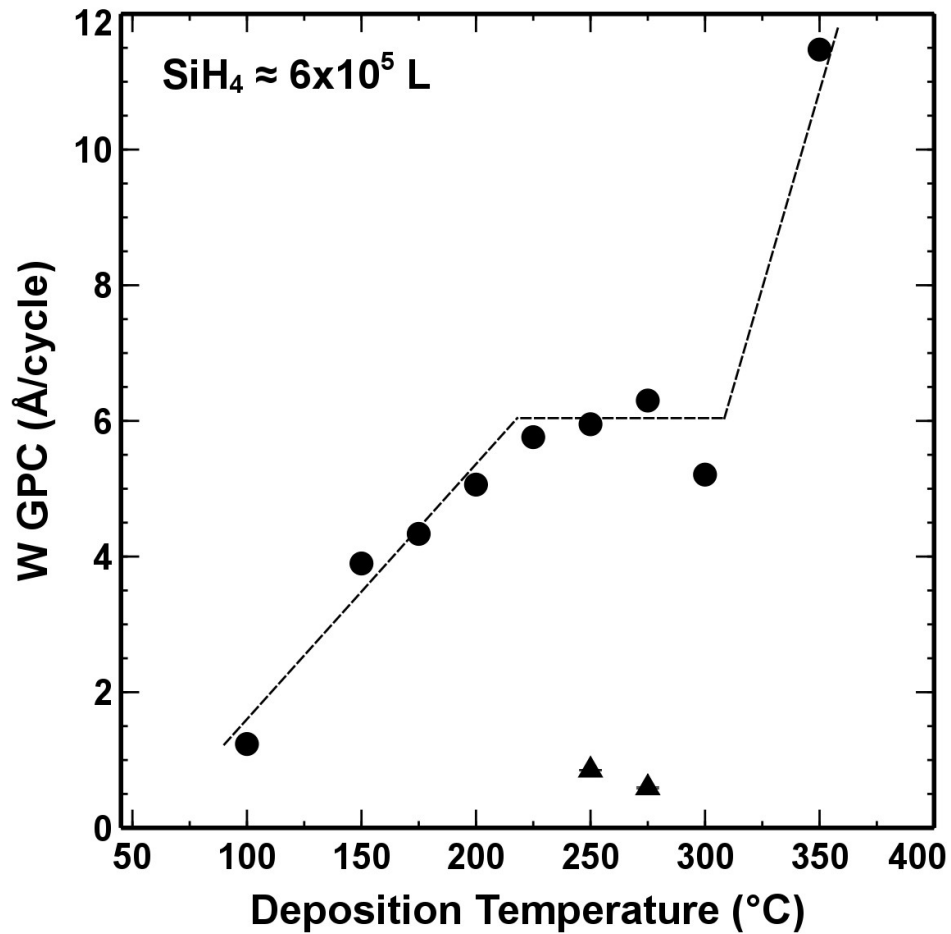


Figure 2.4. ALD temperature window for the WF₆/2% SiH₄ process using SiH₄ exposure of ~6×10⁵ L. An approximately flat temperature window appears between 200 and 300 °C. Some runs (▲) showed very low growth rates, as discussed in the text.

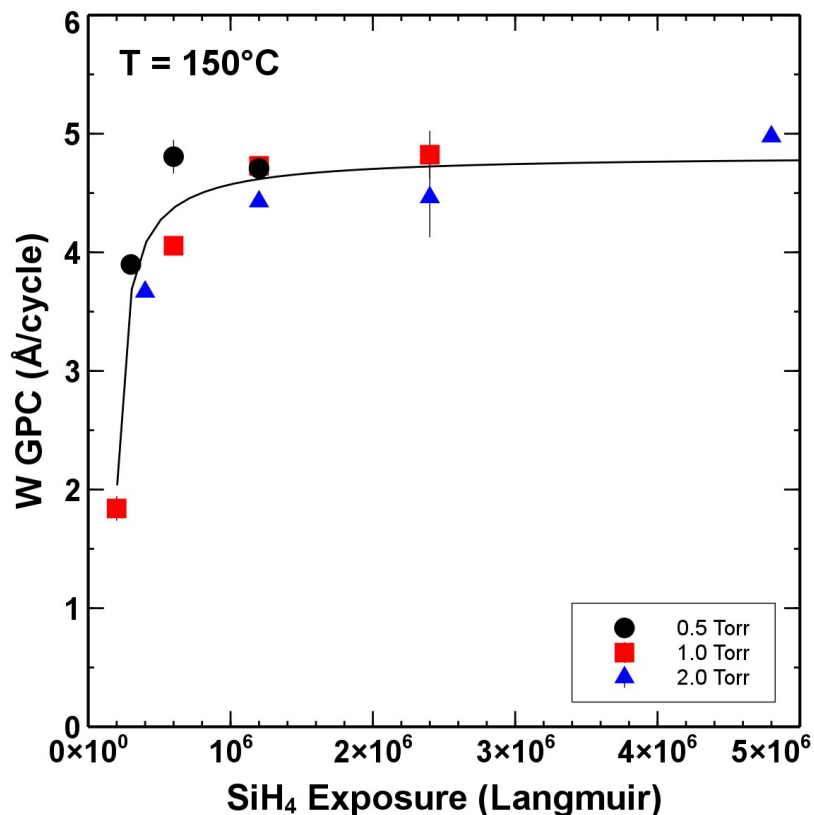


Figure 2.5. Tungsten thickness per cycle after 100 ALD cycles at 150 °C plotted versus SiH₄ exposure using a fixed WF₆ exposure. Silane exposure was adjusted by changing the exposure time at fixed partial pressure, and by changing the partial pressure with fixed exposure time. The symbols correspond to the total pressure change during the dilute silane exposure. All the data sets fall on a single trend line indicating the silicon reaction rate scaling is no dependent on silane dilution. Growth shows gradual saturation with increasing silane exposure.

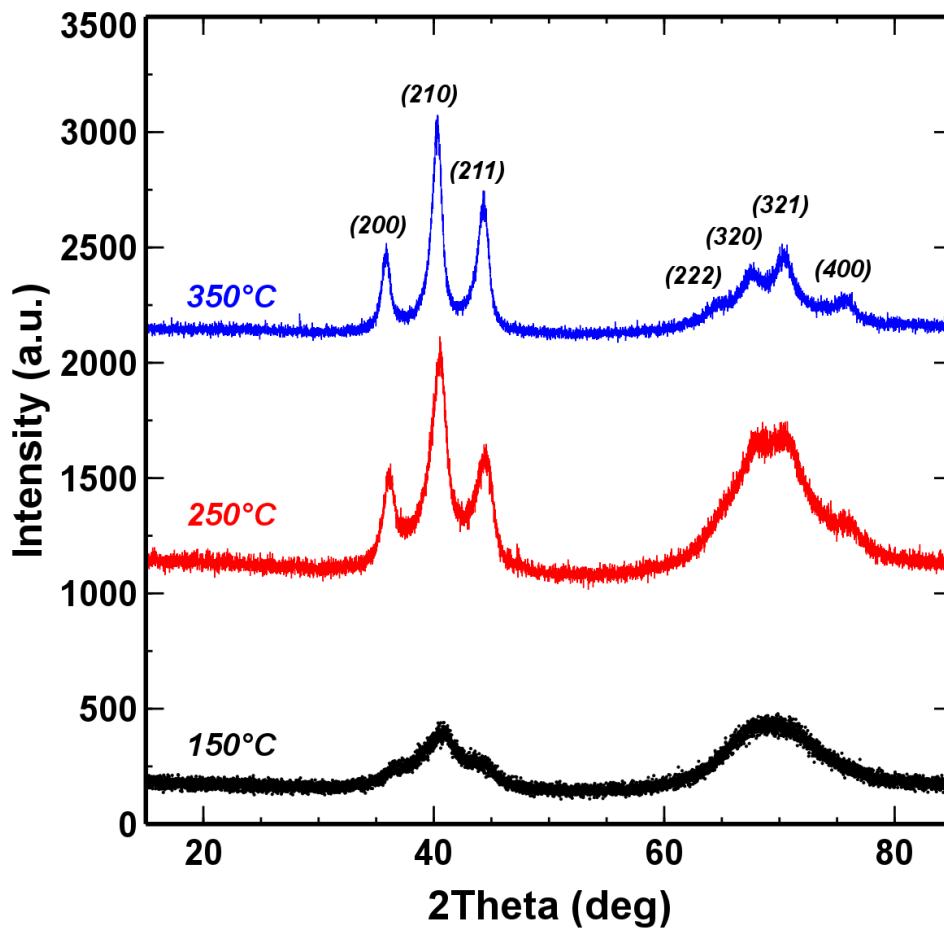


Figure 2.6. X-ray diffraction results from W samples deposited at three different temperatures using a silane exposure of 1.2×10^6 L. The data shows increasing crystallinity at higher deposition temperature.

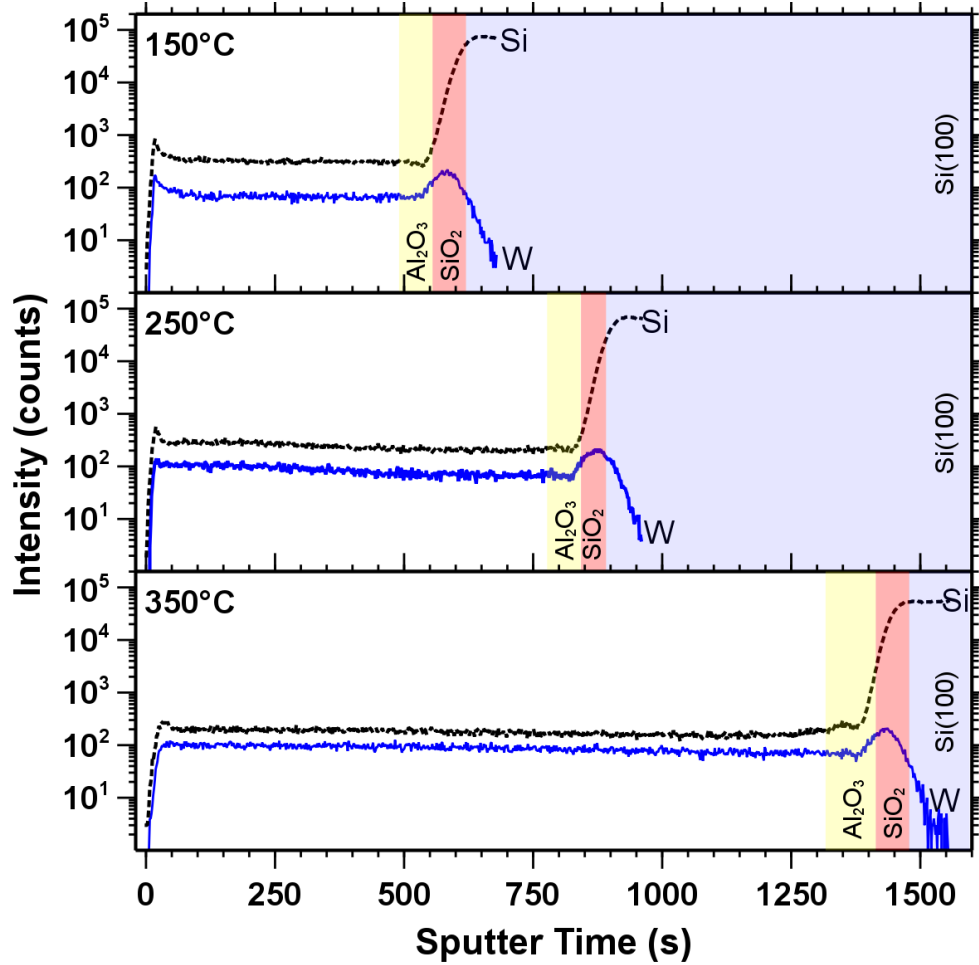


Figure 2.7. SIMS depth profile showing W and Si signals collected from W samples deposited using 100 cycles at 150, 250, and 350°C. The silane ΔP and exposure time are 0.5 Torr and 30 seconds, respectively, corresponding to 1.2×10^6 L.

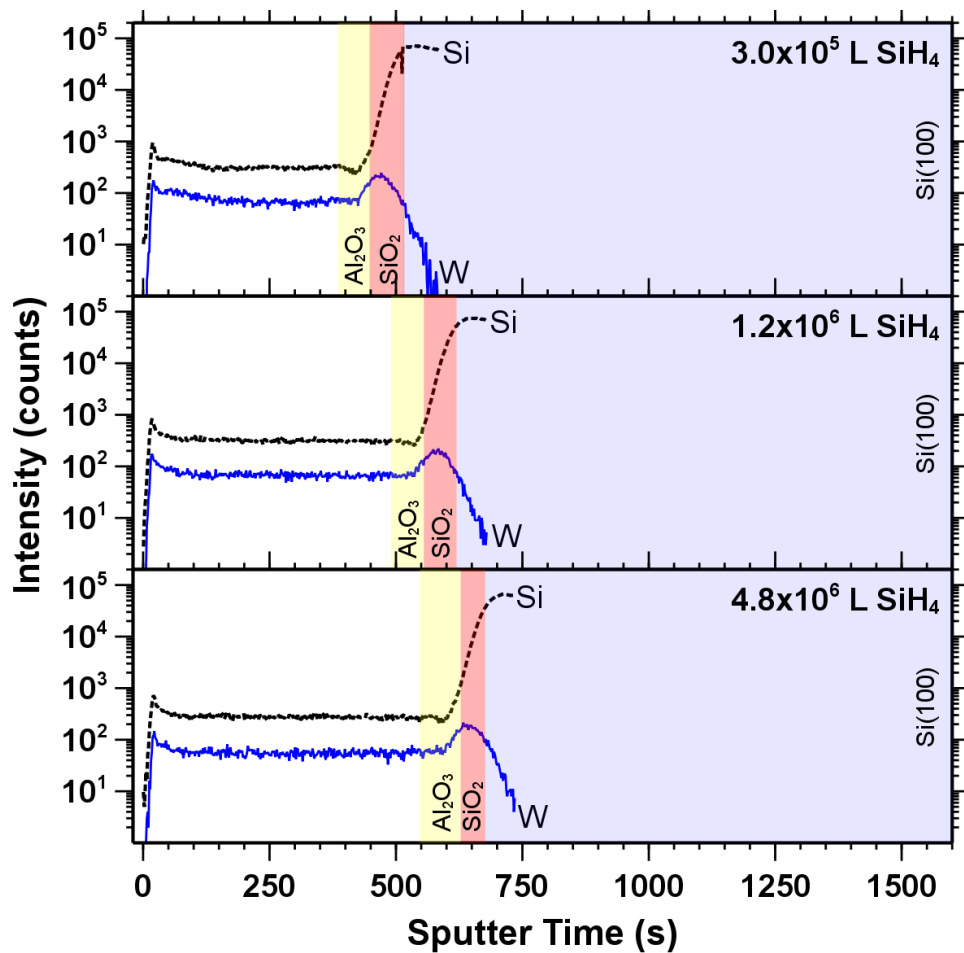


Figure 2.8. SIMS depth profile of W films formed using 100 ALD cycles using different SiH_4 exposure at 150°C . Data shows a small increase in silicon content with increasing silane exposure.

2.6 References

- [1] F. Tamanini, J. -L Chaffee, R. -L. Jambor, *Process Saf. Prog.* **1998**, *17*, 243–258.
- [2] J. Klaus, S. Ferro, S. George, *Thin Solid Films* **2000**, *360*, 145–153.
- [3] S.-H. Kim, N. Kwak, J. Kim, H. Sohn, *J. Electrochem. Soc.* **2006**, *153*, G887.
- [4] S.-H. Kim, E.-S. Hwang, B.-M. Kim, J.-W. Lee, H.-J. Sun, T. -E. Hong, J.-K. Kim, H. Sohn, J. Kim, T.-S. Yoon, *Electrochem. Solid-State Lett.* **2005**, *8*, C155–C159.
- [5] F. -H. Fabreguette, R. -A. Wind, S. -M. George, *Applied Physics Letters* **2006**, *88*, 013116.
- [6] F. -H. Fabreguette, S. -M. George, *Thin Solid Films* **2007**, *515*, 7177–7180.
- [7] J. -S. Jur, W. -J. Sweet, C. Oldham, G. -N. Parsons, *Adv. Funct. Mater.* **2011**, *21*, 1993.
- [8] D. Seghete, G. -B. Rayner, A. -S. Cavanagh, V. -R. Anderson, S. -M. George, *Chem. Mater.* **2011**, *23*, 1668–1678.
- [9] Y. -T. Kim, J. -H. Park, *Phys. status solidi (a)* **2005**, *202*, R164–R166.
- [10] J. Klaus, S. Ferro, S. George, *Appl. Surf. Sci.* **2000**, *162-163*, 479–491.
- [11] R. -K. Grubbs, C. -E. Nelson, N. -J. Steinmetz, S. -M. George, *Thin Solid Films* **2004**, *467*, 16–27.
- [12] F. -H. Fabreguette, Z. -A. Sechrist, J. -W. Elam, S. -M. George, *Thin Solid Films* **2005**, *488*, 103–110.
- [13] W. Lei, L. Henn-Lecordier, M. Anderle, G. -W. Rubloff, M. Barozzi, M. Bersani, *J. Vac. Sci. Technol., B: Nanotechnol. Microelectron.: Mater., Process., Meas., Phenom.* **2006**, *24*, 780.
- [14] M. -W. Chase, National Institute of Standards and Technology (U.S.) *NIST-JANAF thermochemical tables*; American Chemical Society□; American Institute of Physics for the National Institute of Standards and Technology: [Washington, D.C.]; Woodbury, N.Y., **1998**.
- [15] J. Elam, C. Nelson, R. Grubbs, S. George, *Surf. Sci.* **2001**, *479*, 121–135.

- [16] R. -W. Wind, F. -H. Fabreguette, Z. -A. Sechrist, S. -M. George, *Journal of Applied Physics* **2009**, *105*, 074309–074309–13.
- [17] T. -N. Bell, K. -A. Perkins, P. -G. Perkins, *J. Phys. Chem.* **1984**, *88*, 116–118.

CHAPTER 3. Highly Conductive and Flexible Nylon-6 Nonwoven Fiber Mats Formed using Tungsten Atomic Layer Deposition

Berc Kalanyan¹, Christopher J. Oldham¹, William J. Sweet III¹ and Gregory N. Parsons^{1*}

¹*North Carolina State University, Department of Chemical and Biomolecular Engineering, North Carolina 27695*

This chapter is a reprint from an article published in *ACS Appl. Mater. Interfaces* **2013**, *5*, 5253–5259.

3.1 Abstract

Low temperature vapor-phase tungsten atomic layer deposition (ALD) using WF_6 and dilute silane (SiH_4 , 2% in Ar) can yield highly conductive coatings on nylon-6 microfiber mats, producing flexible and supple nonwovens with conductivity of ~ 1000 S/cm. We find that an alumina nucleation layer, reactant exposure, and deposition temperature all influence the rate of W mass uptake on 3D fibers, and film growth rate is calibrated using high surface area anodic aluminum oxide. Transmission electron microscopy (TEM) reveals highly conformal tungsten coatings on nylon fibers with complex ‘winged’ cross-section. Using reactant gas ‘hold’ sequences during the ALD process, we conclude that reactant species can transport readily to reactive sites throughout the fiber mat, consistent with conformal uniform coverage observed by TEM. The conductivity of 1,000 S/cm for the W-coated nylon is much larger than found in other conductive nonwovens. We also find that the nylon mats maintain 90% of their conductivity after being flexed around cylinders with radii as small as 0.3 cm. Metal ALD coatings on nonwovens make possible the solvent-free functionalization of textiles for electronic applications.

3.2 Introduction

Conductive fibers have applications in medicine, fluidics, catalysis, filtration, separation, energy storage, electromagnetic shielding,¹ smart textiles,² and chemical sensing.²⁻⁴ Natural and synthetic fibers are made electrically conductive using a variety of methods including incorporation of metal fillers into fibers,⁵ application of exterior conductive polymer coatings by in-solution polymerization⁶ or spray-coating,^{7,8} and core-shell fiber structures with conductive core or shell.⁹ Fibers that incorporate organic conductive coating or blends,^{6,10-12} result in fibers with conductivity values less than 2 S/cm. Composite nanofibers containing oriented multiwalled carbon nanotubes reach about 1 S/cm conductivity¹³ and Kevlar fibers coated with single-walled nanotubes result in 65 S/cm⁷. Metallic coatings on fibers are inherently more conductive. Successively Ni- and Au-plated Kevlar fibers can display electrical conductivity values of 6 S/cm¹⁴. Silicone fibers filled with Ag flakes⁵ reach 470 S/cm, while nylon fiber mats coated with Ag using a commercial electroless plating solution exceed ~1800 S/cm when loaded with ~17 wt.% Ag.⁴

Another method of imparting conductivity to materials with complex geometries, such as nonwoven fabrics, is by applying coatings using vapor deposition techniques. In a previous work, we showed the application of tungsten coatings on woven quartz fiber mats by atomic layer deposition (ALD) for chemical sensing applications.⁴ Here, we use the tungsten ALD process to coat nonwoven polyamide nylon-6 mats that have complex fibril cross-sections. The atomic layer deposition process allows for precise thickness control and film conformality on complex and high surface area substrates. Furthermore, WF_6 and TMA employed in this study are common ALD precursors in the electronics industry. ALD

processing is highly scalable and is more recently available in roll-to-roll configurations (e.g. Beneq WCS 500).

Tungsten ALD was first developed by adapting existing tungsten chemical vapor deposition (CVD) reactions.¹⁵ Specifically, ALD of tungsten was conceived as a conformal nucleation layer for tungsten plug contacts typically prepared by CVD^{16,17} for microelectronics applications. More recently, W ALD films were deposited on polymeric substrates^{18,19}, nanoparticles²⁰, and carbon nanotubes²¹. In this work we expose nylon-6 mats to sequential doses of tungsten hexafluoride (WF_6) and 2% silane (SiH_4) diluted in argon in a flow-tube reactor to deposit tungsten thin films. We characterize the resultant conductive fibers using transmission electron microscopy, mass gain analysis, and four-probe conductivity. The W-coated fibers show excellent electrical conductivity and film conformality. Using the W-ALD process we reach conductivity values of 1,000 S/cm which exceed most fabricated conductive fiber systems. The dry ALD process avoids common issues with substrate wetting and coating uniformity. We also show that W-coated nylon fiber mats maintain high conductivity upon bending around small cylinders. These features make W-ALD coated fibers attractive for flexible textile-based electronics or other related applications.

3.3 Experimental

We deposited tungsten in a custom built hot-walled ALD reactor housed inside a walk-in fume hood. The main reactor chamber consists of a 24 inch long stainless-steel tube with inside diameter of ~1.6 inches. Precursors are delivered into the reaction zone through 1/4-inch stainless steel tubes, heated to 70°C to preheat the process gas and prevent any

precursor condensation. Pressure is monitored using a convection enhanced Pirani gauge installed downstream from the reaction zone, near the gas flow outlet. All gas flow rates are metered using needle valves and switched on and off by pneumatically actuated diaphragm valves. The reactor chamber was pumped by an Alcatel Pascal 2010SD rotary vane pump (9.7 L/min).

For aluminum oxide deposition we used 98% trimethyl aluminum (TMA) (Strem Chemicals) and reagent grade water (Ricca Chemicals) as precursors. The tungsten source was 99.9% tungsten hexafluoride (WF_6) from Sigma-Aldrich. The tungsten co-reactant was a dilute mixture (2% by weight) of silane in 99.999% Ar (Custom Gas Solutions, Durham NC). We used 99.999% pure N_2 as the carrier gas passed through an Entegris GateKeeper inert gas purifier to remove any residual water and oxygen from the nitrogen gas supply. Excess precursor and product gases are pumped out of the reactor using an Alcatel Pascal 2010SD (9.7 L/min) rotary vane pump filled with fluorocarbon oil (Fomblin 25/6 grade). Before reaching the pump, gases are scrubbed using two in-line filters (Visi-Trap by Mass-Vac Inc.). Nylon-6 (polyamide-6, PA-6) samples used were hydro-entangled winged fibers, ~ 70 g/m², from Allasso Industries Inc., Morrisville NC. Since nylon-6 melts at 215°C²² we limit deposition to a maximum temperature of $\sim 200^\circ\text{C}$. The fiber mat basis weight is 70 g/m², and the Brunauer Emmett Teller (BET) specific surface area was measured to be 2.5 m²/g using a Quantachrome Autosorb-1. Anodic aluminum oxide (AAO) disk substrates were purchased from Whatman (Anopore Anodisc). The disks were 13 mm in diameter and 60 μm thick, and the average pore diameter was 200 nm. Silicon wafers for process monitoring were purchased from WRS Materials (wafers manufactured by MEMC) and were used as received.

Before each tungsten deposition, the carrier gas pressure was adjusted to 2.0 Torr. P-type silicon (100) wafers were cleaved into 1 x 1 cm pieces and loaded into the chamber using a flat sample boat, positioned at the midpoint of the reaction zone (12" downstream from gas inlet). The fiber and AAO substrates were held in place between two pieces of fine stainless steel mesh. The silicon and fiber samples were placed in the reactor so that precursor gases flowed parallel to the samples (i.e. perpendicular to the sample normal), whereas the AAO samples were positioned upright in the reactor (gas flow parallel to the sample normal, i.e. 'flow-through' configuration) to help promote gas transport through the substrates.

After loading the samples, the reactor was pumped down to 80 mTorr followed by dry N₂ flow for 30 minutes at the operating pressure between of 2.0 Torr to allow the sample to reach the reaction temperature. Prior to tungsten deposition, all samples were coated with 25 cycles of Al₂O₃ in order to promote W nucleation.^{23,24} One ALD cycle for aluminum oxide consisted of the sequence TMA/N₂/H₂O/N₂ with times of 0.3/30/0.3/30 s respectively, producing 1.1-1.2 Å of growth per cycle. Film thickness was measured after deposition using spectroscopic ellipsometry (J.A. Woollam Co. alpha-SE) with the CompleteEASE data analysis software package. The Al₂O₃ optical constants were obtained by fitting ellipsometry data from a ~100 nm alumina film on silicon to a Cauchy model. The typical native silicon oxide thickness was measured to be ~1.7 nm and was included in the model.

Tungsten ALD films were deposited by dosing 2% SiH₄ and WF₆ precursor gases into the reactor in alternating pulses. The pulse sequence followed the WF₆/N₂/SiH₄/N₂ pattern with typical exposure times of 1/30/45/30 seconds. For some runs, we used a "hold" step where we closed all the valves in the reactor immediately after a precursor dose in order to

expose the sample to precursor vapor for an extended period of time. We recently studied the effect of silane exposure and deposition temperature on W ALD using WF_6 and dilute silane.²⁵ Using silane and WF_6 exposures of $\sim 6 \times 10^5$ and $\sim 10^6$ Langmuirs, respectively, we find an ALD “temperature window” between 200°C and 300°C with a W growth rate of $\sim 6.0 \pm 0.5$ Å/cycle. At 150°C, a silane exposure of 6×10^5 L leads to saturated growth at ~ 4 Å/cycle. Using 2% silane in Ar, this exposure is attained for a 30 second exposure when the pressure change during the SiH_4/Ar dose is controlled at 1.0 Torr.²⁵ In this work, we investigate the role of silane and WF_6 dose on mass uptake and effective conductivity of the coated nylon fiber mats.

The gas exposure is estimated by the net pressure change multiplied by the dose time. When the WF_6 cycle produces $\Delta P = 0.2$ Torr, a 1 second gas pulse time corresponds to $0.2 \text{ Torr} \times 1 \text{ sec} = 2.0 \times 10^5$ L exposure. For the 2% silane in argon, the exposure times are longer, so for $\Delta P = 0.5$ Torr, a 30 second gas pulse time corresponds to $0.5 \text{ Torr} \times 0.02 \times 30 \text{ sec} = 3.0 \times 10^5$ L. These exposure values are rough estimates. The analysis neglects gauge sensitivity to non-inert gases, the contributions of reaction by-products to the measured pressure, as well as effects of gas flow dynamics (including pressure transients and any composition-dependent pumping speed). We use these estimates only to compare relative exposures under various run conditions.

Growth rate on fibers was determined by measuring the mass of the substrate before and immediately after deposition (Fisher Scientific Accu 124 mass balance). The percent mass gain is the difference between the mass before and after coating divided by the starting mass. All of our nylon samples were cut into uniform sizes from the same fabric stock.

Conductivity of tungsten-coated nylon-6 fiber mats was measured using a four-probe apparatus.⁴ Briefly, coated fiber substrates were contacted by four parallel gold contact pads with the outer electrode pair connected to a current source and the inner pair connected to a volt meter (Keithley 2605 source meter). Samples were then subjected to a normal compressive force of known magnitude to enhance contact between the individual fibers. Assuming that the conductive coating is uniform between the electrode contacts, the effective conductivity of the coating was determined by normalizing to the coating mass and coating material density (taken to be the coating material bulk density). For comparison, the resistivity of tungsten films on oxide-coated silicon was measured using a Jandel four-point probe with an RM3-AR head.

Transmission electron microscopy was performed on nylon-6 fiber samples prepared by microtome (Leica Ultracut 7 equipped with a diamond knife). The fibers were embedded in Spurr's epoxy (EMS) and cured using a standard curing schedule. The embedded fibers were cut at room temperature into 90–110 nm thick slices. Sections collected on 300 mesh sample holder were imaged using a cold field emission electron source with an accelerating voltage of 200 kV (Hitachi HF2000).

Porous AAO samples were imaged in an FEI XL30 scanning electron microscope system equipped with a field emission electron gun. Prior to imaging, bare AAO samples were coated with Au/Pd (80%/20%) for 2 minutes in a sputter coater. Tungsten ALD coated AAO samples did not require any sputtering due to the high conductivity of the thin films.

3.4 Results and Discussion

3.4.1 *W ALD Growth Rate Calibration on Anodic Aluminum Oxide*

As a first step in characterizing tungsten deposition on nylon substrates, we deposited tungsten films on commercial anodic aluminum oxide substrates and examined film thickness by SEM and TEM. These substrates have an effective aspect ratio of $>300:1$, which is larger than that for the nonwoven nylon fibers mats. Although the effect of gas exposure and reactant ‘hold’ times were not explored for these structures, we used hold steps for TMA, H_2O , and WF_6 doses. The silane doses consisted of long exposure times (i.e. 120 seconds) without hold steps. After coating with 25 cycles of Al_2O_3 , we deposited 25, 45, or 100 cycles of W, all at $200^\circ C$. The Al_2O_3 recipe was $TMA/N_2/H_2O/N_2 = 0.3(20)/60/0.3(20)/90$ seconds, respectively. Similarly, the W ALD cycle followed $SiH_4/N_2/WF_6/N_2 = 120/90/1(60)/60$ seconds. The pressure change in the reactor was 1.0 Torr during the 2% silane dose and the WF_6 dose.

Figure 1 shows a series of plan-view SEM images of the partially filled AAO pores after Al_2O_3 and W ALD. Figure 1(a) shows an uncoated AAO substrate coated with a thin Pd/Au layer to facilitate electron imaging. The pores are not highly uniform, but the average diameter is estimated to be 251 ± 14 nm. Image (b) was collected after 25 W ALD cycles. Average pore diameter is reduced to 212 ± 13 nm after the ALD coating. Edge definition is also lost to some extent, as features appear less sharp. After 45 W cycles, image (c) shows pore sizes further reduced to 186 ± 30 nm and edge features are rounded as would be expected from a conformal coating. Increasing the coating thickness to 100 cycles in image (d), the average pore diameter becomes 94 ± 17 nm. Some smaller pores appear to be closed

completely and the top surface of the AAO is rounded. The change in pore size yields a growth rate of ~ 7.8 Å/cycle. Considering the nonuniform starting surface, this is reasonably similar to the ~ 6 Å/cycle we observed on planar Si(100) substrates coated separately under similar conditions.²⁵ Growth thickness versus cycle number for deposition on AAO (from TEM) and on silicon are shown in Figure 2.

We also verify the thickness of the W films in AAO by imaging the pores at an angle. Figure 3 shows micrographs of W-coated AAO after mechanical breaking. In addition to a cross-section view of the W coating, the cracking also removed parts of the AAO walls to reveal the W formed along the inner pore walls (see for example the arrow in Figure 3(a)). The coating in image Figure 3(b) is $\sim 2\times$ thicker than in (a), consistent with the increased coating cycles. The W growth rate from these images is 6.6 Å/cycle. The results on AAO confirm that the W ALD process using dilute silane can produce good W ALD coatings on high aspect ratio structures.

3.4.2 W ALD Nucleation and Conformality on Nylon-6 Nonwovens

While the amide functional group in nylon-6 is reactive with trimethylaluminum, and to a lesser extent, with diethyl zinc^{26,27} the reactions for direct deposition of W from WF_6 and SiH_4 on nylon are not known. Tungsten ALD on various polymers including polyethylene, polyvinyl chloride, polystyrene, polycarbonate, polypropylene, polymethylmethacrylate, Kapton[®] polyimide and polyethylene naphthalate has previously been reported,^{19,24} and results show that W ALD nucleates well when the polymer is pretreated with several cycles of ALD Al_2O_3 . We find that a thin (25 cycle) Al_2O_3 pretreatment also helps promote W nucleation on nylon-6. Figure 4 shows two nylon-6 fiber samples after 100 W ALD cycles at 140°C, with

and without 25 cycles of alumina pretreatment. The sample without pretreatment shows no visible tungsten nucleation and is electrically resistive when measured with the four-probe apparatus. The pretreated sample shows a uniform tungsten coating and shows good overall conductivity (as discussed later on). Previous infrared analysis of TMA/H₂O on nylon fibers showed significant sub-surface precursor diffusion, reaction, and nucleation during ALD at 90°C, producing detectable nuclei more than 100 nm from the fiber surface.^{26,28} The alumina pretreatment used here was done at the same temperature as the W ALD (between ~140° and 200°C), so alumina is expected to be present on and below the surface of the nylon fiber.

Transmission electron micrographs from PA-6 samples with 25 cycles of alumina pretreatment and 100 cycles of W are shown in Figure 5. The cross-sectional images show the high surface area “winged” structure of the fiber. The dark contrast in the images corresponds to the tungsten coating which is uniform and conformal on the fiber. The highest magnification image (panel c) shows a “wing” edge where the apparent layer thickness is ~75 nm. The actual film thickness is difficult to quantify for polymers after microtome sectioning. The microtome slice is in the range of ~100 nm, so it is possible that when the microtome cuts the relatively soft polymer, the hard metal coating folds partly onto its side, distorting the thickness analysis. The metal film can be thought as a ribbon or a strip wrapped conformally around the fiber. When a cross-section is cut by mechanical shearing, the metal strip may twist, exposing its planar side to the electron beam, rather than its line edge. What appear to be film thickness non-uniformities, especially visible in panels (a) and (c) on the wing tips, are likely an artifact of TEM sample preparation.

3.4.3 Effect of WF_6 and SiH_4 Exposure on W ALD on Nylon Fibers

We explored the effect of temperature on mass uptake for W ALD on nylon. Using silane and WF_6 exposures of $\sim 4.5 \times 10^5$ and $\sim 2 \times 10^5$ Langmuirs, we see minimal growth at $T < 140^\circ C$, with more growth at higher temperatures up to $180^\circ C$. The amount of W deposited during the WF_6 exposure half-cycle is affected by the amount of silicon left on the growth surface during the previous silane half-cycle step.²⁹ Tungsten ALD can be achieved at near room temperature using very large silane and WF_6 exposure steps. For example, Wilson et al.²⁴ report good W ALD at $80^\circ C$ using repeated static Si_2H_6/WF_6 doses which produce large gas exposures. For some runs, we also observe anomalously low growth rates, especially at higher temperatures near $200^\circ C$. The decreased deposition on the polymer fiber is ascribed to reactor wall effects in our tubular hot-wall reactor system. Specifically, under the high silane exposures used here, the reaction between SiH_4 and the W surface is thermally activated, so silane may be consumed upstream on the walls before a sufficient amount reaches the high surface area fiber mat substrate. Studies of the dilute silane process²⁵ suggest that the silane depletion occurs even when the reactor walls are pretreated with a thin (2-3 nm) layer of alumina. Pretreating the reactor wall with large silane doses before loading the substrate (and before depositing the alumina nucleation layer) appears to eliminate the unexpected low growth rates.²⁵ Although the mechanisms are not clear, these observations suggest that the thin alumina nucleation layer may permit some transport of silicon species.

Tungsten and silane exposure affect W growth on the nylon mats. Mass uptake saturation as a function of silane and WF_6 exposure is shown in Figure 6 for deposition at

145°C. For varying WF_6 exposure, the silane pulse was fixed at $\sim 4.5 \times 10^5$ L, and for varying SiH_4 exposure, the WF_6 was fixed at $\sim 2 \times 10^5$ L. The mass uptake increases with both SiH_4 and WF_6 exposure, although the rate is more sensitive to the silane exposure in the range studied. Using the sample basis weight, measured fiber surface area, and expected W density, the mass uptake values are $\sim 2\times$ smaller than expected for uniform $\sim 3\text{\AA}$ /cycle at 145°C.²⁵ The BET surface area for the complex 3D network measured using N_2 adsorption may be larger than the surface area that can be reached by the SiH_4 and WF_6 precursors. Figure 7 shows the effective conductivity for the same samples in Figure 6 prepared with various SiH_4 and WF_6 exposures at 145°C, and we find that the conductivity is nearly constant at $\sim 1,000$ S/cm when the precursor doses produce sufficient deposition.

3.4.4 Reactant Species Transport through the 3D Fiber Network

It is important to understand if the growth on the fibers is limited by reactant species transport through the fiber network. That is, we want to know if the ALD process sequence is sufficient for the reactants to fully reach all exposed surface area within the nonwoven fiber mat during the specified gas pulse times. The TEM images in Figure 5 show good conformal coverage over the areas examined, demonstrating complete exposure at the sites imaged. The mass change after ALD coating, however, can give insight into the extent of reaction over the entire surface area of the fiber. Mass change analysis with W ALD works particularly well because of the high density of the W metal. Working specifically in the sub-saturation gas exposure region, i.e. where the extent of reaction is sensitive to the amount of reactants reaching the growth surface, we can use the mass change to explore the extent of reaction and thereby probe reactant transport effects. To probe reactant transport, we introduce a

reactant ‘hold’ step into the process sequence. Specifically, after a 10 s SiH₄ dose, we closed the reactor valves to cease the gas flow for some period of time (20 – 120 seconds) then opened the valves to purge for 30 s. The cycle then finished with the same 1 s WF₆ exposure and 30 s N₂ purge. The reaction sequence for a 10 s silane dose with a 60 s SiH₄ hold, for example, is denoted as SiH₄/N₂/WF₆/N₂ = 10(60)/30/1/30 seconds. This ‘hold’ step provides time for gas that is in the chamber to diffuse and move through the tortuous fiber structure. This differs from a longer pulse time, where gas flow continues to supply reactant. If the growth is limited by the reactant transport through the fiber network structure, the hold steps will give reactants more time to reach reactive sites, leading to a net increase in film growth. If species transport is facile through the network, the reaction will go to completion during the pulse time and the hold time will not significantly affect the overall mass uptake.

For this analysis, we also consider the total fiber surface area. The fiber mat has a basis weight of 70 g/m² and the BET surface area is 2.5 m²/g so the surface area per unit 2D area of fabric sample is ~175 m²/m². This surface area value can be roughly related to a trench aspect ratio, where 175 m²/m² corresponds to a set of equally spaced vertical trenches with aspect ratio of ~87:1. This aspect ratio is reasonable for conformal coating by ALD. However, unlike vertical trenches on a fabricated semiconductor wafer, the fiber mat surface includes many ‘hidden’ regions with variable sizes and shapes, well outside the line-of-sight. This complex 3D structure will likely affect the growth, and the hold sequence may help improve uniformity.

We test effects of species transport through the fiber mat by comparing changes in mass when we change: i) silane gas pulse time; or ii) silane hold time with fixed silane pulse

time. We started with silane pulse times less than the full saturation exposure where mass uptake will be sensitive to the number of reactant/surface interactions. Using the same conditions as used for the data in Figure 6, we performed 100 ALD cycles at 145°C with and without hold steps, and results are shown in Figure 8.

The data show that increasing the silane gas flow time from 15 to 120 seconds without the hold sequence leads to increased mass, whereas the silane hold step after a fixed 10 s silane flow does not increase mass uptake. This indicates that the relatively short gas dose time is sufficient for silane to reach reactive sites throughout the fiber matrix under the conditions investigated. Different growth conditions, or different fiber size, density or composition will affect reactant transport, so we sometimes use reaction hold steps to help ensure uniform surface reaction.

3.4.5 Mechanical Response of W-Coated Nylon-6 Nonwovens

We are also interested in the mechanical response of the W-coated nylon fiber samples. After coating, the micro-fiber mat still retains the “soft” feel of the uncoated fabric, suggesting that the W-coated fibers retain flexibility. To test the flexibility of the coated fibers, we measured conductivity after bending the fiber mats around radii of increasing curvature. We first measuring conductivity with the sample laid flat in our test apparatus then we molded the mat around a large cylinder. The sample was then laid flat again to measure conductivity. This was repeated several times for the same fiber sample bent around cylinders of decreasing radius, and the results are shown in Figure 9.

Also shown are results from similar analysis³⁰ of a conductive ZnO layer conformally deposited by ALD onto a polypropylene fiber mat. The results show that the W-coated

nylon retains ~90% of its conductivity after bending around a radius as small as 3 mm, and the performance is much better than ZnO material. This suggests that W-coated nylon may be a good material for future flexible electronic systems integrated with textiles.

3.5 Summary and Conclusions

We successfully used WF_6 and 2% SiH_4 in Ar in an ALD sequence to produce conductive coatings on nylon-6 fiber mats at 145°C. Pretreating the fiber mats with 25 cycles of TMA/ H_2O ALD helps promote W nucleation. The W mass uptake on the nylon fiber mats shows saturated behavior with increasing silane and WF_6 exposure. The process offers good thickness control and produces conformal coatings on fiber mats and on nanoporous and high aspect ratio alumina structures. High surface area winged nylon-6 samples coated with W ALD show very high effective conductivities in the 1,000 S/cm range, and the conductivity remains high even after bending around a small diameter. Good conductivity can be achieved with less than ~20% mass loading. The conductivity values we measure greatly exceed those reported in previous studies using electrospinning, injection forming, and bulk treatment techniques.³¹⁻³³ Results demonstrate that the dilute SiH_4/WF_6 process is suitable for producing high quality conductive nylon-6 nonwoven fiber mats which may enable electronic structures to be integrated into nonwoven or textile media. Potential applications for conductive fibrous media include chemical sensing, wearable electronics, biomedical devices, and energy conversion and storage.

3.6 Acknowledgments

We thank Christina Devine for helping with SEM imaging performed at Duke University, and Dr. Jess Jur of NC State College of Textiles who helped with the construction

of the first version of the ALD reactor. We acknowledge Allasso Industries Inc. for supplying the PA-6 fibers and for SEM images of the untreated fiber cross-sections.

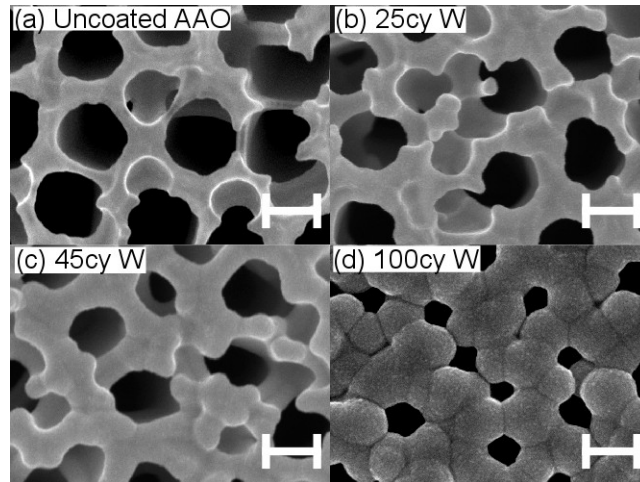


Figure 3.1. Top-down SEM micrographs of anodic aluminum oxide samples treated with different thicknesses of ALD tungsten at 250,000X magnification (scale bars are 200 nm). The imaged AAO substrates have approximately 250 nm diameter pores. Image (a) is an uncoated substrate. Image (b), (c), and (d) were collected after 25 cycles of Al_2O_3 and 25, 45, and 100 cycles of W respectively at 200°C. These images show pore shrinkage due to increasing ALD coating thicknesses. Samples coated with higher cycle numbers show increasingly rounded edges and softer features in the nanometer scale due to the conformality of the coatings.

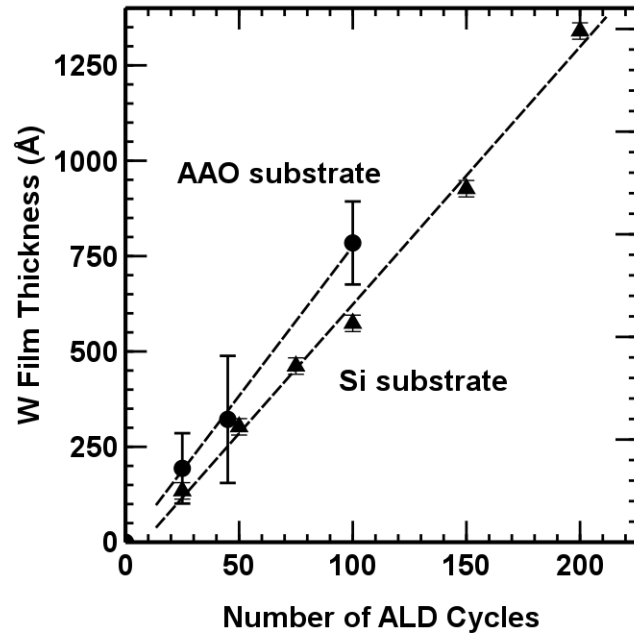


Figure 3.2. Tungsten film thickness versus ALD cycle number on AAO and silicon substrates. Samples are pre-treated with 25 cycles of Al_2O_3 and processed at 200°C . Film thickness on the AAO were extracted from top-down SEM images of AAO pores shown in Figure 1.

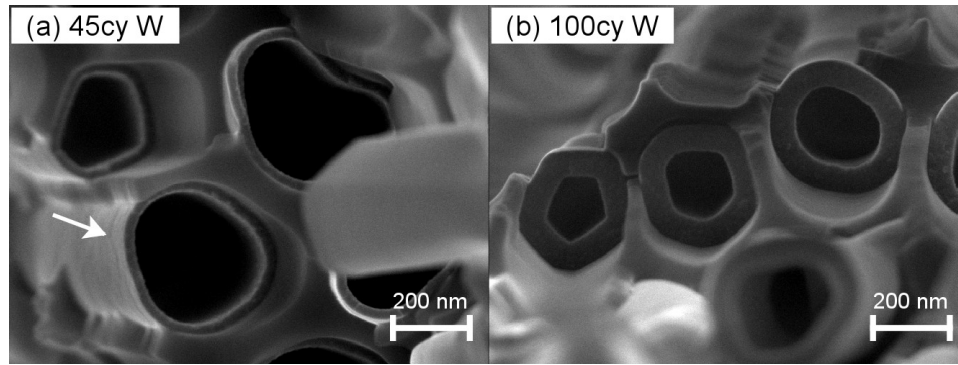


Figure 3.3. A cross-sectional view of AAO pores with: (a) 45 cycles; and (b) 100 cycles of W ALD after breaking the coated AAO. The AAO templates are pre-treated with 25 cycles of Al_2O_3 and processed at 200°C . In each image, an inner tube of tungsten is surrounded by an outer AAO substrate shell, and the W thickness increases with ALD cycle number. The arrow in image (a) points to the outer side-wall of a W tube where the AAO shell was removed.

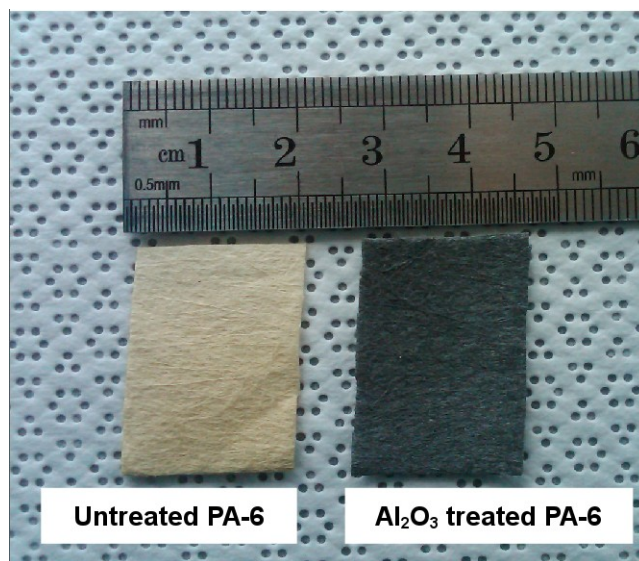


Figure 3.4. Photograph showing nonwoven nylon-6 fiber mats after coating with 100 cycles of W ALD at 140°C. The sample on the left is not treated with Al₂O₃, resulting in poor tungsten nucleation on the fibers, whereas the sample on the right shows proper W nucleation as a result of pre-treatment with 25 cycles of Al₂O₃ at 140°C.

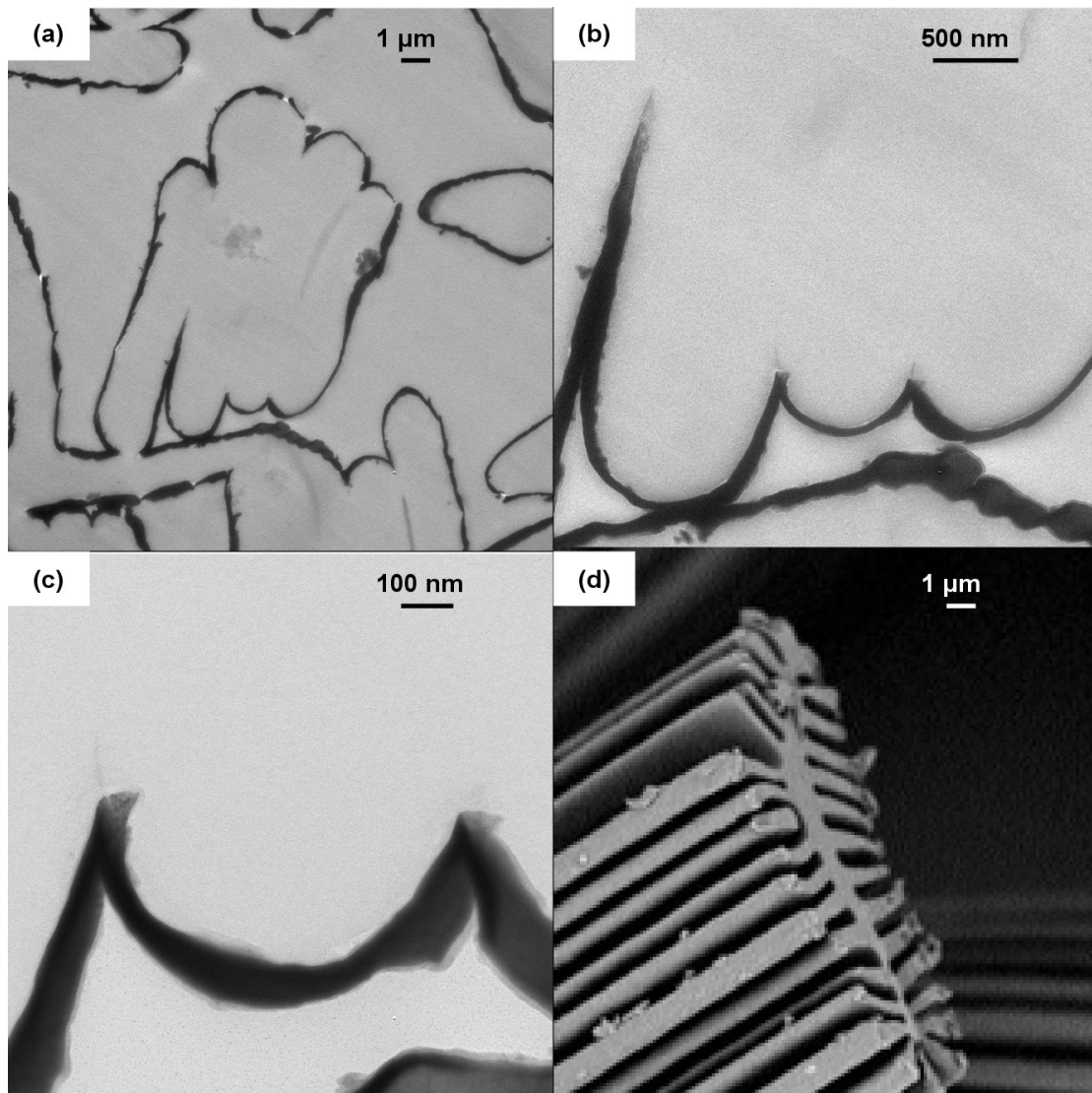


Figure 3.5. Micrographs of nylon-6 fibers (Allasso, Winged Fibers™) coated with 25 cycles of Al_2O_3 followed by 100 cycles of W at 160°C . The dark contrast is from the tungsten coating, which grows conformally around the fiber wings. The Al_2O_3 deposition is not visible at these magnifications. A cross-sectional SEM image of a PA-6 fibril is shown in (d), reproduced with permission from Allasso Industries Inc.

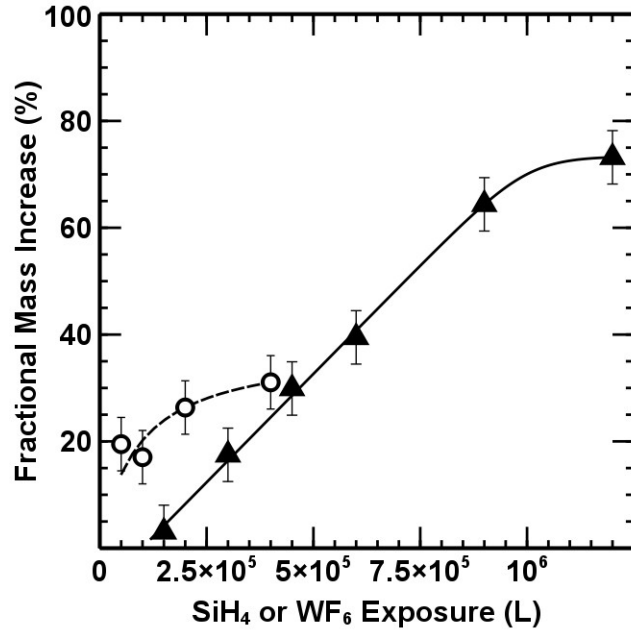


Figure 3.6. The effect of SiH_4 and WF_6 exposure on substrate mass gain after 25 Al_2O_3 cycles and 100 W ALD cycles at 145°C . The data points show mass uptake on the nylon fiber mat for: (open triangles) increasing silane exposure with fixed WF_6 exposure ($\approx 2 \times 10^5$ L); and (closed squares) increasing WF_6 with fixed silane exposure ($\approx 4.5 \times 10^5$ L). The pressure change during silane and WF_6 doses was 0.5 and 0.2 Torr, respectively. For films with 20% or more mass loading, the maximum error of the mean for fractional mass increase was $\pm 5\%$, as shown by the error bars. The lines are a guide for the eye.

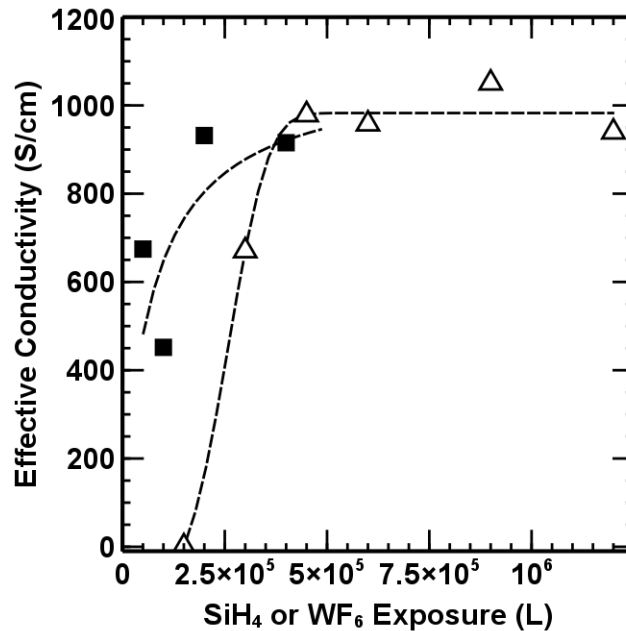


Figure 3.7. Fiber mat effective conductivity as a function of SiH₄ and WF₆ exposure for 25 cycles of Al₂O₃ and 100 cycles of W deposition at 145°C. The data symbols correspond to the samples shown in Figure 6. The conductivity is approximately 1000 S/cm, independent of exposure conditions when sufficient coating thickness is present. The data points show effective conductivity on the nylon fiber mat for: (open triangles) increasing silane exposure with fixed WF₆ exposure (= ~2×10⁵ L); and (closed squares) increasing WF₆ with fixed silane exposure (= ~4.5×10⁵ L). The lines are a guide for the eye. Each data point represents an average of 7 measurements for each sample. The standard error of the mean is smaller than the size of the data points.

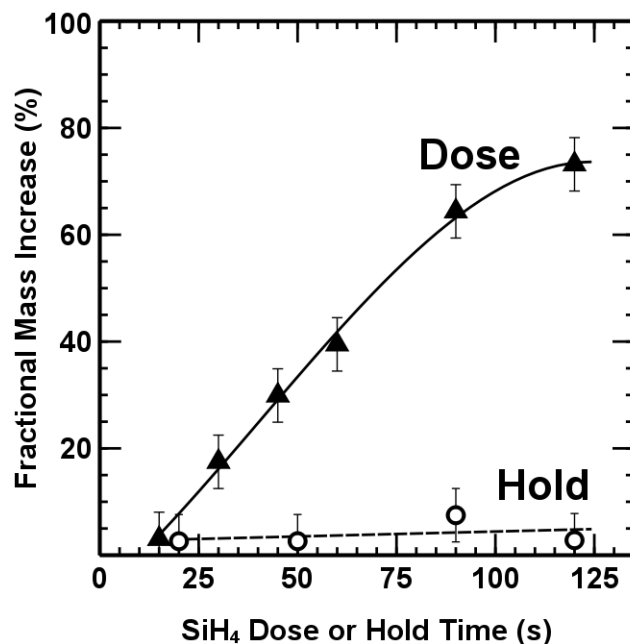


Figure 3.8. The effect of varying silane dose times and short silane doses combined with varying hold times on W mass uptake on nylon-6 fiber mats. All samples were coated with 25 Al₂O₃ and 100 W cycles at 145°C. For the “hold” sequence, the silane dose time is set at 10 seconds after which the reactor is closed for a set hold time between 20 and 120 seconds. The remainder of the ALD cycle proceeded unchanged. We also compare runs done with different silane dose times without the hold step (triangle symbols, data from Figure 6). With the 10 second silane exposure, the hold step does not enhance W mass uptake on the fiber mat substrates. The error bars represent an uncertainty of ±5% in the mass loading analysis.

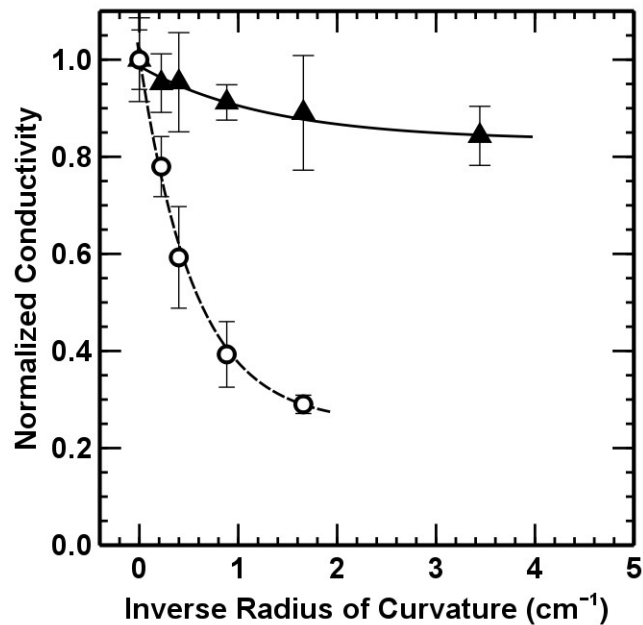


Figure 3.9. Change in conductivity for conducting layers deposited on fiber substrates when the fiber mats are bent around increasingly smaller cylinders. The conductivity of ZnO on polypropylene fibers is approximately 20 S/cm as prepared, but it decreases substantially upon bending. Similar experiments for the W-coated nylon studied here shows ~90% conductivity retention upon bending. Data from ZnO coated polypropylene is from reference 20. Tungsten-coated samples were prepared with 25 Al₂O₃ and 100 W cycles at 145°C. Each data point represents the mean of two conductivity values collected from each sample, and the error bars show typical variation.

3.7 References

- (1) Fox, R. T.; Wani, V.; Howard, K. E.; Bogle, A.; Kempel, L. J. *J. Appl. Polym. Sci.* 2008, 107, 2558–2566.
- (2) Devaux, E.; Koncar, V.; Kim, B.; Campagne, C.; Roux, C.; Rochery, M.; Saihi, D. *Trans. Inst. Meas. Control* 2007, 29, 355–376.
- (3) Burger, C.; Hsiao, B. S.; Chu, B. *Annu. Rev. Mater. Res.* 2006, 36, 333–368.
- (4) Jur, J. S.; Sweet, W. J.; Oldham, C. J.; Parsons, G. N. *Adv. Funct. Mater.* 2011, 21, 1993.
- (5) Wakuda, D.; Suganuma, K. *Appl. Phys. Lett.* 2011, 98, 073304.
- (6) Varesano, A.; Tonin, C. *Text. Res. J.* 2008, 78, 1110–1115.
- (7) Xiang, C.; Lu, W.; Zhu, Y.; Sun, Z.; Yan, Z.; Hwang, C.-C.; Tour, J. M. *ACS Appl. Mater. Interfaces* 2012, 4, 131–136.
- (8) Invernale, M. A.; Ding, Y.; Sotzing, G. A. *ACS Appl. Mater. Interfaces* 2010, 2, 296–300.
- (9) Li, D.; McCann, J. T.; Xia, Y. *Small* 2004, 1, 83–86.
- (10) Norris, I. D.; Shaker, M. M.; Ko, F. K.; MacDiarmid, A. G. *Synth. Met.* 2000, 114, 109–114.
- (11) Chen, D.; Miao, Y.-E.; Liu, T. *ACS Appl. Mater. Interfaces* 2013, 5, 1206–1212.
- (12) Ding, Y.; Invernale, M. A.; Sotzing, G. A. *ACS Appl. Mater. Interfaces* 2010, 2, 1588–1593.
- (13) Ge, J. J.; Hou, H.; Li, Q.; Graham, M. J.; Greiner, A.; Reneker, D. H.; Harris, F. W.; Cheng, S. Z. D. *J. Am. Chem. Soc.* 2004, 126, 15754–15761.
- (14) Little, B. K.; Li, Y.; Cammarata, V.; Broughton, R.; Mills, G. *ACS Appl. Mater. Interfaces* 2011, 3, 1965–1973.
- (15) Klaus, J. .; Ferro, S. .; George, S. . *Thin Solid Films* 2000, 360, 145–153.
- (16) Kim, S.-H.; Hwang, E.-S.; Kim, B.-M.; Lee, J.-W.; Sun, H.-J.; Hong, T. E.; Kim, J.-K.; Sohn, H.; Kim, J.; Yoon, T.-S. *Electrochem. Solid-State Lett.* 2005, 8, C155–C159.

- (17) Kim, S.-H.; Kwak, N.; Kim, J.; Sohn, H. J. *Electrochem. Soc.* 2006, 153, G887.
- (18) Fabreguette, F. H.; Wind, R. A.; George, S. M. *Appl. Phys. Lett.* 2006, 88, 013116.
- (19) Fabreguette, F. H.; George, S. M. *Thin Solid Films* 2007, 515, 7177–7180.
- (20) Wilson, C. A.; Goldstein, D. N.; McCormick, J. A.; Weimer, A. W.; George, S. M. *J. Vac. Sci. Technol., A* 2008, 26, 430–437.
- (21) Cavanagh, A. S.; Wilson, C. A.; Weimer, A. W.; George, S. M. *Nanotechnology* 2009, 20, 255602.
- (22) Palmer, R. J. In *Encyclopedia of Polymer Science and Technology*; John Wiley & Sons, Inc., 2002.
- (23) Grubbs, R. K.; Nelson, C. E.; Steinmetz, N. J.; George, S. M. *Thin Solid Films* 2004, 467, 16–27.
- (24) Wilson, C. A.; McCormick, J. A.; Cavanagh, A. S.; Goldstein, D. N.; Weimer, A. W.; George, S. M. *Thin Solid Films* 2008, 516, 6175–6185.
- (25) Kalanyan, B.; Oldham, C., J.; Losego, M. D.; Parsons, G., N. *Chem. Vap. Deposition* 2013, 19.
- (26) Spagnola, J. C.; Gong, B.; Arvidson, S. A.; Jur, J. S.; Khan, S. A.; Parsons, G. N. *J. Mater. Chem.* 2010, 20, 4213.
- (27) Oldham, C. J.; Gong, B.; Spagnola, J. C.; Jur, J. S.; Senecal, K. J.; Godfrey, T. A.; Parsons, G. N. *J. Electrochem. Soc.* 2011, 158, D549–D556.
- (28) Jur, J. S.; Spagnola, J. C.; Lee, K.; Gong, B.; Peng, Q.; Parsons, G. N. *Langmuir* 2010, 26, 8239–8244.
- (29) Elam, J. .; Nelson, C. .; Grubbs, R. .; George, S. . *Surf. Sci.* 2001, 479, 121–135.
- (30) Sweet, W. J.; Jur, J. S.; Parsons, G. N. *J. Appl. Phys.* 2013, Submitted.
- (31) Chronakis, I. S.; Grapenson, S.; Jakob, A. *Polymer* 2006, 47, 1597–1603.
- (32) Xia, Y.; Yun Lu *Compos. Sci. Technol.* 2008, 68, 1471–1479.
- (33) Miyauchi, M.; Miao, J.; Simmons, T. J.; Lee, J.-W.; Doherty, T. V.; Dordick, J. S.; Linhardt, R. J. *Biomacromolecules* **2010**, 11, 2440–2445.

CHAPTER 4. Selective Nucleation of Tungsten ALD on Silicon and Silicon Oxide

Berc Kalanyan^{1*}, Paul Lemaire¹, Sarah Atanasov¹, Jeanette Robers², Scott Clendenning², and Gregory N. Parsons¹

¹*North Carolina State University, Department of Chemical and Biomolecular Engineering, North Carolina 27695*

²Intel Corporation, Components Research, Hillsboro Oregon, 97124

4.1 Abstract

Atomic layer deposition (ALD) holds promise as the next-generation technology for advanced patterning. Area selective deposition processes may help in mitigating patterning and alignment issues in the sub-10 nm technology nodes. Many ALD processes show inherent selectivity for silicon surfaces at different oxidation states, however, selectivity is lost after a small number of cycles. Here we demonstrate methods for tuning metal ALD selectivity on Si/SiO₂ and Au/SiO₂ surfaces without the use of blocking layers and subsequent etching steps. We deposit W films from dilute SiH₄ and WF₆ at 220°C with modifications to the standard gas pulsing scheme. We show that tungsten ALD nucleation is surface dependent and can be modified using intermittent surface cleaning steps and H₂ co-exposures during the WF₆ half-cycle. We observe inherent selectivity to Si and the presence of an incubation period of 20-30 cycles on SiO₂. On carbon-rich SiO₂ surfaces, we extend this incubation time by ~5 cycles. And on piranha cleaned SiO₂ surfaces, we delay nucleation by another 10 cycles by flowing H₂ during the WF₆ exposure. On macroscopically patterned surfaces, we show the existence of surface loading effects for the first time for an ALD process. Parallels between W ALD and selective W chemical vapor deposition are shown to

be important in identifying potential issues relating selectivity loss and selectivity enhancement for ALD.

4.2 Introduction

Modern integrated circuit fabrication demands increasingly small feature sizes for interconnects, diffusion barriers, and gate dielectrics. Vertical architectures such as FinFETs and 3D memory are rapidly moving toward single digit technology nodes. Lithographic patterning at sub 10 nm length scales is a grand challenge for manufacturing. Deposition techniques with chemical selectivity toward certain surfaces will be critical in fabricating emerging device structures. Blanket atomic layer deposition (ALD) is widely used for the deposition of metals and dielectric thin films. Area selective ALD of metals is particularly desirable for inherently aligned patterning on existing surfaces without requiring additional lithography steps. However, the chemistry and process conditions required for reliable and manufacturing-compatible selective metal ALD are currently unknown.

While steady-state ALD growth on as-grown thin films is well-studied, early nucleation chemistry on bare substrates is poorly understood with respect to site selectivity. Native selectivity for one surface (growth surface) over another (non-growth surface) is often initially observed, but unwanted nucleation and growth on the non-receptive surface will eventually take place. Identifying nuclei-producing steps and surface conditions during an A-B type ALD process is critical in developing area selective deposition. In this work we use tungsten (W) ALD as a model process to study the influence of the starting surface on film incubation and growth rate. Previous studies of W ALD have shown nucleation trends on Al_2O_3 ¹, hydroxilated thermal SiO_2 ², and hydroxilated CVD SiO_2 (amorphous)^{3,4}. However,

native selectivity of the process to Si surfaces over SiO₂ has not been shown to date. Furthermore, most efforts have focused on modifying substrate surfaces with organic blocking layers, rather than modifying the ALD reaction chemistry for the purposes of improving selectivity. In this paper, we start by characterizing the native selectivity of the SiH₄/WF₆ chemistry on Si and SiO₂ surfaces. We then show surface and process modifications that promote and retard metal nucleation on SiO₂ without influencing nucleation or steady-state deposition on Si surfaces.

4.3 Background

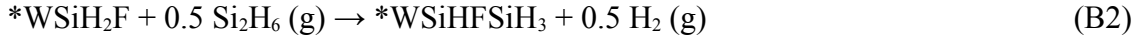
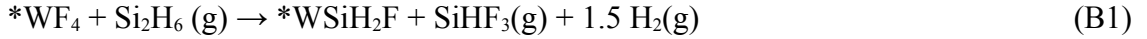
ALD is a cyclic vacuum deposition process based on self-limiting gas-solid reactions. In a typical process, two gas-phase reactants are pulsed into a heated chamber in alternating fashion, with an inert gas purge following each pulse. Upon exposure to the first reactant, surfaces with the appropriate functionality become saturated with chemisorbed species. Surface reactions proceed to completion and terminate the surface with ligands that are reactive only with the second reactant (i.e. co-reactant), but not with the first. Byproducts and excess reactant are removed from the reactor with an inert gas purge, completing the first half-cycle. Exposure to the second reactant and a second purge step complete one full cycle. Due to the self-limiting nature of the surface reactions, a known thickness of material is deposited during each ALD cycle. As a consequence, ALD processes produce extremely conformal films over high aspect ratio structures with discrete control over film thickness.

Surface selective CVD chemistries have been demonstrated using sacrificial reactions on the growth surface⁵, activation of the growth surface⁶, and removal of nucleating species⁷⁻⁹. Although some CVD chemistries can be adapted to work in ALD mode, efforts in selective

ALD have been largely focused on surface passivation using organic blocking layers¹⁰⁻¹⁴. While blocking layers are very effective at preventing deposition, they add to process complexity by requiring the alignment of the blocking layer and its subsequent removal after deposition. Additional reports on selective deposition include spatial deposition, which delivers a directed flux of precursor to a targeted area^{15,16}. Chemical approaches to patterning include recent reports on selective metal oxide (ZrO_2) ALD on SiO_2/Cu patterns, selective to SiO_2 ¹⁷. Researchers have also reported partial inhibition of ALD reactions for metal oxides using a range of volatile organic species (alcohols and ketones)¹⁸. These and similar methods hold promise for the development of new selective processes. While some selective oxide deposition routes are emerging, selective metal ALD has not been explored.

Tungsten CVD processes that use tungsten hexafluoride and a silane reducing agent (mono- or disilane) are well known to show inherent selectivity between oxide and silicon surfaces^{19,20}. Reports from ALD researchers have largely focused on tungsten process characteristics on receptive substrates such as Al_2O_3 . However, the tungsten ALD process warrants further study for the surface specificity of both WF_6 and SiH_4 reaction half-cycles. Here we studied the control of tungsten nucleation on SiO_2 (a non-receptive surface) while allowing deposition to take place uninhibited on H-terminated Si (receptive surface). Drawing inspiration from selective chemical vapor deposition (CVD) chemistries, we used hydrogen as an intermediate reactant or as a carrier gas to affect reaction equilibrium on the non-receptive oxide surface.

Based on previously reported mass spectrometry and our own measurements, the steady-state growth of tungsten can be written as two surface reactions:



The reactions above show stoichiometries for the $\text{Si}_2\text{H}_6/\text{WF}_6$ system, but the chemistry for the SiH_4/WF_6 system is similar. Compounds prefixed with an asterisk (*) denote adsorbed (surface) species. Note that all elementary reaction steps result in hydrogen production, which we observe using QMS (discussed in the results section). Adsorbed silicon-containing groups are consumed during the WF_6 exposure (A1). From empirical evidence, it is well known that reaction B proceeds more easily on Si:H surfaces than on SiO_2 . It is also observed that elevated temperatures (higher than commonly used for ALD) are required for SiH_4 reactions on SiO_2 ²¹. However, even trace quantities of Si deposition on SiO_2 may be sufficient to nucleate W during the subsequent WF_6 exposure. Given that the primary reaction product is H_2 , exposing the surface to H_2 following step B1 (where the $-\text{SiH}_2\text{F}$ group is incorporated into the surface) is our first approach toward driving back potential Si deposition on SiO_2 . This may cause the removal of potential nucleation sites. Alternatively, H_2 can be injected simultaneously with SiH_4 into the reactor to shift reaction equilibrium toward reactants. In terms of initial nucleation, the WF_6 reaction (step A1) proceeds readily on Si, even at room temperature^{22,23}. WF_6 can be easily reduced by the Si substrate until a critical thickness (<40 nm) of the wafer surface has been converted to W^{23} . There is existing evidence that WF_6 reactions on Si can generate reactive byproduct species that can react with nearby SiO_2 sites to deposit W^{24} . Therefore, nucleation pathways

originating from the WF_6 half-cycle need to be suppressed. Simultaneous H_2 exposure during the WF_6 half-reaction is one way in which we implement nucleation control on SiO_2 .

4.4 Experimental

4.4.1 Substrate surface preparation

Boron doped Si(100) 6-10 Ω -cm and Si(100) with 100 nm thermal SiO_2 (WRS Materials) wafers were cut into 12 x 12 mm chips. Si pieces were cleaned in hot piranha solution (1:1 H_2SO_4 : H_2O_2 by volume) for 30 minutes, rinsed with deionized (DI) water, and stored in DI water. Immediately prior to vacuum deposition, Si wafers were dipped in dilute hydrofluoric acid (5 vol%, Sigma-Aldrich) for 30 s, rinsed under flowing DI water for 30 s, and blown dry with 99.999% N_2 (100 psi). Two types of SiO_2 surfaces were studied for deposition: Thermal oxide used as received from the vendor ($\text{SiO}_2(\text{C})$) and SiO_2 surfaces oxidized in hot piranha (SiO_2). In general, $\text{SiO}_2(\text{C})$ surfaces contained more surface carbon and were not subjected to a DI rinse. Patterned substrates were prepared by evaporating 100 nm Au onto a thermal SiO_2 wafer using a hard mask. 20 nm of Ti was used as an adhesion layer. Cleaning of the patterned surfaces involved a 1 min dip in hot piranha solution, followed by a DI water rinse.

4.4.2 Reactor configuration

Depositions were carried out in a dual chamber home-built ALD reactor (Figure 1). Precursor and inert gases were diverted to one of two cylindrical process chambers by gas switching valves. The larger deposition chamber was a hot-walled stainless steel tube (60 cm long, 10 cm in diameter) with gate valves installed at the inlet and at the outlet of the tube. This metal chamber was used for most of the deposition studies in this paper. A second

reaction chamber made of fused quartz (60 cm long, 4 cm diameter tube) was positioned in parallel to the steel reactor and shared the same upstream and downstream gas piping. The quartz tube was only heated near the substrate in order to minimize exposed hot metal surfaces. Before each run, a liner tube (15 cm long, 3.5 cm diameter) also made of quartz was inserted into the quartz reactor. Wafer coupons were placed on a rectangular quartz boat. After a deposition run, the quartz liner and the boat were both etched in hydrogen peroxide (30% by volume, Sigma-Aldrich) and rinsed with DI water. Both reaction chambers were heated resistively to 220°C using PID controllers. Research grade N₂ or Ar (99.999%, Machine & Welding Supply Company) was passed through a purifier (Entegris Gate-Keeper) and served as the process carrier gas. The operating pressure was maintained at 1.6 Torr with a carrier flow rate of 300 SCCM. The chamber was pumped by an Alcatel Adixen 2010C1 pump (9.8 m³/h) filled with fluorocarbon oil and fitted with an N₂ oil casing purge line. Reactor effluent was filtered through activated charcoal and Sodasorb® filter elements (Mass-Vac Inc).

4.4.3 Gas pulsing sequences for tungsten growth

Tungsten deposition was achieved by alternately pulsing SiH₄ (Custom Gas Solutions, Durham NC) and WF₆ (Sigma-Aldrich) with inert gas purge steps following each exposure. Several process modifications were carried out using H₂ (99.999%, Machine & Welding Supply Company) pulses. Silane was supplied as a dilute mixture (2% in Ar) in order to mitigate pyrophoricity hazards. As reported previously, the dilute-SiH₄/WF₆ process behaves comparably to ALD processes that utilize 100% silane²⁵. Small (15 x 15 mm) wafer coupons were loaded into the reactor and allowed to reach thermal equilibrium with the walls by

flowing carrier gas for 30 min prior to deposition. After ALD cycling, the wafers were removed from the reactor while hot, cooled rapidly by touching a cold surface, and kept in clean polypropylene (Entegris Fluoroware) containers. The gas pulsing sequence for conventional ALD was (45 s SiH₄ / 45 s Ar / 1 s WF₆ / 60 s Ar) and will be referred to as the A/B process. A modified gas pulsing scheme with intermediate H₂ exposures was realized by pulsing H₂ for 1 s following the SiH₄ purge step and was subsequently purged for 45 s (A/H/B process). A series of processes with H₂ co-flow were also investigated. We denote the simultaneous flow of H₂ with a precursor gas with a “+” symbol. For instance, A/H+B means that precursor A (SiH₄) was pulsed normally and then purged, but precursor B (WF₆) was dosed simultaneously with H₂, and then purged. For H₂ co-flow experiments, H₂ flow was started 1 s prior to the precursor exposure step. Since the residence time of gases inside the reactor are <1 s, we assume that starting H₂ flow one second ahead of WF₆ is sufficient to guarantee H₂+WF₆ co-exposure.

4.4.4 Characterization methods

Film nucleation and growth were characterized using *ex situ* analytical tools. Spectroscopic ellipsometry (SE) data were obtained with a J.A. Woollam alpha-SE ellipsometer at an incidence angle of 70°. X-ray reflectivity data were collected using a Rigaku SmartLab diffraction system fitted with parallel beam optics. Thickness fringes were fitted to an optical model generated by Panalytical XPert Pro software. Briefly, the model consisted of layers for the wafer substrate (Si or Si with thermal oxide), interfacial silicide, tungsten metal, and tungsten surface oxide. Layer thickness, density, and roughness were all fitted using a segmented fit method. Simulations were iterated until a best fit value of <1 was

obtained. Chemical analysis was done using a SPECS X-ray photoelectron spectroscopy (XPS) system with a PHOIBOS 150 analyzer. Spectra were generated using an Al K α X-ray source operated at 400 W. Data reduction and fitting was done using CasaXPS software with charge calibration based on the C 1s (C-C, C-H) peak set to 284.8 eV. Tungsten nuclei were imaged using an FEI Verios 460L scanning electron microscope (SEM). Wafers were imaged without the application of additional conductive coatings. Stage biasing and immersion optics were used to image the surface with minimal surface charging. Furthermore, ultra-high resolution images were obtained after an *in situ* low-power oxygen plasma clean (5 min) prior to imaging. Gas phase reactants and products during the ALD process were sampled at the reactor exhaust using an MKS Vision 2000C quadrupole mass spectrometer.

4.5 Results and Discussion

4.5.1 Substrate dependent nucleation of W on Si and SiO₂

We monitored the nucleation of tungsten on various Si and SiO₂ surfaces using complementary techniques, including spectroscopic ellipsometry (SE), scanning electron microscopy (SEM), X-ray reflectivity (XRR), and X-ray photoelectron spectroscopy (XPS). Electron microscopy shows notable differences in nanoscale evolution of metal nuclei on Si and SiO₂ surfaces. In Figure 4.1 we show a sequence of micrographs of W deposition on three different surfaces (scale bars are 200 nm, 250k magnification). The top row shows snapshots from Si:H substrates processed with 3, 5, and 10 ALD cycles (additional images in SI). At 3 cycles, metal nuclei are <5 nm in diameter and are uniformly distributed within the image frame. As the process is cycled, nuclei increase in diameter and fill in the gaps between existing particles. For this process surface roughness is quite high, as evident in the

micrographs. X-ray reflectivity measurements indicate layer roughnesses on the order of $\sigma < 2$ nm for Si substrates. This is typical for W films produced by CVD and ALD methods²⁶. Deposition on SiO₂ surfaces produces notably rougher films with large and sparse nuclei (middle and bottom rows, Figure 4.1). For both types of SiO₂, we imaged surfaces after 15, 30, and 40 ALD cycles, which correspond to three distinct stages of film growth: Incubation, nucleation, and coalescence. Nuclei density and size on low-carbon SiO₂ surfaces are markedly lower than on high-carbon wafers. For instance, 40 ALD cycles on SiO₂ produces a surface comparable to 30 cycles on SiO₂(C). This is likely due to differences in surface hydroxyl content of the treated surface and subsequent changes in the SiH₄ sticking coefficient. It is known that piranha treated and DI water rinsed surfaces show a lower SiH₄ sticking coefficient compared with fresh SiO₂ (HF etched + DI rinsed)²⁷. For a more fine grained observation of nucleation, we monitored changes to the Si and SiO₂ surfaces using ellipsometry.

We recorded the SE parameter Δ as a function of ALD cycles. In SE, Δ expresses the phase change between p- and s-polarized reflected light. As the ALD process is cycled, tungsten content on the surface increases and we observe measurable changes in Δ . This observation is consistent with the physical interpretation of Δ , which is related to light absorption, and therefore changes in the extinction coefficient (k) of the surface²⁸. The SE parameter can reliably indicate the onset of metal nucleation and remains useful until the metal film is thick enough to block all light transmission (~30 nm) to the underlying interface. In Figure 4.2 panel (a) we show the ellipsometric parameter Δ as a function of the number of ALD cycles applied on the Si:H surface. In the first 10 cycles, the Si surface is

decorated with small W nuclei and Δ decays rapidly from its initial value of 177° . Over the course of 50 cycles, Δ approaches an asymptote at approximately 138° , where the surface is fully covered with W and the underlying substrate no longer interacts with the incident beam. In panel (b), the corresponding trends are shown for the two SiO₂ surfaces, circles (●) and triangles (▲) corresponding to high-carbon (SiO₂(C)) and low-carbon (SiO₂) surfaces respectively. For silicon oxide substrates, Δ remains constant during the first 20 ALD cycles, which indicates an incubation period. This was also observed in the the micrographs discussed earlier. Island nucleation progresses for about 20 cycles, as evidenced by a large drop and a subsequent increase in Δ . Since Δ is influenced by both surface morphology (island size and distribution) and film extinction coefficient, the curve shows a complex trend. Without imposing any physical interpretation on the shape of the curves, it is evident that SiO₂(C) and SiO₂ surfaces show an approximately 10 cycle difference in incubation time. At a tungsten deposition rate of 7 Å/cycle, this corresponds to a 7 nm lag in film thickness. These trends are also visually evident to a large extent by noting color changes on the wafer. As SiO₂ substrates are coated with W, the surface gradually changes from dark violet to silver gray (Figure 4.S1). Comparisons with the SEM analyses confirm that *ex situ* SE measurements may be used to accurately track W nucleation on Si and SiO₂ surfaces. Furthermore, incubation times extracted from SE trends track well with XPS measurements of the Si 2p substrate signal. In the following sections, we will present modifications to the W ALD process and observe changes in nucleation using SE, SEM, and XRR analyses.

4.5.2 Nucleation control by a modified ALD scheme

The native selectivity of W ALD may be modified by introducing reaction steps that hold back unwanted nucleation on SiO₂ surfaces. Previous ALD studies of tungsten growth have shown that H₂ is a reaction product for both half-cycles²⁹. Quadrupole mass spectrometry measurements recorded during the ALD process confirm this (Figure 4.S1). A large amount of H₂ is generated ($m/z = 2$) during the SiH₄ exposure. Since WF₆ alone is not reactive with SiO₂ at ALD temperature ranges, it is to be expected that the surface reactions with SiH₄ play a part in nucleating W on SiO₂. By exposing the oxide surface to excess H₂ after or during precursor exposure, we expected to modify metal nucleation on SiO₂ without affecting growth on Si. We used two approaches toward this end: Intermediate H₂ exposure steps between the SiH₄ and WF₆ half-cycles and H₂ co-flow during one or both half-cycles. In this section, we will explore these two H₂-modified processes in detail.

Intermediate H₂ exposures

We compared tungsten selectivity between Si and SiO₂ for the conventional and the intermediate H₂ exposure process. As noted before, the conventional tungsten process (SiH₄/Ar/WF₆/Ar) and the H₂-modified process (SiH₄/Ar/H₂/Ar/WF₆/Ar) are abbreviated as “A/B” and “A/H/B”, respectively. In Figure 4.3 the filled symbols show SE parameter Δ at various cycle numbers from the A/B process and hollow symbols show the same measurement for the A/H/B cycles. The two processes both show a rapid and monotonic decrease in Δ on the Si substrate (Figure 4a). It is evident that there is not a significant difference in W nucleation time and growth rate on Si. On the SiO₂(C) surface (high carbon content), the two Δ curves have the same overall shape, but the curve for the A/H/B process

is shifted in the positive direction toward higher cycle numbers (Figure 4.3b). The shift in the Δ curve shows that by inserting an intermediate H_2 pulse into the ALD process after the SiH_4 exposure we can lengthen the incubation period of W on SiO_2 by approximately 10 cycles. When we use a piranha cleaned SiO_2 surface (SiO_2), however, no incubation shift is observed in response to the A/H/B process (Figure 4.3c). As demonstrated in previous studies³⁰, the initial state of the SiO_2 surface can influence the amount of W deposition. It is evident that for the A/H/B tungsten process, the effectiveness of the intermediate H_2 exposure is sensitive to the amount of carbon present on the thermal oxide surface. XPS measurements show that the only detectable difference between $SiO_2(C)$ and SiO_2 is the amount of carbon present: 3.2 and 1.9 at%, respectively (Figure 4.S2). Comparing the two oxide surfaces, we do not observe significant shifts in O 1s and Si 2p peak positions (energy resolution of the instrument is 0.1 eV). In terms of chemical binding, the two surfaces appear to be identical. Therefore, we ascribe the influence of the intermediate H_2 exposure to an *in situ* surface cleaning effect. Similar to a low temperature H_2 pre-bake³¹, the intermediate pulsing of H_2 during the ALD process may remove surface contamination that otherwise would contribute to metal nucleation. Furthermore, the observation that the SE Δ curves for the A/H/B process on $SiO_2(C)$ (Figure 4.3b) and the A/B process on SiO_2 (Figure 4.3c) look nearly identical, supports our hypothesis that a surface cleaning effect is indeed taking place.

We have also observed the incubation shift predicted by the SE Δ data by imaging the same surfaces with high resolution SEM. A series of the snapshots that illustrate process dependent metal nucleation and growth are given in Figure 4.4. The top row shows surfaces taken out of the ALD reactor after a number of A/B cycles. Likewise, the bottom row shows

various surfaces after applying a number of A/H/B cycles. The first set of three columns are from Si:H substrates. Here, the nuclei size and density are comparable between A/B and A/H/B cycles for the 3, 5, and 10 cycle snapshots shown. The middle three columns show the SiO₂(C) substrate, which experiences an incubation delay for tungsten deposition upon the application of A/H/B cycles. This is especially evident at 15 and 30 cycles, where the A/H/B process produces fewer and smaller nuclei on SiO₂ as compared to the conventional tungsten ALD process. On the SiO₂ surface, however, the difference between the two processes is negligible. From both sets of micrographs of W nucleation on SiO₂, one may also note that deposition largely proceeds by the growth of existing nuclei, rather than the addition of new nuclei. This indicates that W growth on the oxide surface is not as facile as on the Si surface. Furthermore, the appearance of small diameter (<10 nm) nuclei next to larger (>100 nm) nuclei may suggest that new nuclei are slowly generated on the oxide surface, not due to surface defects alone, but from surface-precursor or surface-byproduct reactions. This speaks to the strong contribution that loading effects make toward W nucleation on silicon oxide.

In developing a more selective W process, one would like to extend incubation time on the non-receptive surface without affecting the ALD process on the receptive surface. For this reason, it is important to check that deposition rate on the Si surface is not affected by the H₂-modified ALD process. We measured film thicknesses *ex situ* after different cycle numbers by X-ray reflectivity. Thicknesses obtained from this analysis are plotted as a function of cycle number in Figure 4.5. We show that the deposition rate on Si at 220°C is approximately 7 Å/cycle with either process. This deposition rate corresponds to 2-3 monolayers per cycle, which demonstrates the non self-limiting nature of the SiH₄

exposure³². From the thickness data, deposition rates on the SiO₂(C) surfaces may be slightly higher than on Si, however, an interpretation of incubation time is difficult due to the limited number of data points and large variations in surface roughness at different cycle numbers.

H₂ co-flow during precursor exposure

A further modification of the conventional ALD process was explored by pulsing H₂ immediately before, during, or immediately after one or both half-cycles. This approach draws inspiration from H₂/WF₆ selective CVD methods, while maintaining a high degree of film thickness control afforded by ALD-type reaction schemes. While this process bears some resemblance to the H₂ reduction CVD scheme, the reactor temperatures in this study are lower than selective CVD W conditions³³. We have verified that no additional deposition takes place as a result of H₂/WF₆ co-flow at 220°C (Figure S4). In order to study the effect of H₂ exposure in close succession with WF₆ or SiH₄ precursor pulses, we recorded XPS spectra from thermal oxide surfaces (SiO₂) exposed to 30 cycles of A/B, A+H/B, A/B+H, and A+H/B+H reactions. The sequence of W 4f photoemission spectra are shown in Figure 4.6. The doublet at the higher binding energies (37.8 and 35.8 eV) are ascribed to the presence of a surface oxide, WO_x. Lower binding energy doublet corresponds to metallic tungsten (W⁰). In comparing the four H₂ co-flow conditions, we note a general trend toward decreasing W 4f signal intensity with more H₂ steps added to the pulsing sequence. In particular, a dramatic reduction in surface W⁰ content is evident between the A/B and the A/B+H process. While the H₂ flow during the SiH₄ step (A+H) appears to diminish 4f_(7/2) and 4f_(5/2) slightly, it is clear that the WF₆ exposure is more strongly modified by H₂. We observe the same trend when we compare SiO₂ surface treated with 40 and 50 cycles of these modified ALD sequences. Since

the WF₆ step appears to have a strong influence on W nucleation on SiO₂, we investigated the A/B+H process further.

In Figure 4.7 we show ellipsometry trends similar to those shown earlier in the text. Here, we compare A/B and A/B+H processes on Si and SiO₂ surfaces. While the A/H/B cycles (intermediate H₂ pulsing) did not modify W incubation on SiO₂ (Figure 4.3c), the A/B+H process is shown to cause a clear delay in nucleation (Figure 4.7b). The deposition process on the Si surface, however, appears to proceed in a similar fashion with either process (Figure 4.7a). We therefore expect deposition rates from the A/B+H process on the growth surface to be comparable to the A/B scheme. Thickness measurements confirm this interpretation of the ellipsometry trends. In Figure 4.8 we show that deposition rates are approximately 0.7 Å/cy for the three processes investigated in this work: A/B, A/H/B, and A/B+H gas pulsing sequences.

4.5.3 Influence of reactor walls and wafer loading effects on deposition

It is known that tungsten CVD processes are highly susceptible to wafer loading effects³⁴. Therefore, one would also expect to see similar phenomena during ALD processes that share some surface chemistry with their CVD counterparts. To our knowledge, loading effects for ALD processes have not been reported to date. For inherent patterning applications, unwanted reactions originating from vicinal surfaces will be highly undesirable and significantly impede technology development for selective ALD. The data shown up to this point were collected by loading one type of surface into the reactor for a given deposition run. However, patterned surfaces are needed to evaluate selectivity. In Figure 4.9 we show two sets of wafer coupons loaded into the quartz tube reactor, with gas flow direction

indicated by the arrow. We used quartz as the reactor surface in order to eliminate wall reactions on hot metal surfaces that may contribute to unwanted nucleation on SiO_2 surfaces. Wafer coupons with gray coatings are Si:H and the purple/blue wafers are thermal SiO_2 surfaces. When the Si wafer is loaded upstream (Si:H first) we observe a parabolic streamline on the SiO_2 piece immediately downstream from the growth surface. This shows that macroscopic loading effects are present during the A/B tungsten process. When the order of the wafers is reversed (Si:H last) we do not observe the same degree of deposition on the middle SiO_2 piece. However, we still observe a thin strip of W deposition upstream from the Si wafer (indicated by a white arrow). This indicates that reactive products generated on the Si surface can diffuse a short distance in the upstream direction (against gas flow). These effects may be difficult to overcome in selective metal ALD and other processes that generate reactive byproducts.

We have also prepared SiO_2 wafers with an array of thin Au strips 5 mm apart. These patterned coupons were coated with 30 A/B cycles or 30 A/B+H cycles. As expected, W deposits readily on the Au strips, but 30 cycles only produce a thin layer of W/WO_x on the SiO_2 surface. Photographs of uncoated and ALD processed wafers are shown in Figure 10. Encroachment effects are evident between the Au strips. Comparing A/B and A/B+H cycles, it is clear that W deposition near the edges of the Au pattern is significantly reduced with the H_2 modified process. The spotty areas on the SiO_2 regions show the presence of a thin W/WO_x film. We show this to illustrate some of the critical challenges faced in developing truly site selective ALD processes.

4.6 Summary and Conclusions

Site selective deposition processes are critical for the current scaling requirements in semiconductor manufacturing processes. As lithographic patterning techniques are hindered by compounding alignment errors, selective deposition may play a role in eliminating lithography steps from the process flow. Chemical vapor deposition processes that are inherently aligned (and selective) with respect to existing surfaces need to be developed. For this and similar applications, we studied the surface dependent nucleation of tungsten on Si:H and SiO₂ surfaces toward the development of selective ALD chemistries. We observed that the W ALD process shows inherent selectivity toward Si surfaces and exhibits a 20-30 cycle nucleation delay on SiO₂. Oxide surface with more and less carbon content showed notable differences in nucleation time, as observed by ellipsometry and electron microscopy. We presented a modified W ALD recipe where intermittent H₂ exposures help to slow down unwanted nucleation of W on carbon rich SiO₂ surfaces. While this improvement was limited to certain SiO₂ surfaces, we have also developed a second modified W ALD process where nucleation on clean SiO₂ surfaces is delayed by 10 cycles without affecting deposition rates on Si. While it should be possible to deposit 10-20 nm of W on Si, without depositing any W on SiO₂, we show that macroscopic loading effects dominant on patterned wafers. When two dissimilar surfaces are in close proximity, as would be found in microelectronic devices, reactions on the receptive surface (Si or Au) give rise to unwanted deposition on the non-receptive surface (SiO₂). These loading issues need to be addressed for the development of selective ALD processes.

4.7 Acknowledgments

The authors acknowledge the use of the Analytical Instrumentation Facility (AIF) at North Carolina State University, which is supported by the State of North Carolina and the National Science Foundation. Funding for this project was provided by the Semiconductor Research Corporation (SRC task# 2401.001).

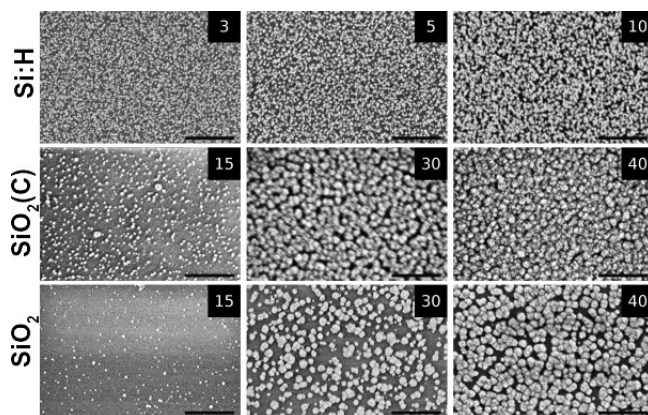


Figure 4.1. Micrographs of W nucleation on Si:H and SiO₂ substrates. ALD cycle numbers are indicated on each frame. Scale bars correspond to 200 nm.

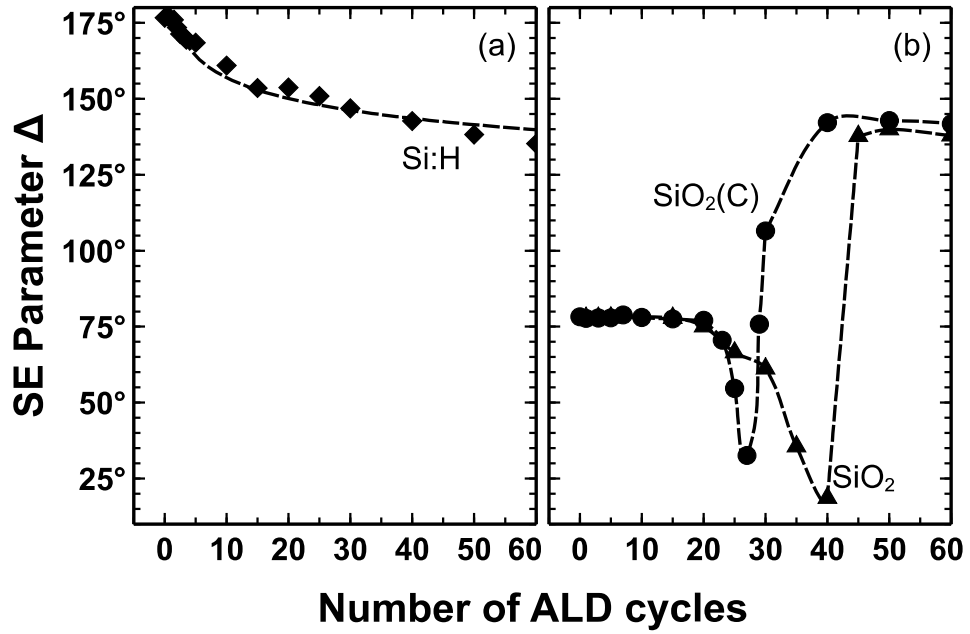


Figure 4.2. SE parameter delta (Δ) is plotted as indicators of W nucleation on Si:H and SiO₂ surfaces. Diamond (\blacklozenge) symbols indicate Si:H, circles (\bullet) indicate SiO₂(C), and triangles (\blacktriangle) indicate SiO₂.

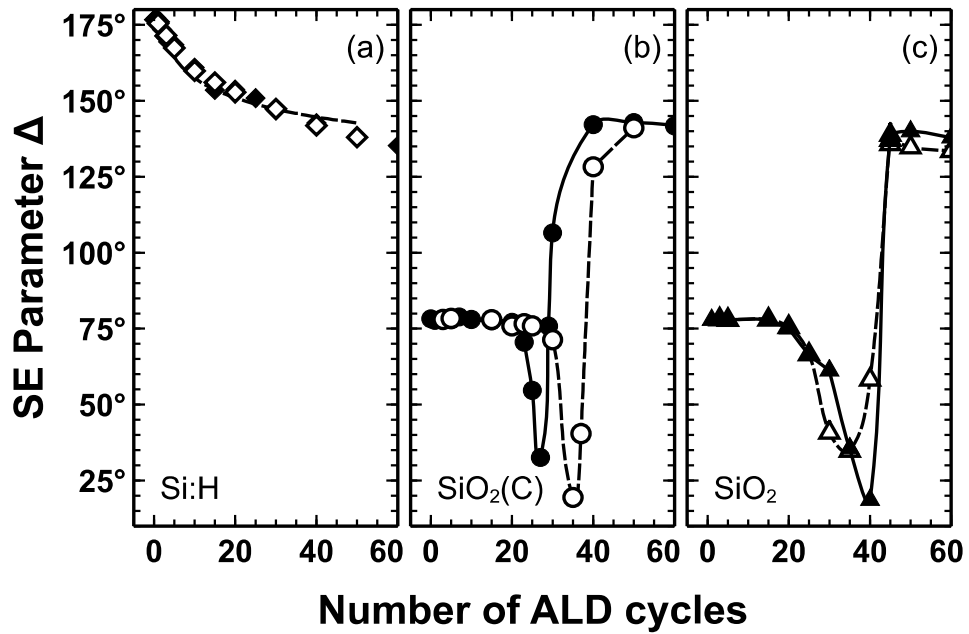


Figure 4.3. SE parameter delta is indicators of W nucleation on different surfaces prepared with different gas pulsing sequences. Diamonds (◆) denote Si:H, circles (●) indicate SiO₂(C), and triangles (▲) correspond to SiO₂ surfaces. Filled symbols represent A/B and hollow symbols represent A/H/B ALD cycles.

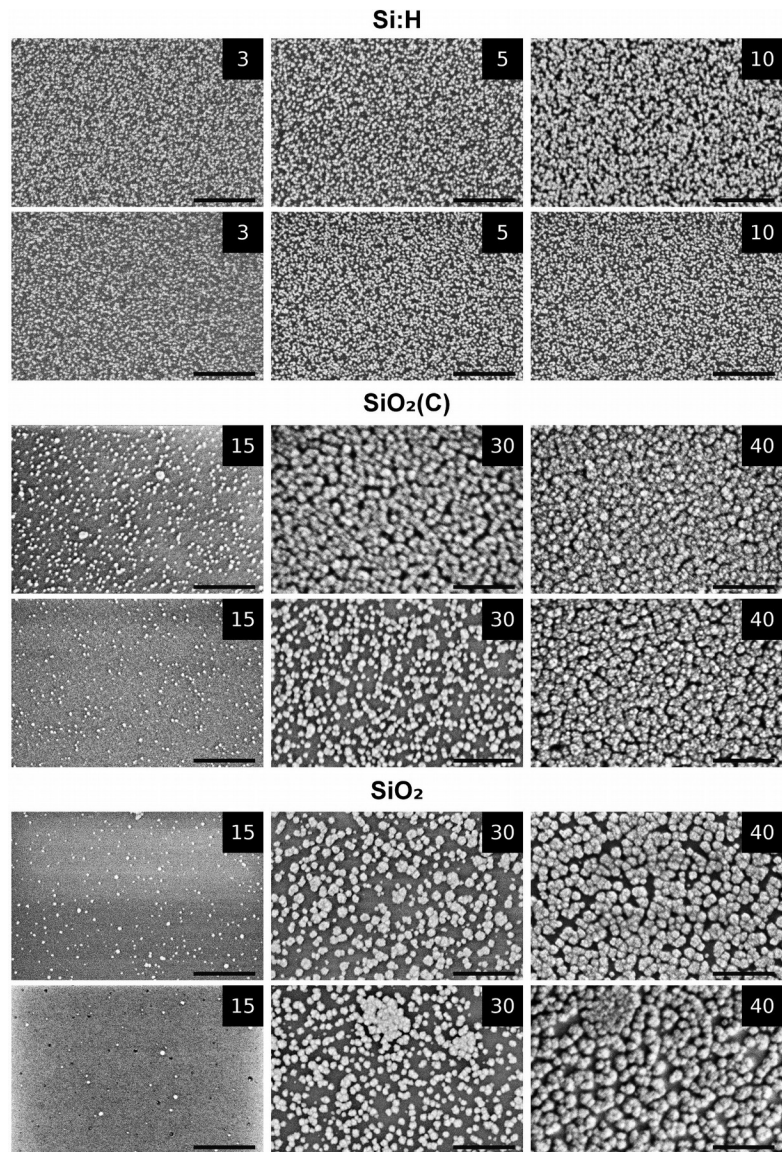


Figure 4.4. Micrographs of W nucleation on Si:H, SiO₂(C), and SiO₂ with A/B (top rows) and A/H/B processes (bottom rows). ALD cycle numbers are indicated on each frame. Scale bars correspond to 200 nm.

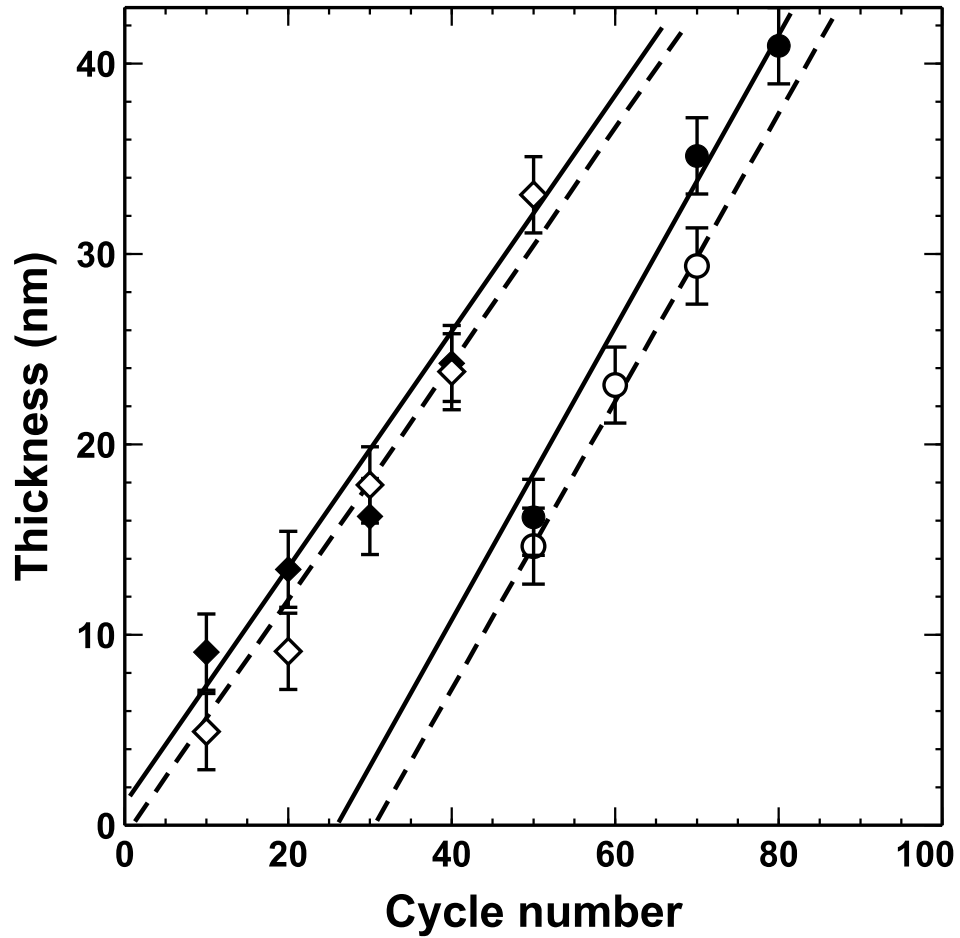


Figure 4.5. Film thickness measured by XRR for (♦) Si:H and (●) SiO₂(C) surfaces. Data reported include the thickness of the silicide interface. Filled symbols represent A/B and hollow symbols represent A/H/B ALD pulsing sequences.

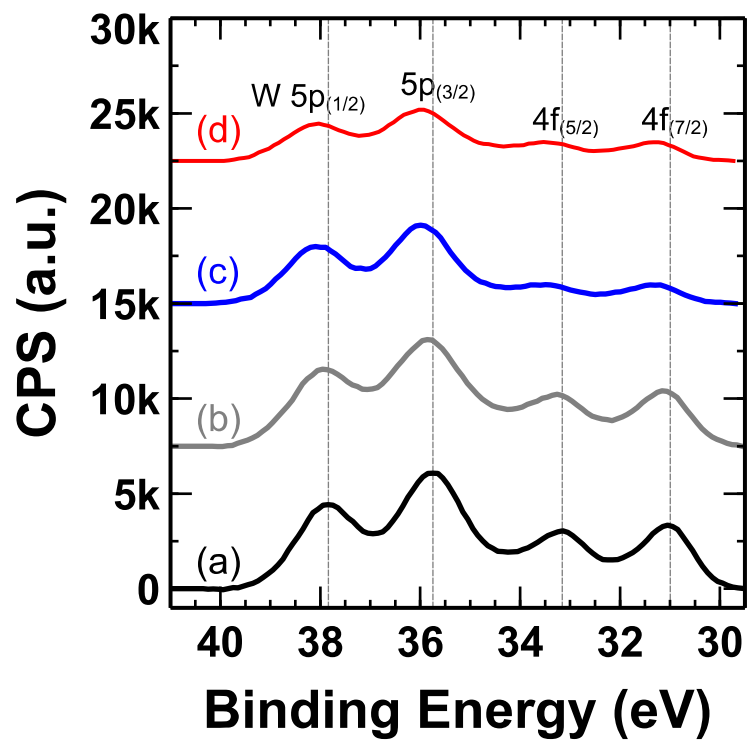


Figure 4.6. XPS spectra for the W 4f region on SiO₂ substrates, after 30 cycles of: a) A/B; b) A+H/B; c) A/B+H; and d) A+H/B+H.

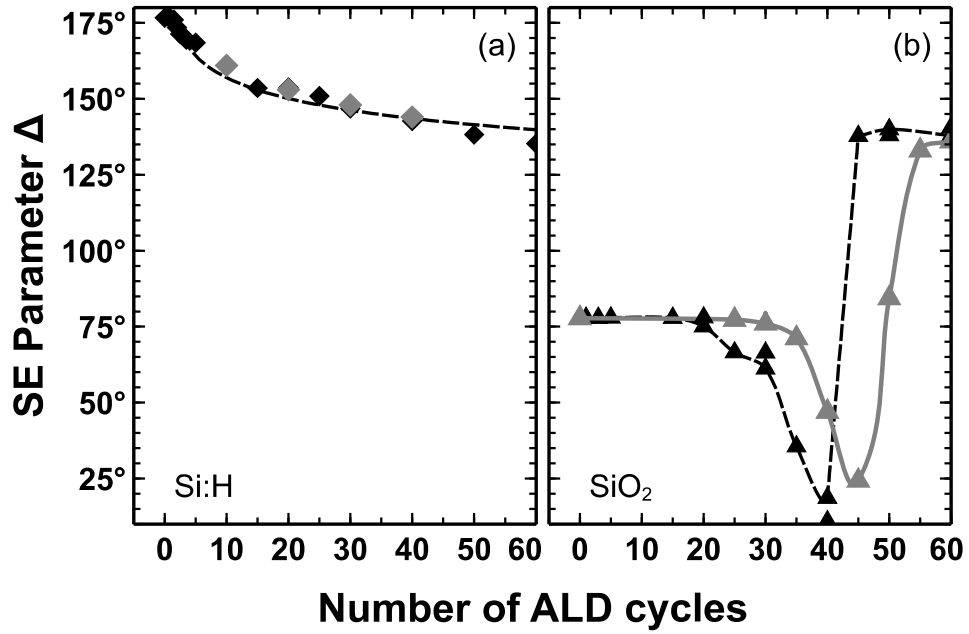


Figure 4.7. SE parameter delta (Δ) is plotted for Si:H and SiO₂ surfaces. Diamond (\blacklozenge) symbols indicate Si:H and triangles (\blacktriangle) indicate SiO₂. The black symbols are from the conventional A/B process, while the gray symbols indicate the modified A/B+H process.

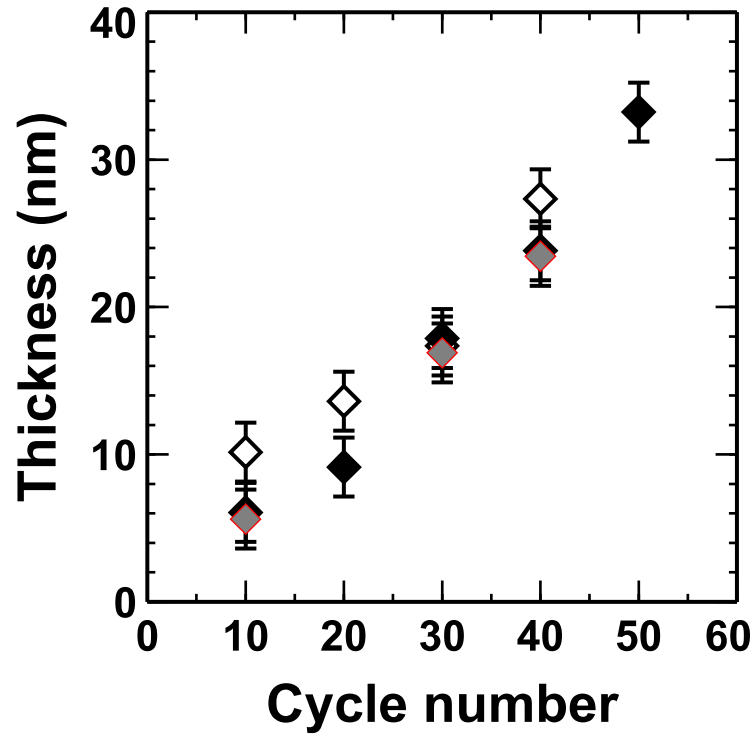


Figure 4.8. Film thickness on Si:H substrates measured by XRR for (◆) A/B, (◇) A/H/B, and (◆) A/B+H gas pulsing sequences (gray diamonds). Thickness points in the plot include the thickness of the silicide interface.

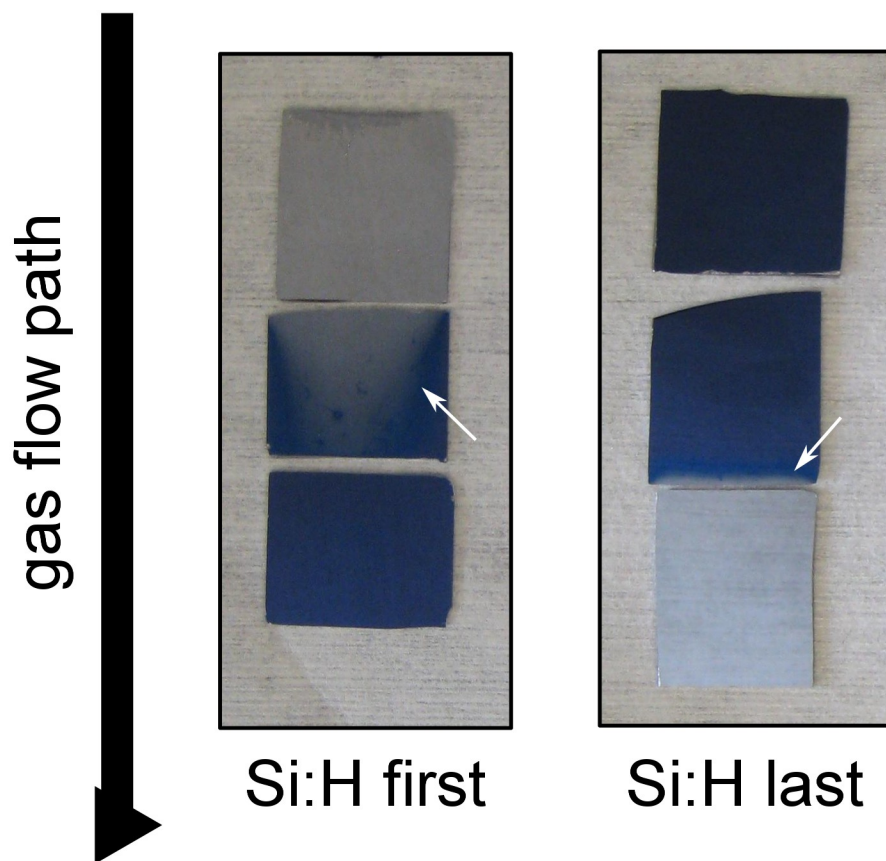


Figure 4.9. Photographs of one Si:H and SiO₂ surfaces that were loaded simultaneously into the ALD reactor. On the left, one Si:H surface is upstream from two SiO₂ chips. On the right, Si:H is downstream from the SiO₂ surfaces. The large black arrow indicates gas flow direction and small white arrows point to spurious W deposition due to loading effects. Wafer pieces are ~ 15x15 mm.

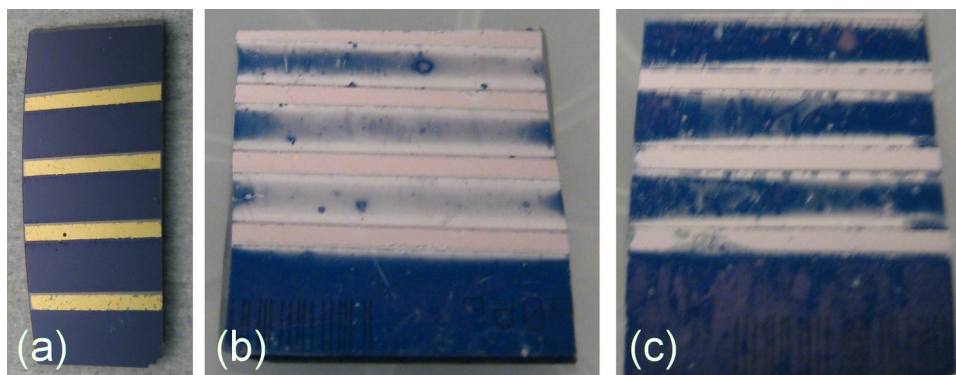


Figure 4.10. Photographs of Au-patterned SiO_2 surfaces that were processed coated with: (a) 0 cycles; (b) 30 A/B cycles; (c) 30 A/B+H cycles at 220°C . The distance between the Au strips is ~ 5 mm.

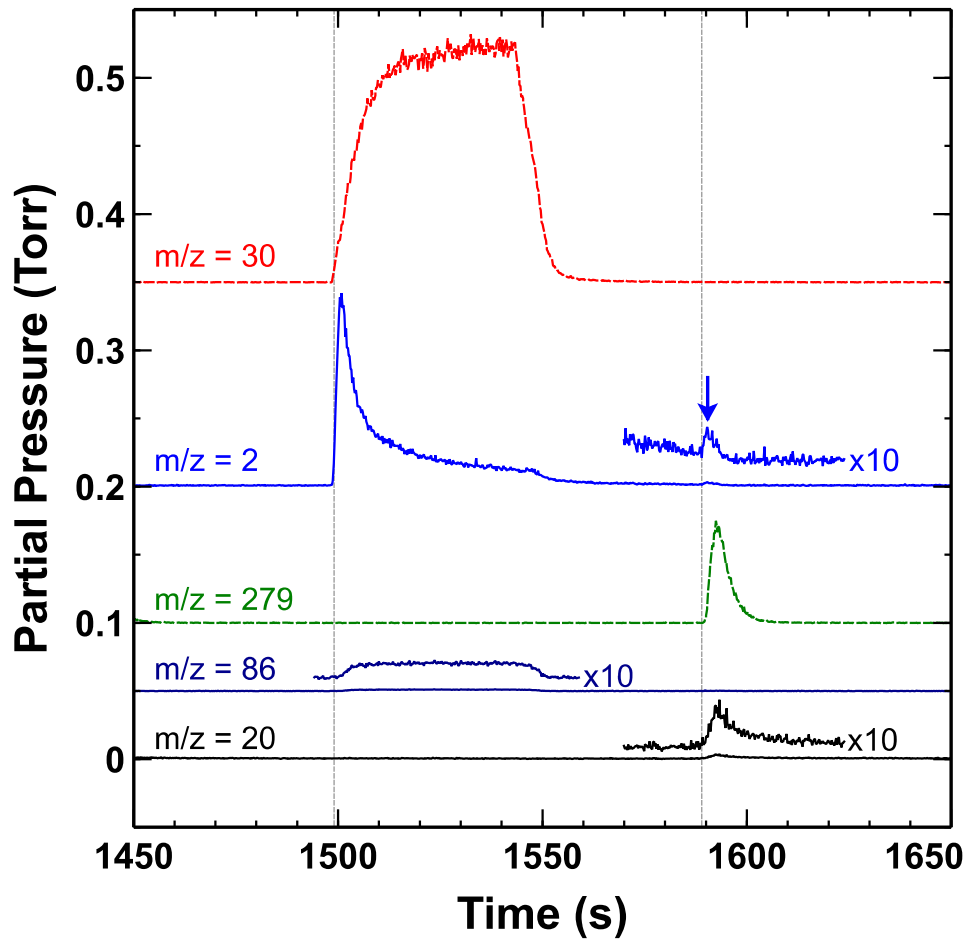


Figure 4.S1. Time traces for m/z 30, 2, 279, 86, and 20 are shown for the SiH_4/WF_6 ALD process. The data are representative for steady-state deposition in an empty reactor at 220°C . Gas phase products are from gas-solid reactions on reactor walls and substrate holder.

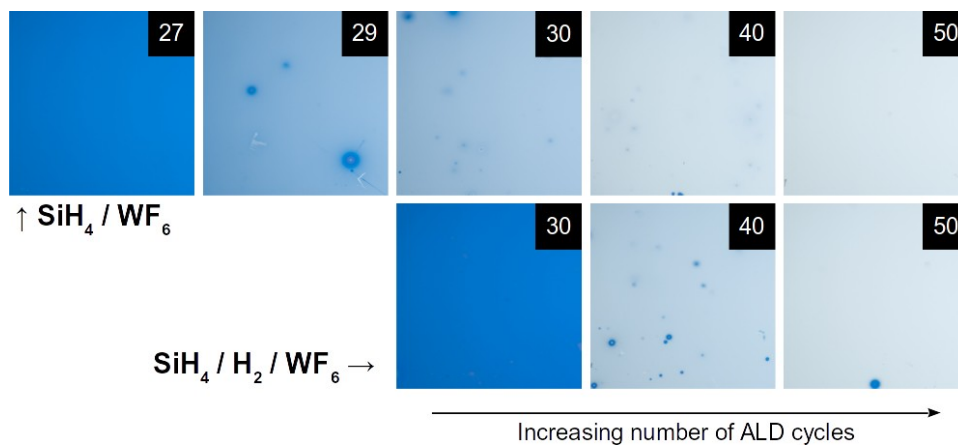


Figure 4.S2. Photographs of W nucleation on Si:H and $\text{SiO}_2(\text{C})$ substrates. ALD cycle numbers are indicated on each frame. Surfaces shown are 5 x 5 mm in size.

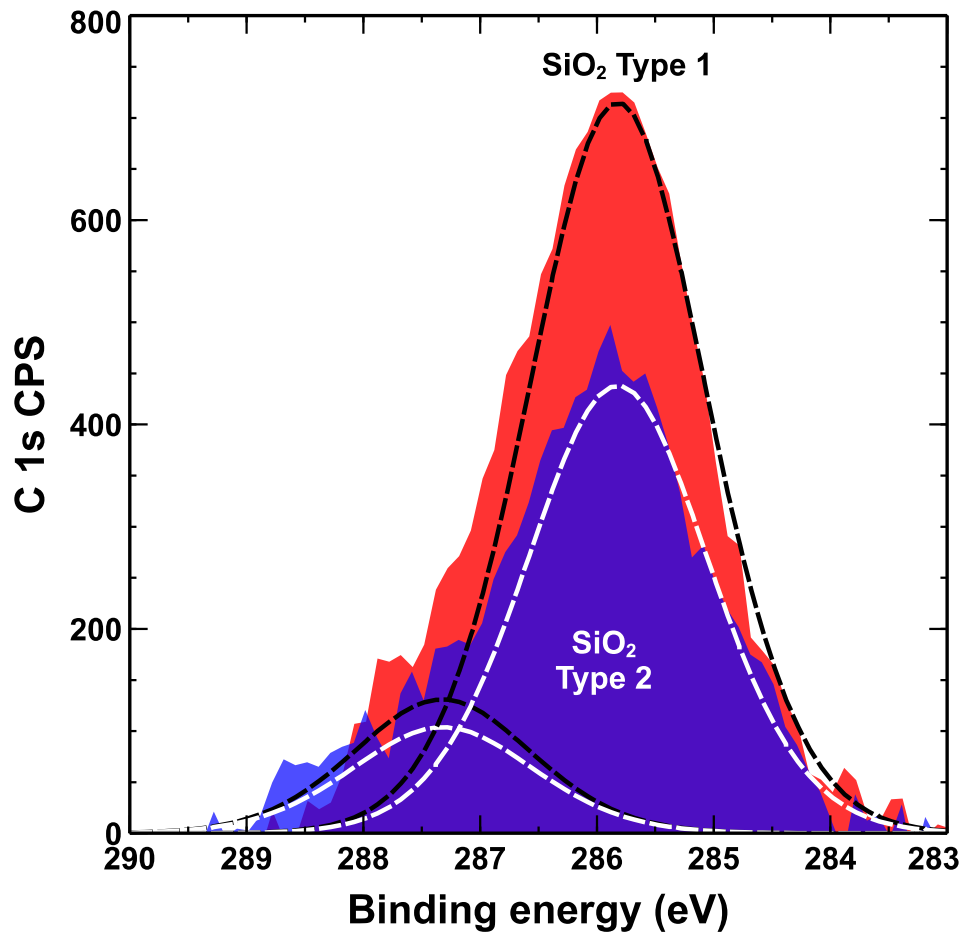


Figure 4.S3. XPS spectra from the C 1s region for SiO₂(C) and SiO₂ substrates. Carbon content is significantly higher on the SiO₂(C) surface.

4.8 References

- (1) Grubbs, R. K.; Nelson, C. E.; Steinmetz, N. J.; George, S. M. Nucleation and Growth during the Atomic Layer Deposition of W on Al₂O₃ and Al₂O₃ on W. *Thin Solid Films* **2004**, *467*, 16–27.
- (2) Klaus, J. .; Ferro, S. .; George, S. . Atomically Controlled Growth of Tungsten and Tungsten Nitride Using Sequential Surface Reactions. *Appl. Surf. Sci.* **2000**, *162-163*, 479–491.
- (3) Elam, J. W.; Nelson, C. E.; Grubbs, R. K.; George, S. M. Nucleation and Growth during Tungsten Atomic Layer Deposition on SiO₂ Surfaces. *Thin Solid Films* **2001**, *386*, 41–52.
- (4) Elam, J. .; Nelson, C. .; Grubbs, R. .; George, S. . Kinetics of the WF₆ and Si₂H₆ Surface Reactions during Tungsten Atomic Layer Deposition. *Surf. Sci.* **2001**, *479*, 121–135.
- (5) McConica, C. M. Tungsten Nucleation on Thermal Oxide during LPCVD of Tungsten by the Hydrogen Reduction of Tungsten Hexafluoride. *J. Electrochem. Soc.* **1988**, *135*, 1003.
- (6) Lecohier, B.; Calpini, B.; Philippoz, J.-M.; Bergh, H. van den. Low pressure Chemical Vapor Deposition of Copper: Dependence of the Selectivity on the Water Vapor Added to a Hydrogen or Helium Carrier Gas. *J. Appl. Phys.* **1992**, *72*, 2022–2026.
- (7) Reisman, A. Selective Tungsten on Silicon by the Alternating Cyclic, AC, Hydrogen Reduction of WF₆. *J. Electrochem. Soc.* **1990**, *137*, 722.
- (8) Reisman, A.; Temple, D. Alternating Cyclic Pressure Modulation Process for Selective Area Deposition. US5201995 A, April 13, 1993.
- (9) Creighton, J. R.; Parmeter, J. E. Metal CVD for Microelectronic Applications: An Examination of Surface Chemistry and Kinetics. *Crit. Rev. Solid State Mater. Sci.* **1993**, *18*, 175–237.
- (10) Farm, E.; Kemell, M.; Ritala, M.; Leskela, M. Self-Assembled Octadecyltrimethoxysilane Monolayers Enabling Selective-Area Atomic Layer Deposition of Iridium. *Chem. Vap. Depos.* **2006**, *12*, 415–417.

- (11) Färm, E.; Kemell, M.; Santala, E.; Ritala, M.; Leskelä, M. Selective-Area Atomic Layer Deposition Using Poly(vinyl Pyrrolidone) as a Passivation Layer. *J. Electrochem. Soc.* **2010**, *157*, K10.
- (12) Chen, R.; Bent, S. F. Highly Stable Monolayer Resists for Atomic Layer Deposition on Germanium and Silicon. *Chem. Mater.* **2006**, *18*, 3733–3741.
- (13) Park, K. J.; Doub, J. M.; Gougousi, T.; Parsons, G. N. Microcontact Patterning of Ruthenium Gate Electrodes by Selective Area Atomic Layer Deposition. *Appl. Phys. Lett.* **2005**, *86*, 051903.
- (14) Hashemi, F. S. M.; Prasittichai, C.; Bent, S. F. A New Resist for Area Selective Atomic and Molecular Layer Deposition on Metal–Dielectric Patterns. *J. Phys. Chem. C* **2014**, *118*, 10957–10962.
- (15) Ellinger, C. R.; Nelson, S. F. Selective Area Spatial Atomic Layer Deposition of ZnO, Al₂O₃, and Aluminum-Doped ZnO Using Poly(vinyl Pyrrolidone). *Chem. Mater.* **2014**, *26*, 1514–1522.
- (16) Levy, D. H.; Ellinger, C. R.; Nelson, S. F. Metal-Oxide Thin-Film Transistors Patterned by Printing. *Appl. Phys. Lett.* **2013**, *103*, 043505.
- (17) Selvaraj, S. K.; Parulekar, J.; Takoudis, C. G. Selective Atomic Layer Deposition of Zirconia on Copper Patterned Silicon Substrates Using Ethanol as Oxygen Source as Well as Copper Reductant. *J. Vac. Sci. Technol. A* **2014**, *32*, 010601.
- (18) Yanguas-Gil, A.; Libera, J. A.; Elam, J. W. Modulation of the Growth Per Cycle in Atomic Layer Deposition Using Reversible Surface Functionalization. *Chem. Mater.* **2013**, *25*, 4849–4860.
- (19) Van der Jeugd, C. A.; Verbruggen, A. H.; Leusink, G. J.; Janssen, G. C. a. M.; Radelaar, S. Selective Chemical Vapour Deposition of Tungsten Using SiH₄/WF₆ Chemistry. In *Symposium L – Chemical Vapor Deposition of Refractory Metals and Ceramics I*; MRS Online Proceedings Library; 1989; Vol. 168.
- (20) Macdonald, N. C.; Chen, L. Y.; Yao, J. J.; Zhang, Z. L.; McMillan, J. A.; Thomas, D. C.; Haselton, K. R. Selective Chemical Vapor Deposition of Tungsten for Microelectromechanical Structures. *Sens. Actuators* **1989**, *20*, 123–133.
- (21) Dana, S. S.; Liehr, M.; Anderle, M.; Rubloff, G. W. Kinetics of Nucleation and Growth of Si on SiO₂ in Very Low Pressure SiH₄ Chemical Vapor Deposition. *Appl. Phys. Lett.* **1992**, *61*, 3035–3037.

- (22) Kepten, A.; Reisman, A.; Ray, M.; Smith, P. L.; Temple, D.; Tapp, F. Studies of the Possible Reaction of WF₆ with SiO₂ and Si₃N₄ at Several Temperatures. *J. Electrochem. Soc.* **1992**, *139*, 2331–2337.
- (23) McConica, C. M. Tungsten Nucleation on Thermal Oxide during LPCVD of Tungsten by the Hydrogen Reduction of Tungsten Hexafluoride. *J. Electrochem. Soc.* **1988**, *135*, 1003.
- (24) Creighton, J. R. The Surface Chemistry and Kinetics of Tungsten Chemical Vapor Deposition and Selectivity Loss. *Thin Solid Films* **1994**, *241*, 310–317.
- (25) Kalanyan, B.; Losego, M. D.; Oldham, C. J.; Parsons, G. N. Low-Temperature Atomic Layer Deposition of Tungsten Using Tungsten Hexafluoride and Highly-Diluted Silane in Argon. *Chem. Vap. Depos.* **2013**, *19*, 161–166.
- (26) Smith, S.; Aouadi, K.; Collins, J.; van der Vegt, E.; Basso, M.-T.; Juhel, M.; Pokrant, S. Low Resistivity Tungsten for Contact Metallization. *Microelectron. Eng.* **2005**, *82*, 261–265.
- (27) Kajikawa, Y.; Tsuchiya, T.; Noda, S.; Komiyama, H. Incubation Time during Chemical Vapor Deposition of Si onto SiO₂ from Silane. *Chem. Vap. Depos.* **2004**, *10*, 128–133.
- (28) Fujiwara, H. *Spectroscopic Ellipsometry: Principles and Applications*; John Wiley & Sons, Ltd: Chichester, UK, 2007.
- (29) Grubbs, R. K.; Steinmetz, N. J.; George, S. M. Gas Phase Reaction Products during Tungsten Atomic Layer Deposition Using WF₆ and Si₂H₆. *J. Vac. Sci. Technol. B Microelectron. Nanometer Struct.* **2004**, *22*, 1811.
- (30) Tsao, K. Y.; Busta, H. H. Low Pressure Chemical Vapor Deposition of Tungsten on Polycrystalline and Single-Crystal Silicon via the Silicon Reduction. *J. Electrochem. Soc.* **1984**, *131*, 2702–2708.
- (31) Brabant, P. D.; Italiano, J. P.; Wen, J. Low Temperature Load and Bake. US7108748 B2, September 19, 2006.
- (32) Wind, R. W.; Fabreguette, F. H.; Sechrist, Z. A.; George, S. M. Nucleation Period, Surface Roughness, and Oscillations in Mass Gain per Cycle during W Atomic Layer Deposition on Al₂O₃. *J. Appl. Phys.* **2009**, *105*, 074309–074309 – 13.
- (33) Broadbent, E. K.; Ramiller, C. L. Selective Low Pressure Chemical Vapor Deposition of Tungsten. *J. Electrochem. Soc.* **1984**, *131*, 1427–1433.

- (34) Holleman, J. Loading Effects on Kinetic and Electrical Aspects of Silane-Reduced Low-Pressure Chemical Vapor Deposited Selective Tungsten. *J. Electrochem. Soc.* **1993**, *140*, 818.

CHAPTER 5. Effect of Precursor Chemistry and Delivery Conditions on Coating Uniformity In Mesoporous Metal Oxide Scaffolds During ALD Processes

Berc Kalanyan^{1*}, Eric Stevens¹, Moataz B. Mousa¹, Mark D. Losego², Byron H. Farnum³, Leila Alibabaei³, Thomas J. Meyer³, and Gregory N. Parsons¹

¹*North Carolina State University, Department of Chemical and Biomolecular Engineering, Raleigh, North Carolina, 27695*

²*Georgia Institute of Technology, Department of Material Science and Engineering, Atlanta, Georgia, 30332*

³*University of North Carolina at Chapel Hill, Department of Chemistry, Chapel Hill, North Carolina, 27599*

This chapter is a manuscript in preparation for submission to the Journal of the American Vacuum Society: A.

5.1 Abstract

Metal oxide mesoporous scaffolds with surface areas greater than 100 m²/g are used in a variety of applications, most notably in photovoltaic and photoelectrochemical energy conversion. Atomic layer deposition (ALD) is the preferred technique for applying shell coatings over the scaffold particles. As a vapor-phase coating technique, ALD is unique in its capacity to deposit conformal films over high aspect ratio structures. For these applications, the interplay between precursor chemistry and coating uniformity are complex and difficult to assess with post-deposition analyses. In this work we adapt the *in situ* quartz crystal microbalance (QCM) technique to monitor deposition into mesoporous scaffolds in real time. This technique allows us to observe features that are unique to porous substrates, including

pore clogging, precursor infiltration effects, and the presence of long time scale diffusion and reaction events. We compare ALD coatings applied with conventional precursor flow and hold-step ALD sequences. We choose two Ti-containing precursors, titanium tetrachloride (TiCl_4) and titanium tetraisopropoxide (TTIP), to understand the influence of precursor chemical structure on coating formation inside porous substrates. We validate our results from the QCM analysis with secondary ion mass spectrometry (SIMS) depth profiling and electron microscopy. While the bulkiness of the TTIP precursor is expected to present diffusion limitations, we find that the metal halide precursor exhibits unwanted side reactions that impede self-limiting and conformal deposition inside pores. We also find that long purge times, on the order of tens of hours, are required to completely purge nanostructured oxide scaffolds with either precursor. Films deposited from TTIP/ H_2O produce highly uniform films, but process times for completely self-limiting growth are extremely long.

5.2 Introduction

Mesoporous metal oxide scaffolds are an integral component in electrochemical energy conversion devices, such as dye-sensitized solar cells (DSSC) and dye-sensitized photoelectrochemical cells (DSPEC). A typical anode for a DSSC consists of TiO_2 nanoparticles (10-20 nm) cast as a thick film (1.5-12 μm) on a transparent conductive oxide (TCO) substrate. The scaffold in these devices serves as a high surface area platform on which the light absorber (molecular dyes or quantum dots) is anchored. Since the scaffold surface defines the photoanode/electrolyte interface, there is a clear benefit in maximizing the scaffold surface area. As pathways for efficiency losses in DSSCs were investigated, a

clear need for thin film coatings emerged. However, since the anode is a mesoporous structure, many vacuum coating techniques cannot deliver material into the pores due to line-of-sight restrictions. Atomic layer deposition (ALD) has been demonstrated as a suitable technique for applying thin film coatings on the DSSC anode. One of the challenges faced in applying ALD coatings is that, depending on the total surface area and the tortuosity of the scaffold, reactant diffusion and byproduct removal can be slow. Determining the correct deposition conditions for mesoporous substrates can be time consuming, since many *ex situ* cross sectional analyses (TEM, SIMS) have a low throughput and are expensive. Therefore, *in situ* diagnostics that allow for real-time tracking of the deposition process, including endpoint detection during each reactant exposure, are appealing for porous substrates. In this work, we address this need by adapting the quartz crystal microbalance (QCM) technique to explore the conditions needed to produce conformal coatings over mesoporous structures by ALD. Thus far, the QCM technique has been used to study two-dimensional film growth over flat QCM crystals. We now extend the QCM tool to study transport and reaction phenomena that take place inside three-dimensional nanostructured substrates.

When mesoporous oxide scaffolds are coated with a thin film layer, the resulting structure is often referred to as a core-shell structure. The core is a large particle (tens of nm in diameter), which may be part of a scaffold, and the shell is a conformal thin film around the core, often prepared by ALD. Core-shell structures see a wide range of applications including photodiodes¹, water splitting photoanodes², plasmonic solar cells³, supported catalysts⁴, pseudocapacitors⁵, and dye-sensitized solar cells⁶⁻⁹. For DSSCs in particular, metal oxide ALD films have been used for the following purposes: 1) As blocking layers between

the TCO and the scaffold (inhibit TCO-to-electrolyte e^- transfer); 2) As electron transfer barriers on inorganic scaffolds (inhibit scaffold-to-electrolyte e^- transfer); 3) As passivation layers to block scaffold surface states (inhibit dye-to-scaffold recombination); 4) As scaffold surface modifiers to improved dye loading¹⁰; 5) As protective coatings deposited over the dye to slow down dye desorption¹¹. For all these applications, the potential benefits gained from the thin film coating hinge on the ability to apply the coating conformally and uniformly throughout the nanostructured scaffold. Film thicknesses are often optimized for the specific application. For instance, a thin insulator prepared by ALD may block detrimental surface states on the scaffold while allowing forward electron transfer from dye to scaffold by tunneling. With too thick a film, however, one can impede forward electron transport. If the ALD film thickness is nonuniform, the portions of the scaffold that received a thicker coating may detract from overall device performance, while the particles with too thin a shell will not properly block back electron transfer. For these reasons, it is critical to understand mass transport and gas-solid interactions that take place during ALD processing.

With scaffold pore sizes on the order of ~ 10 nm, a $10\ \mu\text{m}$ thick scaffold would have a minimum aspect ratio of 1,000 (disregarding tortuosity). This figure is an order of magnitude higher than what is typically encountered in integrated circuit fabrication ($<100:1$ for 3D NAND). Consequently, ALD process development for electrochemical energy applications will require the determination of physical and chemical parameters that influence coating uniformity and infiltration in mesoporous structures. QCM is a well-established diagnostic technique for ALD. Before a set of measurements, a new QCM electrode is first covered with a thick layer of the ALD material of interest. This essentially eliminates phenomena

associated with film nucleation on the electrode material (typically gold). Mass changes are then recorded during steady-state deposition cycles. For two-dimensional substrates, gravimetric data give critical information on surface saturation with reactants during each exposure. When coated with a three-dimensional template, QCM can give additional pieces of information including gas diffusion time scales, surface coverage, and pore blockage. This technique may also be applicable to studies on fixed-bed powder coating processes.

5.3 Experimental

Atomic layer deposition of TiO₂ films was performed on two type of scaffolds: nanoTiO₂ and tin-doped indium oxide (nanoITO). 6µm thick nanoTiO₂ scaffolds were cast from a suspension of TiO₂ particles on QCM crystals (Inficon 6 MHz AT-cut quartz, 0.55” diameter, Au electrodes, not polished). Prior to TiO₂ deposition, each crystal was cleaned with high purity N₂ to remove dust or loose particles. TiO₂ paste (Ti-nanoxide H/SP, Solaronix) consisting of 20 nm (or 400 nm diameter) particles dispersed in terpineol was deposited onto the top electrode of the QCM crystal by doctor-blading. A 9/32” diameter hole punch (McMaster-Carr) was used on a single piece of 3M Scotch Magic tape™ to obtain the desired aperture for doctor-blading. The tape was removed and the crystal was placed in an ethanol saturated atmosphere for 15 seconds to promote leveling of the TiO₂ film. Following the leveling, the crystal was pre-baked on a preheated hotplate at 120°C for 10 minutes. Subsequently, the crystal was placed in an oven and heated to 500°C for 30 minutes with a ramp rate of 5°C/minute to evaporate the solvent and sinter the particles together. After cooling to room temperature, the crystal was cleaned with a N₂ stream to remove loose particulates that may have accrued from oven insulation. nanoTiO₂ scaffolds were used

exclusively for QCM studies due to compatibility with the QCM crystal and to eliminate any nucleation effects. For depth profiling experiments, nanoITO scaffolds were prepared on FTO slides by spin casting a colloidal suspension of ITO nanoparticles (10-20 nm, Licochem, Taiwan), followed by a multi-step sintering process (described elsewhere¹²). The ITO scaffolds were coated by ALD TiO₂ independently of the QCM crystals under identical deposition conditions.

Mass uptake measurements were first performed on planar Au electrodes. A specially modified QCM fixture (Inficon, Cool Drawer) was inserted into a custom-built viscous flow ALD reactor. Each QCM crystal was first coated with 500 cycles of TiO₂. Steady-state deposition measurements were recorded after a thermal equilibration period (4-10 hours) using an Inficon SQM-160 controller at a sampling rate of 10 Hz. The reactor was heated resistively to an internal temperature of 150°C. Purified N₂ was used as the carrier gas and vacuum was supplied by a rotary-vane pump (Alcatel Adixen 2016) filled with fluorocarbon oil. The reactor pressure was set to 0.6 Torr using a metering valve. Pressure measurements were recorded using a Convector gauge (Granville Phillips), which is not an absolute pressure gauge. For two-dimensional QCM studies, the QCM fixture was purged with a low flow rate of purified N₂ (~50 SCCM) in order to prevent deposition on the back of the crystal. For high surface area QCM measurements, the QCM fixture was not operated with a back purge, since the surface area of the mesoporous template is several orders of magnitude higher than the surface area on the back of the crystal.

Two Ti sources were used for TiO₂ deposition: Titanium tetrachloride (TiCl₄, Strem Chemicals) and titanium tetraisopropoxide (TTIP, Sigma Aldrich). TiCl₄ was dosed directly

from a 3-port ALD valve (Swagelok). TTIP delivery included a N₂ boost step, where the TTIP vessel was pressurized with N₂ prior to opening the delivery valve. The mixture of TTIP and N₂ was delivered to the reactor chamber as a ~2 Torr plug. The oxygen source in all cases was reagent grade H₂O (Ricca Chemical Company). All precursor delivery lines were resistively heated. Three types of gas pulsing sequences were investigated: 1) Conventional ALD pulsing (1s exposure, 60s inert purge); 2) Short hold steps (1s exposure, 60s hold, 60s inert purge); 3) Long hold and purge steps (1s exposure, 3600s hold, 3600s inert purge). Each new high surface area crystal was conditioned with 10 cycles of the relevant reaction chemistry. This was done to eliminate spurious gravimetric data due to physisorbed water trapped inside the scaffold. After the application of the conditioning cycles, 60 ALD cycles were applied onto each crystal, unless indicated otherwise. Since pore shrinkage and blockage were a concern, each set of data presented in this work were collected from a new QCM crystal. This ensured that the results we report here are not due to the history of the high surface area functionalized crystal.

To study TiO₂ film uniformity, an different scaffold material was chosen to facilitate secondary ion mass spectrometry (SIMS) depth profiling measurements. For this purpose, nanoITO films of similar thickness and particle diameter were prepared on FTO glass. Slides with similar geometric area to the QCM crystal were loaded into the ALD reactor and coated under the same conditions as the QCM measurements. The TiO₂-coated ITO scaffolds were subsequently analyzed in a time of flight SIMS instrument (TOF.SIMS5, ION TOF, Inc. Chestnut Ridge, NY). The scaffold was sputtered using a Bi liquid metal ion gun and the surface was analyzed using a Cs⁺ beam. Sputtering was stopped once the FTO/glass interface

was detected. Bare and coated scaffold surfaces were additionally imaged using an FEI Verios 460L scanning electron microscope (SEM). No conductive coatings were used for SEM imaging. Refractive index and deposition rates for TiO₂ films on Si surfaces were determined by spectroscopic ellipsometry (J.A. Woollam Company, alpha-SE). Thick TiO₂ films were prepared on Si by applying 500 ALD cycles. Film thickness and optical constants were determined by fitting the ellipsometric parameters to a Cauchy model.

5.4 Results and Discussion

To illustrate the potential challenges associated with applying thin film coatings over nanostructured templates, we first studied film uniformity by SIMS. In Figure 5.1 we show a depth profile from a 5 μm thick nanoITO film coated with 60 cycles of TiO₂ (TiCl₄/H₂O) at 150°C. This particular structure is composed of three interfaces: Air/ITO, ITO/FTO, and FTO/glass. The air interface contains adventitious carbon and potential contaminants, therefore signal collected during the first minute of sputtering should be disregarded. Based on the expected compositions of the layers, the ITO/FTO interface should be marked by an increase in Sn concentration, since Sn is only a dopant in ITO (Sn-doped In₂O₃), while Sn makes up the bulk of the FTO (In-doped SnO₂) layer. Finally, the FTO/glass interface can be identified by the onset of Si signal and a decrease in Sn concentration. Sputtering is an energetic process and will invariably cause a certain amount of interlayer mixing during depth profiling. Furthermore, matrix effects may result in different ion yields for different constituents of the sample under analysis. For these reasons not all secondary ion signals are well-aligned with respect to the precise depth of the material interfaces. However, the trends in ion counts vs sputter time are qualitatively meaningful. For the data shown in Figure 5.1,

we conclude that TiO^- ($m/z = 63.944$) ion counts are representative of the TiO_2 coating applied by ALD (uncoated scaffolds register less than 10 TiO^- counts). Therefore, we conclude that for the deposition conditions studied here, the ALD coating is reasonably uniform, all the way down to the bottom of the scaffold. However, the SIMS analysis does not give us an indication of the thickness of the film. In order to better assess the amount of deposition inside the template we take a ratio between TiO^- and a similar molecular species associated with the scaffold. This effectively normalizes the amount of TiO_2 deposited against the substrate and corrects for the shape of the scaffold signal.

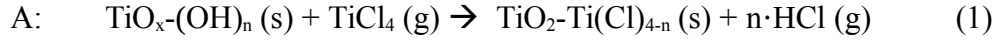
Depth profiles for two nanoITO scaffold thicknesses are shown in Figure 5.2. The horizontal axes for the two measurements are normalized based on the known thicknesses of the scaffolds and the interface locations determined from SnO^- and Si^- ion counts. Here the coating is 60 cycles of $\text{TiCl}_4/\text{H}_2\text{O}$ with 1s exposures and 60s purges (which is a typical ALD cycle used for flat substrates). The top panel (a) shows TiO^- distribution for a 5 μm thick scaffold. While the depth profile is fairly uniform near the surface, the $\text{TiO}^-/\text{SnO}^-$ ratio starts to decay halfway down the scaffold depth. The bottom panel (b) shows the same coating applied onto a 15 μm thick scaffold. For this substrate, coating uniformity is very poor, especially beyond 2.5 μm away from the surface. In fact, compared to the surface TiO_2 concentration, there is two orders of magnitude less TiO_2 10 μm into the scaffold. One might expect the first 5 μm of the depth profile for the thicker scaffold to match that of the thinner scaffold, but we observe that TiO_2 content decays earlier for the thick scaffold. After sputtering the top 2.5 μm of nanoITO, we see that there is about an order of magnitude less TiO_2 inside the thick scaffold compared to the thin scaffold. This behavior is likely related to

precursor (TiCl_4 or H_2O) or byproduct (HCl) transport into and out of the nanostructured template. In other words, reactive species trapped deep inside the structure may influence deposition closer to the surface. However, these types of conclusions are difficult to reach with post-deposition measurements alone.

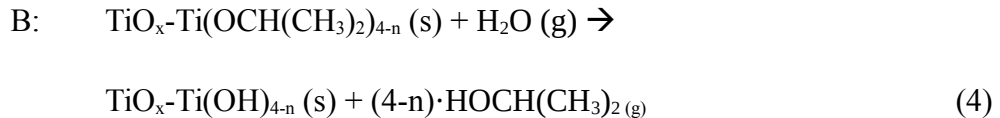
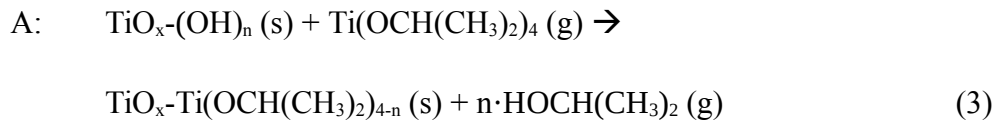
5.4.1 Mass uptake on planar TiO_2

We start our analysis by measuring mass changes during steady-state ALD reactions on planar QCM crystals. In Figure 5.3 (a) we show mass uptake for $\text{TiCl}_4/\text{H}_2\text{O}$ (blue) and $\text{TTIP}/\text{H}_2\text{O}$ (red) processes during 200 cycles of deposition at 150°C . Mass change is reported as ng/cm^2 , which is normalized against the projected surface area of the crystal, and not necessarily the true surface area, which will be affected by surface roughness. After about 100 cycles of incubation on the Au crystal (250 minutes), steady-state conditions are reached. The average mass uptake is $16.5 \text{ ng}/\text{cm}^2/\text{cycle}$ for $\text{TiCl}_4/\text{H}_2\text{O}$ and $11.9 \text{ ng}/\text{cm}^2/\text{cycle}$ for $\text{TTIP}/\text{H}_2\text{O}$. For the same processes, film refractive indices at 632 nm were measured as $n_{\text{TiCl}_4/\text{H}_2\text{O}}=2.367$ and $n_{\text{TTIP}/\text{H}_2\text{O}}=3.257$ by ellipsometry. By applying the Lorentz-Lorenz relation¹³, we can estimate the mass density ratio between the two films by using the measured refractive indices. Accordingly, the mass density of films deposited using TTIP is ~25% higher than those deposited from TiCl_4 . Deposition rates measured on planar Si surfaces were $0.43 \text{ \AA}/\text{cy}$ and $0.28 \text{ \AA}/\text{cy}$ for TiCl_4 and TTIP, respectively. Taking thickness and density measurements into account, we expect that the $\text{TiCl}_4/\text{H}_2\text{O}$ process will deposit ~20% more mass per cycle as compared to the $\text{TTIP}/\text{H}_2\text{O}$ process. This estimate is comparable to the QCM measurements, which indicate ~40% higher mass uptake during the $\text{TiCl}_4/\text{H}_2\text{O}$ process.

In Figure 5.3 (b) we enlarge the steady-state region of the QCM curve and show individual mass gain and loss steps associated with each ALD half-cycle. The expected ligand exchange reactions during each process are given below:



Reactions 1 and 2 show a simple ligand exchange reaction that takes place between: 1) Surface hydroxyls and TiCl_4 ; and 2) Surface chloride and H_2O . TiO_x represents the surface and the multiplier n ($=1, 2, \text{ or } 3$) indicates the number of surface $-\text{OH}$ groups that are involved in the TiCl_4 reaction (depending on mono-, bi-, or tridentate binding). Based on this model, each TiCl_4 exposure should remove $(\text{H})_n$ from the surface and add $\text{Ti(Cl)}_{(4-n)}$ in its place. Next, the H_2O exposure should remove $(\text{Cl})_{(4-n)}$ and add $(\text{OH})_{(4-n)}$ to the surface. A different quantity of hydrogen chloride is evolved during each exposure. A simple mass balance on the surface shows that 116.8 units of mass are added to the surface during the TiCl_4 half-cycle and 36.9 units are removed during the H_2O exposure. Therefore, we expect the $m_{\text{gain}}/m_{\text{loss}}$ ratio to equal 3.2 for this reaction with n set to 2. Depending on the number of $-\text{OH}$ groups on the surface, this ratio will vary from 2.8 to 4.4 for $n=1$ and $n=3$. A similar calculation can be carried out for the TTIP/ H_2O process:



Similar ligand exchange reactions take place during the TTIP and H₂O exposures, as shown in reaction 3 and 4. Here, mass gains and losses are 164.0 and 84.2 units of mass, respectively. For different values of n , the $m_{\text{gain}}/m_{\text{loss}}$ ratio is 1.8, 2.0, and 2.5 for $n=1,2,3$. We can measure $m_{\text{gain}}/m_{\text{loss}}$ from the gravimetric data shown in Figure 5.3 (b). For the TiCl₄/H₂O chemistry, this ratio ranges from 2 to 3, depending on which part of the curve is used to measure the mass change values. Mass change steps well-defined and repeatable for the TTIP/H₂O process. This produces a $m_{\text{gain}}/m_{\text{loss}}$ ratio of ~ 1.8 for this chemistry. Based on the QCM half-cycle measurements we estimate that TTIP only binds to the oxide substrate through a single –OH site. On the other hand, TiCl₄ interacts with 1-2 –OH sites. These observations will guide the discussion for QCM measurements on nanostructured substrates.

5.4.2 Mass uptake on mesoporous TiO₂

Based on a 100 m²/g specific surface area, mesoporous TiO₂-coated QCM crystals had approximately 10³ larger surface area than planar crystals. This results in large mass uptakes during ALD cycling, as shown in Figure 5.4 (a). While mass gains during TiO₂ deposition are on the order of tens of ng/cm²/cycle on planar crystals, mesoporous substrates result in micrograms (μg) of mass uptake per cm²/cycle. In panel (a) and (b), detailed mass change profiles are shown for TiCl₄ and TTIP, respectively. As TiCl₄ is pulsed into the reactor for 1 s, we observe a mass gain of ~ 2 μg followed by a slow mass decay during the 60 s purge step. The H₂O exposure produces an initial increase in mass, but results in the net loss of mass by the end of the purge step. The origin of the initial mass increase is not obvious and may be related to local cooling during the H₂O exposure, which would result in a mass increase (temperature and crystal frequency are inversely related). It is clear from each

exposure that mass removal from the scaffold is incomplete during the purge steps. Therefore, longer purge steps will be required to ensure that only self-limiting surface reactions, not gas phase reactions, take place inside the mesoporous template. QCM analysis makes it clear that diffusion time scales for excess reactant and reaction byproduct removal are significantly greater than 1 minute and that the $\text{TiCl}_4/\text{H}_2\text{O}$ ALD chemistry requires a different pulsing scheme. In panel (b), the corresponding measurement is shown for TTIP and H_2O exposures. Compared with the TiCl_4 precursor, TTIP exposures produce a larger mass increase ($\sim 5 \mu\text{g}$) and the purge step exhibits relatively rapid byproduct removal. The same is true during the H_2O exposure and purge. The overall TTIP/ H_2O reaction produces a $m_{\text{gain}}/m_{\text{loss}}$ ratio of ~ 1.9 , which is very similar to the exchange reactions we observed on the planar QCM crystal. These observations indicate that the high $m_{\text{gain}}/m_{\text{loss}}$ ratio of 4.1 noted for the $\text{TiCl}_4/\text{H}_2\text{O}$ process is specific to that chemistry and is not solely related to the physical properties of the template itself. The momentary mass increases shown with the H_2O exposures following a TiCl_4 purge are likely a result of gas-phase interactions between successive exposure steps (i.e. chemical vapor deposition). In other words, vapors (TiCl_4 and HCl) trapped inside the scaffold react with incoming reactants (H_2O) to form excess and uncontrolled deposits.

We further investigated reaction conditions by allowing the precursor to diffuse into the nanostructure for 60 seconds. To do this, we inserted a “hold step” into the ALD pulsing sequence, where immediately following a precursor pulse, we closed the process gas valve (inlet) and the pump valve (outlet). Any precursor that remained in the reactor at that time was held in place for 60 s. Following the hold step, we opened the pump valve and purged

the chamber with inert gas for 60 s. Figure 5.5 shows QCM data from this experiment. General trends over the course of 60 cycles are similar to those observed during short precursor exposures: TTIP/H₂O exhibits linear deposition rates, but TiCl₄/H₂O cycles produce decreasing mass gains per cycle. Mass gain and loss profiles shown in panels (a) for TiCl₄ and (b) for TTIP illustrate precursor saturation that was not noticeable with short exposures. Compared with shorter exposures, the hold step produces about 2x the mass gain during the TiCl₄ exposure. During TiCl₄ hold steps, a rapid mass increase is followed by a distinct mass loss. This behavior may be indicative of a slow secondary process that occurs as a result of interactions between the nanostructure and reactive byproducts (HCl). The water hold step produces a mass increase similar to that observed during short TiCl₄/H₂O exposures. This mass uptake saturates during the hold step. At the completion of the hold step, the purge step removes enough mass from the scaffold to cause a net mass loss during the H₂O half-cycle. We note that the mass increase and subsequent saturation during the H₂O hold step must not be due to water physisorption or trapping alone, since the TTIP/H₂O process does not exhibit the same level of difficulty in purging the H₂O half-cycle. Therefore, this effect must be related to the removal of the HCl byproduct. Data from the TTIP/H₂O process in panel (b) shows mass saturation during both TTIP and H₂O hold steps. While there is some mass loss at the end of the purge steps, byproduct purging is significantly faster than with the TiCl₄/H₂O chemistry. We also note that the $m_{\text{gain}}/m_{\text{loss}}$ ratio for TTIP/H₂O is only slightly higher with the hold step pulsing sequence. This ratio is higher with TiCl₄/H₂O, which highlights some of the challenges associated with promoting self-limiting chemistry inside mesostructured templates.

Crystals coated with the short and long exposure ALD processes were imaged in a high resolution SEM to elucidate the effects of the process on the surface. Since the surface of the mesostructure is the entry point for electrolyte in a DSSC-type electrochemical device, pore accessibility (and therefore coating uniformity) is of utmost importance. Figure 5.6 shows a series of micrographs for nanoTiO₂ functionalized QCM crystals before and after ALD coating. In (a) we show an as-prepared high surface area crystal. Individual particles and the interconnected conductive network are visible along with a distribution of pore sizes. The particles are in the range of 10 to 20 nm. Panels (b) and (c) show the same type of scaffold after 60 cycles of short (1 s) and hold step (60 s) exposures to TiCl₄/H₂O. In (b), most of the smaller pores appear to be closed and black areas that indicate a deep pore are significantly reduced. In (c), there appear to be more open pores, but the coating thickness is significantly larger. Panels (d) and (e) show scaffolds coated with 60 cycles of TTIP/H₂O with short and hold step exposures. The two images are very similar and show that the porosity of the scaffold is largely preserved. From ellipsometry measurements on planar substrate, we expect the coating (shell) thickness on the particles to be 1.65 nm thick, which should not cause an observable decrease in pore size. These images are largely in agreement with the QCM measurements.

To see the effect a significantly longer purge times, we conducted a further QCM experiment with 1 hour long hold and purge steps. The results from this measurement are shown in Figure 5.7. The mass loss phenomena observed during the short hold steps are fully observable with 1 hr long holds. For instance, we noted earlier that the initial mass uptake was followed by a slow mass loss during the hold step. When the hold steps are 60

min long, we can see that the mass loss is in fact part of a slow process that plateaus after 20 minutes. Mass gain during the 60 min TiCl_4 exposure is $1.3 \mu\text{m}$, as compared with 2.1 and $3.8 \mu\text{g}/\text{cm}^2$ with 1 s and 60 s exposures. An etching mechanism as a result of extended HCl exposure might explain this result. We observe that the 60 min purge following the hold step does not reach completion. This shows that purge times may need to be an order of magnitude longer for this process. Similarly long diffusion times for trimethyl aluminum were suggested for fixed-bed particle coating reactors¹⁴. Looking at the second half-cycle, the H_2O hold step reaches saturation after about 50 minutes, however, the need for longer purge time is evident. We also note that, under the given conditions, the H_2O half-cycle no longer leads to a net mass loss. With longer purge times, a small mass loss may be observed.

The TTIP/ H_2O process shows similarly complex trends in Figure 5.7 (b). During the TTIP hold the mass uptake curve takes on a bimodal shape, but reaches saturation after 50 minutes. After the exposure step, we also see evidence that complete gas removal (isopropanol and excess TTIP) from the scaffold will require longer purge times. Independent QCM measurements conducted with a non-reactive vapor (isopropanol or IPA) indicate that desorption times are on the order of 20 hours. The same purge effect is observed after the H_2O exposure. The desorption curves after each half-cycle show approximately the same decay constant. Since IPA is evolved during each reaction step, the desorption curves may be explained by a slow IPA removal process. Comparing mass uptake to previous experiments, we note that 60 minute exposures produce $\sim 10 \mu\text{g}$ of mass gain during the TTIP exposure and $\sim 2.5 \mu\text{g}$ of mass loss during the H_2O step. Assuming a 10^3 surface area enhancement for the mesoporous scaffold, we expect mass gain on the high surface area crystal to be 10^3 times

greater than on the planar crystals. Indeed, a net mass gain of 7.5 $\mu\text{g}/\text{cycle}$ closely approximates 12 $\mu\text{g}/\text{cycle}$, which is what we would expect based on the surface area enhancement alone.

5.4.3 Pore filling of mesoporous TiO_2 and ITO scaffolds

One would expect that after a critical number of pores have been closed off, parts of the mesoporous structure would become inaccessible to fluid transport. Pore blockage makes uniform deposition difficult and is undesirable for electrochemical applications that need to fully utilize the high surface areas offered by the scaffold. To investigate the onset of pore blocking during the ALD process we coated nano TiO_2 and nanoITO structures with several hundred cycles of TiO_2 ALD. Since the longer gas exposure steps would have produced extremely long deposition times, we chose to use 1 s exposures and 60 s purge times. Again, we compared TiCl_4 and TTIP as different Ti sources. In Figure 5.8 we show SIMS depth profiles from (a) 60 cycles of $\text{TiCl}_4/\text{H}_2\text{O}$, (b) 200 cycles of $\text{TiCl}_4/\text{H}_2\text{O}$, and (c) 350 cycles of TTIP/ H_2O applied on an ITO scaffold of 5 μm thickness. The profile in (a) clearly illustrates that the TiO_2 film is thin and fairly non-uniform. However, the coating appears to reach the bottom of the scaffold. This is the same profile shown in Figure 5.2. When we apply more cycles, however, the non-uniformity of the coating becomes increasingly apparent. In Figure 5.8 (b), we see that after 200 $\text{TiCl}_4/\text{H}_2\text{O}$ cycles coating infiltration is limited to the top 60% of the scaffold. In principle this shows that higher deposition rates near the surface of the scaffold impede gas transport and deposition away from the surface. As predicted by the high surface area QCM measurements in Figure 5.4, the TTIP/ H_2O process deposits TiO_2 more uniformly. The depth profile in Figure 5.8 (c) shows that even after 350 cycles of TTIP/ H_2O ,

coating uniformity is fairly high all the way down to the bottom of the scaffold. Furthermore, there is no evidence of significant pore blockage, as seen with the $\text{TiCl}_4/\text{H}_2\text{O}$ process.

Accompanying QCM measurements with 200 and 350 cycles of $\text{TiCl}_4/\text{H}_2\text{O}$ and TTIP/ H_2O applied on mesoporous TiO_2 are shown in Figure 5.9. In panel (a) the mass uptake curve shown in gray has been magnified by 5x for clarity. With the $\text{TiCl}_4/\text{H}_2\text{O}$ process, we observe a clear inflection point after ~ 90 cycles. After this point, mass uptake per cycle decreases significantly, which indicates that some fraction of the pores become inaccessible to precursor vapors. An equivalent coating thickness calculated from planar growth rates does not account for such early pore blockage. We therefore conclude that non self-limiting behavior and gas-phase reactions are likely responsible for excess deposition near the surface, which in turn blocks access to the lower parts of the scaffold. The starting and ending mass uptake values measured during this process are indicated on the curve. By the end of the 200 cycles, mass gain per cycle approaches that of the planar QCM measurement (81 vs 17 $\text{ng}/\text{cm}^2/\text{cy}$). In panel (b) we show a similar measurement for the TTIP/ H_2O chemistry. Here, the deposition rate is highly linear until about 300 cycles, after which we observe a slow decrease in mass gain per cycle. At 300 cycles, we would expect an equivalent film thickness of 8.25 nm, which would shrink pores by 16.5 nm. From the micrographs shown in Figure 5.6, it is reasonable to conclude that 300 cycles of TTIP/ H_2O should result in pore clogging.

5.5 Summary and Conclusions

We have demonstrated a new method by which the QCM technique can be extended to study vapor deposition processes inside three-dimensional nanostructured substrates. QCM

crystals functionalized with mesoporous metal oxide structures can be used to assess critical deposition parameters such as deposition uniformity, pore shrinkage, long time scale transport phenomena, and side reactions. We have applied the technique to study two different ALD chemistries to identify a favorable process for electrochemical energy applications, including dye-sensitized solar cells. With the aid of *ex situ* SIMS and SEM measurements, we have correlated film uniformity and pore blockage to gravimetric data gathered from *in situ* QCM. We show that the metal halide Ti source for ALD shows exhibits several challenges in coating high surface area porous substrates. With short exposure and purge times, as would be found with a conventional ALD process, the $\text{TiCl}_4/\text{H}_2\text{O}$ chemistry produces highly non-uniform coatings that quickly block the surface of the mesoporous scaffolds. When processed with extended exposures (gas hold steps), the existence of secondary gas-phase reactions become evident, which is caused by reactions between successive precursor pulses and acidic reaction byproducts trapped within the scaffold. TiO_2 deposition from the organometallic Ti source TTIP, on the other hand, produces high uniform films as a function of scaffold depth. The process can be cycled up to 300 times until we observe pore blockage under our experimental conditions. Hour long exposure times with the TiCl_4 process result in a sharp decrease in mass uptake, as suggested by earlier modeling studies¹⁵. Mass uptake for the TTIP process, however, increases significantly with long exposure times. This indicates that completely conformal and self-limiting deposition inside nanostructured materials may require prohibitively long deposition times. With either ALD chemistry, longer exposure and purge times make it evident that byproduct removal is extremely time intensive, on the order of tens of hours. There are clear parallels between this

work and fixed-bed reactors used for loose particle coatings. We expect that the technique outlined in this work will be generally applicable to particle ALD studies as well as other high surface area substrates such as carbon scaffolds, aerogels, and porous low- κ dielectric films.

5.6 Acknowledgements

The authors acknowledge the use of the Analytical Instrumentation Facility (AIF) at North Carolina State University, which is supported by the State of North Carolina and the National Science Foundation.

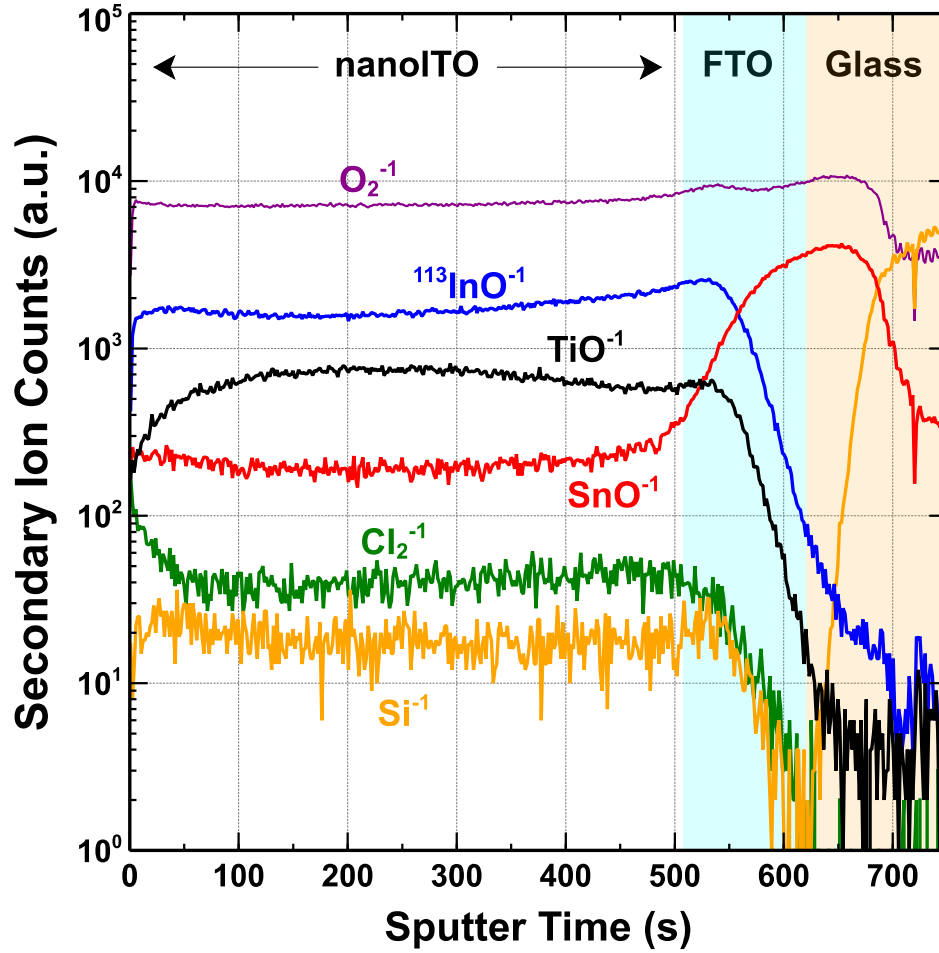


Figure 5.1. SIMS depth profile from a 5 μm thick nanoITO scaffold coated with 60 cycles of $\text{TiCl}_4/\text{H}_2\text{O}$ at 150°C . The location of the ITO/FTO and FTO/glass interfaces are deduced from changes in the SnO^- and Si^- secondary ion counts.

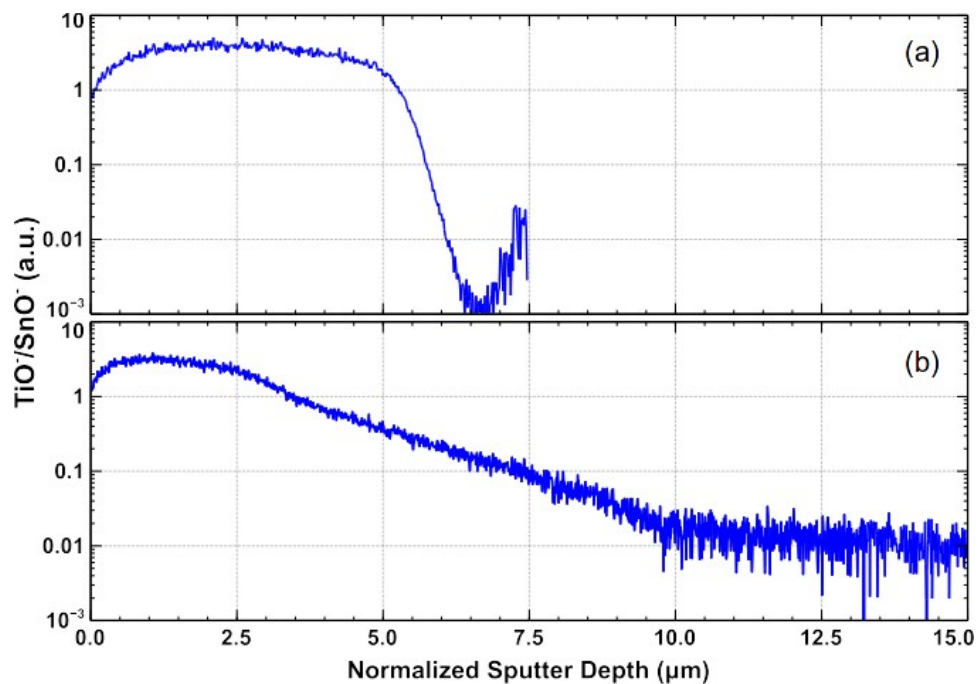


Figure 5.2. SIMS depth profile showing $\text{TiO}^-/\text{SnO}^-$ secondary ion ratio as an indicator of coating uniformity. Two scaffold depths are shown: (a) $5\ \mu\text{m}$ and (b) $15\ \mu\text{m}$ of nanoITO. Both scaffolds have 60 cycles of $\text{TiCl}_4/\text{H}_2\text{O}$ applied at 150°C , with 1s exposures and 60s purges. Sputter time has been normalized to nominal nanoITO film thickness.

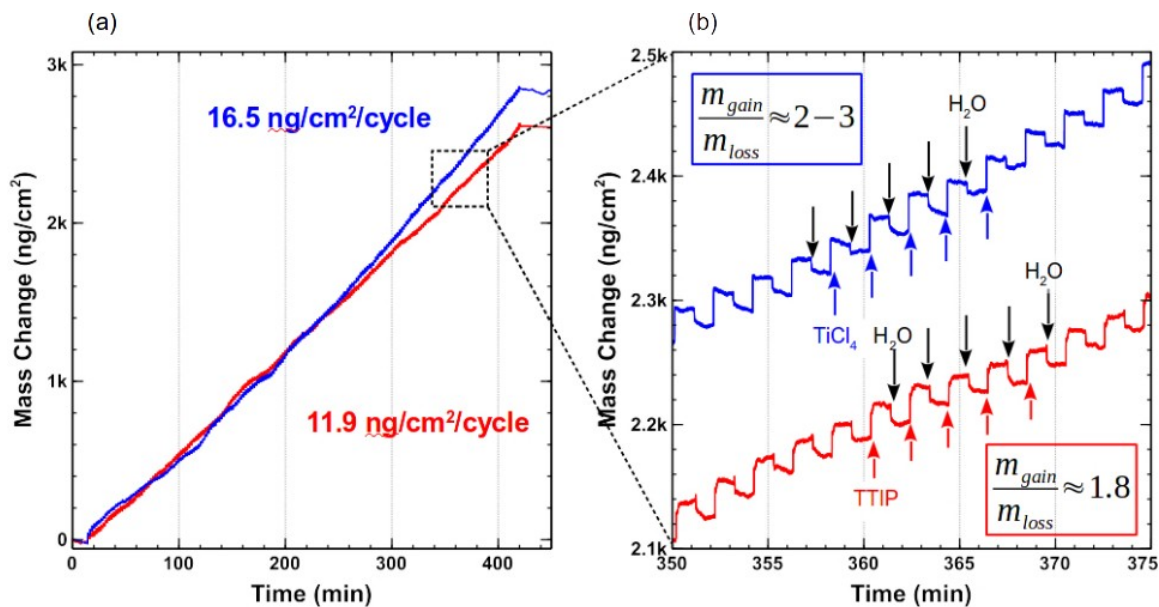


Figure 5.3. Mass uptake measurements from a planar QCM crystal. Panel (a) shows linear mass increase during 200 cycles of deposition on the crystal. The blue curve denotes the TiCl₄/H₂O process and the red curve denotes the TTIP/H₂O process. A magnified section of panel (a) is shown in panel (b). Individual mass gain and loss values from TiCl₄, TTIP, and H₂O exposures are given as mass gain:loss ratios. Arrows indicate the beginning of exposure and purge steps.

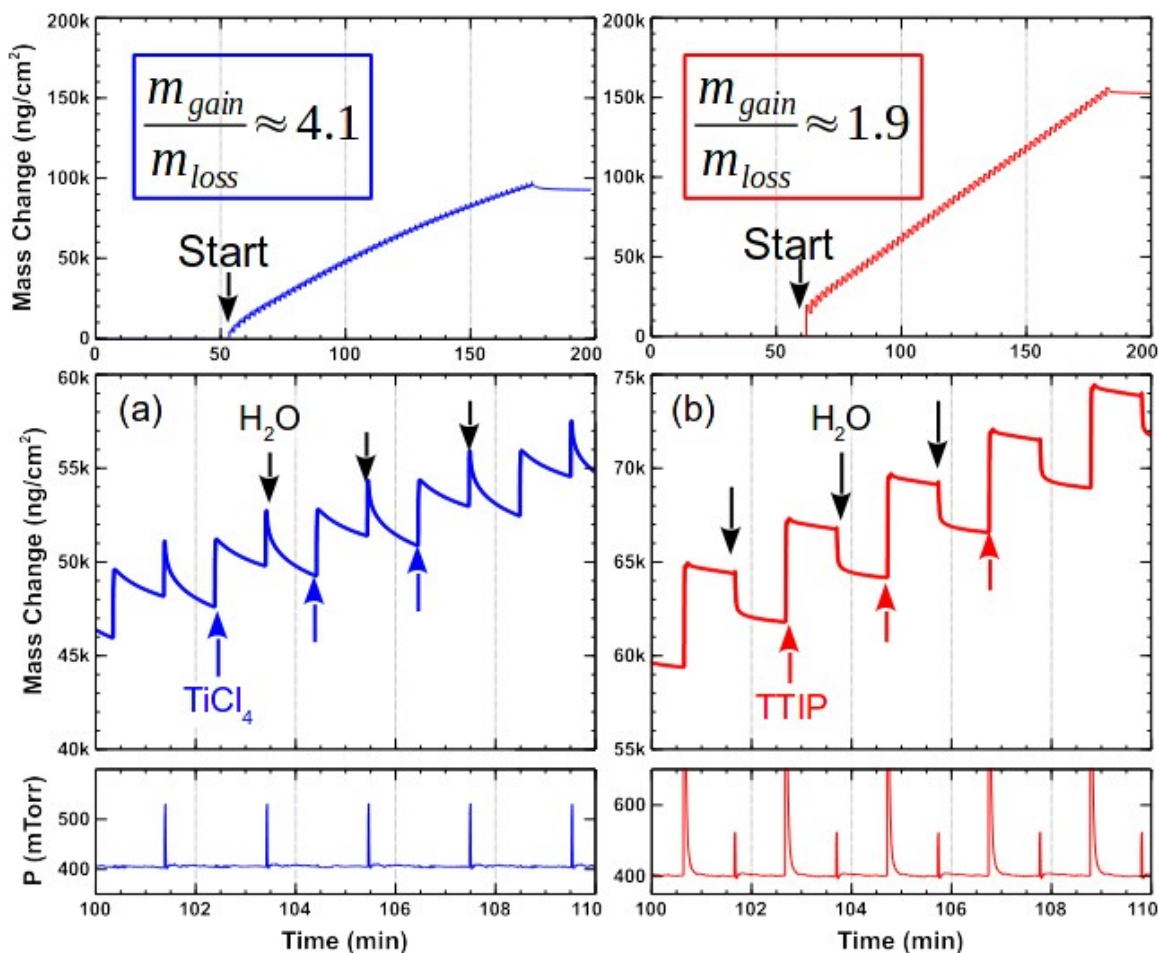


Figure 5.4. Mass uptake measurements from a high surface area QCM crystal (nanoTiO₂). Panel (a) shows mass uptake during 5 cycles of the TiCl₄/H₂O ALD process. Panel (b) shows the same measurement for the TTIP/H₂O chemistry. For both chemistries, exposure and purge times are 1s and 60s, respectively. Above each main panel are the mass gain trends for the entire process (60 ALD cycles). Individual mass gain and loss values from TiCl₄, TTIP, and H₂O exposures are given as a gain/loss ratio. Below each panel are the corresponding pressure pulses recorded during each measurement.

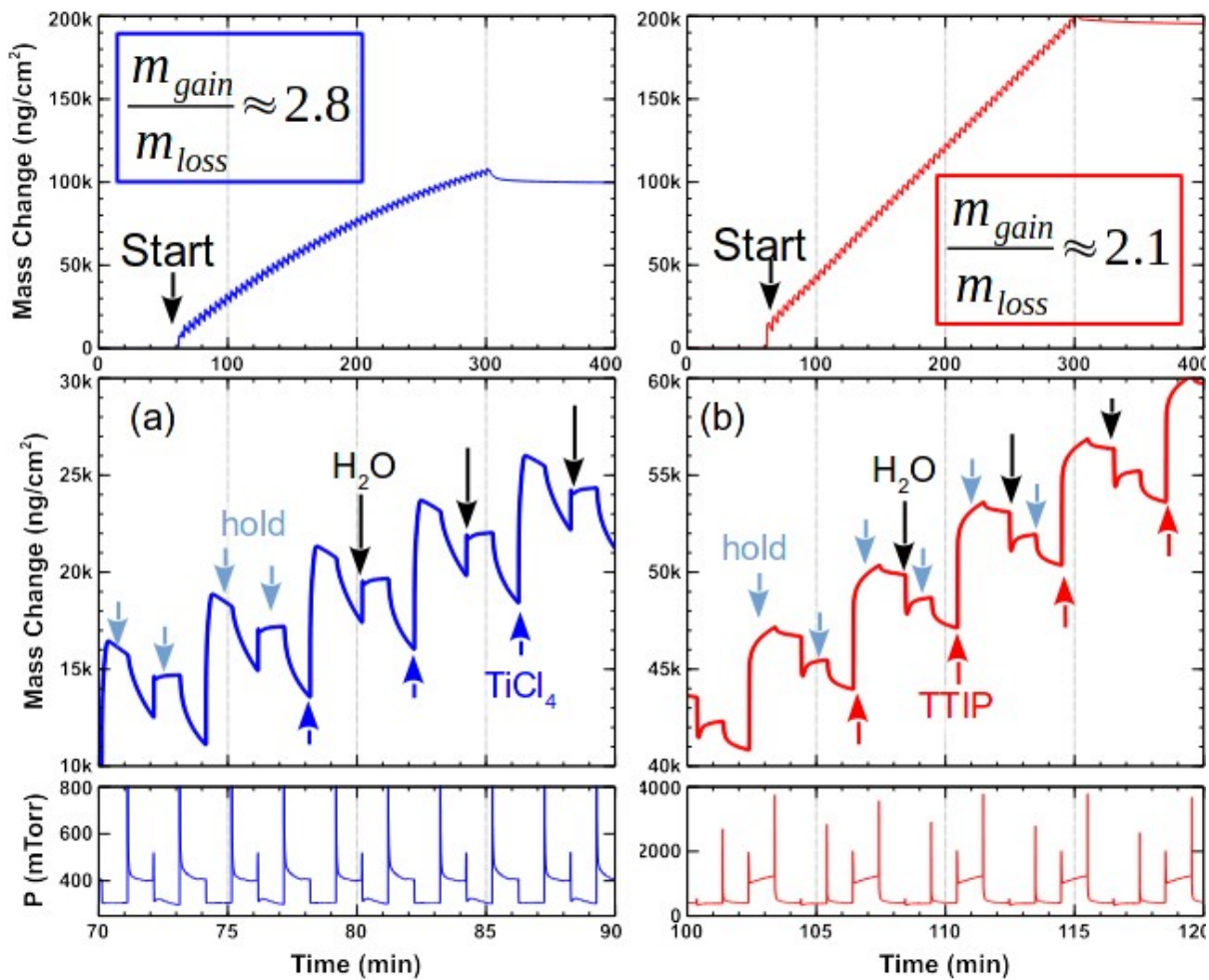


Figure 5.5. Mass uptake measurements showing the effect of 60 s gas hold steps inserted into the ALD sequence. Exposure and purge times are the same as in Figure 4.

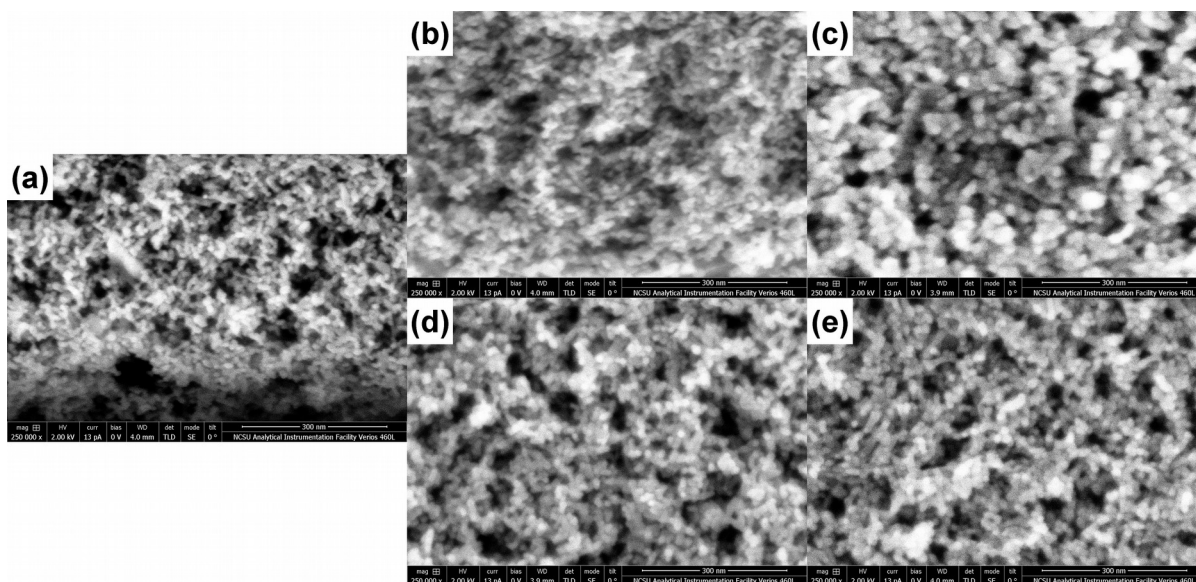


Figure 5.6. Plan-view SEM images of nanoTiO₂ scaffolds with: (a) no coating; (b) TiCl₄/H₂O 1 s exposures; (c) TiCl₄/H₂O, 60 s exposures; (d) TTIP/H₂O 1 s exposures; and (e) TTIP/H₂O 60 s exposures. All coatings were applied at 150°C. Scale bars are 300 nm and the images were collected under the same conditions without sputtering of conductive films.

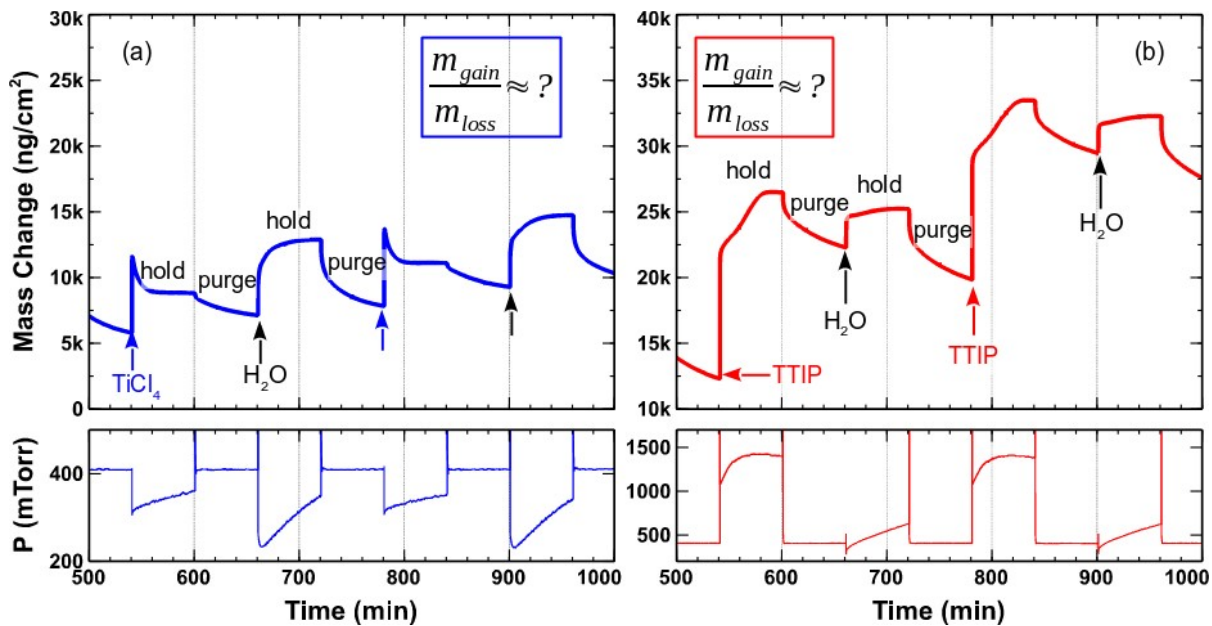


Figure 5.7. Mass uptake measurements on nanoTiO₂ showing the effect of extended hold and purge steps. Exposure, hold, and purge times are 1 s, 60 min, and 60 min. Only 5 cycles were recorded. The process conditions are the same as in Figure 4.

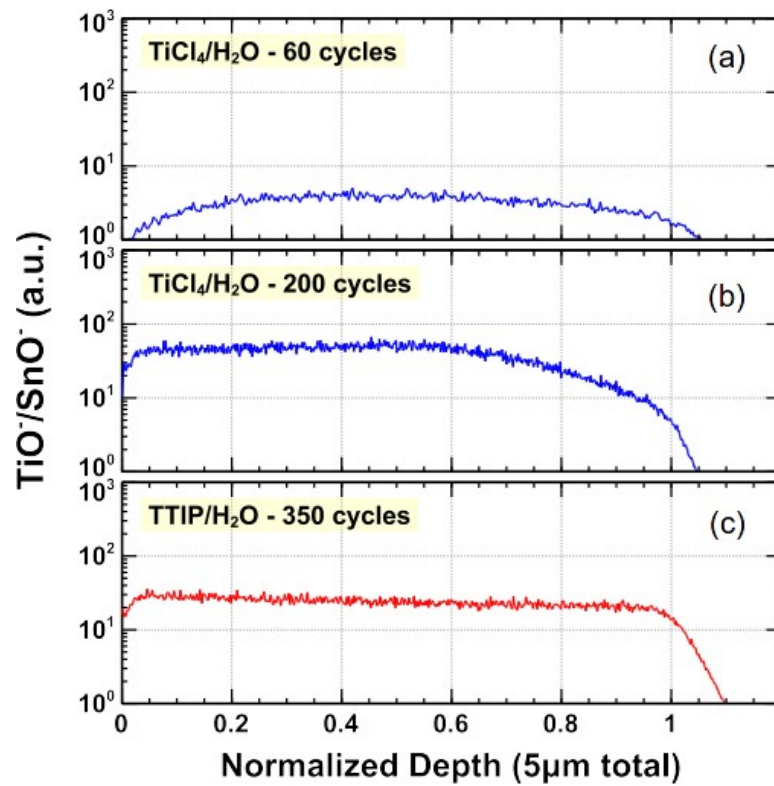


Figure 5.8. SIMS depth profiles from a $5\ \mu\text{m}$ thick nanoITO scaffold coated with (a) 60 cycles of $\text{TiCl}_4/\text{H}_2\text{O}$, (b) 200 cycles of $\text{TiCl}_4/\text{H}_2\text{O}$, and (c) 350 cycles of $\text{TTIP}/\text{H}_2\text{O}$ at 150°C .

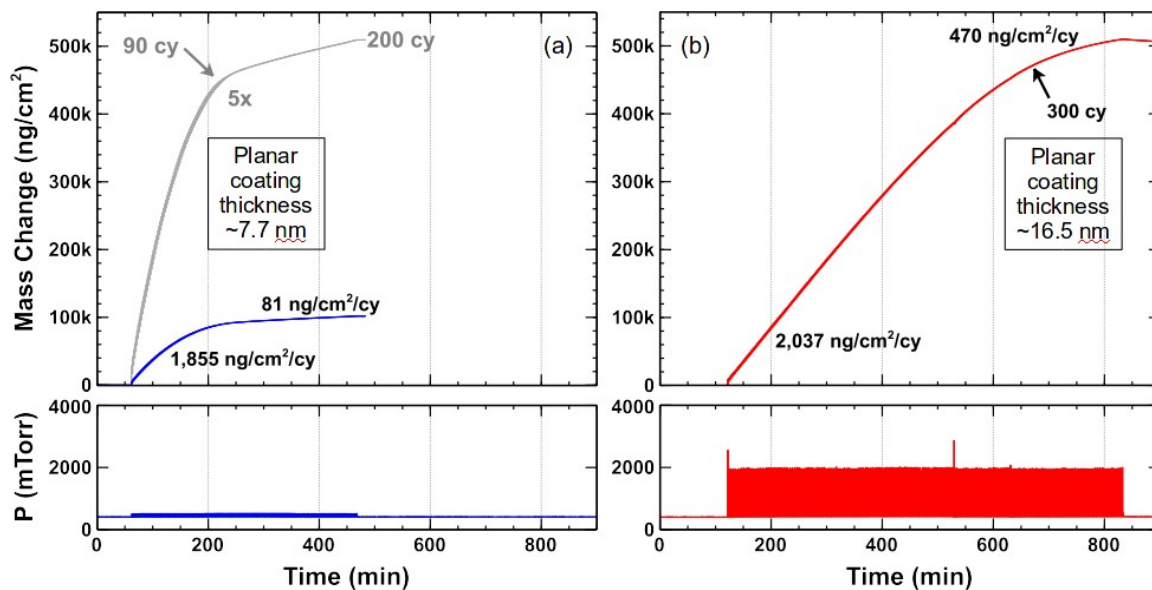


Figure 5.9. Microbalance data from nanoTiO₂ coated crystals showing changes in mass uptake per cycle after a large number of ALD cycles. Panel (a) shows 200 cycles of TiCl₄/H₂O and panel (b) shows data recorded during 350 cycles of TTIP/H₂O. The gray curve in (a) has been magnified by 5x for clarity.

5.7 References

- (1) Kim, H.; Ko, K.; Kang, H. High Performance Core-Shell Nanowire Array Devices Prepared by Atomic Layer Deposition. *ECS Trans.* **2013**, *50*, 127–133.
- (2) Weng, B.; Xu, F.; Xu, J. Core-Shell Photoanode Developed by Atomic Layer Deposition of Bi₂O₃ on Si Nanowires for Enhanced Photoelectrochemical Water Splitting. *Nanotechnology* **2014**, *25*, 455402.
- (3) Standridge, S. D.; Schatz, G. C.; Hupp, J. T. Toward Plasmonic Solar Cells: Protection of Silver Nanoparticles via Atomic Layer Deposition of TiO₂. *Langmuir* **2009**, *25*, 2596–2600.
- (4) Lu, J.; Low, K.-B.; Lei, Y.; Libera, J. A.; Nicholls, A.; Stair, P. C.; Elam, J. W. Toward Atomically-Precise Synthesis of Supported Bimetallic Nanoparticles Using Atomic Layer Deposition. *Nat. Commun.* **2014**, *5*.
- (5) Rauda, I. E.; Augustyn, V.; Saldarriaga-Lopez, L. C.; Chen, X.; Schelhas, L. T.; Rubloff, G. W.; Dunn, B.; Tolbert, S. H. Nanostructured Pseudocapacitors Based on Atomic Layer Deposition of V₂O₅ onto Conductive Nanocrystal-Based Mesoporous ITO Scaffolds. *Adv. Funct. Mater.* **2014**, *24*, 6717–6728.
- (6) Law, M.; Greene, L. E.; Radenovic, A.; Kuykendall, T.; Liphardt, J.; Yang, P. ZnO–Al₂O₃ and ZnO–TiO₂ Core–Shell Nanowire Dye-Sensitized Solar Cells. *J. Phys. Chem. B* **2006**, *110*, 22652–22663.
- (7) Ganapathy, V.; Karunakaran, B.; Rhee, S.-W. Improved Performance of Dye-Sensitized Solar Cells with TiO₂/alumina Core–shell Formation Using Atomic Layer Deposition. *J. Power Sources* **2010**, *195*, 5138–5143.
- (8) Park, K.; Zhang, Q.; Garcia, B. B.; Zhou, X.; Jeong, Y.-H.; Cao, G. Effect of an Ultrathin TiO₂ Layer Coated on Submicrometer-Sized ZnO Nanocrystallite Aggregates by Atomic Layer Deposition on the Performance of Dye-Sensitized Solar Cells. *Adv. Mater.* **2010**, *22*, 2329–2332.
- (9) Alibabaei, L.; Farnum, B. H.; Kalanyan, B.; Brennaman, M. K.; Losego, M. D.; Parsons, G. N.; Meyer, T. J. Atomic Layer Deposition of TiO₂ on Mesoporous nanoITO: Conductive Core–Shell Photoanodes for Dye-Sensitized Solar Cells. *Nano Lett.* **2014**, *14*, 3255–3261.
- (10) Ganapathy, V.; Karunakaran, B.; Rhee, S.-W. Improved Performance of Dye-Sensitized Solar Cells with TiO₂/alumina Core–shell Formation Using Atomic Layer Deposition. *J. Power Sources* **2010**, *195*, 5138–5143.

- (11) Hanson, K.; Losego, M. D.; Kalanyan, B.; Ashford, D. L.; Parsons, G. N.; Meyer, T. J. Stabilization of [Ru(bpy)₂(4,4'-(PO₃H₂)bpy)]²⁺ on Mesoporous TiO₂ with Atomic Layer Deposition of Al₂O₃. *Chem. Mater.* **2013**, *25*, 3–5.
- (12) Hoertz, P. G.; Chen, Z.; Kent, C. A.; Meyer, T. J. Application of High Surface Area Tin-Doped Indium Oxide Nanoparticle Films as Transparent Conducting Electrodes. *Inorg. Chem.* **2010**, *49*, 8179–8181.
- (13) Harris, M.; Macleod, H. A.; Ogura, S.; Pelletier, E.; Vidal, B. The Relationship between Optical Inhomogeneity and Film Structure. *Thin Solid Films* **1979**, *57*, 173–178.
- (14) Longrie, D.; Deduytsche, D.; Detavernier, C. Reactor Concepts for Atomic Layer Deposition on Agitated Particles: A Review. *J. Vac. Sci. Technol. A* **2014**, *32*, 010802.
- (15) Siimon, H.; Aarik, J. Thickness Profiles of Thin Films Caused by Secondary Reactions in Flow-Type Atomic Layer Deposition Reactors. *J. Phys. Appl. Phys.* **1997**, *30*, 1725.

CHAPTER 6. Tungsten atomic layer deposition using WF_6 and a silyl pyrazine reducing agent

Berc Kalanyan^{1*}, Philip S. Williams¹, and Gregory N. Parsons¹

¹*North Carolina State University, Department of Chemical and Biomolecular Engineering, Raleigh, North Carolina, 27695*

This chapter is a manuscript in preparation.

6.1 Abstract

Tungsten thin film deposition is an industrially significant process for metallization applications in integrated circuits manufacturing. Existing vapor deposition processes utilize silane and borane based reducing agents to deposit W from the WF_6 precursor. We have studied a new reducing agent 1,4-dihydro-1,4-bis[tris(1-methylethyl)silyl]-pyrazine (DHP) for the tungsten atomic layer deposition (ALD) process. *In situ* mass spectrometry and *ex situ* surface analyses suggest that a surface reaction between WF_6 -exposed surfaces and DHP does take place, but this reaction is temperature sensitive and may exhibit slow kinetics. Deposition in the form of nanoparticles was observed on Si and SiO_2 surfaces, with larger particles present on the oxide surface. A significant quantity of organic species were detected by photoelectron spectroscopy on both Si and SiO_2 wafers. Thin films produced with DHP/ WF_6 largely consisted of WO_x , which is likely due to the incomplete reduction of fluorinated surfaces and their subsequent oxidation in air.

6.2 Introduction

Conformal tungsten deposition is an important process for back end of line integration, especially with new device geometries requiring smaller contact holes and

thinner vias. Tungsten chemical vapor deposition (CVD) has been widely used for plug and via fill. Emerging 3D logic and memory devices, however, require high aspect ratio metal interconnects at the local and intermediate levels. Metals formed by atomic layer deposition (ALD) may meet these higher conformality requirements better than existing CVD technologies. Up until now, a small selection of reducing agents have been used for tungsten deposition by ALD, namely monosilane^{1,2} (SiH₄) and disilane^{3,4} (Si₂H₆). While boranes⁵⁻⁷ have been studied as reducing agents for WF₆, boron contamination of films is a concern for device reliability due to the large neutron cross section of ¹⁰B.⁸ Furthermore, diborane presents toxicity hazards not associated with silane for gas processing and abatement. Consequently, alternative reducing agents for WF₆ and other metal halides are of interest for interconnect applications. In addition to thin film growth properties, new reducing agents that show area selectivity will be potentially appealing for chemically aligned patterning applications.

Recent reports suggest that classes of organosilicon compounds may be used for metal halide reduction for cyclical ALD-type reactions⁹. Preliminary results on elemental Ti and Zn deposition have been demonstrated using disilyl pyrazines, but film purity, deposition conditions, and whether the deposition process is self-limiting are unknown. 1,4-bis-(trimethylsilyl)-1,4-diaza-2,5-cyclohexadiene and methyl substituted derivatives have been previously synthesized for the salt-free reduction of chloride-containing and other early transition metal complexes^{10,11}. As powerful reducing agents, these compounds may enable the deposition of early transition metals by ALD and similar vapor phase deposition techniques. Empirically, WF₆ is readily reduced by Si surfaces and silane-based reducing

agents^{12,13}. Tungsten is considered to have a higher electrochemical reduction potential ($W^{6+} + e \rightarrow W^{5+}$, 0.26 V vs NHE)¹⁴ than most early transition metals, therefore, one might expect WF_6 to be easily reduced by disilyl pyrazine and derivatives. Here, we use 1,4-dihydro-1,4-bis[tris(1-methylethyl)silyl]-pyrazine (abbreviated as DHP) to deposit W on Si and SiO_2 surfaces from a WF_6 source.

6.3 Experimental

Deposition experiments were carried out in a custom-built atomic layer deposition reactor. The specifics of the reactor were discussed in detail elsewhere¹⁵. Reaction conditions studied were 120°C and 220°C. Purified Ar (99.999%, Machine & Welding Supply Company) was passed through a purifier (Entegris Gate-Keeper) and metered into the reactor at 300 SCCM. Precursors were delivered into the reactor in a direct-port configuration. The WF_6 source was not heated and the DHP vessel was heated to 120°C along with downstream delivery lines. At 120°C, DHP was in the liquid state and was vaporized for delivery. The following pulsing sequence was used for ALD recipes: DHP/Ar/ WF_6 /Ar for 0.5/45/1/60 s. Boron doped Si(100) 6-10 Ω -cm and Si(100) with 100 nm thermal SiO_2 (WRS Materials) wafers were cut into 12 x 12 mm chips. Wafer pieces were cleaned in hot piranha solution (1:1 $H_2SO_4:H_2O_2$ by volume) for 30 minutes, rinsed with deionized (DI) water, and stored in DI water. Immediately prior to vacuum deposition, Si and SiO_2 pieces were dipped in dilute hydrofluoric acid (10 vol%, Sigma-Aldrich) for 30 and 5 s, respectively. Following the etch, wafer pieces were rinsed under flowing DI water for 30 s and blown dry with 99.999% N_2 (100 psi).

Tungsten hexafluoride (WF₆) was used as received from the manufacturer. The reducing agent 1,4-bis-(trimethylsilyl)-1,4-diaza-2,5-cyclohexadiene (DHP) was synthesized using procedures described elsewhere^{11,16}. Briefly, pyrazine was reacted with a 3-fold excess of trimethylsilyl chloride (TMS-Cl) and lithium metal in THF at 0°C and allowed to warm to room temperature over 6 hours. Metal salts were filtered under inert atmosphere and excess solvent was evaporated under reduced pressure. The purified product was confirmed by ¹H and ¹³C NMR as a yellow crystalline solid. Typical reaction yield was ~50%.

In situ mass spectrometry measurements were conducted using an MKS Vision 2000C quadrupole mass spectrometer (QMS). This instrument had a triple-filtered quadrupole with a mass range of 1-300 amu. The ionization source was a thoriated iridium filament and the detector used for measurements was an electron multiplier with a gain of 100. Partial pressures were calibrated against a capacitance manometer with the electrode multiplier was references against the Faraday cup detector. Fast gas sampling was achieved by flowing all process exhaust gases past the mass spectrometer sampling orifice. The sampling lines had an inner diameter of 1" or greater in order to maintain good conductance to the pump. Precursor condensation was prevented by heating the sampling and exhaust lines to ~100°C and maintaining the mass spectrometer sampling volume at 85°C. Prior to analog scan measurements, reactor walls were coated with 200 cycles of Al₂O₃ using trimethyl aluminum and water. This was done to overcoat exposed surfaces with a halogen-free film and minimize halogen sources in piping and on reactor walls. Analog mass scans for DHP were conducted over the course of 2.5 minutes while delivering 0.1 s long DHP pulses every 0.9 seconds. Similarly, WF₆ was pulsed using 0.1 s long doses every 4.9 seconds.

Reagents were delivered in pulses in order to avoid depleting precursor vapor inside the source bottle. Cracking patterns from the NIST mass spectrometry database were used for QMS data interpretation.¹⁷

Surface analysis was done using a SPECS X-ray photoelectron spectroscopy (XPS) system with a PHOIBOS 150 analyzer. Spectra were generated using an Al K α X-ray source operated at 400 W. Data reduction and fitting was done using CasaXPS software with charge calibration based on the C 1s (C-C, C-H) peak set to 284.8 eV. Spectral identification was done using NIST X-ray Photoelectron Spectroscopy Database, Version 4.1.¹⁸ Tungsten nuclei on Si and SiO₂ surfaces were imaged using an FEI Verios 460L scanning electron microscope (SEM). Wafers were imaged without the application of additional conductive coatings. Stage biasing and immersion optics were used to image the surface with minimal surface charging. Furthermore, ultra-high resolution images were obtained after an *in situ* low-power oxygen plasma clean (5 min) prior to imaging.

6.4 Results and Discussion

Mass spectrometry was used to track DHP delivery into the reactor. Gas-phase species associated with DHP were deduced by pulsing DHP into the reaction chamber while recording mass spectra. Since the reactor was under low vacuum, O₂ and hydrocarbons were present in the chamber at <1 mTorr concentrations. By subtracting the reactant background from the scan obtained during DHP pulsing, major species associated with DHP were identified. An analog scan of this type is shown in Figure 6.1 with some peaks of interest identified at mass-to-charge ratios (m/z) = 27.7, 46.9, 49.1, 72.9, 76.6, and 146.5. The absence of strong peaks at m/z = 42, 71, and 72 indicate that THF has been removed during

DHP purification. The peak at 27.7 is best explained by the presence of N_2 in the DHP source vessel. The intensity of mass 27.7 is at a ratio of 3:1 with that of mass 13.9, which is close to the expected 5:1 ratio for molecular and atomic nitrogen. The peaks at $m/z = 46.9, 49.1, 62.8,$ and 76.6 strongly suggest the presence of trimethylsilyl fluoride (TMS-F), since they match the fragmentation pattern reported in the NIST database.¹⁷ We expect TMS-F and pyrazine to be the primary reaction product between DHP and fluorides (surface or vapor-phase) based on previously reported multielectron reduction reactions. Mashima *et al.* showed the reduction of WCl_6 with 1-methyl-3,6-bis(trimethylsilyl)-1,4-cyclohexadiene to produce two units of TMS-Cl for each unit of reducing agent.¹⁰ The observation of TMS-F implies the availability of chemisorbed halides in the reactor chamber, even though reactor walls were conditioned with 200 cycles of Al_2O_3 . In subsequent sections we use $m/z = 76.6$ to track the extent of fluorine stripping reactions. An additional volatile product is suggested by the species at $m/z = 72.9$ and 146.5. These species likely represent a fragment and the parent ion, however, a clear match for the species could not be determined based on tabulated spectrometry data. Likely candidates that explain the two peaks are $(CH_3)_3Si-Si(CH_3)_3$ and fragments of the parent DHP molecule (i.e. N,N-diethyl-1,1,1-trimethylsilylamine), but the relative intensities of the parent and the fragment are not consistent with either identification. On an empirical basis, however, we consistently observed the presence of the larger peak at $m/z = 146.5$ during DHP pulsing and we attribute it to DHP, rather than a reaction product. The expected signal for the parent DHP ion ($m/z = 226$) was not detected during analog scans. This may be due to the low concentration of the molecule at the reactor exhaust and the low ion transmission through the quadrupole filter for heavier species (>200 amu). We

also note that a peak attributed to pyrazine ($m/z = 80$) was detected following DHP exposures at low partial pressures. Fragments associated with pyrazine ($m/z = 26, 53$) were also observed at partial pressures commensurate with the parent ion. Interestingly, $m/z = 80$ persisted inside the quadrupole chamber and could not be removed after filament degassing and repeated bakeouts.

Reaction products generated during WF_6 exposures were also identified using *in situ* mass spectrometry. In Figure 6.2 (a) an analog scan during DHP exposure is shown without background subtraction. As discussed in the previous section, species associated with DHP and its reaction products (TMS-F) are observed in this scan. After a 5 minute Ar purge of the reaction chamber, WF_6 is introduced into the reaction chamber. The resulting analog scan is shown in panel (b). Methane, water, and hydrogen fluoride are initially observed at <10 mTorr partial pressures. Furthermore, TMS-F is detected at a 10 mTorr partial pressure, which indicates that, despite the Ar purge that preceded WF_6 exposure, DHP must have persisted within the vacuum system either in the reactor chamber or inside the QMS analysis chamber. We do not observe species associated with vapor-phase DHP ($m/z = 146.5$) during the WF_6 exposure, or prior to it. This supports the stipulation that TMS-F must be produced as a result of WF_6 -surface reactions, rather than in the vapor phase. A second WF_6 exposure, shown in panel (c), does not produce TMS-F in significant quantities (less than 1% of the intensity measured during the first exposure). We therefore conclude that the first WF_6 exposure was sufficient to consume most of the surface-bound DHP within the reactor. While WF_6 exposures may saturate exposed surfaces, repeated DHP exposures (up to 20 times) continued to produce TMS-F. It is likely that DHP mass transport into the reactor is

insufficient. Although there is some evidence that DHP may be “sticky”, additional experiments will be needed to determine whether adsorbed DHP is responsible for the generation of TMS-F during WF_6 pulsing. Although the DHP reaction was anticipated to produce a clean metal surface, it is possible that the DHP-surface interaction proceeds in a multi-step fashion and leaves byproducts on the surface. After stripping one fluorine from the surface, DHP could be bound to the surface and remain there until additional metal halide is delivered. This may explain the generation of TMS-F during both DHP and WF_6 exposures. The absence of significant pyrazine generation during DHP exposures suggests that a pyrazine may not be a primary reaction product.

With a preliminary identification of gas-phase species, we tracked the concentration of several species of interest during ALD cycling at 120 and 220°C. Partial pressure vs time trends are shown for DHP, WF_6 , TMS, TMS-F, and HF in Figure 6.3. The DHP source temperature and other reactor conditions were the same for low and high temperature depositions. The critical observations from the partial pressure trends is that a larger quantity of DHP exits the reactor at 220°C. At the same time, the concentration of TMS and TMS-F are significantly lower at the higher temperature. These two trends indicate that the DHP reaction proceeds more readily at 120°C, generating a higher concentration of byproduct and consuming more of the reducing agent. One should also note that TMS-F is only generated during DHP doses, but TMS is detected during both DHP and WF_6 exposures. We also observe that a comparatively small quantity of HF is produced during the WF_6 step.

To evaluate the films produced by the DHP reduction of WF_6 , we applied 50 cycles of DHP/ WF_6 to Si and SiO_2 surfaces. At these low cycle numbers, the DHP/ WF_6 process

produced a thin and lustrous film on Si and deposited a tan-gray metallic film on SiO₂. Both surfaces were analyzed using electron microscopy (SEM) and photoelectron spectroscopy (XPS). We used tungsten films produced using the SiH₄/WF₆ ALD process as a comparison. In Figure 6.4 we show plan-view SEM images from depositions carried out at 220°C. Si and SiO₂ surfaces with 50 cycles of DHP/WF₆ are shown in (a) and (b). These images were acquired without the application of conductive coatings, therefore any high-contrast features on the surface are representative of deposited material. The sparsely distributed white spots are tungsten (W) nuclei, with larger particles evident on the SiO₂ surface. It is well known that Si surfaces can directly reduce WF₆ to produce thick W films in CVD mode.¹⁹ The lack of a continuous W film on the Si surface suggests that DHP exposures are inhibiting the reduction of WF₆ by the Si. For comparison, a film produced from 10 cycles of SiH₄/WF₆ on a Si surface is shown in panel (c). Even though the film is not fully coalesced, W produced from just 10 cycles of SiH₄/WF₆ is visibly metallic and has a thickness of 5-10 nm. In contrast, 50 cycles of SiH₄/WF₆ on a SiO₂ produce a rough film with a thickness of ~15 nm. These observations suggest that the DHP-based process may exhibit long nucleation times on Si surfaces and deposition rate on SiO₂ appears to be low. Further saturation studies with DHP are required before further conclusions can be made.

Chemical analysis of the wafer surfaces with XPS show the presence of carbon, nitrogen, oxygen, fluorine, and tungsten. Figure 6.5 shows F 1s, N 1s, and C 1s core levels for Si and SiO₂ surfaces processed with 50 cycles of DHP/WF₆ at 120°C (lower frames) and 220°C (upper frames). All surfaces contained a broad feature at 401.8 eV, likely the result of two peaks where N could be bound to a fluorine or to carbon(s) in an amine, isocyanide, or

similar structure. Since DHP is the only nitrogen source in the reactor, this N-R feature indicates the presence of DHP or pyrazine fragments on all wafer surfaces. The C 1s levels show carbon in various oxidation states. The larger C-C (C-H) and C-O features at 284.8 and 286.3 eV are ascribed to adventitious carbon. The C-C peak was also used for charge correction. The intensity ratio of C-O to C-C is larger on surfaces prepared at 120°C. Adventitious carbon alone does not explain the higher C-O counts. The additional C-O likely originates from surface bound DHP or fragments that could not be fully removed at lower temperature. The low temperature depositions also produce a high binding energy shoulder at 287.8, attributed to a fluorocarbon (C-F). In terms of F, N, and C 1s levels, the Si and SiO₂ surfaces at low temperature are very similar.

Surfaces prepared at 220°C show several features not found on the low temperature substrates. The Si surface exhibits a low binding energy carbon feature at 283 eV, which we attribute to C-W. The high binding energy carbon at 288.5 eV is likely from a carbonate, a carboxylate, or an isocyanide. Another feature that is only found on the Si wafer is an N-W peak at 397.4 eV. The Si surface also exhibits a large fluorine peak at 685 eV, which is indicative of F-W binding. The F 1s region shows little to no F on the SiO₂ surface at 220°C. The likely explanation for this is that since crystalline Si can reduce WF₆, some amount of W was initially deposited on the Si surface during the first few WF₆ exposures. After several cycles, the Si sites were blocked by DHP, organic ligands, or “sticky” byproducts left on the surface as a result of DHP exposures. Regardless of the extent of DHP-surface reactions (or lack thereof), it is evident that significant quantities of F remained on the surface. We suspect

that under our experimental conditions, DHP was either unable to reduce WF_6 or the reduction suffered from very slow kinetics.

Photoelectron spectra from the W 4f region are shown for the same surfaces (Si and SiO_2) prepared at 120°C and 220°C in Figure 6.6. In general, we only observed metallic tungsten at 31.8 and 33.8 eV binding energies (W $4f_{7/2}$ and $4f_{5/2}$) on the Si substrate at 220°C . Si surfaces at 120°C and SiO_2 surfaces processed either temperature only exhibit metal oxide peaks (WO_x). The amount of oxide is greater on the low temperature surfaces, which suggests that DHP may have higher reactivity at lower temperatures. This is in agreement with the observation of greater TMS-F generation during low temperature processing. It is, however, not clear why so much oxide was formed on the surface, given the absence of oxygen sources in the ALD reactor. Wafers were removed from the reactor while hot and immediately cooled on a ceramic surface. We know from previous experiments that a self-limiting native oxide does form on W surfaces that have been exposure to room air. On W deposited from SiH_4/WF_6 , this amount of tungsten oxide is typically accompanied by a correspondingly large quantity of W^0 . Since atmospheric oxidation of W is the likely explanation for large amounts of WO_x , one must conclude that surfaces prepared with DHP/ WF_6 must contain a large quantity of unreacted fluorine. Upon removal from the vacuum chamber, WF_x -coated surfaces were quickly oxidized by air and the trapped F was liberated as HF. This may explain the large quantity of WO_x on wafer surfaces with little to no metallic W.

6.5 Summary and Conclusions

We have shown *in situ* mass spectrometry measurements and *ex situ* surface analyses of thin films prepared using WF_6 and a silyl pyrazine reducing agent (DHP). The measurement of reactants and volatile byproducts during the ALD process indicate that trimethylsilyl fluoride (TMS-F) is generated during DHP exposures, but pyrazine is only detected at quantities close to the detection limit of the spectrometer. More TMS-F is generated during low temperature (120°C) depositions and this observation is accompanied by lower fluorine content on surfaces, as confirmed by XPS. Surface analysis reveals a significant quantity organic species on wafer surfaces. Some of the species suspected to be present on the surface include isocyanide, hydrocarbons, fluorocarbons, and amines. Electron micrographs show thin nanoparticle films on Si and SiO_2 surfaces and exhibit good Z-contrast. Chemical analysis suggests that the particles are WO_x , rather than metallic tungsten, except for Si surfaces prepared at 220°C . However, we attribute the W^0 growth on the Si surface to the Si reduction of WF_6 , which is expected to occur to a greater extent at 220°C . While we show some evidence for DHP surface reactions, we were unable to show surface saturation or complete halogen stripping using the DHP reducing agent.

6.6 Acknowledgments

The authors acknowledge the use of the Analytical Instrumentation Facility (AIF) at North Carolina State University, which is supported by the State of North Carolina and the National Science Foundation. Funding for this project was provided by the Semiconductor Research Corporation (SRC task# 2401.001).

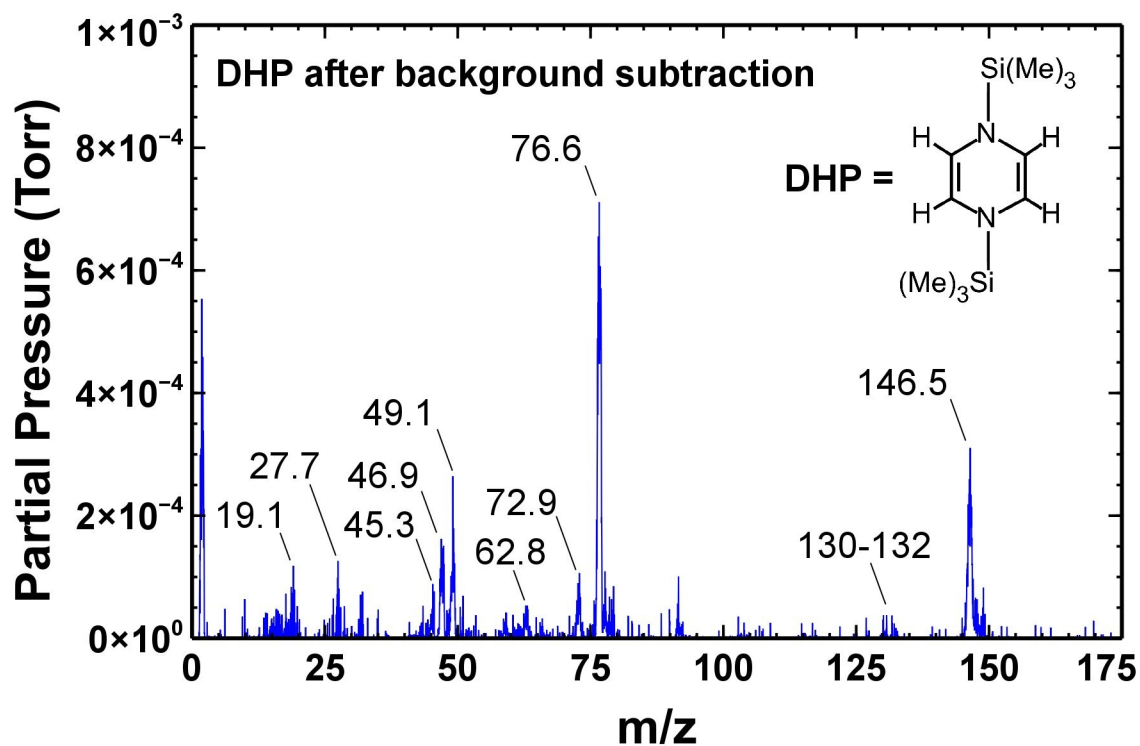


Figure 6.1. Analog scan recorded in a clean, Al₂O₃-coated, deposition chamber while DHP was introduced into the chamber in short (0.1 s) pulses. Background signal from the reactor chamber was subtracted out in order to show peaks associated with DHP.

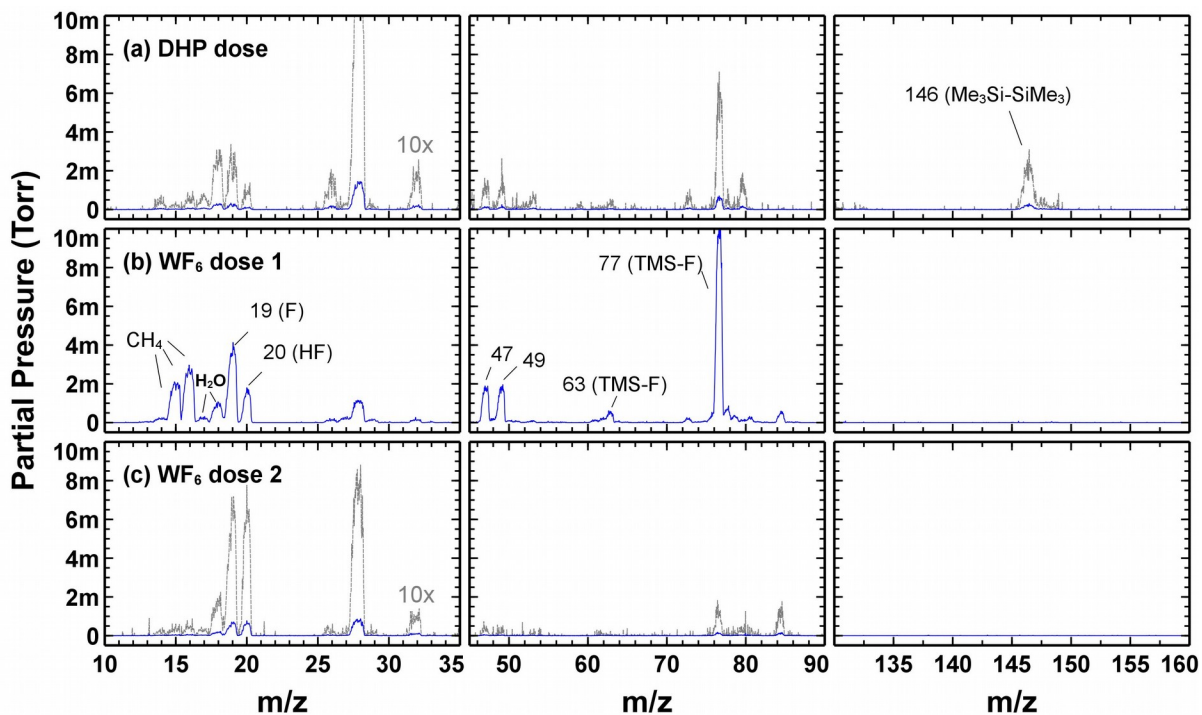


Figure 6.2. Analog scan recorded in sequence during DHP (top row) and WF_6 (middle and bottom rows) exposures. A second WF_6 exposure is shown to illustrate surface saturation. Some species of interest are labeled with their corresponding m/z value. Dashed (gray) lines have been magnified by a factor of 10 for clarity.

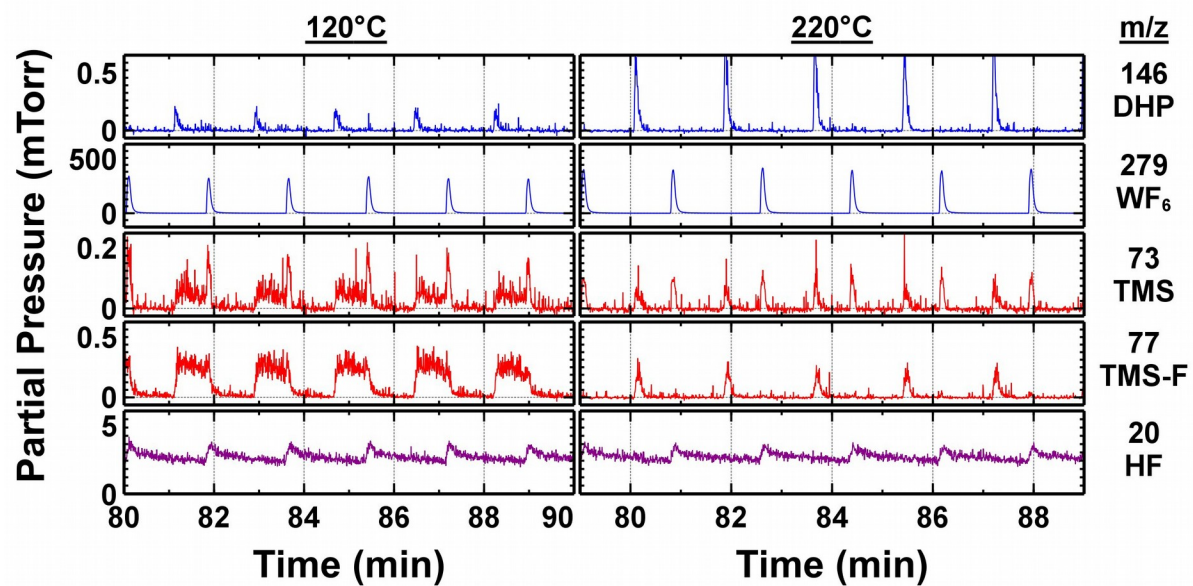


Figure 6.3. Selected reactant and product species tracked during 50 cycles of DHP/WF₆ at 120°C (bottom row) and 220°C (top row). Traces for m/z = 146, 279, 73, 77, and 20 are shown. The reactor chamber was empty during the measurements.

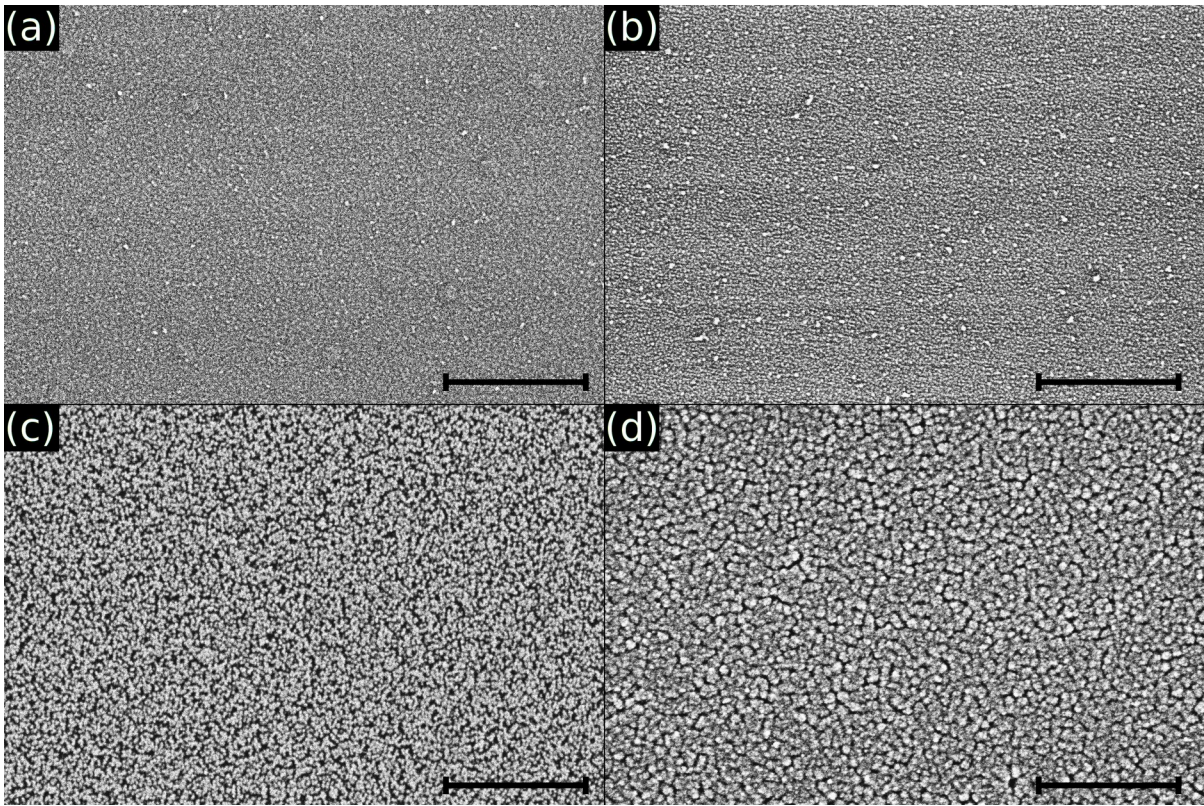


Figure 6.4. SEM images from depositions carried out at 220°C: (a) 50 cycles DHP/WF₆ on Si; (b) 50 cycles DHP/WF₆ on SiO₂; (c) 10 cycles SiH₄/WF₆ on Si; and (d) 50 cycles SiH₄/WF₆ on SiO₂. All scale bars represent 300 nm.

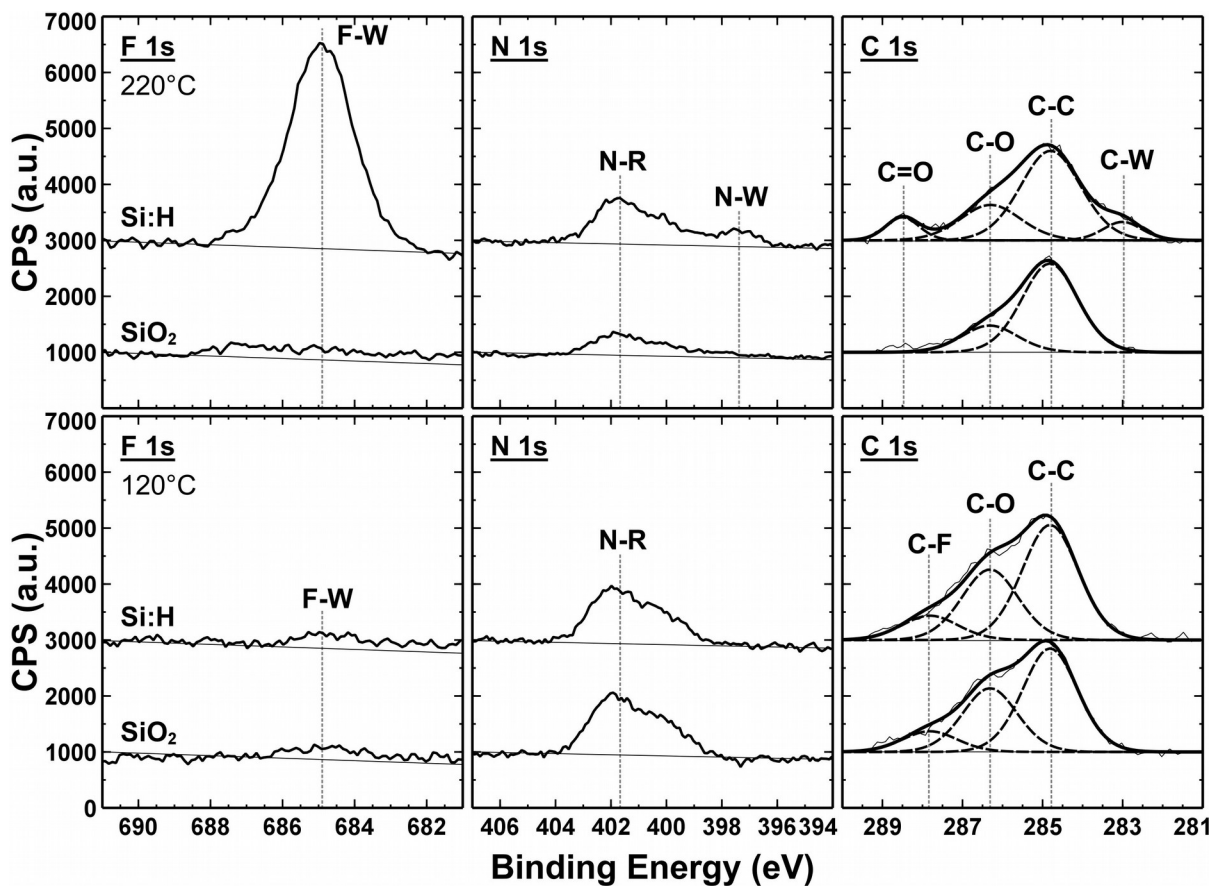


Figure 6.5. Photoelectron spectra from Si and SiO₂ surfaces processed with 50 cycles of DHP/WF₆ at 120°C (bottom row) and 220°C (top row). F 1s, N 1s, and C 1s regions are shown with some of the peaks identified with labels.

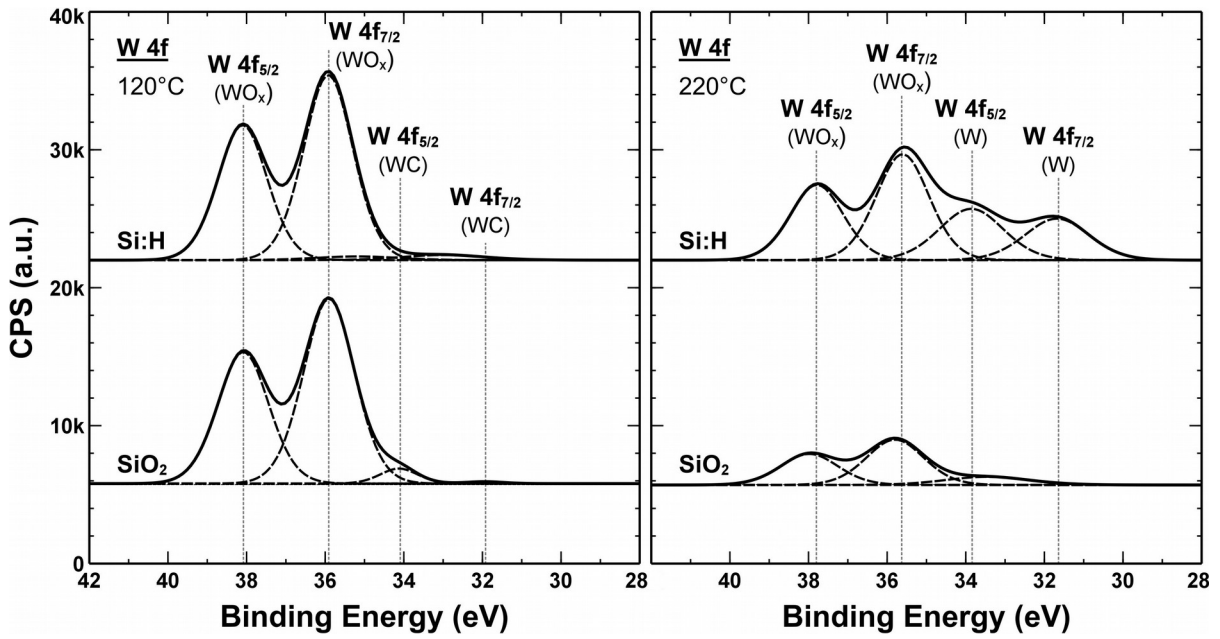


Figure 6.6. Photoelectron spectra from Si and SiO₂ surfaces processed with 50 cycles of DHP/WF₆ at 120°C (left panel) and 220°C (right panel). For each surface, the W 4f region is shown with peak identifications.

6.7 References

- (1) Yamamoto, Y.; Matsuura, T.; Murota, J. Surface Reaction of Alternately Supplied WF₆ and SiH₄ Gases. *Surf. Sci.* **1998**, *408*, 190–194.
- (2) Klaus, J. .; Ferro, S. .; George, S. . Atomic Layer Deposition of Tungsten Using Sequential Surface Chemistry with a Sacrificial Stripping Reaction. *Thin Solid Films* **2000**, *360*, 145–153.
- (3) Elam, J. .; Nelson, C. .; Grubbs, R. .; George, S. . Kinetics of the WF₆ and Si₂H₆ Surface Reactions during Tungsten Atomic Layer Deposition. *Surf. Sci.* **2001**, *479*, 121–135.
- (4) Grubbs, R. K.; Steinmetz, N. J.; George, S. M. Gas Phase Reaction Products during Tungsten Atomic Layer Deposition Using WF₆ and Si₂H₆. *J. Vac. Sci. Technol. B Microelectron. Nanometer Struct.* **2004**, *22*, 1811.
- (5) Kim, S.-H.; Hwang, E.-S.; Kim, B.-M.; Lee, J.-W.; Sun, H.-J.; Hong, T. E.; Kim, J.-K.; Sohn, H.; Kim, J.; Yoon, T.-S. Effects of B₂H₆ Pretreatment on ALD of W Film Using a Sequential Supply of WF₆ and SiH₄. *Electrochem. Solid-State Lett.* **2005**, *8*, C155–C159.
- (6) Kim, S.-H.; Kwak, N.; Kim, J.; Sohn, H. A Comparative Study of the Atomic-Layer-Deposited Tungsten Thin Films as Nucleation Layers for W-Plug Deposition. *J. Electrochem. Soc.* **2006**, *153*, G887.
- (7) Kim, S.-H.; Yeom, S.-J.; Kwak, N.; Sohn, H. Phase and Microstructure of ALD-W Films Deposited Using B₂H₆ and WF₆ and Their Effects on CVD-W Growth. *J. Electrochem. Soc.* **2008**, *155*, D148–D154.
- (8) Baumann, R. C.; Smith, E. B. Neutron-Induced ¹⁰B Fission as a Major Source of Soft Errors in High Density SRAMs. *Microelectron. Reliab.* **2001**, *41*, 211–218.
- (9) Charles H. Winter; Joseph P. Klesko; Chatu T. Sirimanne. Silyl Elimination Reactions in the Atomic Layer Deposition of Titanium, Zinc, and Other Element Films, 2014.
- (10) Tsurugi, H.; Tanahashi, H.; Nishiyama, H.; Fegler, W.; Saito, T.; Sauer, A.; Okuda, J.; Mashima, K. Salt-Free Reducing Reagent of Bis(trimethylsilyl)cyclohexadiene Mediates Multielectron Reduction of Chloride Complexes of W(VI) and W(IV). *J. Am. Chem. Soc.* **2013**, *135*, 5986–5989.
- (11) Saito, T.; Nishiyama, H.; Tanahashi, H.; Kawakita, K.; Tsurugi, H.; Mashima, K. 1,4-Bis(trimethylsilyl)-1,4-Diaza-2,5-Cyclohexadienes as Strong Salt-Free Reductants for

Generating Low-Valent Early Transition Metals with Electron-Donating Ligands. *J. Am. Chem. Soc.* **2014**, *136*, 5161–5170.

- (12) Tsao, K. Y.; Busta, H. H. Low Pressure Chemical Vapor Deposition of Tungsten on Polycrystalline and Single-Crystal Silicon via the Silicon Reduction. *J. Electrochem. Soc.* **1984**, *131*, 2702–2708.
- (13) Colgan, E. G.; Chapple-Sokol, J. D. Characterization of Selective Chemical Vapor Deposited Tungsten Using SiH₄ Reduction. *J. Vac. Sci. Technol. B Microelectron. Nanometer Struct.* **1992**, *10*, 1156–1166.
- (14) Plambeck, J. A.; Bard, A. J.; Lund, H. *Encyclopedia of Electrochemistry of the Elements. Vol. 5* Vol. 5; 1973.
- (15) Kalanyan, B.; Losego, M. D.; Oldham, C. J.; Parsons, G. N. Low-Temperature Atomic Layer Deposition of Tungsten Using Tungsten Hexafluoride and Highly-Diluted Silane in Argon. *Chem. Vap. Depos.* **2013**, *19*, 161–166.
- (16) Kaim, W. Effects of Cyclic 8 π -Electron Conjugation in Reductively Silylated Nitrogen Heterocycles. *J. Am. Chem. Soc.* **1983**, *105*, 707–713.
- (17) S.E. Stein. Mass Spectra. In *NIST Chemistry WebBook, NIST Standard Reference Database Number 69*; P.J. Linstrom; W.G. Mallard, Eds.; National Institute of Standards and Technology: Gaithersburg MD, 20899.
- (18) *NIST X-Ray Photoelectron Spectroscopy Database, Version 4.1*; National Institute of Standards and Technology: Gaithersburg MD, 20899, 2012.
- (19) McConica, C. M. Tungsten Nucleation on Thermal Oxide during LPCVD of Tungsten by the Hydrogen Reduction of Tungsten Hexafluoride. *J. Electrochem. Soc.* **1988**, *135*, 1003.

APPENDICES

APPENDIX A1. Reproducible Fabrication of High-Performance Silicon Photocathodes for Water Splitting

Berc Kalanyan, Mark D. Losego, Gregory N. Parsons

Appendix A1 is an unpublished manuscript to be revised and resubmitted for publication.

A1.1 Abstract

Recently, silicon-based photoelectrochemical water-splitting has received renewed interest as a means to sustainable hydrogen fuel generation. Modifications to silicon surface chemistry and structure all show promise for improved performance. Unfortunately, the intricacies of silicon photocathode fabrication preclude direct comparisons of results from different research teams—limiting the productivity of the research community. In this work we detail a facile fabrication method for reproducible and predictable silicon photoelectrode performance that can be used as a standard experimental system for all future silicon-based photoelectrochemical studies. Our hope is that this report explains historical variability in the silicon photocathode literature and that the experimental procedures outlined here will better unify future studies.

A1.2 Introduction

Hydrogen generation via solar water splitting is one potential path to renewable transportation fuels¹. Since Fujishima and Honda's seminal work on TiO₂ photoelectrodes in the early 1970s,² a wide set of semiconductor materials have been tested for aqueous photoelectrochemical activity and stability, including group IV materials (Si and Ge)^{3,4} III-V

materials (GaAs, GaN^{5,6}, GaP)⁷ and II-VI materials (CdSe, ZnTe)⁸, primarily in single-crystal form. Other efforts have been devoted to characterizing polycrystalline materials (mainly metal oxides, notably Fe₂O₃⁹, Cu₂O¹⁰, and more recently BiVO₄¹¹) including combinatorial approaches to non-stoichiometric mixtures¹². However, even after 40 years of exploration, silicon remains an important semiconductor platform for photoelectrochemical cells (PEC). Silicon is earth-abundant and produced in single-crystal form at industrial scales. Its surface chemistry is well studied and routes to surface modification, lithographic patterning, and 3D structuring (rods, terraces, uniform pores, density-graded pores, opals) make silicon a versatile photoelectrode platform. While silicon's narrow band-gap of 1.1 eV makes it a less than ideal photocathode, it is a good material choice for tandem cells where it is coupled with a larger band-gap (e.g. III-V or metal oxide) photoanode. Typical p-type silicon photocathodes show high photocurrent densities under standard 1 sun illumination conditions and are cathodically stabilized against corrosion during illuminated H₂ evolution.

Despite silicon's prevalence in photoelectrochemical research, the fabrication of silicon photocathodes is non-trivial. Photoelectrochemical characteristics for silicon such as onset potential, saturation current density, and rate of current rise vary substantially in the literature.¹¹⁻¹⁵ It is well known that the performance of silicon photocathodes will depend on doping level and surface orientation. For example, highly doped silicon (i.e. >10¹⁸ cm⁻³) will tend to show limited photoresponse as a result of its shallow depletion width under illumination. Crystal orientation, on the other hand, will define the energetics of the semiconductor/electrolyte interface, thus shifting the onset potential depending on the activity of the exposed crystal face. Considering all of these potential effects, we collected

published voltammograms for various p-Si electrodes and plotted them in Figure 1¹³⁻¹⁷. All potentials are adjusted to NHE to account for reference electrode differences. We note that all of these traces were collected under similar experimental conditions, summarized in Table S1. Each curve is found to show a different onset potential for H₂ evolution and a different slope for the current density increase. Moreover, the trend in onset potential appears to be independent of the rate of current increase. For instance, electrodes (a) and (b) in Figure 1 have similar onset potentials near 0 V vs NHE, yet electrode (b) is slower to reach current saturation due to its shallower slope. No two electrodes show the same onset voltage and current increase trace. In many studies, a key motivation is to understand the effect of surface engineering, i.e. 3D structuring, band-edge tuning, surface passivation, etc. on electrode function. While control experiments often provide a basis for analysis, variability in the performance of unmodified p-Si photocathodes makes it difficult to meaningfully compare device performance amongst research groups after different modification schemes. Moreover, variability in published silicon electrochemical data raises questions about how to best prepare semiconductor electrodes (including materials beyond silicon) for optimum experimental performance.

Optimizing these performance parameters also have critical practical implications. In order to satisfy charge conservation, tandem PEC cells operate at the point where the photocathode and photoanode current-voltage (I-V) curves intersect. While the onset potential of an electrode may be fixed by surface features (catalyst, morphology, crystal orientation, etc.), the slope of the I-V curve is largely defined by series resistances in the device. With high-performance photoelectrodes, even a small decrease in I-V curve slope can

dramatically reduce the fill factor and hence overall conversion efficiency as demonstrated in this inset (i.e., as resistance increases from R_1 to R_2 , the tandem cell's photocurrent decreases from I_1 to I_2).

For this work, we systematically prepared a range of silicon photocathodes using different electrical contact methods and examined the effect of contact area and fabrication method on current increase rate and hydrogen evolution onset voltage. We find that the backside contact preparation method and relative area are important in optimizing performance and ensuring reproducibility. We clearly enumerate the steps that should be taken to produce high-performance silicon photoelectrodes both reliably and reproducibly..

A1.3 Experimental

Silicon photoelectrodes used for this study were fabricated using a sequence of steps summarized in Scheme S1. Electrodes consist of prime grade single-crystal Si pieces (10×12 mm) with an electrical contact formed on the backside and subsequently encased in epoxy. This approach follows commonly used methodologies, but here we explicitly examine the impact of back-contact formation and size. Due to the simplicity of their design, electrodes can be fabricated from common laboratory materials, and large batches of electrodes (i.e 10 at a time) can be prepared and tested in succession. In most published studies, backside electrical contacts are typically formed using either a liquid metal, a conductive paste, or vacuum-deposited metal films. All three approaches were evaluated, but most effort here focused on the liquid metal contact method because of its relative simplicity and equivalent performance when optimized.

Our silicon photoelectrodes were formed from lightly doped single-side polished p-Si (111) wafers, 4-6 Ω -cm, and p-Si(100) electrodes, 5-8 Ω -cm. To remove the native oxide, the wafer backside was either mechanically abraded or chemically etched in dilute hydrofluoric acid (HF) or ammonium fluoride (NH_4F). For mechanical abrasion, we used either a tungsten carbide or a diamond tipped scribe. The diamond scribe created deeper scratches on silicon and visibly removed more material from the back surface. For all electrodes, we scratched uniformly and methodically by drawing dense horizontal, vertical, and diagonal lines in both directions (Figure S2). For chemical etching, we mounted the wafer chips on a fluoropolymer mold and masked the wafer edges using tape. The wafer surface was then covered with a drop of 15% HF. After 30 seconds, the droplet was withdrawn using a syringe, and the wafer was rinsed in deionized (DI) water. Control samples were also prepared where the wafer back-side was used as-received, with neither etching nor mechanical abrasion. Next, we introduced liquid eutectic indium gallium (>99.99% GaIn, Sigma Aldrich) to the wafer backs using a nylon applicator (ITW polyester swabs, TX743B). A flattened Ag wire (7 mm diameter) was then placed on top of the GaIn layer. The Ag wire is readily wet by the liquid GaIn forming a liquid AgGaIn alloy. We avoided using Cu as the wire material due to its large diffusivity through Si. The Ag electrode was held in place using a two-part epoxy (Hysol 9462) that encapsulates the entire back and the sides of the wafer piece, leaving an exposed rectangular Si surface on the electrode front. The epoxy is then heat cured at $\sim 70^\circ\text{C}$ for 15 minutes. Next, the Ag wire is threaded through a small quartz tube which is epoxy sealed to the electrode. The finished electrode can be readily submerged into an electrochemical cell, where only the polished silicon surface comes in contact with the liquid.

We used a custom glass cell with a quartz window ~ 5 cm in diameter. A Pt mesh of approximately 5 cm^2 was used as the anode, and Ag/AgCl as the reference electrode. All electrodes were inserted into the cell and sealed using polymer gaskets and fluorocarbon fittings. The gas-tight cell was filled with 0.5 M sulfuric acid (H_2SO_4) at pH 0 and bubbled with Ar for one hour prior to the experiments to remove dissolved oxygen from the electrolyte. A magnetic stir bar is spun at $\sim 1,000$ RPM during measurements to aid in bubble release from the electrode surface. For photocurrent density measurements, electrodes were illuminated using a 150 W Xe bulb (Newport Oriel 6255), the output of which was filtered through an AM1.5G filter, and was calibrated to 1 sun (100 mW/cm^2) irradiance using a standard solar cell (Newport Oriel 96000). Immediately before measurement, Si(111) electrodes were dipped in a 40% aqueous NH_4F solution (Sigma Aldrich) to strip the native oxide and then briefly rinsed with DI H_2O to achieve hydrogen termination. Likewise, Si(100) surfaces were dipped in dilute (7 vol%) HF solution for 30 s and then rinsed with DI water. Voltammograms were recorded using a Princeton Applied Research VersaStat3 potentiostat. Three sweeps were recorded for each electrode at a scan rate of 20 mV/s, and bubbles were observed on the photocathode and the Pt anode. The I-V traces were recorded for several scan cycles, and the data reported in this paper were collected during the return sweep of the third I-V cycle. The abscissae are shifted by +197 mV to convert the Ag/AgCl potential to the normal hydrogen electrode (NHE) scale. Scans from a Pt-Pt electrode system are shown in Figure S1 to verify the position of the hydrogen evolution reaction (HER). In this article we interpret the rate of current rise in the linear region of the I-V curve as a series resistance.

A1.4 Results and Discussion

In Figure 2 we artificially illustrate the impact of series resistance on the I-V curves of silicon photocathodes. Here we show a sequence of I-V curves obtained from the same optimized silicon photocathode with different resistors wired to it in series, ranging in resistance value from 5 to 150 Ω . This plot is intended to physically illustrate the consequences of a non-optimized silicon photocathode construction. Before each measurement, we dipped the electrode in NH_4F to remove any surface oxide. For all resistors tested, increasing the resistance decreases the slope of the I-V curves. We plot the reciprocal of the IV curve slope against resistance used for each IV curve (inset to Figure 2). A linear fit gives a slope of 1.05 and a y-intercept of 9.6 Ω . This lumped value includes contributions from contact, charge transfer, and bulk wafer resistances. In the subsequent discussion we take this value as the best-case series resistance for a well-made photocathode and use it to quantify any series resistance incurred by poor electrical contacts.

Figure 3 is a plot of current density against voltage vs NHE (= Ag/AgCl + 197 mV) for various silicon photocathodes. Backside treatments include: native oxide, as received (control), tungsten carbide (WC) scribing, diamond scribing, dilute HF etching and diamond scribing plus HF etching (Figure 3). The sequence of steps used to construct the diamond scribed electrode are listed to the right of the figure. As expected, the control electrode shows a large overpotential for H^+ reduction, corresponding to a high series resistance. Also, current saturation is achieved only for overpotentials greater than -1 V (not shown). When the back contact is prepared by scratching with a WC scribe, the onset potential shifts positively to approximately -0.1 V vs NHE. However the slope within the linear region of the I-V curve is

low (21.3Ω) and the electrode requires > 600 mV to reach current saturation. The series resistance observed in the control electrode is similar (19.2Ω) to that found in a recent publication¹⁸ where native oxide was left intact on the back contacts made on n-Si photoanodes. Scratching with a diamond tip gives rise to I-V curves with sharper slopes (11.5Ω series resistance) and current saturation within ~ 0.3 V of onset. Chemically etched backsides also exhibit low series resistance (9.0Ω) and low onset potentials (-0.1 V vs NHE) that are similar to diamond scratched back contacts. Using combined mechanical and chemical oxide removal, we observe similarly low series resistances (10.5Ω) and onset potentials (-0.1 V vs NHE). Saturation current densities for these electrodes fluctuate around 23 mA/cm^2 , with $\pm 10\%$ error due to electrode alignment with respect to incident light (Figure S4). From this result, we conclude that the combination of etching and scratching helps ensure a low contact resistance. This analysis also indicates that poor contact preparation adds approximately 10Ω of series resistance to photocathodes. Noise in the traces is ascribed to bubble nucleation and release, which can be mitigated with rapid stirring or the addition of a surfactant. In the inset to Figure 3 we compare liquid-metal based back contacts to those prepared by physical vapor deposition (PVD) metal evaporation onto HF etched wafers. We find that electrodes prepared with high work-function PVD metal contacts (aluminum and gold deposited onto HF etched p-Si) have comparable series resistances to diamond scribed back contacts formed with GaIn.

We have also examined the effect of backside electrode contact size on photoelectrode performance. We prepared three electrodes, each with the same electrochemical surface area but with different GaIn back contact areas, ranging in size from

greater than the front area to much less than the front electrode area (see Scheme S1, step 3). The resulting current-voltage sweeps are shown in Figure 4. The three electrodes show similar onset potentials and saturation current densities, but the rate of current rise depends markedly on back contact area. The electrode with the largest back contact shows the most rapid change in current with applied bias. Smaller back contacts result in slower current rise, and current saturation requires large applied voltages. The change in current rise is consistent with spreading resistance associated with lateral current flow. The difference in series resistance between a small and a large back contact is on the order of 50 Ω . Thus, complete metallization of the electrode's backside is critical to optimizing photoelectrode construction.

Finally, we examine the reproducibility of our simplest but equivalently high-performing method—diamond-scribed backsides with GaIn electrodes. Benchtop fabrication simplicity combined with no HF usage makes this process especially appealing for lab-scale studies. Data for three independently prepared photoelectrodes is plotted in Figure S3. It is important to note that in comparing electrodes to one another, we have fabricated cathodes from the same Si wafer. Moreover, because measurements can be sensitive to electrochemical cycling history, each electrode received the same sequence of measurements. We find that onset potentials are reproducible to within ± 20 mV, and variations in series resistance remain $< 15\%$ ($11.9 \pm 1.7 \Omega$). In summary, Figure 3 illustrates the processing steps we recommend to reproducibly generate high-performance silicon photocathodes intended for photoelectrochemical studies.

A1.5 Summary and Conclusions

In this work we have shown the influence of benchtop electrode fabrication techniques on the photoelectrochemical performance of p-Si photocathodes used for solar fuels applications. We discussed the methods available for native oxide removal from the wafer back surface prior to back electrical contact formation. Specifically, we compare electrodes prepared with HF-etched and mechanically abraded back contacts and emphasize the importance of using hard materials (such as diamond) for mechanical abrasion in order to minimize series resistance. We find that electrodes prepared with HF treatment combined with diamond abrasion produce sharp IV curves with reproducible H^+ reduction onset potentials, saturation current densities, and rates of photocurrent rise. We also show that back electrode contact size alters spreading resistance causing a significant decrease in the rate of current rise (fill factor) in silicon photocathodes with larger contact resistance. With consistent electrode fabrication techniques, good quality self-contained Si electrodes can be fabricated using benchtop techniques, without the need for PVD processing or high-temperature contact annealing. We argue that the large variability in I-V curves reported in the literature for Si photocathodes can be attributed in part to these inconsistencies in electrode fabrication, and we hope that the detailed fabrication procedures presented herein will improve reproducibility of future reports within the photoelectrochemical research community.

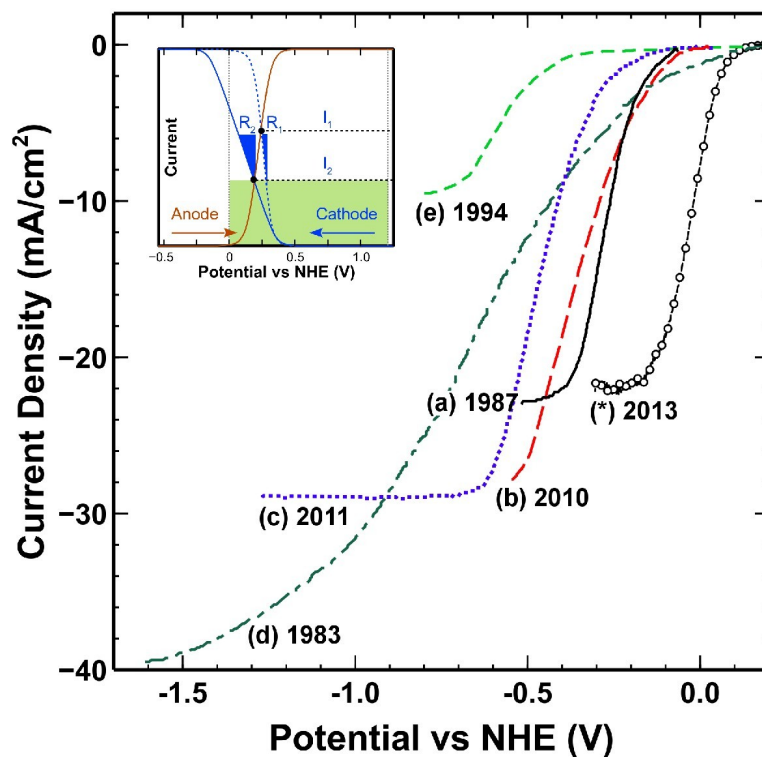


Figure A1.1. Representative polarization curves for p-Si photocathodes from the literature. From right to left, the curves were replotted from (a) *J. Electroanal. Chem.* 228 1987, (b) *Electrochem. Commun.* 12 2010, (c) *Energy Environ. Sci.* 4 2011, (d) *Appl. Phys. Lett.* 42 1983, (e) *Appl. Surf. Sci.* 75 1994, and (*) this article. Specific experimental conditions for the data are tabulated in the supplemental information. Inset: Current matching in tandem PEC systems is shown as two intersecting IV curves. The blue curves (solid and dashed) represent the cathode with two different series resistance values and the orange curve corresponds to the anode. The green rectangle represents the maximum power at which one of the devices can operate. Dashed horizontal lines I_1 and I_2 correspond to the maximum current at which the tandem cell can operate with series resistance R_1 and R_2 respectively.

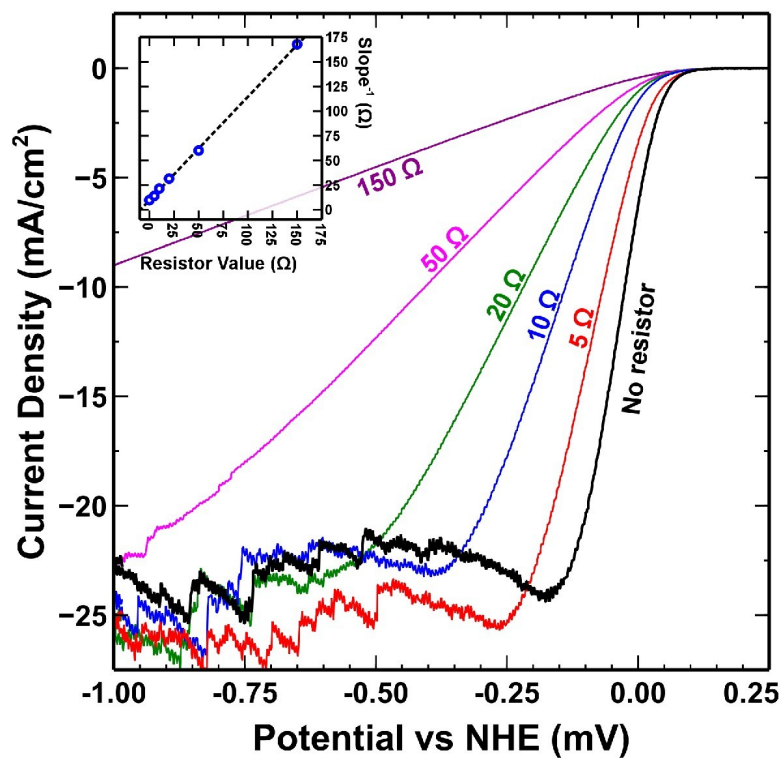


Figure A1.2. Electrical resistance in diamond scratched back contacts is physically modeled using resistors wired in series with the working electrode. Higher resistor values impede photocurrent rise, analogous to our observations with electrodes that have poor back contacts. Inset shows the reciprocal slopes of IV curves plotted against resistor value.

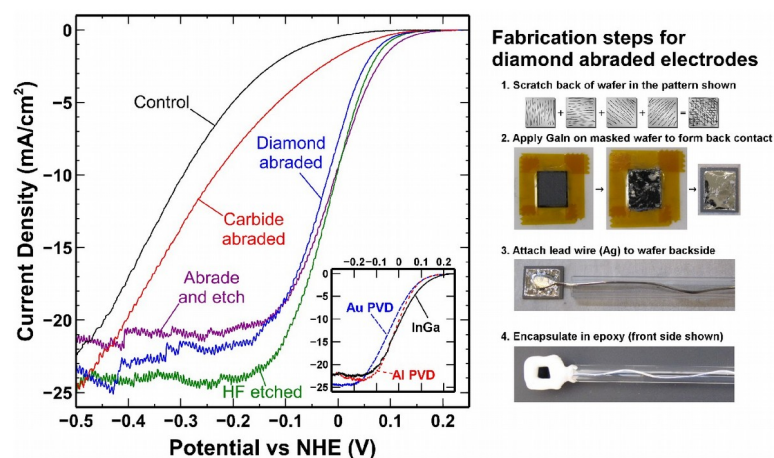


Figure A1.3. Comparison of electrodes constructed using different native oxide removal methods: No treatment (native oxide is present as a control), mechanically abraded using tungsten carbide pen, mechanically abraded using diamond pen, chemically etched using 10 M HF, and a combination of diamond abrasion and HF etching applied in sequence. The inset shows evaporated Au and Al back contacts compared to a diamond abraded back contact. The series of steps used to construct a diamond abraded back contact are enumerated on the right.

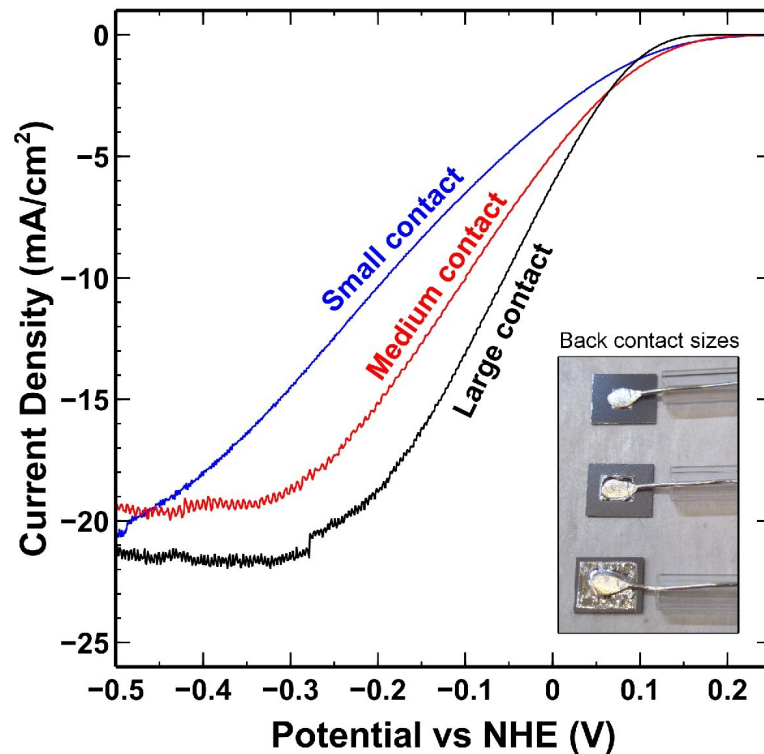


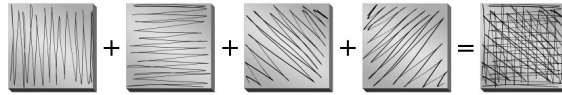
Figure A1.4. The influence of back contact geometric area on the performance of silicon photocathodes. Polarization curves are shown for electrodes with small, medium, and large InGa back contacts. Geometric areas for the metal contacts are 0.16, 0.24, and 0.90 cm² respectively (photographed in inset).

Table A1.S1. Experimental conditions reported for voltammograms from p-Si photocathodes plotted in the main text (Figure 1). Cells marked with a diamond (◆) indicate that the data were not reported in the referenced article.

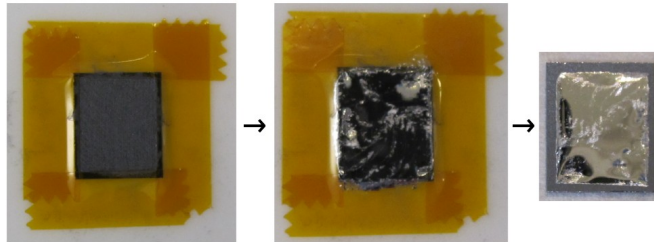
Figure 1 Key	Crystal Orient.	Bulk resistivity (Ωcm)	Back contact	Electrode surface preparation	Electrolyte	Illumination type (mW/cm^2)	Series Resistance (Ω/cm^2)
(a) ¹³	(111)	2-5	InGa	HF/HNO ₃ / Br ⁻ , DMK/H ₂ O, 10% HF	1M HCl	Tungsten halogen (◆)	8.3
(b) ¹⁴	(111)	◆	◆	40% NH ₄ F	1M H ₂ SO ₄	Tungsten halogen (65)	11.9
(c) ¹⁵	(100)	2.5	Al screen printed	10% HF 60s	0.5M H ₂ SO ₄	250W tungsten halogen, IR filter, AM1.5 filter (100)	10.2
(d) ¹⁶	◆	◆	◆	◆	0.5M H ₂ SO ₄	Solar simulator (96)	21.7
(e) ¹⁷	(111)	7.5-12.5	Al PVD	HF 30s	1M H ₂ SO ₄	150W tungsten halogen (◆)	26.6

Scheme A1.S1. Back contact fabrication steps are shown in sequence. 1) Wafer back surfaces are masked using polyimide tape and successively scratched with a diamond pen in four directions; 2) After oxide removal, GaIn liquid metal layer is applied to each wafer; 3) Polyimide masks are removed and flattened Ag wires are first wetted with GaIn and then placed on the back contact – three different back contact sizes are shown; 4) Epoxy encapsulated electrode is ready for testing. The Si pieces are all 10 x 12 mm in size.

1. Scratch back of wafer in the pattern shown



2. Apply GaIn to form back contact



3. Attach lead wires (Ag)



4. Encapsulate in epoxy



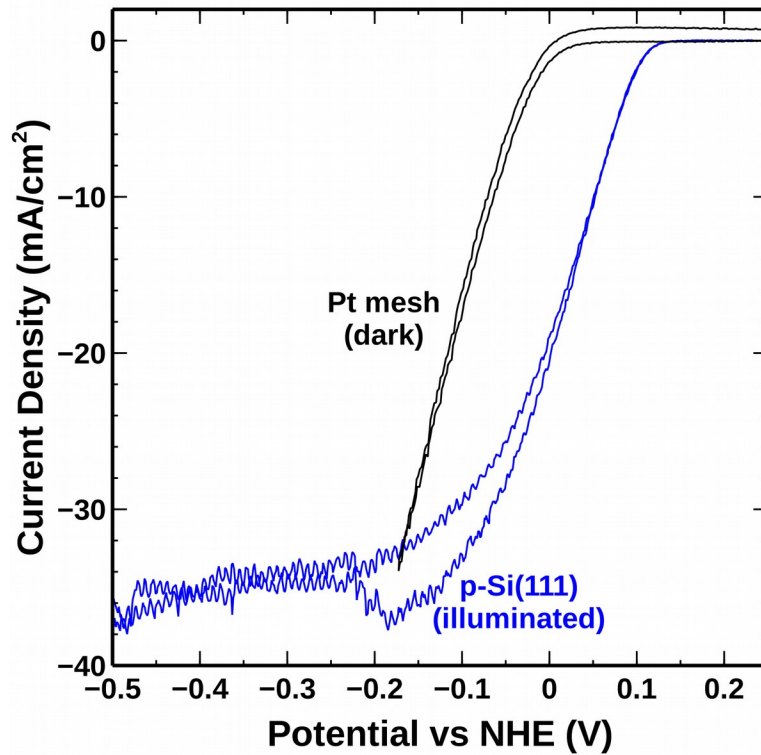


Figure A1.S1. The position of the HER is shown for two Pt mesh electrodes ($\sim 5 \text{ cm}^2$ surface area each) stored in concentrated H_2SO_4 . Scans are recorded in $0.5\text{M H}_2\text{SO}_4$ ($\text{pH} = 0$) electrolyte at 20 mV/s . For comparison, a p-Si(111) electrode is also shown measured under 1 sun illumination, immediately after dipping in NH_4F and rinsing under DI water.

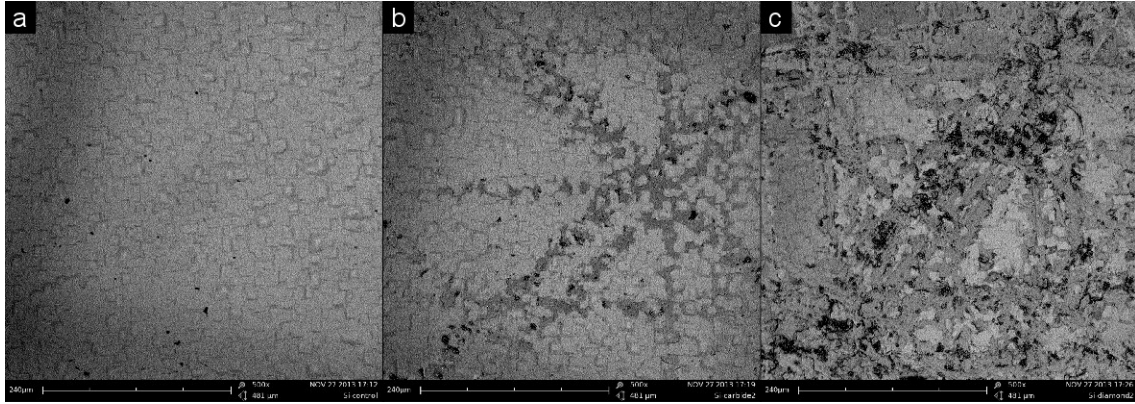


Figure A1.S2. Electron micrographs of Si back contacts with (a) no contact preparation, (b) tungsten carbide scratching, and (c) diamond scribing. Scale bars represent 240 μm . Horizontal, vertical, and diagonal trenches are evident in (b) and (c).

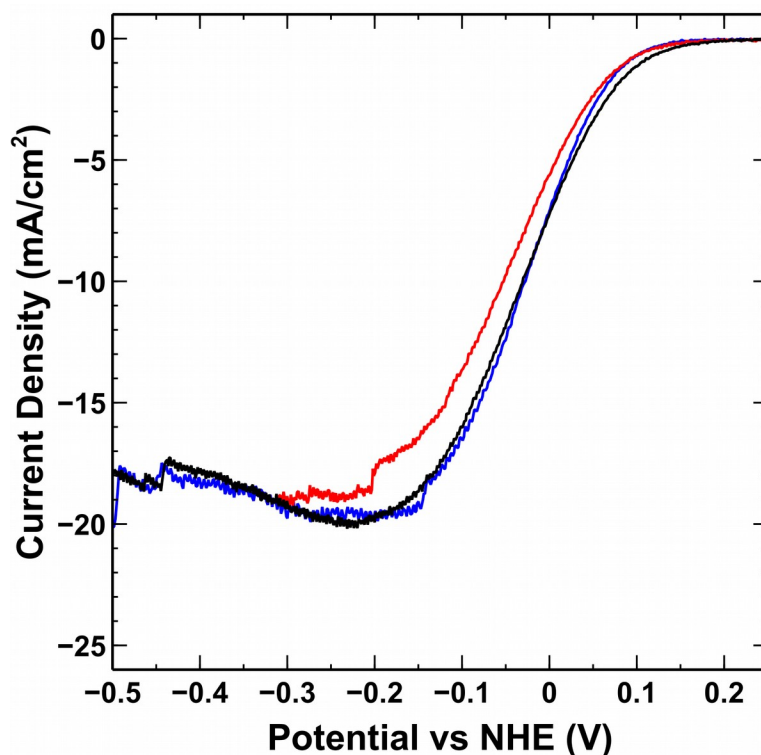


Figure A1.S3. Reproducibility characteristics from three silicon cathodes with back contacts prepared by mechanical scratching using a diamond pen. Saturation occurs at approximately -0.2 V vs NHE, but noise from bubble release makes this interpretation difficult. We attribute variations in saturation current density to several source of error, including vertical sample positioning as well as sample rotation with respect to the incident beam (off-normal rotation). Small variations in electron rotation can result in current density differences up to $\pm 10\%$ (shown in Figure S4).

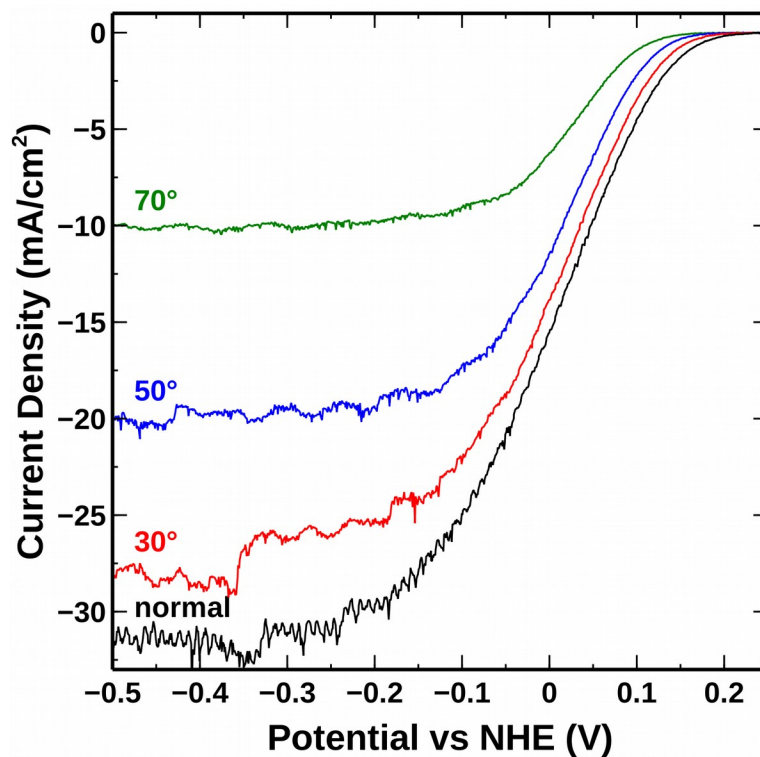


Figure A1.S4. Current density dependence on illumination angle of incidence is shown for a cathode prepared by diamond abrading the back surface. The same electrodes is measured repeatedly at different angles of incidence. The successive increase in series resistance is due to surface oxide formation when illumination is blocked as electrode rotation is adjusted. Compared to current densities at normal incidence, rotated electrodes show a roughly cosine dependence on the angle of illumination. The vertical position of the electrode is controlled reproducibly with an o-ring, and is therefore not a significant source of error in measurements. Noise is due to steady-state gas evolution on the electrode surface.

A1.6 References

1. J. Newman, P. G. Hoertz, C. A. Bonino, and J. A. Trainham, *Journal of the Electrochemical Society*, **159**, A1722–A1729 (2012).
2. A. Fujishima and K. Honda, *Nature*, **238**, 37 (1972).
3. R. M. Candea, M. Kastner, R. Goodman, and N. Hickok, *Journal of Applied Physics*, **47**, 2724–2726 (1976).
4. R. Memming and G. Neumann, *Journal of Electroanalytical Chemistry*, **21**, 295 (1969).
5. S.Y. Liu, J.K. Sheu, C.K. Tseng, J.C. Ye, K.H. Chang, M.L. Lee, and W.C. Lai, *Journal of The Electrochemical Society*, **157**, B266 (2010).
6. S. S. Kocha et al., *Journal of the Electrochemical Society*, **142**, L238–L240 (1995).
7. J. F. McCann and L. J. Handley, *Nature*, **283**, 843–845 (1980).
8. D. Liu and P. V. Kamat, *The Journal of Physical Chemistry*, **97**, 10769 (1993).
9. T. Hisatomi, H. Dotan, M. Stefik, K. Sivula, A. Rothschild, M. Grätzel, and N. Mathews, *Advanced Materials*, **24**, 2699–2702 (2012).
10. A. Paracchino, V. Laporte, K. Sivula, M. Grätzel, and E. Thimsen, *Nature Materials*, **10**, 456–461 (2011).
11. F. F. Abdi, N. Firet, and R. van de Krol, *ChemCatChem*, **5**, 490–496 (2013).
12. M. Woodhouse and B. A. Parkinson, *Chemical Society Reviews*, **38**, 197 (2009).
13. Y. Nakato, H. Yano, S. Nishiura, T. Ueda, and H. Tsubomura, *Journal of Electroanalytical Chemistry*, **228**, 97 (1987).
14. M. Lublow, K. Skorupska, S. Zoladek, P.J. Kulesza, T. Vo-Dinh, and H.J. Lewerenz, *Electrochemistry Communications*, **12**, 1298–1301 (2010).
15. J. Oh, T. G. Deutsch, H.-C. Yuan, and H. M. Branz, *Energy & Environmental Science*, **4**, 1960–1964 (2011).
16. M. Szklarczyk and J. O. Bockris, *Applied Physics Letters*, **42**, 1035–1036 (1983).

17. G. Bilger, M. Specht, C. U. Maier, A. Eicke, and M. Gillmann, *Applied Surface Science*, **75**, 157 (1994).
18. M.J. Kenney, M. Gong, Y. Li, J.Z. Wu, J. Feng, M. Lanza, and H. Dai, *Science*, **342**, 836–840 (2013).

APPENDIX A2. Atomic Layer Deposited Oxides for Passivation of Silicon Photoanodes for Solar Photoelectrochemical Cells

*Berc Kalanyan and Gregory N. Parsons**

Appendix A2 is a conference proceedings article, published in ECS Transactions.

A2.1 Abstract

Although crystalline silicon is an industrially significant device substrate, its use in photoelectrochemical cells is complicated by the thin oxide film that forms at the electrode surface. We applied thin coatings of atomic layer deposited films on n- and p-type Si substrates to block the growth of SiO₂ during solar light-driven water splitting reactions. Voltammetry accompanied by ellipsometric measurements show us that metal oxide coatings as thin as 1.6 nm are effective at stopping electrode oxidation during dark and photoelectrochemistry. We observed similar passivating behavior among TiO₂, ZnO, and Al₂O₃ thin films. Titania and zinc oxide films enhanced photocurrent due to their absorption in the UV wavelengths. We also applied a common water oxidation catalyst, cobalt, to show the feasibility of catalyst integration on top of ALD passivating films.

A2.2 Introduction

There is significant interest in new semiconductor nanostructured materials systems that allow chemically stable and affordable photoelectrochemical (PEC) water dissociation using sunlight. Atomic layer deposition (ALD) chemistry allows ultra-thin film semiconductors, insulators (1, 2), quantum dots (3), and catalyst nanoparticles (4) to be produced and integrated with low-cost semiconductors, such as silicon and common metal

oxides, to achieve nano-engineered device structures not available with other deposition technologies (5). ALD proceeds through a set of self-limiting surface reactions to achieve thin film coatings with sub-nanometer level control of film thickness and film composition (6). Early results from several groups show that TiO₂ ALD can be used, for example, to help stabilize silicon photoanodes to oxidation upon exposure to alkaline and acidic solutions necessary for optimal PEC functionality (7). Other efforts to passivate silicon against corrosion made use of thick chemical vapor deposited TiO₂ films (8), molecular assemblies (9), metallic Ti layers (10), Al-doped ZnO ALD films (11), and sputtered transparent oxides such as ITO (12).

Semiconductor electrodes are suitable for photoelectrochemical applications, such as water splitting, provided they have suitable energetics and show sufficient stability in dark and under illumination. Crystalline silicon has a bandgap low enough to allow both UV and visible light collection. However, the valence band of Si is not low enough to drive the water oxidation reaction without applied bias. Metal oxides such as TiO₂ and ZnO both have conduction bands above and valence bands significantly below that of Si. TiO₂ is especially important in this context as it is the first reported water splitting photoelectrode (13). Due to their band positions, barrier materials such as titania and zinc oxide are suitable for passivating Si electrodes, since they both allow for the flow of electrons and holes between the light absorbing substrate and the overlying thin film. Moreover, the low valence bands of TiO₂ and ZnO are well below the water oxidation potential, extending the usability of Si for photoelectrochemical water oxidation. We used atomic layer deposition to investigate the effects of TiO₂ and ZnO films on Si photoelectrodes. Likewise, we also deposited very thin

films of Al₂O₃, an insulator, to gauge its effectiveness in protecting Si electrodes from oxidation.

A2.3 Materials and Methods

A2.3.1 Atomic Layer Deposition

Metal oxide films of various thicknesses were deposited in hot-walled stainless steel tube ALD reactors constructed in-house. Exposures of the metal organic precursors and oxygen source were controlled using a custom LabVIEW program. All depositions were carried out at low temperatures (approximately 100°C) and low vacuum (2 Torr). A nitrogen carrier gas was used during all depositions with a flow rate of about 200 sccm. Precursors used were diethylzinc for ZnO (98%, Strem Chemicals), trimethylaluminum (98%, Strem Chemicals) for Al₂O₃, and either titanium tetraisopropoxide (97%, Sigma-Aldrich) or titanium tetrachloride (99%, Gelest) for TiO₂ deposition. For all organometallic or metal halide precursors, deionized water (H₂O) vapor was used as the oxygen source. In general, zinc oxide and alumina were found to have two to three times higher growth rate per ALD cycle when compared to titania. For this reason, we report metal oxide film thicknesses rather than the number of ALD cycles for our passivation studies. Unless otherwise stated, all ALD films were used as-deposited, without post-deposition annealing.

A2.3.2 Electrode Preparation and Testing

Electrochemical and ellipsometric experiments were performed on p- or n-type (100) Si (1-10 Ω-cm) wafer pieces. Photoelectrodes were fabricated by seating a silicon wafer

piece on a conductive glass slide with a metal wire (Cu or Ag) serving as the electrode lead. Each electrode was sealed with epoxy leaving an approximately 1 cm² exposed area for electrochemistry. Ohmic contacts were formed between the substrate and the wafer and between the substrate and the wire by a small amount of eutectic indium gallium. Uncoated electrodes were either dipped in 10% HF for 30 seconds or in proprietary buffered oxide etch (BOE) for 5 minutes, then placed into an electrochemical cell containing sulfuric acid electrolyte (approximately 0.5M, pH 0-1). Electrodes selected for passivation were dipped in etchant immediately before ALD and then formed into electrodes. Metal layers were deposited on glass substrates in a Telemark electron beam evaporator. Cobalt was deposited in a Cooke Vacuum Products thermal evaporator. The counter electrode was a Pt mesh (area >5 cm²), and the reference electrode used was Ag/AgCl. Data plots were shifted +0.197 V to represent potentials versus the normal hydrogen electrode (NHE). Before each measurement, the cell was purged for 20 min in N₂, and a N₂ blanket was maintained during analysis. We used a Pine Instruments WaveNow potentiostat for cyclic voltammetry (CV), using a scan rate of 20 mV/s between -0.5 and 4 V versus Ag/AgCl. Corrections for uncompensated solution resistance were not made. The light source was a filtered 150W Xe lamp with overall photon flux comparable to the AM 1.5G spectrum. Light intensity was calibrated to 100 mW/cm² using a reference solar cell. We measured silicon oxide and metal oxide thicknesses at a 70° angle using an α -SE spectroscopic ellipsometer from J.A. Woollam Co. Each electrode was modeled as a stack of layers consisting of an opaque Si substrate, a native oxide layer, a metal oxide layer, and a catalyst layer in that order. We used a Cauchy model

for analysis of the ALD films. In our data analysis we assumed that the thickness of metal oxide remained constant across measurements.

A2.4 Results and Discussion

Uncoated n-Si photoanodes show significant current decay with successive electrochemical cycling. To illustrate this, we measured SiO₂ thicknesses before and after electrochemical measurements on bare n-Si electrodes. A typical plot for such an experiment is given in Figure 1. For both dark and light current traces, less than 30% of the original current density is observed after five sweeps. With subsequent scans, current decay is accompanied by an increase in the oxidation onset potential. Overall current decay in dark is lower due to the smaller amount of total charge passed through the electrode. Under illumination, both Si surface oxidation and water oxidation proceed at a higher rate. As such, a thicker SiO₂ film is formed after the first sweep with light on than it does without illumination. Ellipsometry shows that SiO₂ film thicknesses reach within 90% of their steady-state values after the first CV scan under illumination. Successive sweeps build the oxide thickness at a slower rate. Correspondingly, current decay gets smaller in magnitude with successive sweeps. These observations are consistent with data reported by Lewerenz (14). After 20 scans in light, less than 3% of the original current density remains. In the following sections we discuss results from electrodes constructed on various flat conductive substrates and coated with atomic layer deposited metal oxides.

A2.4.1 Electrodes on FTO Glass

Three types of metal oxide films were deposited by ALD on n-Si substrates at thicknesses less than 15 nm. ZnO films thinner than 5 nm resulted in photocurrents

comparable to that of uncoated n-Si electrodes on FTO glass, in the range of 0.3 mA/cm². Moreover, photocurrent decay during CV cycling was slightly retarded. Thicker ZnO films resulted in significantly reduced current densities indicating that electron transfer was impeded by the thick metal oxide layers. ZnO coatings of 2.3 and 5.1 nm gave maximum dark and photocurrent densities in the 50 μ A/cm² range.

Insulating Al₂O₃ films behaved similarly, in that films 6 nm or thinner did not interfere with electron transfer, resulting in no loss of current density compared to uncoated electrodes. We measured SiO₂ film thicknesses for a set of Al₂O₃ electrodes and noted that the interfacial oxide did not grow after 5 voltammetric sweeps in dark and 5 additional sweeps under illumination. The thickest film we tested was 11.6 nm thick, which was effective at blocking SiO₂ growth, but it also reduced current density to the low 1- μ A/cm² scale.

TiO₂ passivating films were tested at thicknesses between 2.2 and 5.1 nm. Both thick and thin titania films resulted in enhanced dark and photocurrent densities. Figure 2 shows a voltammogram for one such electrode that was treated with 3.3 nm of titania and tested as-deposited. Photocurrent density was an order of magnitude higher when compared with a bare n-Si electrode on FTO glass. Ellipsometry revealed that oxide growth was completely blocked by the TiO₂ film and current decay was significantly lower. After five CV sweeps under illumination, photocurrent density remained at 85% of the value for a fresh as-deposited electrode. We observed less significant photocurrent enhancements over bare electrodes with thicker TiO₂ films.

TiO₂ coatings for n-Si electrodes on Cu-coated glass behave similarly to ZnO coatings in terms of passivation behavior. Very thin metal oxide layers less than 1 nm do not have a

significant oxide blocking effect. Once over 1.9 nm thick, TiO₂ films completely stop silicon oxide growth as verified by spectroscopic ellipsometry. When electrodes are coated with more than 10 nm of TiO₂, current-potential characteristics of the electrodes degrade. Unlike FTO-backed electrodes, however, TiO₂ on Cu-backed electrodes does not enhance current densities. We also noted Cu oxidation and reduction peaks on some of our electrodes, which we attributed to either the leakage of copper from the back contact or the diffusion of Cu through the Si substrate. To eliminate the possibility of Cu diffusion through Si, we fabricated Ag-backed electrodes.

A2.4.2 Electrodes on Ag-coated Glass

Conducting silver substrates were prepared in a similar fashion to the Cu-coated glass substrates, except that a 15 nm Ti layer was used as an adhesion promoter. We only tested TiO₂ coated electrodes in this configuration. Titania films thinner than 1.6 nm did not block oxide growth. Thicker films, however, completely stopped oxide growth and showed improved current stability over the course of 5 voltammetry cycles. Especially in dark, measured current densities did not decay significantly. Under illumination, current decay was less than 40% over the course of 5 cycles. We found TiO₂ coatings as thick as 3.5 nm to be effective passivation layers. To scale up the performance of passivated n-Si electrodes, a thin layer of Co metal was evaporated on top of 1.9 nm of TiO₂. Electrochemical data from this electrode is given in Figure 4. Photocurrent for such an electrode is two orders of magnitude greater than a bare n-Si electrode constructed on Ag-coated glass. Photocurrent decay is very large after the first scan, but subsequent scans show a smaller drop in performance. Dark

current and onset potentials are very stable, however. Table I shows a brief summary of results from TiO₂-coated n-Si electrodes on Ag-coated substrates.

A2.4.3 Tandem PV-PEC Electrodes

We have also initiated experiments using p-Si photocathodes connected to an a-Si p/i/n photovoltaic cell to apply back-bias. Using a Pt counter electrode and no catalyst metal on the photocathode, we observe approximately 0.1 mA/cm² of reductive current without any externally applied bias. This open-circuit current is shown in Figure 5 where data from a two-electrode CV experiment is given. This particular electrode was treated with 3 nm of TiO₂. However, since both the photoelectrode and the solar cell need to be illuminated simultaneously, the efficiency of the combined device is very low without any catalyst layer.

A2.5 Conclusions

We determined that nm-thick ALD metal oxide films are effective at stopping silicon oxide growth on n-Si photoanodes. For electrodes constructed on FTO substrates, we also noted substantial photocurrent improvements from TiO₂ films under 5 nm thick in the absence of other oxidation catalysts. Most of the electrodes we tested did not employ catalysts and the resistivity of our n-Si wafers were fairly high, resulting in overall low current densities both in dark and under illumination. However, our results constitute a baseline for future studies on anodic oxidation as we consider higher performance photoanode materials.

A2.6 Acknowledgments

Funding for this research was provided under DOE grant number 08NT0001925.

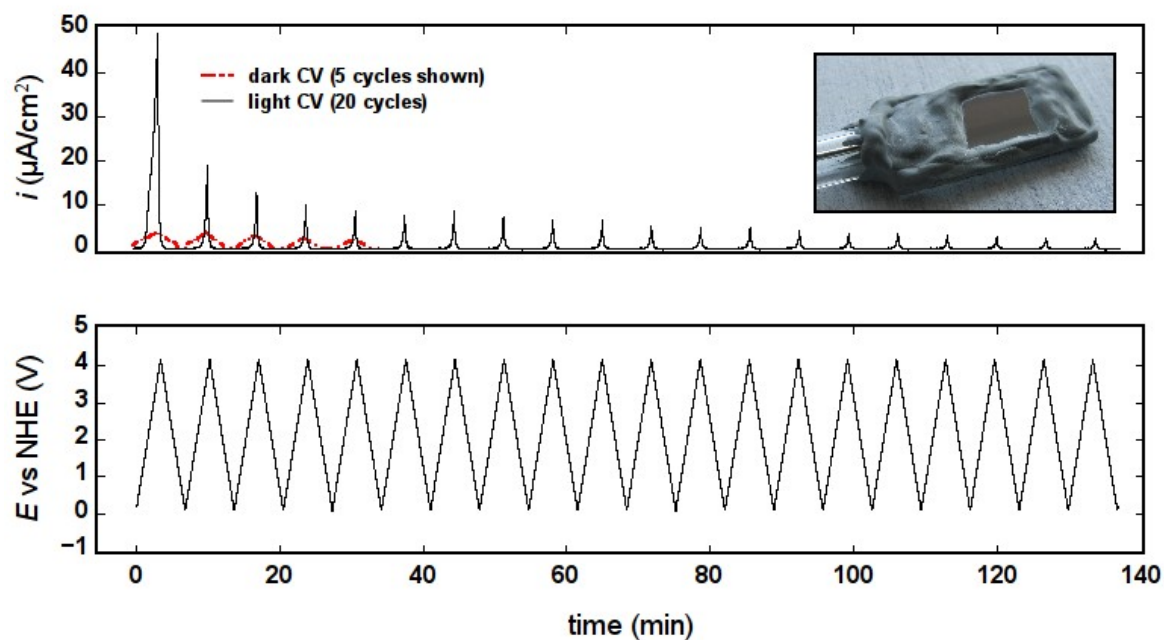


Figure A2.1.1. Current and potential plots from bare n-Si photoanodes showing dark and photocurrent decay with each voltammetric sweep. Current in dark (dashed line) is shown for only the first 5 cycles while current under illumination (solid line) is repeated for 20 linear sweeps at a scan rate of 20 mV/s in 0.5M H_2SO_4 . Inset is a photograph of an electrode showing the exposed Si face surrounded by gray epoxy; a silver wire contact housed in a glass tube is visible on the left.

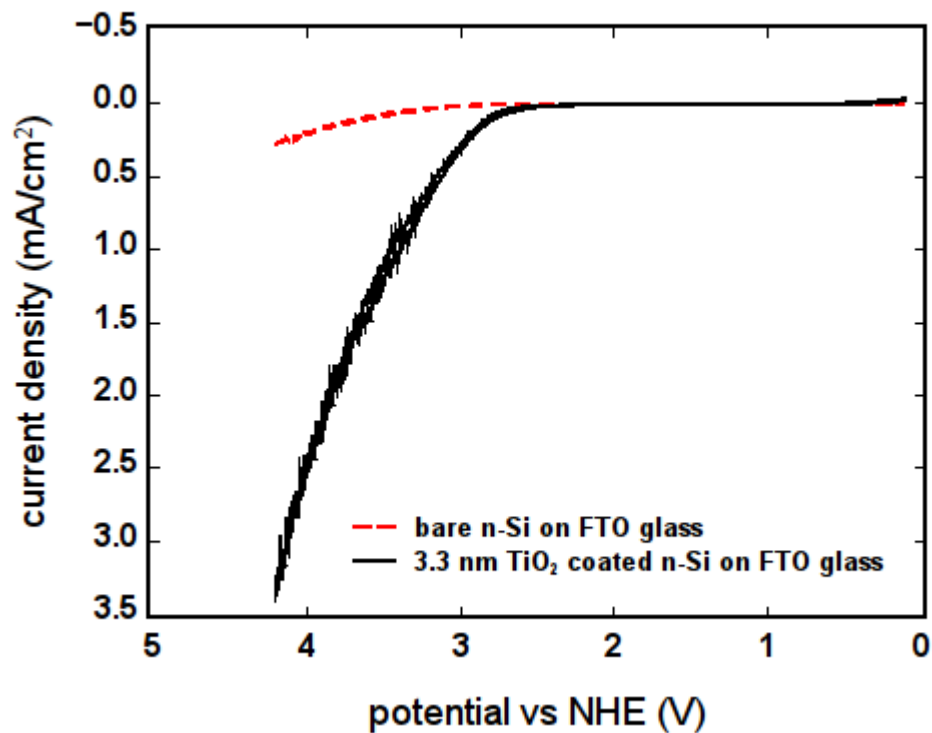


Figure A2.1.2. Voltammogram taken from bare (dashed line) and 3.3 nm ALD TiO₂ coated (solid line) n-Si electrodes on FTO substrates. Both traces show photoelectrochemical oxidation of water under solar illumination at a scan rate of 20 mV/s in 0.5M H₂SO₄. A single sweep is shown.

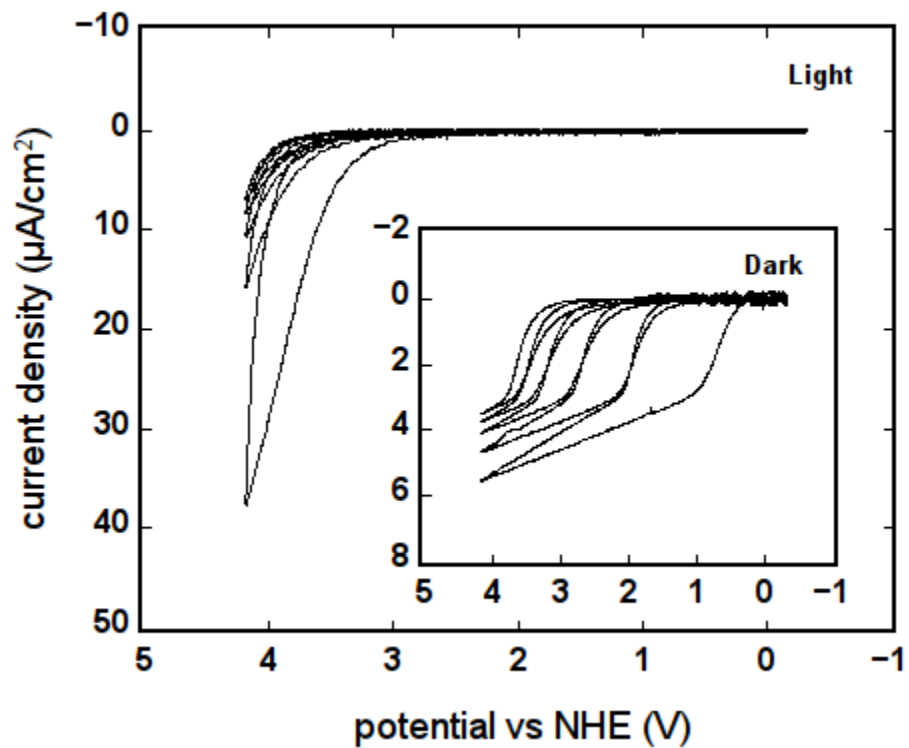


Figure A2.1.3. A typical voltammogram from a ZnO coated n-Si photoanode taken at 20 mV/s in 0.5M H₂SO₄. Here the coating thickness is 0.8 nm. Inset shows current-potential characteristics in dark. Five sweeps are shown for each plot.

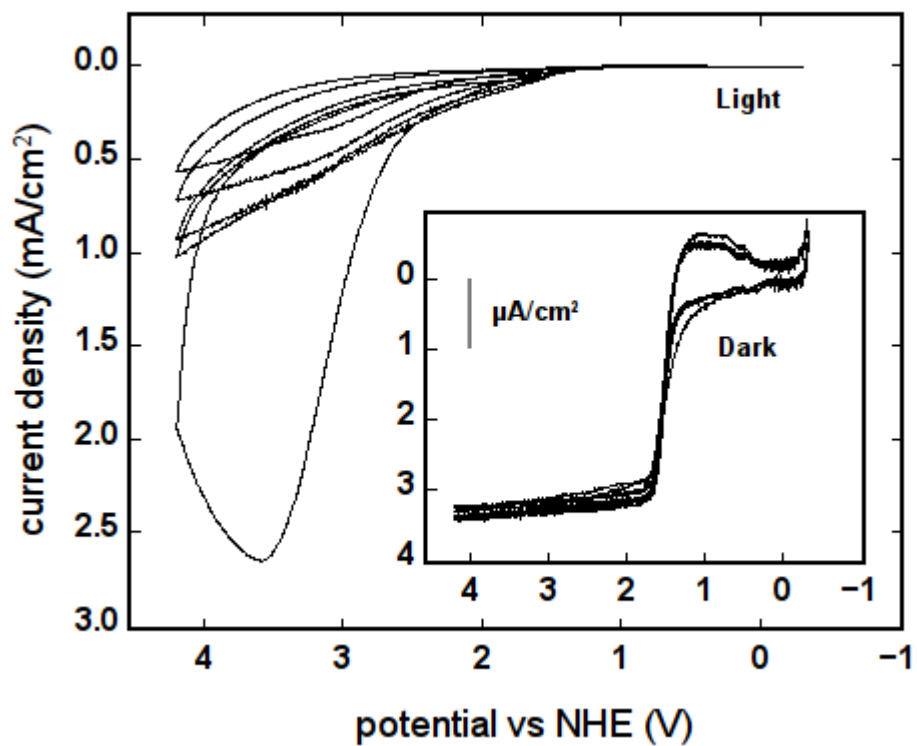


Figure A2.1.4. Voltammogram from a TiO₂ coated n-Si photoanode taken at 100 mV/s in 0.5M H₂SO₄. The ALD TiO₂ coating is 1.9 nm thick with a 1.4 nm catalytic Co metal layer on top. Prior to catalyst deposition, the metal oxide film was annealed at 450°C for 30 minutes. Inset shows dark current-potential characteristics with a different current scale. Five sweeps are shown for each plot.

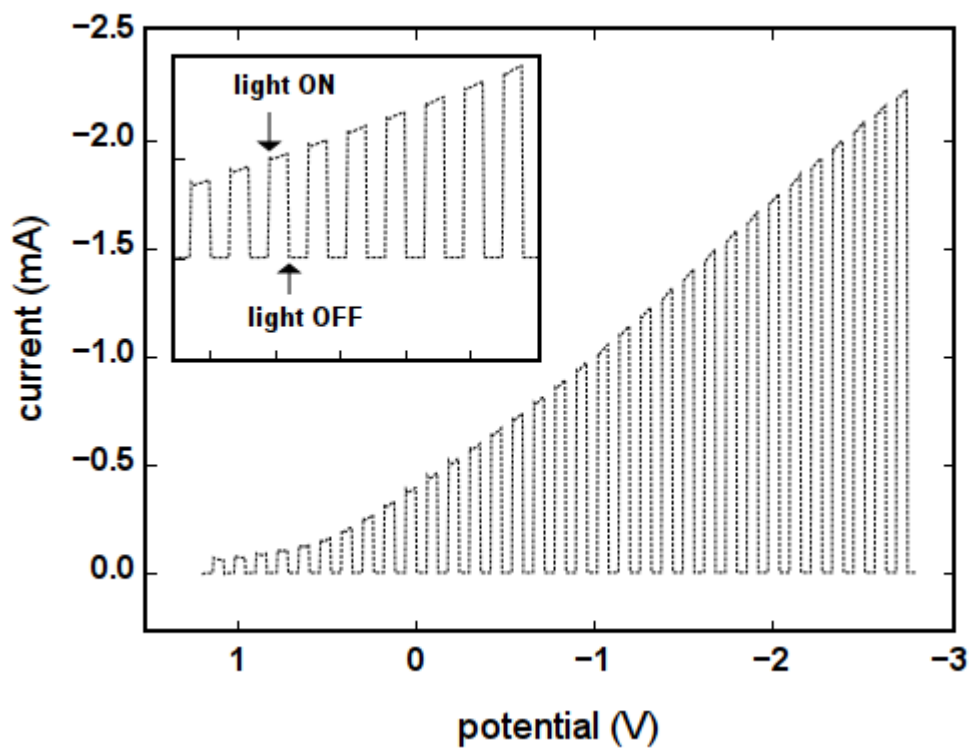


Figure A2.1.4. Two-electrode voltammogram from a photovoltaic-photoelectrochemical tandem device with light chopping every 3 seconds. Here a small ($\sim 1 \text{ cm}^2$) p-Si electrode is connected in series with an a-Si off-the-shelf solar cell. The solar cell supplies about 2.4 V of potential to the electrode driving proton reduction in an acidic environment (0.5M H_2SO_4). The staircase pattern shows the effect of light chopping.

Table A2.1. Ellipsometry results from bare and passivated n-Si photoanodes constructed on Ag-coated glass back contacts. Oxide growth was measured as the difference between native SiO₂ thickness before and after each electrochemical measurement. Dark and light measurements each consisted of 5 sweeps from -0.5 to 4 V and back to -0.5 V vs Ag/AgCl. The scan rate was 20 mV/s. A control electrode was also tested under the same conditions but not connected to the potentiostat. The control sample did not show any oxide growth.

Electrode Treatment	Oxide Growth in Dark (Å)	Oxide Growth in Light (Å)
Bare n-Si	10.58	15.34
Bare n ⁺ -Si	15.36	14.34
1.59 nm TiO ₂	N/A	19.99
1.78 nm TiO ₂	0	0
2.42 nm TiO ₂	0	0

A2.7 REFERENCES

1. Puurunen, R. L., *J. Appl. Phys.* 97 (12), 121301 (2005).
2. Elam, J. W. & George, S. M., *Chem Mater.*, 15 (4), 1020 (2003).
3. King, D. M., Johnson, S., Li, J., Du, X., Liang, X., & Weimer, A. W., *Nanotechnology*, 20 (19), 195401 (2009).
4. Li, J., Liang, X., King, D. M., Jiang, Y., & Weimer, A. W., *Appl. Cat. B: Env.*, 97 (1-2), 220 (2010).
5. Cleveland, E. R., Banerjee, P., Perez, I., Lee, S. B. & Rubloff, G. W., *ACS Nano*, 4 (8), 4637-44 (2010).
6. Knez, M., Nielsch, K., & Niinistö, L. *Advanced Materials*, 19 (21), 3425 (2008).
7. Chen, Y. W., Prange, J. D., Dühren, S., Park, Y., Gunji, M., D, C. E., et al. *Nat Mater*, 10 (7), 539-44 (2011).
8. Hardee, K. L., & Bard, A. J. *Journal of the Electrochemical Society* , 122 (6), 739-742 (1975).
9. Ciampi, S., Eggers, P. K., Saux, G. L., James, M., Harper, J. B., & Gooding, J. J. *Langmuir*, 25 (4), 2530-9 (2009).
10. Lin, Y., Zhou, S., Liu, X., Sheehan, S., & Wang, D. *JACS*, 131 (8), 2772-3 (2009).
11. Paracchino, A., Laporte, V., Sivula, K., Grätzel, M., & Thimsen, E. *Nat Mater*, 10 (6), 456-61 (2011).
12. H, J. J., Winkler, M. T., Surendranath, Y., Buonassisi, T., & Nocera, D. G. *PNAS.*, 108 (25), 10056-61 (2011).
13. Fujishima, A., & Honda, K. *Nature*, 238 (5358), 37 (1972).
14. Lewerenz, H. *Electrochimica Acta* , 37 (5), 847 (1992).

Appendix B. Co-authored publications

APPENDIX B1. Stable anatase TiO₂ coating on quartz fibers by atomic layer deposition for photoactive light-scattering in dye-sensitized solar cells*

Quartz fibers provide a unique high surface-area substrate suitable for conformal coating using atomic layer deposition (ALD), and are compatible with high temperature annealing. This paper shows that the quartz fiber composition stabilizes ALD TiO₂ in the anatase phase through TiO₂-SiO₂ interface formation, even after annealing at 1050 °C. When integrated into a dye-sensitized solar cell, the TiO₂-coated quartz fiber mat improves light scattering performance. Results also confirm that annealing at high temperature is necessary for better photoactivity of ALD TiO₂, which highlights the significance of quartz fibers as a substrate. The ALD TiO₂ coating on quartz fibers also boosts dye adsorption and photocurrent response, pushing the overall efficiency of the dye-cells from 6.5 to 7.4%. The mechanisms for improved cell performance are confirmed using wavelength-dependent incident photon to current efficiency and diffuse light scattering results. The combination of ALD and thermal processing on quartz fibers may enable other device structures for energy conversion and catalytic reaction applications.

*Do Han Kim, Hyung-Jun Koo, Jesse S. Jur, Mariah Woodroof, Berc Kalanyan, Kyoungmi Lee, Christina K. Devine and Gregory N. Parsons. *Nanoscale*, 2012, 4, pp 4731-4738

Appendix B. Co-authored publications

APPENDIX B2. Stabilization of $[\text{Ru}(\text{bpy})_2(4,4'-(\text{PO}_3\text{H}_2)\text{bpy})]^{2+}$ on Mesoporous TiO_2 with Atomic Layer Deposition of Al_2O_3 *

This article does not have an abstract.

*Kenneth Hanson, Mark D. Losego, Berc Kalanyan, Dennis L. Ashford, Gregory N. Parsons, and Thomas J. Meyer. *Chemistry of Materials* 2013, 25, pp 3–5.

APPENDIX B3. Solution-Processed, Antimony-Doped Tin Oxide Colloid Films Enable High-Performance TiO₂ Photoanodes for Water Splitting*

Photoelectrochemical (PEC) water splitting and solar fuels hold great promise for harvesting solar energy. TiO₂-based photoelectrodes for water splitting have been intensively investigated since 1972. However, solar-to-fuel conversion efficiencies of TiO₂ photoelectrodes are still far lower than theoretical values. This is partially due to the dilemma of a short minority carrier diffusion length, and long optical penetration depth, as well as inefficient electron collection. We report here the synthesis of TiO₂ PEC electrodes by coating solution-processed antimony-doped tin oxide nanoparticle films (nanoATO) on FTO glass with TiO₂ through atomic layer deposition. The conductive, porous nanoATO film-supported TiO₂ electrodes, yielded a highest photocurrent density of 0.58 mA/cm² under AM 1.5G simulated sunlight of 100 mW/cm². This is approximately 3× the maximum photocurrent density of planar TiO₂ PEC electrodes on FTO glass. The enhancement is ascribed to the conductive interconnected porous nanoATO film, which decouples the dimensions for light absorption and charge carrier diffusion while maintaining efficient electron collection. Transient photocurrent measurements showed that nanoATO films reduce charge recombination by accelerating transport of photoelectrons through the less defined conductive porous nanoATO network. Owing to the large band gap, scalable solution processed porous nanoATO films are promising as a framework to replace other conductive scaffolds for PEC electrodes.

*Qing Peng, Berc Kalanyan, Paul G. Hoertz, Andrew Miller, Do Han Kim, Kenneth Hanson, Leila Alibabaei, Jie Liu, Thomas J. Meyer, Gregory N. Parsons, and Jeffrey T. Glass. *Nano Lett.*, 2013, 13 (4), pp 1481–1488.

APPENDIX B4. Stabilizing Small Molecules on Metal Oxide Surfaces Using Atomic Layer Deposition*

Device lifetimes and commercial viability of dye-sensitized solar cells (DSSCs) and dye-sensitized photoelectrosynthesis cells (DSPECs) are dependent on the stability of the surface bound molecular chromophores and catalysts. Maintaining the integrity of the solution-metal oxide interface is especially challenging in DSPECs for water oxidation where it is necessary to perform high numbers of turnovers, under irradiation in an aqueous environment. In this study, we describe the atomic layer deposition (ALD) of TiO₂ on nanocrystalline TiO₂ prefunctionalized with the dye molecule [Ru(bpy)₂(4,4'-(PO₃H₂)bpy)]²⁺ (RuP) as a strategy to stabilize surface bound molecules. The resulting films are over an order of magnitude more photostable than untreated films and the desorption rate constant exponentially decreases with increased thickness of ALD TiO₂ overlayers. However, the injection yield for TiO₂-RuP with ALD TiO₂ also decreases with increasing overlayer thickness. The combination of decreased injection yield and 95% quenched emission suggests that the ALD TiO₂ overlayer acts as a competitive electron acceptor from RuP*, effectively nonproductively quenching the excited state. The ALD TiO₂ also increases back electron transfer rates, relative to the untreated film, but is independent of overlayer thickness. The results for TiO₂-RuP with an ALD TiO₂ overlayer are compared with similar films having ALD Al₂O₃ overlayers.

*Kenneth Hanson, Mark D. Losego, Berc Kalanyan, Gregory N. Parsons, and Thomas J. Meyer. *Nano Lett.*, 2013, 13 (10), pp 4802–4809.

Appendix B. Co-authored publications

APPENDIX B5. Three-dimensional self-assembled photonic crystals with high temperature stability for thermal emission modification*

Selective thermal emission in a useful range of energies from a material operating at high temperatures is required for effective solar thermophotovoltaic energy conversion. Three-dimensional metallic photonic crystals can exhibit spectral emissivity that is modified compared with the emissivity of unstructured metals, resulting in an emission spectrum useful for solar thermophotovoltaics. However, retention of the three-dimensional mesostructure at high temperatures remains a significant challenge. Here we utilize self-assembled templates to fabricate high-quality tungsten photonic crystals that demonstrate unprecedented thermal stability up to at least 1,400 °C and modified thermal emission at solar thermophotovoltaic operating temperatures. We also obtain comparable thermal and optical results using a photonic crystal comprising a previously unstudied material, hafnium diboride, suggesting that refractory metallic ceramic materials are viable candidates for photonic crystal-based solar thermophotovoltaic devices and should be more extensively studied.

*Kevin A. Arpin, Mark D. Losego, Andrew N. Cloud, Hailong Ning, Justin Mallek, Nicholas P. Sergeant, Linxiao Zhu, Zongfu Yu, Berc Kalanyan, Gregory N. Parsons, Gregory S. Girolami, John R. Abelson, Shanhui Fan, Paul V. Braun. *Nature Communications* 4, pp 2630.

Appendix B. Co-authored publications

APPENDIX B6. Solar water splitting in a molecular photoelectrochemical cell*

Artificial photosynthesis and the production of solar fuels could be a key element in a future renewable energy economy providing a solution to the energy storage problem in solar energy conversion. We describe a hybrid strategy for solar water splitting based on a dye sensitized photoelectrosynthesis cell. It uses a derivatized, core-shell nanostructured photoanode with the core a high surface area conductive metal oxide film—indium tin oxide or antimony tin oxide—coated with a thin outer shell of TiO₂ formed by atomic layer deposition. A “chromophore-catalyst assembly” **1**, [(PO₃H₂)₂bpy)₂Ru(4-Mebpy-4-bimpy)Ru(tpy)(OH₂)]⁴⁺, which combines both light absorber and water oxidation catalyst in a single molecule, was attached to the TiO₂ shell. Visible photolysis of the resulting core-shell assembly structure with a Pt cathode resulted in water splitting into hydrogen and oxygen with an absorbed photon conversion efficiency of 4.4% at peak photocurrent.

*Leila Alibabaei, M. Kyle Brennaman, Michael R. Norris, Berc Kalanyan, Wenjing Song, Mark D. Losego, Javier J. Concepcion, Robert A. Binstead, Gregory N. Parsons, and Thomas J. Meyer. PNAS, 2013, 110 (50), pp 20008-20013.

Appendix B. Co-authored publications

APPENDIX B7. Crossing the divide between homogeneous and heterogeneous catalysis in water oxidation*

Enhancing the surface binding stability of chromophores, catalysts, and chromophore–catalyst assemblies attached to metal oxide surfaces is an important element in furthering the development of dye sensitized solar cells, photoelectrosynthesis cells, and interfacial molecular catalysis. Phosphonate-derivatized catalysts and molecular assemblies provide a basis for sustained water oxidation on these surfaces in acidic solution but are unstable toward hydrolysis and loss from surfaces as the pH is increased. Here, we report enhanced surface binding stability of a phosphonate-derivatized water oxidation catalyst over a wide pH range (1–12) by atomic layer deposition of an overlayer of TiO₂. Increased stability of surface binding, and the reactivity of the bound catalyst, provides a hybrid approach to heterogeneous catalysis combining the advantages of systematic modifications possible by chemical synthesis with heterogeneous reactivity. For the surface-stabilized catalyst, greatly enhanced rates of water oxidation are observed upon addition of buffer bases. Graphic and with a pathway identified in which O-atom transfer to OH[−] occurs with a rate constant increase of 10⁶ compared to water oxidation in acid.

*Aaron K. Vannucci, Leila Alibabaei, Mark D. Losego, Javier J. Concepcion, Berc Kalanyan, Gregory N. Parsons, and Thomas J. Meyer, PNAS, 2013, 110 (52), pp 20918-20922.

Appendix B. Co-authored publications

APPENDIX B8. Atomic Layer Deposition of TiO₂ on Mesoporous nanoITO: Conductive Core–Shell Photoanodes for Dye-Sensitized Solar Cells*

Core–shell structures consisting of thin shells of conformal TiO₂ deposited on high surface area, conductive Sn-doped In₂O₃ nanoparticle. Mesoscopic films were synthesized by atomic layer deposition and studied for application in dye-sensitized solar cells. Results obtained with the N719 dye show that short-circuit current densities, open-circuit voltages, and back electron transfer lifetimes all increased with increasing TiO₂ shell thickness up to 1.8–2.4 nm and then decline as the thickness was increased further. At higher shell thicknesses, back electron transfer to –Ru^{III} is increasingly competitive with transport to the nanoITO core resulting in decreased device efficiencies.

*Leila Alibabaei, Byron H. Farnum, Berc Kalanyan, M. Kyle Brennaman, Mark D. Losego, Gregory N. Parsons, and Thomas J. Meyer. *Nano Lett.*, 2014, 14 (6), pp 3255–3261.